



DFT STUDIES ON POLYOXOPALLADATES AND POLYOXOMETALATES-SURFACE COMPOSITES: FROM STRUCTURE TO CATALYSIS

Zhongling Lang

ADVERTIMENT. L'accés als continguts d'aquesta tesi doctoral i la seva utilització ha de respectar els drets de la persona autora. Pot ser utilitzada per a consulta o estudi personal, així com en activitats o materials d'investigació i docència en els termes establerts a l'art. 32 del Text Refós de la Llei de Propietat Intel·lectual (RDL 1/1996). Per altres utilitzacions es requereix l'autorització prèvia i expressa de la persona autora. En qualsevol cas, en la utilització dels seus continguts caldrà indicar de forma clara el nom i cognoms de la persona autora i el títol de la tesi doctoral. No s'autoritza la seva reproducció o altres formes d'explotació efectuades amb finalitats de lucre ni la seva comunicació pública des d'un lloc aliè al servei TDX. Tampocs'autoritza la presentació del seu contingut en una finestra o marc aliè a TDX (framing). Aquesta reserva de drets afecta tant als continguts de la tesi com als seus resums i índexs.

ADVERTENCIA. El acceso a los contenidos de esta tesis doctoral y su utilización debe respetar los derechos de la persona autora. Puede ser utilizada para consulta o estudio personal, así como en actividades o materiales de investigación y docencia en los términos establecidos en el art. 32 del Texto Refundido de la Ley de Propiedad Intelectual (RDL 1/1996). Para otros usos se requiere la autorización previa y expresa de la persona autora. En cualquier caso, en la utilización de sus contenidos se deberá indicar de forma clara el nombre y apellidos de la persona autora y el título de la tesis doctoral. No se autoriza su reproducción u otras formas de explotación efectuadas con fines lucrativos ni su comunicación pública desde un sitio ajeno al servicio TDR. Tampoco se autoriza la presentación de su contenido en una ventana o marco ajeno a TDR (framing). Esta reserva de derechos afecta tanto al contenido de la tesis como a sus resúmenes e índices.

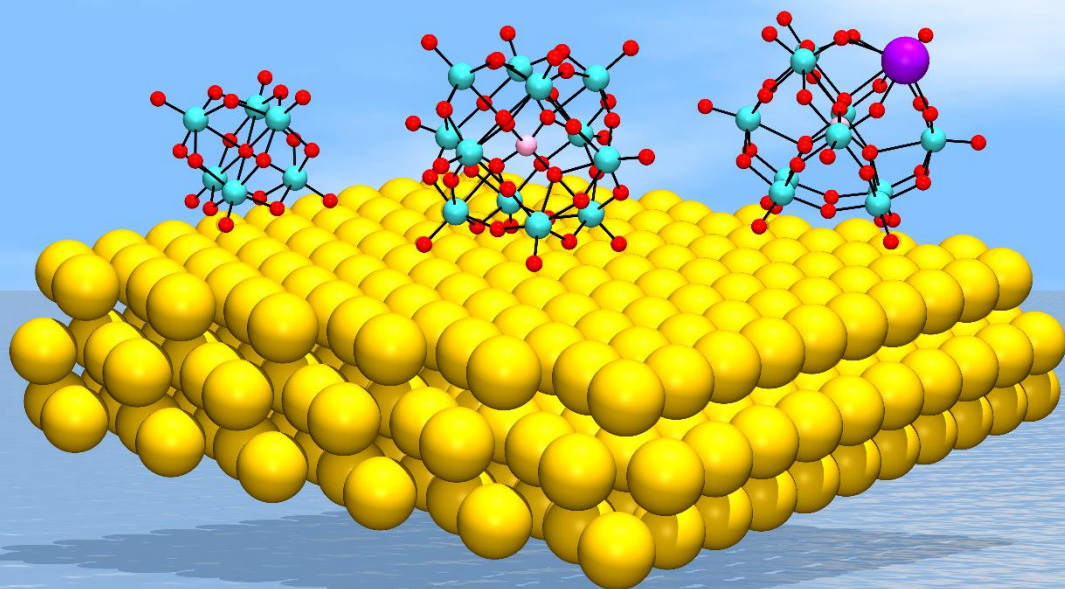
WARNING. Access to the contents of this doctoral thesis and its use must respect the rights of the author. It can be used for reference or private study, as well as research and learning activities or materials in the terms established by the 32nd article of the Spanish Consolidated Copyright Act (RDL 1/1996). Express and previous authorization of the author is required for any other uses. In any case, when using its content, full name of the author and title of the thesis must be clearly indicated. Reproduction or other forms of for profit use or public communication from outside TDX service is not allowed. Presentation of its content in a window or frame external to TDX (framing) is not authorized either. These rights affect both the content of the thesis and its abstracts and indexes.



UNIVERSITAT
ROVIRA I VIRGILI

DFT Studies on Polyoxopalladates and Polyoxometalate-surface Composites: From Structure to Catalysis

Zhongling Lang



DOCTORAL THESIS
2017

DOCTORAL THESIS

DFT Studies on Polyoxopalladates and Polyoxometalate-surface Composites: From Structure to Catalysis

Zhongling Lang

Supervised by Dr. Anna Clotet Romeu
and Prof. Dr. Josep Maria Poble Rius

Departament de Química Física i Inorgànica

Grup de Química Quàntica



UNIVERSITAT ROVIRA I VIRGILI

Tarragona, May 2017



UNIVERSITAT
ROVIRA I VIRGILI

DEPARTAMENT DE QUÍMICA FÍSICA I INORGÀNICA

Anna Clotet Romeu, Professora Titular del Departament de Química Física i Inorgànica de la Universitat Rovira i Virgili i Josep Maria Poblet Rius, Catedràtic del Departament de Química Física i Inorgànica de la Universitat Rovira i Virgili.

FEM CONSTAR


que la present memòria, titulada “DFT Studies on Polyoxopalladates and Polyoxometalate-surface Composites: From Structure to Catalysis” ha estat realitzada sota la nostra direcció al Departament de Química Física i Inorgànica de la Universitat Rovira i Virgili per Zhongling Lang per a optar al títol de Doctor.

Tarragona, 31 de maig de 2017

Dra. Anna Clotet Romeu

Prof. Josep M. Poblet Rius

List of Publications

 **The results of this PhD thesis have delivered the following publications:**

1. **Zhongling Lang**, Xavier Aparicio-Anglès, Ira Weinstock, Anna Clotet, Josep M. Poblet, “Counter-intuitive Adsorption of $[\text{PW}_{11}\text{O}_{39}]^{7-}$ on Au(100)”, *Inorg. Chem.* **2017**, 56, 3961–3969.
2. Peng Yang, Yixian Xiang, Zhengguo Lin, Bassem S. Bassil, **Zhongling Lang**, Pablo Jiménez-Lozano, Jorge J. Carbó, Josep M. Poblet, Linyuan Fan, Jie Cao, and Ulrich Kortz, “Discrete Silver(I) - Palladium(II) - Oxo Nanoclusters, $\{\text{Ag}_4\text{Pd}_{13}\}$ and $\{\text{Ag}_5\text{Pd}_{15}\}$, and the Role of Metal-Metal Bonding Induced by Cation Confinement”, *Angew. Chem. Int. Ed.* **2016**, 55, 15766–15770.
3. **Zhongling Lang**, Isabel Maicas Gabas, Xavier López, Anna Clotet, Jesús M. de la Fuente, Scott G. Mitchell, Josep M. Poblet, “On the formation of gold nanoparticles from $[\text{Au}^{\text{III}}\text{Cl}_4]^-$ and a non-classical reduced polyoxomolybdate as an electron source: a quantum mechanical modelling and experimental study”, *New J. Chem.*, **2016**, 40, 1029–1038.
4. **Zhongling Lang**, Peng Yang, Jorge J. Carbó, Ulrich Kortz, and Josep M. Poblet, “Monitoring the Template Effect of Internal Cations in the Formation of Polyoxopalladates”, *in preparation*.
5. **Zhongling Lang**, Anna Clotet and Josep M. Poblet, “Origin and Catalytic Activity of Polyoxometalate-Au(111) Catalyst for Water-Gas-Shift Reaction”, *in preparation*.

6. Manoj Raula, Adam Weingarten, Gal Gan Or, **Zhongling Lang**, Josep M. Poblet and Ira A. Weinstock, “Ligand Controlled Hydrogen Evolution by Water-Soluble Complexes of Anatase-TiO₂ Cores”, *in preparation*.

Publications non-related with this thesis:

1. Roy E. Schreiber, Lothar Houben, Sharon G. Wolf, Gregory Leitus, **Zhongling Lang**, Jorge J. Carbó, Josep M. Poblet, Ronny Neumann, “Real-Time Molecular Scale Observation of Crystal Formation”, *Nat. Chem.*, **2017**, 9, 369-373.
2. Qi Zheng, Laia Vilà-Nadal, Vihar P. Georgiev, **Zhongling Lang**, De-Liang Long, Alexander Angelov, Jennifer S. Mathieson, Josep M. Poblet and Leroy Cronin, Heteroatom Dopant Selection Leads to Self-Sorting and Self-Assembly of Nano-Scale Cross-Bar Polyoxometalate Clusters with Transport Properties, *submitted*.

Chemistry is no longer a purely experimental science——

Nobel Prize winner : John A. Pople

UNIVERSITAT ROVIRA I VIRGILI

DFT STUDIES ON POLYOXOPALLADATES AND POLYOXOMETALATES-SURFACE COMPOSITES: FROM STRUCTURE TO CATALYSIS

Zhongling Lang

Contents

Abstract	1
Chapter 1: Introduction and Scope of the Thesis	3
1.1 Overview of polyoxometalates	5
1.2 Structure and topology	6
1.2.1 Classical structures	6
1.2.2 Lacunary structures	7
1.2.3 Novel structures	9
1.3 Properties and applications	11
1.3.1 POMs in batteries	11
1.3.2 POMs in water oxidation	12
1.4 POMs based materials in nanoscience	14
1.4.1 POM hybrids in microelectronics/molecular electronics	14
1.4.2 POM monolayer on planar surfaces	15
1.4.3 POMs on nanoparticles	17
1.5 Computational development of POMs	17
1.6 Scope of the thesis	19
Chapter 2: Computational Methodology	27
2.1 The Schrödinger equation	29
2.2 Brief introduction of density functional theory	30
2.2.1 The Kohn-Sham equations	30
2.2.2 The local density approximation for $E_{xc}[\rho]$	31
2.2.3 The generalized gradient approximation for $E_{xc}[\rho]$	32
2.3 Implementation of continuum solvent model in the calculation	32
2.4 Main softwares	34
2.4.1 Gaussian	34
2.4.2 Vienna Ab initio Simulation Package	34
Chapter 3: The Template Effects of Internal and External Cations in Polyoxopalladates	39
3.1 Introduction and background	41

3.2	Motivation and objectives.....	43
3.3	Computational method.....	43
3.3.1	Computational details for internal cation encapsulation.....	44
3.3.2	Computational details for Ag-Pd interactions	45
3.4	The template effect of internal cations	45
3.4.1	Size matching between the cations and the bare Pd _{12/15}	46
3.4.2	Complexation energy and the competition between Pd ²⁺ and other metal cations	49
3.4.3	Potential new candidates for the 12-palladate family	52
3.4.4	Experiments confirm theoretical observations: Synthesis and characterization of cuboid-shaped LaPd ₁₂₋₁ , GaPd ₁₂ , InPd ₁₂ and open-shell type LaPd ₁₂₋₂	53
3.4.5	Selective entrapment of Ga ³⁺ and In ³⁺ in Pd ₁₂ host.....	54
3.4.6	What properties of the metal cation govern its affinity for a given Pd ₁₂ ?	55
3.5	The role of metal–metal bonding induced by cation confinement	57
3.5	Conclusions	63
Appendix Chapter 3.....		69
Chapter 4: A Non-classical Polyoxomolybdate as an Electron Source for [Au^{III}Cl₄] Reduction		77
4.1	Introduction	79
4.2	Motivation and objectives.....	79
4.3	Computational details	80
4.4	Results and discussions	81
4.4.1	Selection of the POM model.....	81
4.4.2	Possible mechanisms of {H ₃ S ₄ Mo ₆ }-mediated Au ^{III} to Au ^I reduction ..	82
4.4.3	Au ^I to Au ⁰ step.....	89
4.4.4	Persistence of POM activity until full oxidation	91
4.5	Conclusions	93
Appendix Chapter 4.....		97
Chapter 5: Effect of Solvent and Cation on the Lindqvist/Keggin-surface Composites		99
5.1	Introduction and background.....	101

5.2	Computational details	102
5.3	Results and discussions	103
5.3.1	Solvent effects on the isolated POMs and bare slabs	103
5.3.2	Solvent and cation effects for a combined system—the low charged $[\text{Mo}_6\text{O}_{19}]^{2-}$ on Au(111)	105
5.3.3	Extending the modeling to moderate charged $\alpha\text{-}[\text{SiW}_{12}\text{O}_{40}]^{4-}$ on the silver/gold surfaces.....	111
5.4	Conclusions	113
Chapter 6: Counter-intuitive Adsorption of $[\text{PW}_{11}\text{O}_{39}]^{7-}$ on Au(100)		117
6.1	Introduction and background.....	119
6.2	Computational details and models.....	120
6.2.1	Computational details.....	120
6.2.2	Models	121
6.3	Results and discussions	123
6.3.1	Cation distribution around the $[\text{PW}_{11}\text{O}_{39}]^{7-}$ anion.....	123
6.3.2	Adsorption of $\text{K}_7\text{PW}_{11}\text{O}_{39}$ on the Au(100) surface.....	125
6.3.3	Affinity of Au(100) for PW_{11}	128
6.3.4	The origin of the counter-intuitive adsorption.....	129
6.3.5	Electronic structure.....	131
6.3.6	The effect of explicit water for the electronic properties	132
6.3.7	The modeling of $[\text{PW}_{11}\text{O}_{39}]^{7-}$ on silver.....	133
6.4	Conclusions	134
Appendix Chapter 6.....		138
Chapter 7: WGSR Cocatalyzed by the POM-gold Composites: The Magic Role of the POMs		141
7.1	Introduction	143
7.2	Computational details and models.....	144
7.2.1	DFT parameters	144
7.2.2	Models	145
7.3	Results and discussions	146
7.3.1	Formation of POM-metal interface	146
7.3.2	Stability of adsorbed intermediates	148

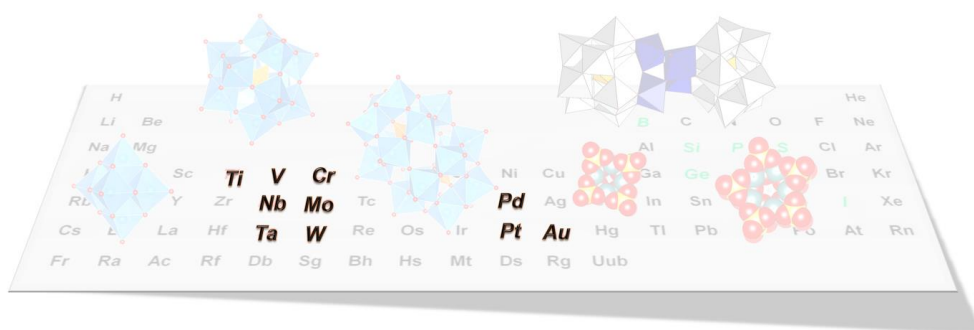
7.3.3	WGSR mechanism on clean Au(111).....	149
7.3.4	Activation of H ₂ O by PMo ₁₂ -Au(111).....	150
7.3.5	Solvation effects on H ₂ O activation.....	153
7.3.6	CO oxidation steps.....	154
7.3.7	Complete reaction network.....	157
7.3.8	The activity of PW ₁₂ -Au(111).....	158
7.4	Conclusions.....	160
Appendix Chapter 7.....		164
Chapter 8: DFT and TD-DFT Calculations for Polyoxometalate-TiO₂ Interface		165
8.1	Introduction and experimental background.....	167
8.2	Computational details.....	168
8.2.1	Models.....	168
8.2.2	Methodology.....	169
8.3	Results and discussions.....	170
8.3.1	Bulk anatase TiO ₂ and clean TiO ₂ (101).....	170
8.3.2	Affinity of TiO ₂ (101) for PW ₁₁ Ti (PW ₁₁ Ti ^{1e}).....	171
8.3.3	Change in electronic structure of TiO ₂ by POM adsorption.....	174
8.3.4	UV-vis spectrum simulation.....	175
8.4	Conclusions.....	179
Chapter 9: Concluding Remarks		183
Acknowledgements		187

Abstract

The overall goal of the present thesis is to rationalize electronic properties of polyoxopalladates and to provide an efficient computational strategy for studying polyoxometalates (POMs) deposited onto surfaces. POMs are molecular metal oxides of transition metals. The first research chapter (chapter 3) deals with the analysis of the cation competition for occupying the central position in a polyoxopalladate. We have studied in detail how the size and charge of the cation control the formation of MPd_{12} clusters. The accurate analysis has allowed to predict the stability of new clusters, some of them have been already synthesized and characterized by Prof. Körtz in Jacobs University. The same group reported novel structures that contain Ag-Ag and Ag-Pd contacts. We have demonstrated that real metal-metal bonds are formed by electrostatic confinement. On the other hand, using a highly reduced POM (Kabanos type) we have discussed the reduction of Au(III) to Au(0) showing that the process is very favorable from a thermodynamic point of view. Four chapters of the thesis are dedicated to the analysis of POMs interacting with surfaces. In chapter 5 and 6, we propose an efficient strategy to study these composites, and applied it to the adsorption of “lacunary” PW_{11} on the gold and silver surfaces. In the last two chapters (chapter 7 and 8) we have explored two important processes. One is the water-gas-shift reaction co-catalyzed by PMo_{12} and Au(111). In addition to the fact that for the first time a heterogeneous catalyzed reaction containing a POM has been studied computationally in deep, we have found that the POM acts as an electron and proton acceptor reducing significantly the apparent activation energy of WGSR ($<10 \text{ kcal mol}^{-1}$). In chapter 8, we have shown that the weak absorption of TiO_2 in the visible region can be improved by the coordination of reduced PTiW_{11} anion to the surface. Simulation of the observed UV-*vis* spectrum suggests that the reduced PW_{11}Ti can transfer electrons to TiO_2 under visible light irradiation.

Chapter 1

Introduction and Scope of the Thesis



As an important family of inorganic metal oxides, polyoxometalate presided many interesting topics due to their unequalled and fascinating properties. This chapter presents a general review of the polyoxometalate world and some polyoxometalates based materials. The rapid development of polyoxometalate requires multi-perspective understandings from both experimental and theoretical. Some related theoretical examples are introduced. At the end of this chapter, the main goals of the thesis are presented.

1.1 Overview of polyoxometalates

Polyoxometalates (POMs) are one class of inorganic, anionic, and nano-sized metal-oxide clusters that have been investigated for about two centuries. As an outstanding class of metal oxo-cluster materials, they have attracted researchers not only chemistry, but also biology and physics. Acid condensation of simple metal oxides (MO_4^{n-} , $\text{M} = \text{W}^{\text{VI}}$, Mo^{VI} , V^{V} , *etc.*) in aqueous or non-aqueous solution is widely used for synthesizing of isopolyanions, and preparing heteropolyanions in the presence of heteroatom groups (XO_4^{n-} , $\text{X} = \text{P}$, Si , and As *etc.*).^[1] The pH condition is one of the most important factors for obtaining POMs. By far the largest number of examples are those containing Mo, W, and V metals in the structure, and less frequently based on Nb, Tb, and other transition or noble metals.

The chemistry of polyoxometalates has a long history and includes contributions from many illustrious scientists like Berzelius, Marginac, Werner, Pauling, and others.^[2] The first $[\text{PMo}_{12}\text{O}_{40}]^{3-}$ was reported by Berzelius in 1826,^[3] and its structure keeps a mystery until the 20th century when J. F. Keggin using *X-ray* diffraction experimentally determined the structure.^[4] However, the development of polyoxometalates was progressed not rapidly as we expected due to the lack of modern experimental techniques and synthetic approaches. Only 25 new X-ray structures were obtained during the following forty years as reviewed by T. H. Evans in 1971.^[5]

In 1991, Müller and Pope stated in a review, “*Polyoxometalates form a class of inorganic compounds that is unmatched in terms of molecular and electronic structural versatility, reactivity, and relevance to analytical chemistry, catalysis, biology, medicine, geochemistry, materials science, and topology*”.^[6] From then on, polyoxometalates started to rise in popularity. This was also promoted by a special issue of POMs in *Chemical Reviews* organized by Hill in 1998, which presented the history, developments, and applications covered by POM chemistry.^[7] The number of polyoxometalates has grown immensely, and now a large diversity of shapes and compositions of POMs have been synthesized and characterized. In order to understand the relationship between different cluster types, as shown in Figure 1.1 “*the polyoxometalate periodic table*” was built for the currently known polyoxometalates by Cronin *et al.* in a recent review.^[8] Therefore, polyoxometalate chemistry is indeed an old field but with new dimensions, which presenting us new and marvellous surprises day by day.

Chapter 1 Introduction and Scope of the Thesis

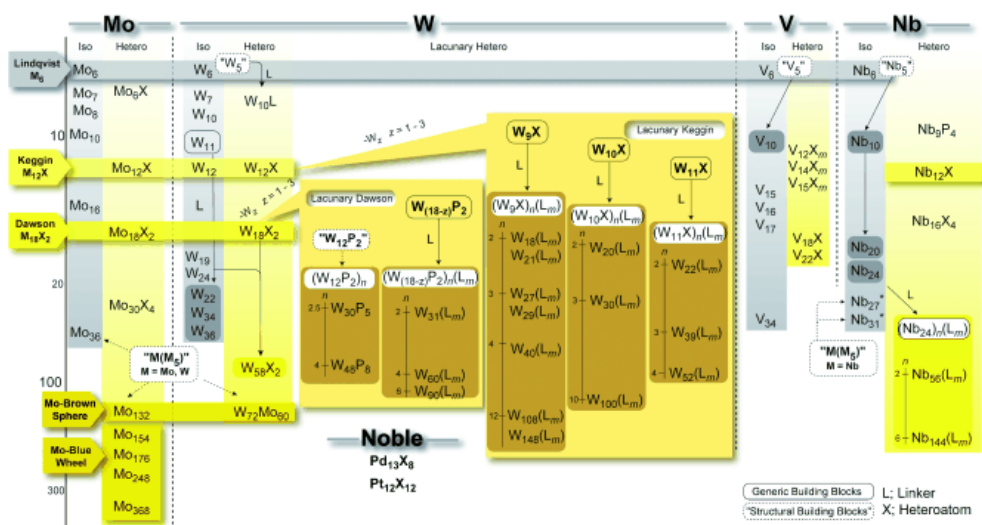


Figure 1.1. A classification for currently known polyoxometalate formulae from the work of Cronin *et al.*^[8]

1.2 Structure and topology

1.2.1 Classical structures

The polyoxometalates are generally governed by the building blocks MO_x through edges and vertexes sharing, in which M shows an octahedron or square pyramid coordination with the oxygen atoms. Nowadays, many thousands of polyoxometalate compounds with a vast range of shapes and sizes have been reported, and new structural types of polyanions continue to be discovered. Three of the most common structures are shown in Figure 1.2. The growing family of polyoxometalates can be divided into two subsets from composition view: *isopolyanions* (IPAs) and *heteropolyanions* (HPAs). The Lindqvist type (Figure 1.2a) is the simplest isopolyanions, where only transition metal and oxygen atoms are involved in the structure. The $[\text{Mo}_6\text{O}_{19}]^{2-}$ and $[\text{W}_6\text{O}_{19}]^{2-}$ compounds can be synthesized easily, whereas for V and Ta incooperated $[\text{M}_6\text{O}_{19}]^{8-}$ are unstable due to the high negative charge density. The Keggin structure $\alpha\text{-}[\text{XM}_{12}\text{O}_{40}]^{n-}$ (Figure 1.2b) is the first reported and most common one in heteropolyanions, which is composed of 12 vertex- and edge-sharing MO_6 ($\text{M} = \text{Mo}^{\text{VI}}$ and W^{VI}) octahedral surrounding a central XO_4 tetrahedron. Heteroatom X can be a wide range in periodic table, typically from IIIA, IVA, and VA groups, such as B^{3+} , Si^{4+} , P^{5+} *etc.* The topology of Keggin structure shows a tetrahedral (T_d) symmetry. Therefore, all 12 MO_6 units are arranged into four groups of three edge sharing M_3O_{13} units, which can lead to isomeric structures such as

Chapter 1 Introduction and Scope of the Thesis

β -, γ -, and ε -Keggin by rotating the M_3O_{13} units.^[9] When the atom ratio between heteroatom and metal increased from 1:12 to 2:18 in the structure, the Wells-Dawson (α - $[X_2M_{18}O_{62}]^{n-}$) type POMs are formed. These two types of POMs can derivative to many compounds. In addition to isomeric forms of the complete structure, the development of lacunary polyoxometalates based upon Keggin $\{M_{12-n}\}$ and Dawson $\{M_{18-n}\}$ is also a large research area.

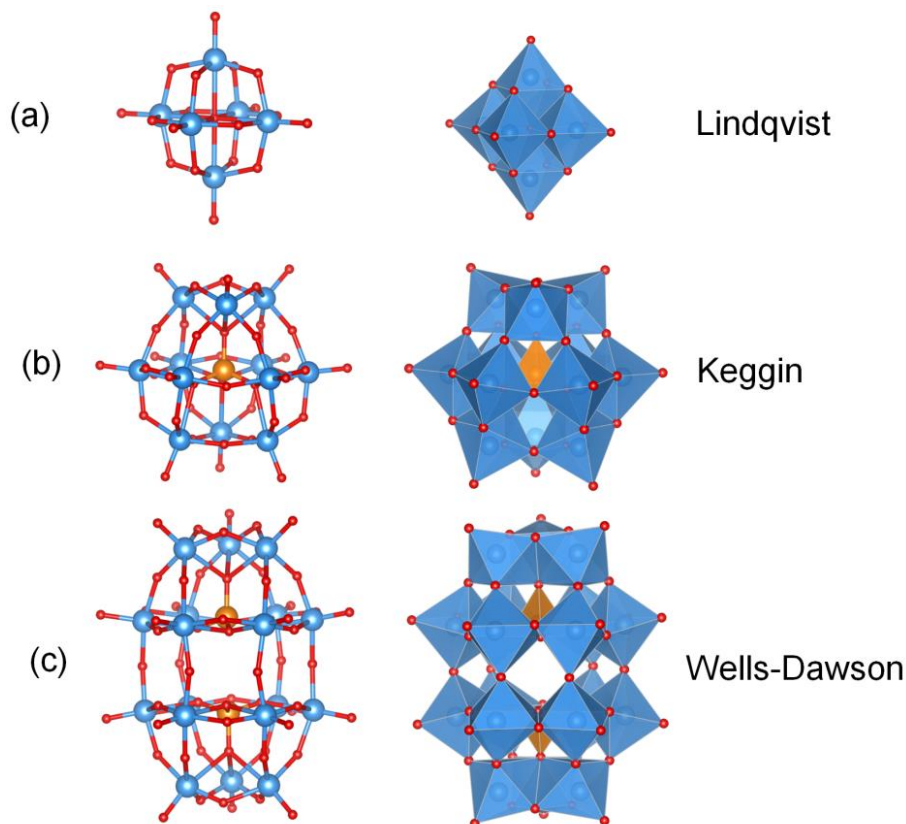


Figure 1.2. Ball-stick and polyhedral representations for three most common polyoxometalate structures. (a) Lindqvist anion: $[M_6O_{19}]^{6-}$; (b) $[\alpha\text{-}\{XO_4\}M_{12}O_{36}]^{6-}$:Keggin anion; (c) $[\alpha\text{-}\{XO_4\}_2M_{18}O_{54}]^{6-}$:Wells-Dawson structure.

1.2.2 Lacunary structures

The rapid progress of polyoxometalates is inseparable from the modification of the lacunary structures. POMs are known to be unstable in alkaline condition. The formation of the lacunary POMs is mainly pH dependent. Figure 1.3 shows an

Chapter 1 Introduction and Scope of the Thesis

example based on the Keggin polyanion. By controlling the pH of Keggin POMs involved solution will lead to some progressive degradations of the polyanion towards lacunary structures $\{M_{12-n}\}$, where 1, 2 or 3 octahedral units may be removed from the complete structures. The most two representative structures are the mono-lacunary $[PW_{11}O_{39}]^{7-}$ (PW_{11}) and three-lacunary $[PW_9O_{34}]^{9-}$ (PW_9). Similar behaviors are also occurred on Dawson type POMs. These lacunary species have generated a tremendous interest for researchers from structure to application. For example, the removal of one MO unit from the Keggin exposes a ‘cavity’, which resulting in a remarkable increase of the charge density in the defective region due to the four new formed oxygen ligands. This vacancy is proved much attractive for $[ML]^{n+}$ units ($M = Fe^{II/III}, Mn^{III/V}, Co^{II/III}, Zn^{II}, Ni^{II}, Ru^{II/III/IV/V}, etc.$; $L = O^{2-}, H_2O, \text{halide}, NH_3, \text{pyridine}, etc.$) to form transition metal-substituted Keggin POMs.^[10] The incorporation of a new metal in the cluster may bring significant electronic property changes, and consequently exhibit fantastic reactivity and electrochemistry. On the other hand, organic groups can also attach on the defect via electrostatic interactions, hydrogen bonds, van der Waals interactions, or covalent interactions to build the organic–inorganic POM hybrids.^[11,12]

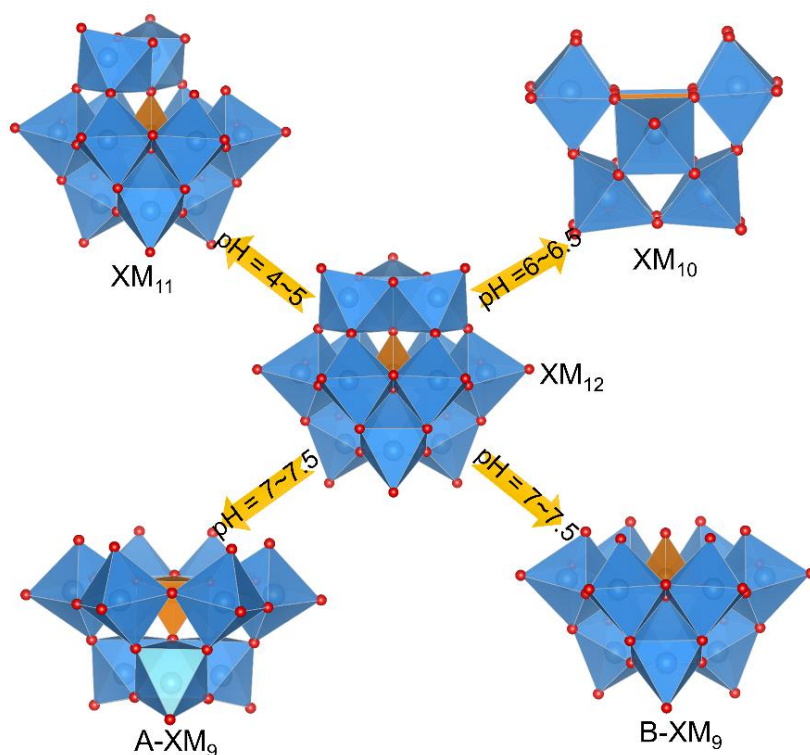


Figure 1.3. Different types of lacunary structures derived from parent Keggin unit.

Chapter 1 Introduction and Scope of the Thesis

1.2.3 Novel structures

Noble metals, a group which contains ruthenium, rhodium, palladium, silver, osmium, iridium, platinum and gold, have received particular attention in catalysis owing to the roles on automobile emission-control systems and clean fuels producing issues. However, most of the catalysts used in industrial are based on heterogeneous process. As proposed by Döbereiner, good models for noble metal catalysts require some oxygen atoms to obtain optimal activity.^[13] The combination of polyoxometalates with noble metals has gained special interests because it allows the noble metal ions soluble in aqueous or organic media. And at the same time encapsulated in a fully inorganic system can keep the thermal stability and redox. Except to incorporate the noble metal into classical W/Mo framework, an entirely new class of POMs with noble metals (to date palladium, platinum, and gold) act as the addenda atoms have been discovered and progressed rapidly in recent ten years.^[14]

In 2004, Wicklered *et al.* discovered and isolated a novel cluster anion $[\text{Pt}_{12}^{\text{III}}\text{O}_8(\text{SO}_4)_{12}]^{4-}$ that built exclusively of d^7 noble metal centers.^[15] As the crystallographic structure shown in Figure 1.4a, six $[\text{Pt}_2]^{6+}$ dumbbells are linked through oxide ions and sulfate groups with each Pt^{III} coordinated with five oxygens. From topology point of view, the short and long Pt–Pt distance character matches well the character of Mo–Mo in the conventional heteropolymolydates $[\text{X}^{\text{IV}}\text{Mo}_{12}\text{O}_{42}]^{8-}$ ($\text{X} = \text{Ce}, \text{Th}, \text{U}, \text{Np}$).^[16] In order to extend the compounds of this new family, Kortz's group from Jacobs University (Bremen, Germany) have developed a strategy for synthesizing of Pd and Au based polyoxoanions, which is generally constructed by condensation of tetra-aqua/hydroxo-complexes of these metals (mainly Pd and Au) in the presence of a heterogroup (As_2O_3 , PhAsO_3H_2 , SeO_2 etc.).^[14] Polyoxopalladates (POPd), in particular, represents by far the largest subclass of polyoxo-noble-metalates. The first reported compound is the distorted cubic $[\text{Pd}^{\text{II}}_{13}\text{As}_8^{\text{V}}\text{O}_{34}(\text{OH})_6]^{8-}$ (**Pd₁₃**) structure, composed of a central Pd^{II} ion surrounded by a shell of twelve Pd^{II} ions linked by eight inner oxo ligands and eight outer tetrahedral heterogroups.^[17] They obtained a lot of derivatives by decorating the central ions and capping groups. As shown in Figure 1.4b, all these Pd_{12} based compounds exhibit structural analogies to the famous Keggin anions, in which twelve peripheral palladium atoms form a distorted icosahedrons/cuboctahedron in the former, and twelve MO_6 octahedral units are found located on the vertices of the distorted cuboctahedron in Keggin. Beyond the **MPd₁₂** cluster, some high nuclearity polyoxopalladate compounds such as **Pd₁₅**, **Pd₁₇**, and **Pd₂₂** have also been synthesized and characterized.^[18] Furthermore, Cronin's group

Chapter 1 Introduction and Scope of the Thesis

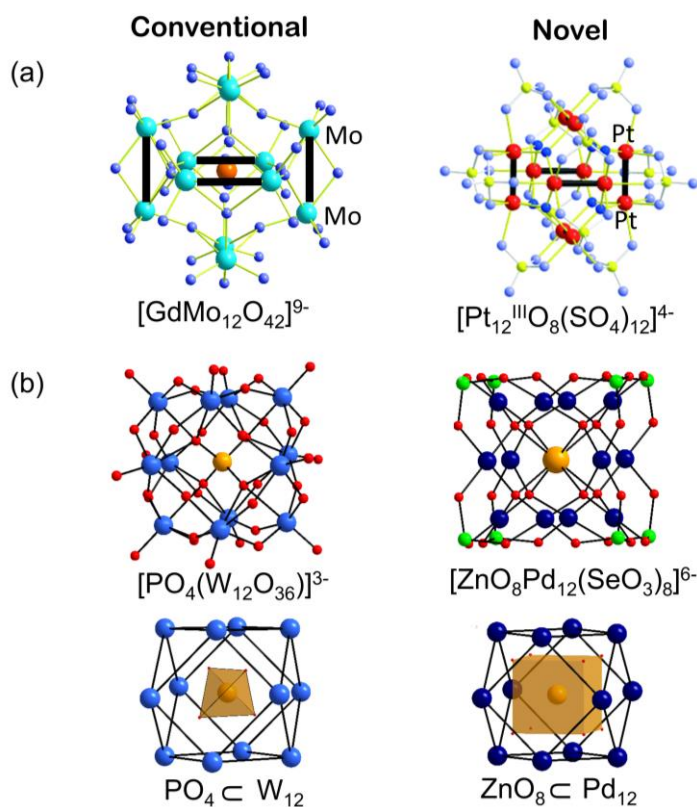


Figure 1.4 Structural comparison for conventional ($[\text{X}^{\text{IV}}\text{Mo}_{12}\text{O}_{42}]^{8-}$ and $[\text{PW}_{12}\text{O}_{40}]^{3-}$) and novel polyoxometalates ($[\text{Pt}_{12}^{\text{III}}\text{O}_8(\text{SO}_4)_{12}]^{4-}$ and $[\text{ZnO}_8\text{Pd}_{12}(\text{SeO}_3)_8]^{6-}$).

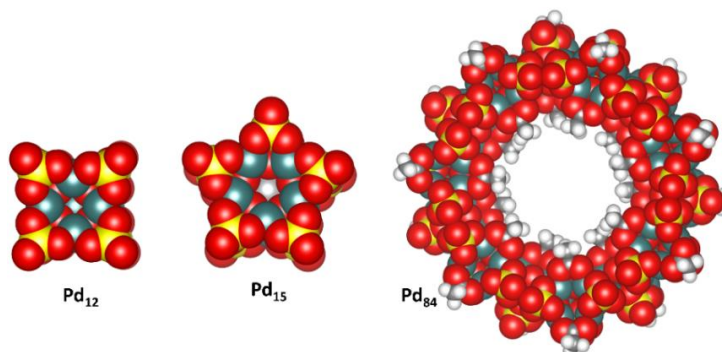


Figure 1.5. Space filling representations for three typical POPd clusters (Pd_{12} , Pd_{15} , and Pd_{84}).

reported several magic ring clusters of Pd by self-assembly.^[19] Figure 1.5 shows an example of palladium oxometalate $\{\text{Pd}_{84}\}$ -ring cluster with 3.3 nm in diameter, with a D_{7d} symmetry containing a C_7 (S_{14}) axis. Respect to the high nuclear cluster of Mo,

Chapter 1 Introduction and Scope of the Thesis

there are still large unknown for the Pd field, they are expecting to add many more members to the palladium family.

1.3 Properties and applications

Table 1.1 General features of polyoxometalates.

Characters	
1	Anionic
2	Metal oxide like
3	High ionic weight
4	Brønsted acids
5	Stable in water and air, and also thermal stable
6	High solubility in water or polar organic solvents (acetonitrile, dimethylformamide, <i>etc.</i>)
7	Discrete size/discrete structure
8	Provide multiple and reversible electron centers (redox properties)
9	Electro/photo-reducible

POMs are structurally and compositionally diverse, and enable fine-tuning of their electronic properties, redox properties, and chemical stability along with robustness for the design of new materials and devices. Although the main property of a given compound is determined by the detailed composition and structure, there exhibits some general features for polyoxometalates as listed in Table 1.1.^[20] It is more appropriate to consider their properties and applications together, since these topics are intimately related. Among them, the acid and redox properties of POM are the most popular characters that employed in catalysis, material, and device areas.

1.3.1 POMs in batteries

POMs exhibit rich electrochemical properties that could be attributed to their fully oxidized addenda atoms (Mo^{VI} , W^{VI} , V^{V}) in the framework. It is common for POMs to display multiple and reversible electron reductions without significant deforming of the POM framework. The well known “heteropoly blues” are basically formed through one- or two- electron reduction of the corresponding oxide heteropolyanions. With these impressive set of properties, they are expected to use as the cathode in lithium

Chapter 1 Introduction and Scope of the Thesis

batteries. In this direction, Yokoyama *et al.* have carried out in operando Mo K-edge X-ray absorption fine structure measurements on the rechargeable molecular cluster batteries (MCBs), in which a Keggin-type $[\text{PMo}_{12}\text{O}_{40}]^{3-}$, was utilized as a cathode active material with a lithium metal anode.^[21] The results revealed that $[\text{PMo}_{12}\text{O}_{40}]^{3-}$ behaves as an “electron sponge” as displayed in Figure 1.6, cycling reversibly by 24 electrons between $[\text{PMo}_{12}\text{O}_{40}]^{3-}$ and $[\text{PMo}_{12}\text{O}_{40}]^{27-}$ during charging/discharging. Interestingly, the molecular structure of $[\text{PMo}_{12}\text{O}_{40}]^{27-}$ showed good stability which was found only slightly diminished in size compared to the original $[\text{PMo}_{12}\text{O}_{40}]^{3-}$. In view of this prior work, Cronin and co-workers performed the charge capacity based on a polyoxovanadate cluster $\text{Li}_7[\text{V}_{15}\text{O}_{36}(\text{CO}_3)]$ which also showed rapid lithium-ion diffusion and good electron conductivity.^[22]

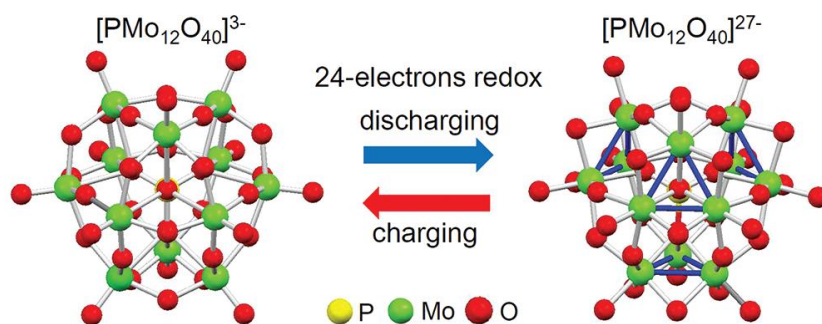


Figure 1.6. 24 electrons redox between $[\text{PMo}_{12}\text{O}_{40}]^{3-}$ and $[\text{PMo}_{12}\text{O}_{40}]^{27-}$ during charging/discharging.^[21]

1.3.2 POMs in water oxidation

The POMs are potentially used in fields such as medicine, magnetism, materials, and others; however, the dominant application of POMs is in catalysis. During the recent ten years, significant improvements have been achieved for POM based catalysts in water oxidation (WOC), owing to their oxidatively, hydrolytically and thermally stability. The major breakthrough in POM WOC development was achieved in 2008, when two independent groups Hill and Bonchio simultaneously reported one same tetra-ruthenium polytungstate, $[\text{Ru}_4(\mu\text{-O})_4(\mu\text{-OH})_2(\text{H}_2\text{O})_4(\gamma\text{-SiW}_{10}\text{O}_{36})_2]^{10-}$ (Ru_4SiPOM), which exhibited unprecedented solubility, catalytic activity, and stability in the transformation of water to O_2 .^[23] Concerning the high catalytic activity, it is proposed largely related to the four-ruthenium core in the molecule in which can serve multiple electron and proton transferring, as shown in Figure 1.7a. The electronic

Chapter 1 Introduction and Scope of the Thesis

properties of the possible intermediates were performed with DFT by Bo *et al.* to help understand the reactive activity.^[24] A mechanism involving four consecutive proton-coupled electron transfer (PCET) processes were proposed in Figure 1.7b, and the energetics of these electrochemical processes were calculated by Piccinin *et al.* using DFT methods.^[25] Aiming to optimize the catalytic properties of these POM-based complexes, various strategies have been explored on Ru₄SiPOM, such as changing the nature of the central heteroatom from Si to P based on the Ru₄-(SiW₁₀)₂ anion,^[26] combining the Ru₄-(SiW₁₀)₂ anion with the carbon nanotube,^[27] introducing the POMs into a light-driven water oxidation format,^[28] and considering the electrolytic environment with ionic liquids, etc.^[29] Hill's group proceeded to investigate several other POMs containing Ir or Ni metal-oxide clusters stabilized by various multi-dentate lacunary polytungstate ligands.^[30] Furthermore, POMs containing only one Ru in the Keggin structure are also proved to viable for WOCs by Fukuzumi *et al.* and a mechanism study from DFT by Su *et al.*^[31]

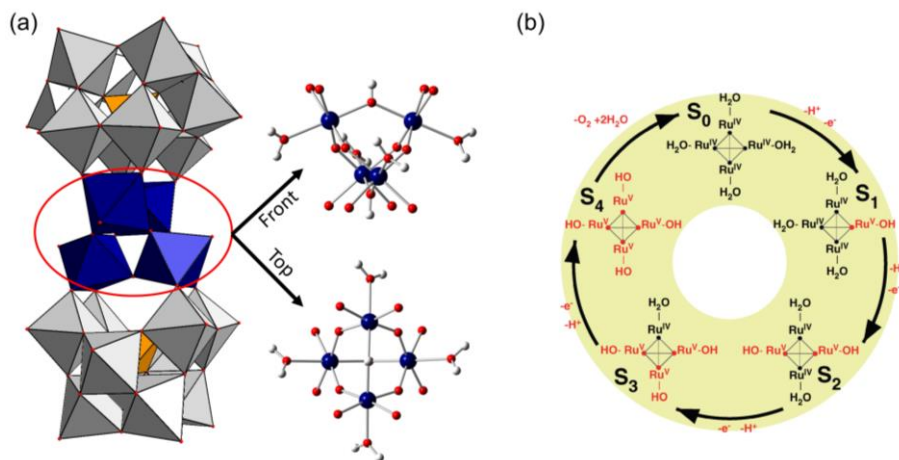


Figure 1.7. (a) Polyhedral representation of the polyanion $[Ru_4(\mu-O)_4-(\mu-OH)_2(H_2O)_4(\gamma-SiW_{10}O_{36})_2]^{10-}$ (Ru_4SiPOM) and top-front views of the central tetraruthenium-oxo-core. The polytungstate fragments are shown as gray octahedra, Si as orange tetrahedra, Ru as dark blue octahedra and balls, and O and H as red and white balls, respectively. (b) Schematic representation of the studied stepwise mechanism for the water oxidation in the presence of Ru_4POM catalyts.^[25]

To avoid using the expensive noble metals, Hill and co-workers made another breakthrough by using the tetracobalt-oxo-core sandwich-type polytungstate $[Co_4(H_2O)_2(PW_9O_{34})]^{10-}$ (Co_4PPOM)^[32]. The water oxidation experiment with

Chapter 1 Introduction and Scope of the Thesis

Co₄POM showed the highest turnover number (TON) per active site metal of any WOC at that moment. Later, Galán-Mascarós shown that the nonanuclear [Co₉(H₂O)₆(OH)₃(HPO₄)₂(PW₉O₃₄)₃]¹⁶⁻ cluster, also exhibited WOC performance both in homogeneous conditions and in the solid state when incorporated into a carbon paste modified electrodes.^[33] This complex shows high oxygen evolution rates in a wide range of pH.^[34] Recent theoretical studies have been reported to disentangle the WOC mechanism for Co-containing POMs.^[35] As a robust yet extensively tunable family of compounds, POMs have considerable promise in the development of multi-electron-transfer catalysis.

1.4 POMs based materials in nanoscience

POM-based materials have been proposed as promising components of devices since 1998,^[36] and the integration of POMs into other functional architectures and devices are progressed uninterruptedly aiming to obtain multifunctional and more efficient materials. The performance of such materials strongly depends on the interactions between the POM and other components, which can range from weak (electrostatic, H-bonds, *VDW*) to covalent interactions.

1.4.1 POM hybrids in microelectronics/molecular electronics

Because POMs are negatively charged, the most efficient strategy to organize them are Layer-by-Layer (LBL) assemblies of POMs with positively charged molecules, such as polyelectrolytes,^[37] porphyrins,^[38] dyes,^[39] long alkyl chain amines, *etc.*^[40, 41] Many POM-based functional films were formed and displayed predominant electrical and photo properties, and it has been nicely reviewed by Liu *et al.*^[42] Recently, Douvas *et al.* reported a hybrid organic-inorganic film via LBL self-assembly of Keggin-structure polyoxometalate (H₃PW₁₂O₄₀) and 1, 12-diaminododecane (DD) fabricated on 3-aminopropyl triethoxysilane-modified silicon surface.^[43] This polyoxometalate-based layered structure was evaluated as molecular materials for electronic devices. As displayed in Figure 1.8, the detailed electron transport mechanisms of POM layers were studied, and the effects from some structural parameters such as the number of layers (1 or 5 layers), the nature of the final layer (POM or DD), and the interelectrode distances (50 or 150 nm) on the mechanism were discussed. On molecular electronics side, Tour and co-workers have investigated the directly covalent grafting of organo-imido hexamolybdate onto Si(111)-H surface to form both monolayer and multilayers.^[44] Such molecular systems were successfully attached atop the pseudo metal-oxide-semiconductor field-effect transistors (MOSFETs) channel with

Chapter 1 Introduction and Scope of the Thesis

controllably tune electronic performance in nanoscale devices. The charge-transfer between the channel and the molecules and their electron donor–acceptor ability are revealed to very important factors for electronic performance.

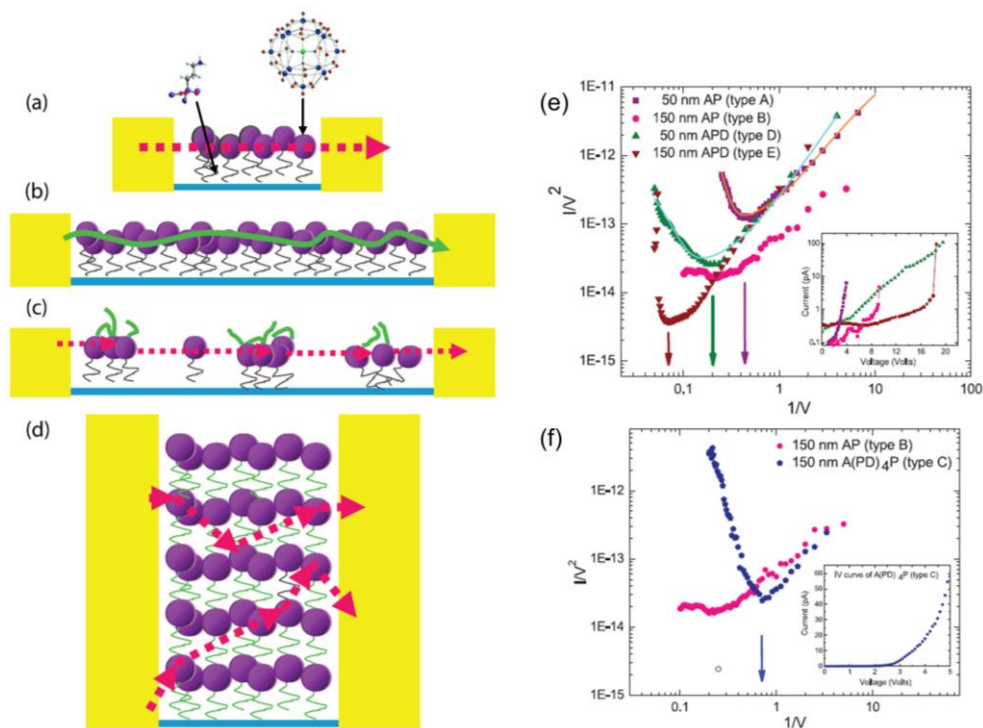


Figure 1.8. (a-d) Schematic diagram of the transport mechanism model through the various film types at the high-voltage regime; (e) Comparison of Fowler-Nordheim curves between POM-ending single-layers (types A and B) and DD-ending single-layers (types D and E) for two different electrode gaps (50 and 150 nm), (f) and also a comparison for POM-ending single-layer (type B) and a POM-ending five-layer (type C) for an electrode gap of 150 nm.^[43]

1.4.2 POM monolayer on planar surfaces

Immobilization of POMs on supports has also received a lot of attention. The interaction between each are generally classified according to the type of support. For POMs adsorbed on the planar-metal (Au, Hg, etc.) surfaces and graphite are mainly obtained by spontaneous adsorption from solution through electrostatic interactions. Some early electrochemical studies of POMs adsorbed onto electrode surfaces revealed these modified materials exhibited interesting catalytic active towards various

Chapter 1 Introduction and Scope of the Thesis

electrochemical process, such as the hydrogen evolution reaction.^[45] By means of scanning tunneling microscopy (STM), monolayers of POMs on planar surfaces were obtained to study the composition and on the effects of counter-cations by Barteau and co-workers,^[46] while Gewirth *et al.* focused their attention on the adsorbed orientation of POMs on the surfaces.^[47] Different unit cells have been proposed by Gewirth *et al.* for the adsorption of α -[SiW₁₂O₄₀]⁴⁻ on Ag(100) and Ag(111) surfaces respectively.

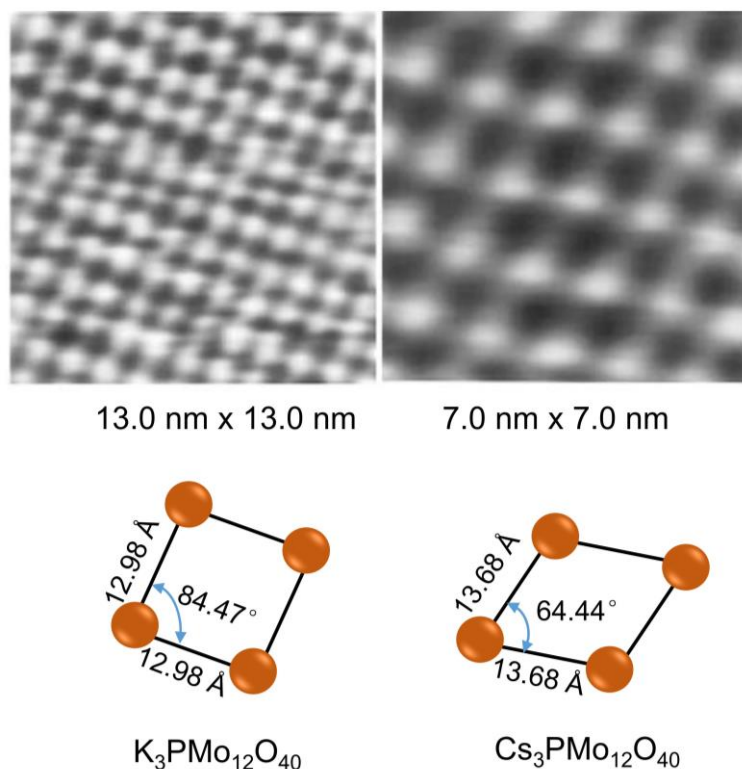


Figure 1.9. STM images and schematic diagrams of $K_3PMo_{12}O_{40}$ and $Cs_3PMo_{12}O_{40}$ unit cells on planar graphite.^[49b] As the counter-cation size increases from K^+ to Cs^+ , nearest-neighbor distances between the POM cluster anions become larger, resulting in a change from square to hexagonal packing.^[48]

It is suggested that monolayers of α -[SiW₁₂O₄₀]⁴⁻ passivate the Ag surface with electron transfer to the POM. In addition, the IR and SER spectroscopy results indicated the $-\text{[SiW}_{12}\text{O}_{40}]^{4-}$ strongly bounded on the silver surface, while the interaction with gold is not as strong as that with silver. On the other hand, Barteau's studies illustrated the roles of counter-cations in constructing 2D ordered arrays. STM images

Chapter 1 Introduction and Scope of the Thesis

(Figure 1.9) revealed both square and hexagonal packing are detected for $[\text{PMo}_{12}\text{O}_{40}]^{3-}$ adsorbed on planar graphite when using a series of counter-cations (H^+ , Na^+ , K^+ , Cs^+). It is strongly supported that counter-cations (including protons) have been structurally integrated into POM monolayers on planar surfaces.^[49] One main topic of this thesis is focused on this area to reveal the interactions between POMs and metallic surfaces by DFT. The second group of supports is focused on those oxide surfaces, *e.g.* SiO_2 , Al_2O_3 , and TiO_2 . For example, the adsorption of $\text{PW}_{12}\text{O}_{40}^{3-}$ on TiO_2 surface to form POM-monolayer have been applied as photocatalyst.^[50] Moreover, Grinval and co-workers obtained the well-defined mono-dispersed $\text{H}_3\text{PMo}_{12}\text{O}_{40}$ onto silica surfaces.^[51] In most these cases, the POMs are relied on covalent linking with the surfaces.

1.4.3 POMs on nanoparticles

Except for adsorption on a planar surface, POMs are also widely investigated on nanoparticles (NPs). Metal(0) nanoparticles (NPs) are typically prepared by reducing of metal salts in the presence of reduction and stabilizing agents. By using the anionic feature of POMs, Finke and co-workers initially carried out systematic work on the synthesis of POM-protected Ir(0) and Rh(0) NPs, and paved the way for their applications in catalytic hydrogenation.^[52] Because many POMs can also be reversibly reduced, it permitted to build systems where POMs serve as both reduction agent and protecting ligands to form POM-stabilized metal nanoparticles. Therefore, Neumann *et al.* prepared the reduced $\text{H}_5[\text{PV}_2\text{Mo}_{10}\text{O}_{40}]$ with Zn(0) powder then reacting with noble metal precursors such as K_2PtCl_4 , AgNO_3 , *etc.* to prepare $\text{PV}_2\text{Mo}_{10}\text{O}_{40}^{5-}$ -stabilized Pt(0), Ag(0), Rh(0), Ru(0), Ir(0) NPs, and worked on the aerobic epoxidations of alkenes.^[53] There showed considerable success in this area, and these topics have been nicely reviewed by Nadjo,^[54] Mitchell,^[55] and Weinstock groups.^[56] Especially the “*built-in*” systems are quite attractive in which d-electron containing metal ions are structurally incorporated during POM syntheses. For example, Nadjo recently reported the preparing of NPs with POMs such as $\text{H}_7[\beta\text{-P}(\text{Mo}^{\text{V}})_4(\text{Mo}^{\text{VI}})_8\text{O}_{40}]$.^[57] Inspired by this, and combined with experiments we have developed the application of highly reduced Kabanos-type POM $\text{Na}\{(\text{Mo}_2^{\text{V}}\text{O}_4)_3(\mu_2\text{-O})_3(\mu_2\text{-SO}_3)_3(\mu_6\text{-SO}_3)_2\}^{15-}$ to reduce Au^{III} to form Au NPs, the details are presented in chapter 4.

1.5 Computational development of POMs

The application of the density functional theory (DFT) methodology to the study of POMs played an important role in the field of POMs during the last two decades, which provides many useful perspectives in electronic properties and reactive activity

Chapter 1 Introduction and Scope of the Thesis

of POMs. Particularly, the combination of experimental and theoretical in the current researches is one very popular mode to provide fast and accurate answers for some complex issues. The earliest quantum chemical calculations on POMs were based on $X\alpha$ and semi-empirical approaches, which were used to gain some molecular orbitals information with low numerical results.^[58] Although some new methods such as Hartree–Fock (HF) approximation have been applied in the following studies, the electronic corrections are still not included in the calculations until the application of DFT method. The development and advances in DFT and effective core potentials for frozen cores have significantly improved both the accuracy and computational economy demands to model the structure and properties of POMs. Regarding the large size, the presence of transition metal ions and the high negative charge features of polyoxoanions, in practice, still relatively few high-level computational studies on POMs have been reported in the initial times. Thanks to the development of powerful hardware and software, the theoretical modelling for POMs is being much faster and accurate nowadays. In addition, present calculations are also included some other effects such as relativistic effects due to the presence of heavy atoms, and solvation effects, as well as large atomic basis sets, hybrid functionals, *etc.* Especially the simulation of solvent effects by means of continuum models (COSMO, PCM or SMD) has been revealed to be one very important factor to correctly describe the electrochemistry or the reactivity of POMs. Based on DFT, the electronic structure, redox properties, reactivity, spectroscopy (IR, UV, ECD, and NMR), and magnetism of POMs have been widely studied in the latest years (Figure 1.10).

The main progresses in these topics have been reviewed by our group in 2003 and 2012 respectively.^[59] Herein, we only have a short introduction for the application of DFT in POMs adsorbed on surface fields, which received the substantive progresses mainly in the recent five years. The starting of this area is responsible for the study of the possible adsorbed orientations of Anderson $[\text{CoMo}_6\text{O}_{24}\text{H}_6]^{3-}$ on the mercury electrode by using a cluster model in 2005.^[60] In 2010, Lefebvre, Sautet and co-workers analyzed the adsorption of $\text{H}_3\text{PMo}_{12}\text{O}_{40}$ on silica surfaces, and revealed the strong H-bonds interaction between the POM protons and OH groups from silica, and finally lead to the dehydration to form POM-O-Si bonds.^[61] In the following years, the adsorption of POMs on some carbon nanocomposites have been investigated by Prof. Su and Valdéz groups.^[62] An initial study of modelling POMs deposited onto the metallic surfaces was carried out in our group in an attempt to identify the main factors that are necessary to take into account to obtain accurate electronic properties.^[63] The reduction of $[\text{SiW}_{12}\text{O}_{40}]^{4-}$ on the Ag surface have been reproduced by combining

Chapter 1 Introduction and Scope of the Thesis

density functional theory (DFT) calculations with molecular dynamic (MD) simulations.

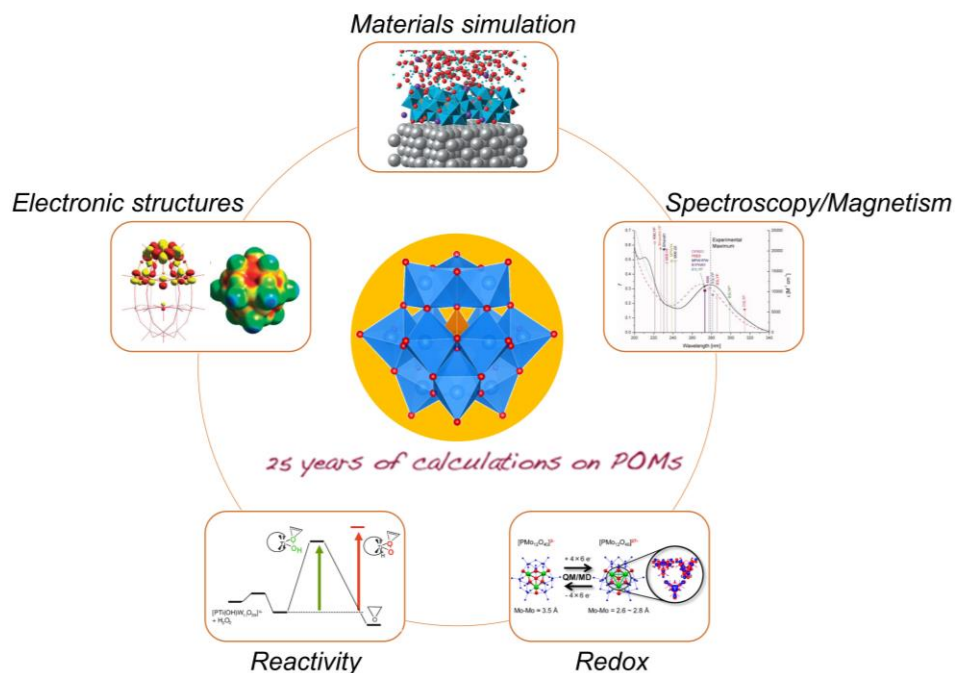


Figure 1.10. The main aspects of theoretical modelling for polyoxometalates.^[59b]

1.6 Scope of the thesis

Present thesis aims to advance in the knowledge of basic concepts as the templating role of cations in the formation of molecular oxide clusters as well as in the modelling of catalytic reactions when they act as co-catalysts with a metal surface. The latter one is still a challenge because of the size and complexity of the systems to deal with. Since the discovery of first polyoxopalladate by Ulrich Kortz group in Bremen, a rapid development of this family has happened. The number of experimental data available has allowed to develop a systematic computational study (Chapter 3) to determine the role that play by internal and external cations on the formation of polyoxopalladates. The final aim is to rationalize experimental results and potentially to guide experiments for rational synthesis of new compounds. On the other hand, the adsorption of POMs on noble-metallic nanoparticles or surfaces (Ag, Pd, Pt, and Au) has aroused interest both in experimental and theoretical groups, due to their potential application in

Chapter 1 Introduction and Scope of the Thesis

catalysis, biotechnology, and materials field. Motivated by processes that involve electron transfer, we have analyzed initial steps in the formation of nanoparticles using a reduced polyoxometalate in chapter 4. Furtherance of previous studies conducted in the thesis of Xavier Aparicio Anglès,^[64] several studies with POMs adsorbed on metallic and metal-oxide surfaces have been carried out and presented from chapters 5 to 8. In these chapters, we have discussed the effects of solvent for the adsorption, electronic structures, and reactivity.

More specifically, the results presented here will concern the following topics:

- (i) Based on the experimental information of Pd₁₂ and Pd₁₅ frameworks and in collaboration with the group of Prof. Kortz, we have combined theoretical and experimental studies to elucidate the factors that governing the metal ion encapsulation, and provide an overall sense of cation selectivity in synthesizing of Pd-based nanoclusters with different size and topology. Then, we have characterized the nature of the rather unusual Pd···Ag interactions in new formed **Ag₄Pd₁₃** and **Ag₅Pd₁₅** systems.
- (ii) Redox activity of Kabanos [Na{(Mo₂^VO₄)₃(μ₂-O)₃(μ₂-SO₃)₃(μ₆-SO₃)₂}]¹⁵⁻ polyoxometalate for Au^{III} reduction to atomic Au. An understanding from both thermodynamic and molecular orbital views have been provided to reveal the role of polyoxometalates in the reduction process.
- (iii) The solvation energies for some polyoxometalate molecules have been calculated with VASP using the implicit solvent model and compared with the results obtained from PCM model in Gaussian. The solvation and counterions effects on the adsorption ability and electronic property have been discussed for systems with low and moderate charged POM on the gold/silver surfaces.
- (iv) The highly charged polyoxometalates (PW₁₁O₃₉⁷⁻) adsorbed on the gold surface were modelled by using a strategy that accounted for the charge of the system and the solvent. The possible adsorption orientations, electronic properties, and the nature of the interaction between the PW₁₁ and the Au(100) surface in both vacuum and solution were studied.
- (v) Based on the experimental information reported by Dumesic. *et al.*, the water gas shift reaction mechanism catalyzed by K₃PMo₁₂O₄₀ adsorbed on Au(111) was investigated by DFT calculations.

Chapter 1 Introduction and Scope of the Thesis

- (vi) In cooperation with Prof. Weinstock group, we provided a detailed characterization of the electronic structure and absorption spectrum for the fully oxide and reduced polyoxometalate modified TiO₂ systems based on DFT and TDDFT calculations.

References and Notes

- [1] M. T. Pope, *Heteropoly and Isopoly Oxometalates*. Springer-Verlag: New York, 1983.
- [2] P. Gouzerh and M. Che, *L'actualité chimique*, 2006, 208, 1.
- [3] J. J. Berzelius, *Annalen der Physik*, 1826, 82, 369–392.
- [4] (a) J. Keggin, *Nature* 1933, 131, 908-909; (b) H. D'Amour, *Acta Crystallographica Section B* 1976, 32, 729–740; (c) B. Dawson, *Acta Crystallographica* 1953, 6, 113–126.
- [5] H. T. Evans, *Perspect. Struct. Chem.* 1971, 4, 1–58.
- [6] M. T. Pope and A. Müller, *Angew. Chem.* 1991, 103, 56–70; *Angew. Chem. Int. Ed. Engl.* 1991, 30, 34–48.
- [7] C. L. Hill, *Chem. Rev.* 1998, 98, 1–2.
- [8] D. L. Long, R. Tsunashima and L. Cronin, *Angew. Chem. Int. Ed.* 2010, 49, 1736–1758.
- [9] L. C. W. Baker and J. S. Figgis, *J. Am. Chem. Soc.* 1970, 92, 3794–3797.
- [10] P. Putaj and F. Lefebvre, *Coord. Chem. Rev.* 2011, 255, 1642–1685.
- [11] A. Dolbecq, E. Dumas, C. R. Mayer and P. Mialane, *Chem. Rev.* 2010, 110, 6009–6048.
- [12] A. Proust, B. Matt, R. Villanneau, G. Guillemot, P. Gouzerh and G. Izzet, *Chem. Soc. Rev.* 2012, 41, 7605–7622.
- [13] J. C. Goloboy and W.G. Klemperer, *Angew. Chem. Int. Ed.* 2009, 48, 3562–3564.
- [14] N. V. Izarova, M. T. Pope and U. Kortz, *Angew. Chem. Int. Ed.* 2012, 51, 9492–9510.
- [15] M. Pley and M. S. Wickleder, *Angew. Chem., Int. Ed.* 2004, 43, 4168–4170.
- [16] (a) D. D. Dexter, J. V. Silverton, *J. Am. Chem. Soc.* 1968, 90, 3589–3590. (b) D. D. Dexter, Ph.D. Thesis, Georgetown University, 1968.
- [17] E. V. Chubarova, M. H. Dickman, B. Keita, L. Nadjo, F. Miserque, M. Mifsud, I. W. C. E. Arends and U. Kortz, *Angew. Chem., Int. Ed.* 2008, 47, 9542–9510.
- [18] (a) Z. G. Lin, B. Wang, J. Cao, B. K. Chen, Y. Z. Gao, Y. N. Chi, C. Xu, X. Q. Huang, R. D. Han, S. Y. Su and C. W. Hu, *Inorg. Chem.* 2012, 51 (8), 4435–4437; (b) N. V. Izarova, R. Ngo Biboum, B. Keita, M. Mifsud, I. W. C. E. Arends, G. B. Jameson and U. Kortz, *Dalton Trans.* 2009, 43, 9385–9387; (c) M. Delferro, C. Graiff, L. Elviri and G. Predieri, *Dalton Trans.* 2010, 39, 4479–4481; (d) P. Yang, Y. X. Xiang, Z. G. Lin, B. S. Bassil, J. Cao, L. Y. Fan, Y. Fan, M. Li, P. Jiménez-

Chapter 1 Introduction and Scope of the Thesis

- Lozano, J. J. Carbó, J. M. Poblet and U. Kortz, *Angew. Chem. Int. Ed.* 2014, 53, 11974–11978; (e) P. Yang, Y. X. Xiang, Z. H. Lin, Z. L. Lang, P. Jiménez-Lozano, J. J. Carbó, J. M. Poblet, L.Y. Fan, C. W. Hu and U. Kortz, *Angew. Chem. Int. Ed.* 2016, 55, 15766–15770. (f) F. Xu, R. A. Scullion, J. Yan, H. N. Miras, C. Busche, A. Scandurra, B. Pignataro, D. L. Long and L. Cronin, *J. Am. Chem. Soc.* 2011, 133, 4684–4686.
- [19] (a) F. Xu, H. N. Miras, R. A. Scullion, D. L. Long, J. Thiel and L. Cronin. *Proc. Natl. Acad. Sci.* 2012, 109, 11609–11612; (b) R. Scullion, A. J. Surman, F. Xu, J. S. Mathieson, D. L. Long, F. Haso, T. Liu and L. Cronin, *Angew. Chem. Int. Ed.* 2014, 53, 10032–10037; (c) L. G. Christie, A. J. Surman, R. A. Scullion, F. Xu, D. L. Long and L. Cronin. *Angew. Chem. Int. Ed.* 2016, 55, 12741–12745.
- [20] D. E. Katsoulis, *Chem. Rev.* 1998, 98, 359–387.
- [21] (a) H. Wang, S. Hamanaka, Y. Nishimoto, S. Irle, T. Yokoyama, H. Yoshikawa and K. Awaga, *J. Am. Chem. Soc.* 2012, 134, 4918–4924; (b) Y. Nishimoto, D. Yokogawa, H. Yoshikawa, K. Awaga and S. Irle, *J. Am. Chem. Soc.* 2014, 136, 9042–9052.
- [22] J. J. Chen, M. D. Symes, S. C. Fan, M. S. Zheng, H. N. Miras, Q. F. Dong and L. Cronin, *Adv. Mater.* 2015, 27, 4649–4654.
- [23] (a) A. Sartorel, M. Carraro, G. Scorrano, R. D. Zorzi, S. Geremia, N. D. McDaniel, S. Bernhard and M. Bonchio, *J. Am. Chem. Soc.* 2008, 130, 5006–5007; (b) Y. V. Geletii, B. Botar, P. Kögerler, D. A. Hillesheim, D. G. Musaev and C. L. Hill, *Angew. Chem., Int. Ed.* 2008, 47, 3896–3899.
- [24] A. Sartorel, P. Miró, E. Salvadori, S. Romain, M. Carraro, G. Scorrano, M. Di Valentin, A. Llobet, C. Bo, and M. Bonchio, *J. Am. Chem. Soc.* 2009, 131, 16051–16053.
- [25] S. Piccinin and S. Fabris, *Phys. Chem. Chem. Phys.* 2011, 13, 7666–7674.
- [26] C. Besson, Z. Huang, Y. V. Geletii, S. Lense, K. I. Hardcastle, D. G. Musaev, T. Lian, A. Proust and C. L. Hill, *Chem. Commun.* 2010, 46, 2784–2786.
- [27] F. M. Toma, A. Sartorel, M. Iurlo, M. Carraro, P. Parisse, C. Maccato, S. Rapino, B. R. Gonzalez, H. Amenitsch, T. D. Ros, L. Casalis, A. Goldoni, M. Marcaccio, G. Scorrano, G. Scoles, F. Paolucci, M. Prato and M. Bonchio, *Nat. Chem.* 2010, 2, 826–831.
- [28] (a) A. L. Kaledin, Z. Huang, Y. V. Geletii, T. Lian, C. L. Hill and D. G. Musaev, *J. Am. Chem. Soc.* 2009, 131, 7522–7523; (b) Z. Q. Huang, Z. Luo, Y. Geletii, J.

Chapter 1 Introduction and Scope of the Thesis

- Vickers, Q. S. Yin, D. Wu, Y. Hou, Y. Ding, J. Song, D. Musaev and C. L. Hill, *J. Am. Chem. Soc.* 2011, 133, 2068–2071.
- [29] G. Bernardini, C. Zhao, A. G. Wedd and A. M. Bond, *Inorg. Chem.* 2011, 50, 5899–5901.
- [30] (a) R. Cao, H. Ma, Y. V. Geletii, K. I. Hardcastle and C. L. Hill, *Inorg. Chem.* 2009, 48, 5596–5598; (b) G. Zhu, E. N. Glass, C. Zhao, H. Lv, J. W. Vickers, Y. V. Geletii, D. G. Musaev, J. Song and C. L. Hill, *Dalton Trans.* 2012, 41, 13043–13049.
- [31] (a) M. Murakami, D. Hong, T. Suenobu, S. Yamaguchi, T. Ogura and S. Fukuzumi, *J. Am. Chem. Soc.* 2011, 133, 11605–11613. (b) Z. L. Lang, G. C. Yang, N. N. Ma, S. Z. Wen, L. K. Yan, W. Guan and Z.-M. Su, *Dalton Trans.* 2013, 42, 10617–10625.
- [32] Q. Yin, J. M. Tan, C. Besson, Y. V. Geletii, D. G. Musaev, A. E. Kuznetsov, Z. Luo, K. I. Hardcastle and C. L. Hill, *Science* 2010, 328, 342–345.
- [33] S. Goberna-Ferrón, L. Vigara, J. Soriano-López and J. R. Galán-Mascarós, *Inorg. Chem.* 2012, 51, 11707–11715.
- [34] (a) J. Soriano-López, S. Goberna-Ferrón, L. Vigara, J. J. Carbó, J.M. Poblet and J. R. Galán-Mascarós, *Inorg. Chem.* 2013, 52, 4753–4755; (b) J. Soriano-López, S. Goberna-Ferrón, J. J Carbó, J. M Poblet and J. R Galán-Mascarós, *Adv. Inorg. Chem.* 2017, 69, 155–179.
- [35] J. Soriano-López, D. G. Musaev, C. L. Hill b, J.R. Galán-Mascarós and J. J. Carbó, J. M. Poblet, *J. Catal.* 2017, 350, 56–63.
- [36] Eugenio Coronado and Carlos J. Gómez-García. *Chem. Rev.* 1998, 98, 273–296.
- [37] M. Jiang, E. Wang, Z. Kang, S. Lian, A. Wu and Z. Li, *J. Mater. Chem.* 2003, 13, 647–649.
- [38] Y. Shen, J. Liu, J. Jiang, B. Liu and S. Dong, *J. Phys. Chem. B* 2003, 107, 9744–9748.
- [39] Y. Wang and C. Hu, *Thin Solid Films* 2005, 476, 84–91.
- [40] K. Z. Wang and L. H. Gao, *Mater. Res. Bull.* 2002, 37, 2447–2451.
- [41] S. Y. Oh, Y. J. Yun, D.-Y. Kim and S. H. Han, *Langmuir* 1999, 15, 4690–4692.
- [42] S. Q. Liu and Z. Y. Tang, *Nano Today* 2010, 5, 267–281.
- [43] A. M. Douvas, E. Makarona, N. Glezos, P. Argitis, J. A. Mielczarski and E. Mielczarski, *ACS Nano.* 2008, 2, 733–742.
- [44] (a) T. He, J. L. He, M. Lu, B. Chen, H. Pang, W. F. Reus, W. M. Nolte, D. P. Nackashi, P. D. Franzon and J. M. Tour, *J. Am. Chem. Soc.* 2006, 128, 14537–

Chapter 1 Introduction and Scope of the Thesis

- 14541; (b) M. Lu, W. M. Nolte, T. He, D. A. Corley and J. M. Tour, *Chem. Mater.* 2009, 21, 442–446.
- [45] M. Sadakane and E. Steckhan, *Chem. Rev.* 1998, 98, 219–238.
- [46] B. A. Watson, M. A. Barteau, L. Haggerty, A. M. Lenhoff and R. S. Weber, *Langmuir* 1992, 8, 1145–1148.
- [47] (a) M. Ge, B. Zhong, W. G. Klemperer and A. A. Gewirth, *J. Am. Chem. Soc.* 1996, 118, 5812–5813; (b) L. Lee, J. X. Wang, R. R. Adzic, I. K. Robinson and A. A. Gewirth, *J. Am. Chem. Soc.* 2001, 123, 8838–8843; (c) L. Lee and A. A. Gewirth, *J. Electroanal. Chem.* 2002, 522, 11–20.
- [48] Y. F. Wang and I. A. Weinstock, *Dalton Trans.* 2010, 39, 6143–6152.
- [49] (a) M. S. Kaba, I. K. Song and M. A. Barteau, *J. Phys. Chem.* 1996, 100, 19577–19581; (b) I. K. Song, M. S. Kaba, G. Coulston, K. Kourtakis and M. A. Barteau, *Chem. Mater.* 1996, 8, 2352–2358.
- [50] C. Chen, P. Lei, H. Ji, W. Ma, J. Zhao, H. Hidaka and N. Serpone, *Environ. Sci. Technol.* 2004, 38, 329–337.
- [51] E. Grinenval, X. Rozanska, A. Baudouin, E. Berrier, F. Delbecq, P. Sautet, J. M. Basset, and F. Lefebvre, *J. Phys. Chem. C* 2010, 114, 19024–19034
- [52] (a) H. Weiner and R. G. Finke, *J. Am. Chem. Soc.* 1999, 121, 9831–9842; (b) Y. Lin and R. G. Finke, *J. Am. Chem. Soc.* 1994, 116, 8335–8353; (c) Y. Lin and R. G. Finke, *Inorg. Chem.* 1994, 33, 4891–4910; (d) J. D. Aiken and R. G. Finke, *Chem. Mater.* 1999, 11, 1035–1047; (e) J. A. Widegren, J. D. Aiken, S. Ozkar and R. G. Finke, *Chem. Mater.* 2001, 13, 312–324. (e) C. R. Graham, L. S. Ott and R. G. Finke, *Langmuir* 2009, 25, 1327–1336.
- [53] (a) G. Maayan and R. Neumann, *Catal. Lett.* 2008, 123, 41–45. (b) G. Maayan and R. Neumann, *Chem. Commun.* 2005, 4595–4597.
- [54] B. Keita, T. B. Liu and L. Nadjo, *J. Mater. Chem.* 2009, 19, 19–33.
- [55] S. G. Mitchell and J. M. de la Fuente, *J. Mater. Chem.* 2012, 22, 18091–18100.
- [56] Y. F. Wang and I. A. Weinstock, *Chem. Soc. Rev.* 2012, 41, 7479–7496.
- [57] G. Zhang, B. Keita, R. N. Biboum, F. Miserque, P. Berthet, A. Dolbecq, P. Mialane, L. Catala and L. Nadjo, *J. Mater. Chem.* 2009, 19, 8639–8644.
- [58] H. Taketa, S. Katsuki, K. Eguchi, T. Seiyama and N. Yamazoe, *J. Phys. Chem.* 1986, 90, 2959–2962.
- [59] (a) J. M. Poblet, X. López and C. Bo, *Chem. Soc. Rev.* 2003, 32, 297–308; (b) X. López, J. J. Carbó, C. Bo and J. M. Poblet, *Chem. Soc. Rev.* 2012, 41, 7537–7571.

Chapter 1 Introduction and Scope of the Thesis

- [60] M. I. Borzenko, R. R. Nazmutdinov, D. V. Glukhov, G. A. Tsirlina and M. Probst, *Chem. Phys.* 2005, 319, 200–209.
- [61] X. Rozanska, P. Sautet, F. Delbecq, F. Lefebvre, S. Borshch, H. Chermette, J.-M. Basset and E. Grinenval, *Phys. Chem. Chem. Phys.* 2011, 13, 15955–15959.
- [62] (a) S. Z. Wen, W. Guan, J. P. Wang, Z. L. Lang, L. K. Yan and Z. M. Su, *Dalton Trans.* 2012, 41, 4602–4607; (b) S. Z. Wen, W. Guan, Y. H. Kan, G. C. Yang, N. N. Ma, L.K. Yan, Z. M. Su and G. H. Chen, *Phys. Chem. Chem. Phys.* 2013, 15, 9177–9185; (c) J. Muñiz, A. K. Cuentas-Gallegos, M. Robles and M. Valdéz, *Theor. Chem. Acc.* 2016, 135, 92; (d) J. Muñiz, C. Celaya, A. Mejía-Ozuna, A. K. Cuentas-Gallegos, L. M. Mejía-Mendoza, M. Roblesa and M. Valdéz, *Theor. Chem. Acc.* 2017, 136, 26.
- [63] (a) X. Aparicio-Angles, A. Clotet, C. Bo and J. M. Poblet, *Phys. Chem. Chem. Phys.* 2011, 13, 15143–15147; (b) X. Aparicio-Angles, P. Miro, A. Clotet, C. Bo and J. M. Poblet, *Chem. Sci.* 2012, 3, 2020–2027.
- [64] X. Aparicio-Angles, Ph. D thesis, Universitat Rovira i Virgili, 2013.

Chapter 2

Computational Methodology



In this chapter, we will introduce the main theoretical foundations and tools we have used in the thesis.

All calculations were performed based on density functional theory (DFT), in which the Schrödinger equation was solved by means of electronic density of the system. DFT methods have been widely applied in the POMs systems that provide reliable, accurate results and very successful techniques for understanding the electronic and structural properties of POMs. Considering many transition metals are involved in the POMs and always exist in solution, thus the relativistic and solvent effects are very important factors during the calculations.

The calculations carried out in this thesis composed of two types, the molecules were performed with Gaussian, whereas the periodic models were performed by using the VASP code.

2.1 The Schrödinger equation

Schrödinger equation is the main and most important equation of quantum mechanics. The ultimate goal of most approaches in solid state physics and quantum chemistry is solving the time-independent, non-relativistic Schrödinger equation of the system. For a system, which is composed of N electrons and M nuclei, the equation can be expressed as below:

$$\hat{H} \Psi_i(\vec{x}_1, \vec{x}_2, \dots, \vec{x}_N, \vec{R}_1, \vec{R}_2, \dots, \vec{R}_M) = E_i \Psi_i(\vec{x}_1, \vec{x}_2, \dots, \vec{x}_N, \vec{R}_1, \vec{R}_2, \dots, \vec{R}_M) \quad (2.1)$$

where \hat{H} is the time-dependent Hamiltonian operator, Ψ is the waver-function of the system associated to the energy level E , \vec{x}_i and \vec{R}_i are the spatial coordinates of the electron and nuclei respectively. It is a very complicated process to solve the equation because of many interactives such as electron-electron, electron-nuclei, and nuclei-nuclei are involved in the system. To simplify this process, it generally uses the Born-Oppenheimer approximation,^[1, 2] which allows the wave-function of a molecule to be separated into its electronic and nuclear components, thus the degrees of freedom of the system are significantly reduced. This approximation is based on the fact that nuclei are much heavier than the electrons and therefore the motion of the nuclei is much slower than that of electrons, the nuclear kinetic energy is assumed to zero and their potential energy is merely a constant. As a result, the electronic Hamiltonian reduces to equation 2.2.

$$\hat{H}_{elec} = -\frac{1}{2} \sum_{i=1}^N \nabla_i^2 - \sum_{i=1}^N \nabla_i^2 \sum_{A=1}^M \frac{Z_A}{r_{iA}} + \sum_{i=1}^N \sum_{j>i}^N \frac{1}{r_{ij}} = \hat{T} + \hat{V}_{Ne} + \hat{V}_{ee} \quad (2.2)$$

The solution of the Schrödinger equation with \hat{H}_{elec} is the electronic wave function Ψ_{elec} and the electronic energy E_{elec} in equation 2.3. The total energy E_{tot} is then the sum of E_{elec} and the constant nuclear repulsion term E_{nuc} :

$$\hat{H}_{elec} \Psi_{elec} = E_{elec} \Psi_{elec} \quad (2.3)$$

$$E_{tot} = E_{elec} + E_{nuc} \quad \text{where} \quad E_{nuc} = \sum_{A=1}^M \sum_{B>A}^M \frac{Z_A Z_B}{R_{AB}} \quad (2.4)$$

Even the equation became much simpler after these approximations; the solving of the electronic Schrödinger wave equation was still a challenging subject. To exactly solve

the Schrödinger equation there are generally two different ways available, with one based on the wave-function method, and another is based on the electronic density. It should be noted that the calculations based on the former method are limited to system with total electrons lower than 100 because of the great scaling with even small systems. Since all the calculations related to this thesis are carried out with density functional theory (DFT) method,^[3,4] thus only DFT are described below instead of all developed methods during the solving of the Schrödinger equation.

2.2 Brief introduction of density functional theory

The DFT is presently the most successful approach to compute the structural, magnetic, and electronic properties for molecules in computational physics and chemistry, which was originated from two theorems that were proved by Hohenberg and Kohn in 1964.^[5] In the Hohenberg-Kohn theorem it asserts that the density of any system determines all ground-state properties of the system. By focusing on the electron density, it allows to derive an effective Schrödinger equation in which the total energy of the system can be expressed as a function of the electron density:^[6]

$$E[\rho] = T[\rho] + V_{\text{ext}}[\rho] + V_{ee}[\rho] \quad (2.5)$$

E is the Hohenberg-Kohn energy functional, T is the kinetic energy, V_{ext} is the external potential that is trivial, and V_{ee} is the electron-electron interactions. From the V_{ee} we can extract the *classical* part $J[\rho]$ and *non-classical* part $E_{\text{ncl}}[\rho]$:

$$V_{ee}[\rho] = \frac{1}{2} \iint \frac{\rho(\hat{r}_1)\rho(\hat{r}_2)}{r_{12}} d\hat{r}_1 d\hat{r}_2 + E_{\text{ncl}} = J[\rho] + E_{\text{ncl}}[\rho] \quad (2.6)$$

$J[\rho]$ is the *classical* coulomb interactions and E_{ncl} is the *non-classical* contribution to the electron-electron interaction: self-interaction correction, exchange and Coulomb correlation. The kinetic and E_{ncl} functionals are the major challenges for DFT development.

2.2.1 The Kohn-Sham equations

There is large unknown for the kinetic ($T[\rho]$) and electron-electron ($E_{\text{ncl}}[\rho]$) functionals at that moment. To solve this problem Kohn and Sham proposed an approach to approximate the kinetic and electron-electron functionals in 1965. They suggested calculating the exact kinetic energy of a non-interacting reference system (a fictitious system with N non-interacting electrons) with the same density as the real interacting one:

$$T_s = -\frac{1}{2} \sum_i^N \langle \varphi_i | \nabla^2 | \varphi_i \rangle \quad \rho_s(\vec{r}) = \sum_i^N \sum_s |\varphi_i(\vec{r}, s)|^2 = \rho(\vec{r}) \quad (2.7)$$

where φ_i are the orbitals of the non-interacting system, and $\rho(\vec{r})$ in terms of a set of single orbitals orthonormal states. It should be emphasized that T_s is not the true kinetic energy of the system but that of a system of non-interacting electrons. Kohn and Sham then introduced the so called “*exchange-correlation energy*” (E_{xc}) into the total energy.^[7] The energy functional can be rearranged as:

$$E[\rho] = T_s[\rho] + V_{\text{ext}}[\rho] + V_H[\rho] + E_{xc}[\rho] \quad (2.8)$$

$$E_{xc}[\rho] = (T[\rho] - T_s[\rho]) + (V_{ee}[\rho] - V_H[\rho]) \quad (2.9)$$

The only unspecified term now is the E_{xc} . Fortunately, this represents a rather small fraction of the total energy, and can be overcome by means of approximations.

2.2.2 The local density approximation for $E_{xc}[\rho]$

The *local density approximation (LDA)* is the simplest approximation among all approximate exchange-correlation functionals. The central idea of LDA is based on the assumption that electron density varies slowly throughout a molecule so that a localized region of the molecule behaves like a *uniform electron gas*, as a consequence the $E_{xc}[\rho]$ can be calculated using formulas derived for a uniform electron density.^[5, 8]

The $E_{xc}[\rho]$ can be written as the following form:

$$E_{xc}^{LDA}[\rho] = \int \rho(\vec{r}) \varepsilon_{xc}(\rho(\vec{r})) d\vec{r} \quad (2.10)$$

Here, $\varepsilon_{xc}(\rho(\vec{r}))$ is the exchange-correlation energy per particle of a uniform electron gas of density $\rho(\vec{r})$. LDA is proved a pretty good approximation for some special case of homogeneous electron gas. Properties such as structure, vibrational frequencies are described reliably for many systems. However, it fails in energy and description with bad accuracy, such as ionization energies of atoms, binding energy, energy barriers in diffusion or chemical reactions, especially for inhomogeneous systems.

2.2.3 The generalized gradient approximation for $E_{XC}[\rho]$

In order to account for the non-homogeneity of the true electron density, LDA can be improved not only use the density $\rho(\vec{r})$ at a particular point (\vec{r}), but also supplement the density with information about the gradient of the charge density $\Delta\rho(\vec{r})$, this is the well-known Generalized Gradient Approximation (GGA). Thus, the $E_{XC}[\rho]$ depends on the gradient of the electron density as well as the density itself:

$$E_{XC}^{GGA}[\rho_\alpha, \rho_\beta] = \int f(\rho_\alpha, \rho_\beta, \nabla\rho_\alpha, \nabla\rho_\beta) d\vec{r} \quad (2.11)$$

Thanks to much thoughtful work, important progresses have been made in deriving successful GGA's, and a great number of functionals have been devised. GGA can give reliable results for many different systems. The BP86, BLYP, PW91, and PBE are the most common used functionals in the research.^[9-15]

To increase the accuracy for some special systems, Becke introduced a successful hybrid functional:

$$E_{XC}^{\text{hyb}} = \alpha E_X^{KS} + (1 - \alpha) E_{XC}^{GGA} \quad (2.12)$$

where E_X^{KS} is the exchange term calculated with the exact KS wave function (the exact exchange of the HF method), E_{XC}^{GGA} is an appropriate GGA (correction from DFT), and α is a fitting parameter. Thus, these methods are in fact a hybrid between DFT and HF. Such functionals like B3LYP and B3PW91 are proved work extremely well for atoms and molecules.^[16,17] In conclusion, GGA's and hybrid approximations has largely reduced the LDA errors, these improvements have made DFT a significant component of quantum chemistry.

2.3 Implementation of continuum solvent model in the calculation

In order to accurate modeling the behavior of molecules in solution, both explicit and implicit solvent models have been developed for considering the interaction of the solvent with the molecules. Explicit solvent models generally rely on a large number of discrete solvent models, which can be carried out with molecular dynamics simulations. The solvent effects are well measured, however, such calculations are quite computationally demanding because of the large number of solvents involved. Therefore, significant interests are paid to develop of implicit models, which treat the

solvents as a uniform polarizable medium of fixed dielectric constant ϵ having a solute molecule **M** placed in a suitably shaped cavity. Several definitions of the cavity have been proposed: the *van der Waals surface (VWS)*, the *solvent accessible surface (SAS)*, and the *solvent-excluding (SES)*.^[18] The VWS is the simplest model that each atom has a force field that surrounded by vdW radius, however, no correlation with the surrounding medium was considered. This was taken into account by the SAS and SES models, as the schematic representation in Figure 2.1. The SAS is defined by the center of a spherical probe, which rolls over the VdW surface of a molecule, in which a sphere is used to "probe" the surface of the molecule. The radius of the probe is an important parameter to be considered. An improvement method SES, in which both the contact surface (part of the van der Waals surface) and reentrant surface (inward facing surface of the probe) have been involved to define the model.

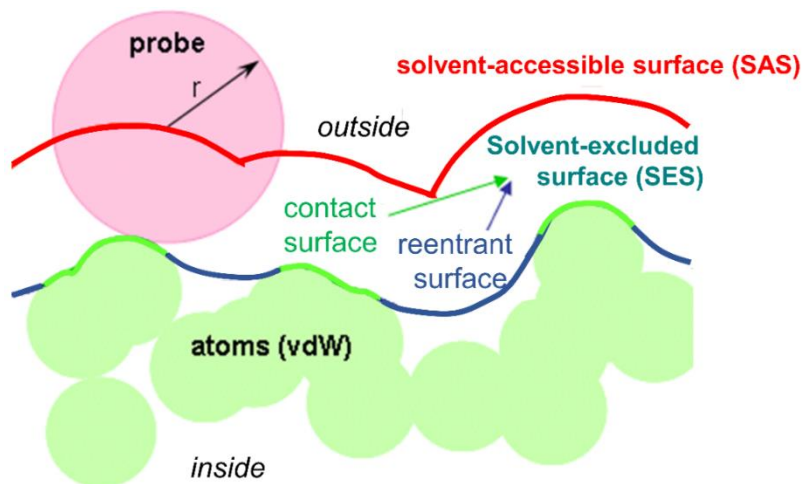


Figure 2.1. Scheme representations of the surface types: Solvent Accessible Surface (red) the Solvent Excluded Surface (green and dark blue), and the van der Waals surface (VWS), both defined by a probe (depicted pink in one sample positions) rolling over the molecule atoms.

The introduction of solvent effects is now becoming a standard procedure in quantum chemical researches due to the development of continuum solvent models. It is known that POMs are negative species that prevalent in solution, the interactions between the polyanions and solvent or counterions generate dramatic influences on the stabilization and properties (redox, reactivity, etc.) of POMs. The most common used implicit solvent models in the fields of POMs are Conductor-like Screening Model (COSMO)^[19] and Polarizable Continuum Model (PCM)^[20] that implemented in ADF^[21] and

Gaussian packages^[22] respectively. In addition, a new SMD model which based on the polarized continuous quantum mechanical charge density of the solute (the “D” in the name stands for “density”) is also widespread in this field during the recent years.^[23] Our group are pioneering in the theoretical study of the redox and electronic structure of POMs by implementing of implicit solvent.^[24] For example, with solvent effect taken into account, the energies of the molecular orbital (MO) could be correctly allocated, which is significantly stabilized with respect to gas phase.

Compared to the advancement for isolated molecules, the solvation effects for solid-liquid is still a challenge to many materials simulation process. Implicit solvation models for plane wave DFT codes were first proposed by Fattebert and Gygi, in which the dielectric medium was defined as a smooth function of the solute electronic charge density.^[25] Very recently, *Hennig et al.* have implemented an implicit solvation model that considers the effect of electrostatics, cavitation, and dispersion on interaction between a solute and solvent into the VASP code (VASP *sol*).^[26] This implementation has been tested to a computationally efficient way to compute the solvent effects for molecules, crystal surfaces, and reaction barriers.

2.4 Main softwares

2.4.1 Gaussian

The Gaussian is one well-known quantum chemical computational packages, which is capable of predicting many properties of atoms, molecules, reactive systems.^[22] Both pure and hybrid functionals are available in this program, and also provide a large amount of basis sets. The calculations for the first two systems were carried out with Gaussian 09 using hybrid functional B3LYP, which has been proved previously well reproduce the geometry and electronic properties of POMs. The pseudopotential (LANL2DZ) basis set was used for the meals involved in the polyoxometalates, whereas the all electron basis sets were used for the nonmetal elements. In order to compute the complexation energy for the Pd₁₂ systems, we have also considered the functional, which can include the dispersion effect in. The solvent effect were simulated with the continuum model PCM or SMD.

2.4.2 Vienna Ab initio Simulation Package

The Vienna ab initio simulation package (VASP) is an efficient DFT code developed by G. Kresse, J. Furthmüller, and J. Hafner, which are used to study 3D bulk systems with periodic boundary condition.^[27] This package works with plane-wave basis set

Chapter 2 Computational Methodology

that delocalized in the cell, instead of local (atom centered Gaussian) basis sets. There are many functional options based on LDA, GGA, and meta-GGA in the new version of VASP, and also some hybrid functionals such as HSE0 have been incorporated in the program. Moreover, VASP code uses pseudopotentials to decrease the number of electrons to be treated, thus to avoid interaction with the core electrons as they are not participate in chemical bonds in the molecules. Projector Augmented Wave-function (PAW) and ultra-soft (US) pseudopotentials are implemented on VASP package. Nowadays, it has become a highly efficient and powerful code for material simulations. With VASP, we can obtain the adsorption energies, equilibrium geometry, transition state, vibrational frequency, charge distribution, and density of states (DOS), as well as the projected density of states (PDOS). In particular, this package is widespread in heterogeneous catalysis area to study the reactivity of the solid materials. NEB algorithm and Dimer algorithm are useful methods to find the transition state, which are both available in VASP. Some detailed parameters and tutorials are described in the VASP program homepage: <https://www.vasp.at/>, and the detailed steps for each system are described in each chapter.

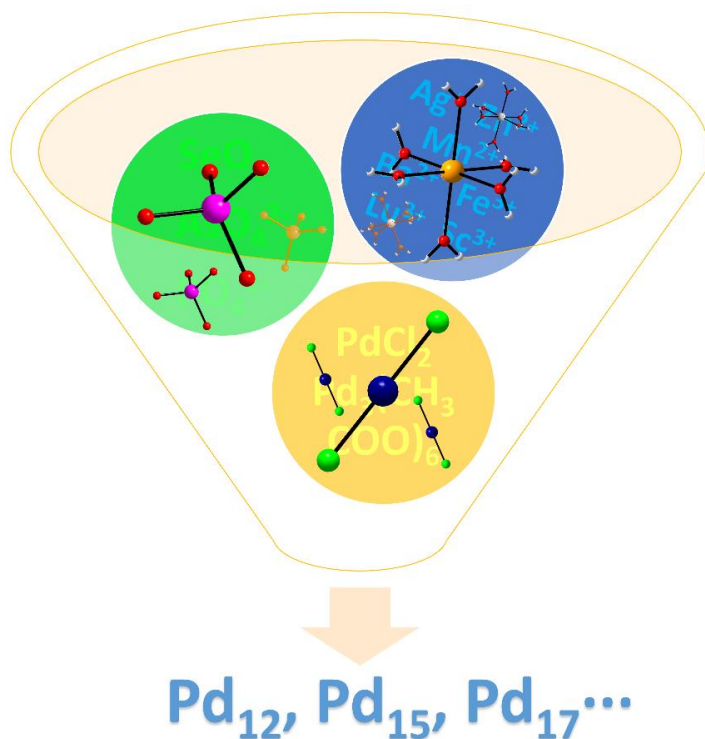
References and Notes

- [1] M. Born and J. R. Oppenheimer Zur quantentheorie der molekeln[J]. *Ann Physik*, 1927, 84, 457–484.
- [2] M. Born, K. Huang, *Dynamical Theory of Crystal Lattices* [M]. New York: Oxford University Press, 1954.
- [3] R. G. Parr and W. Yang, *Density-functional theory of atoms and molecules*. New York, 1980.
- [4] W. Koch and M. C. Holthausen, *A chemist's Guide to Density Functional Theory*. Weinheim, 2000.
- [5] P. Hohenberg and W. Kohn, *Phys. Rev.* 136, B864–B871.
- [6] J. M. Andrés and J. Beltrán, *Química teórica y computacional*. Castelló, 2000.
- [7] W. Kohn and L. J. Sham, *Phys. Rev.* 1965, 140(4A): A1133–A1138.
- [8] L. H. Thomas, *Proceedings of the Cambridge Philosophical Society*, 1927, 23, 542–548.
- [9] A. D. Becke, *J. Chem. Phys.* 1986, 84, 4524–4529.
- [10] J. P. Perdew, *Phys. Rev. B* 1986, 34, 7406–7406.
- [11] J. P. Perdew and W. Yue, *Phys. Rev. B* 1986, 33, 8800–8802.
- [12] J. P. Perdew, K. Burke and M. Ernzerhof, *Phys. Rev. Lett.* 1996, 77, 3865–3868.
- [13] J. P. Perdew, *Phys. Rev. B* 1986, 33, 8822–8824.
- [14] C. T. Lee, W. T. Yang, R. G. Parr, *Phys. Rev. B* 1988, 37, 785–789.
- [15] A. D. Becke, *Physical Review A* 1988, 38, 3098–3100.
- [16] A. D. Becke, *J. Chem. Phys.* 1993, 98, 5648–5652.
- [17] A. D. Becke, *J. Chem. Phys.* 1993, 98, 1372–1377.
- [18] J. L. Pascual-Ahuir, E. Silla and I. Tuñón, *J. Comput. Chem.*, 1994, 15, 1127–1138.
- [19] (a) A. Klamt and G. J. Schüürmann, *Chem. Soc. Perkin Trans.* 1993, 2, 799–805;
(b) J. Andzelm, C. Kölmel and A. Klamt, *J. Chem. Phys.* 1995, 103, 9312–9320;
(c) A. Klamt, *J. Chem. Phys.* 1995, 99, 2224–2235.
- [20] J. Tomasi, B. Mennucci and R. Cammi, *Chem. Rev.* 2005, 105, 2999–3094.
- [21] C. C. Pye and T. Ziegler, *Theor. Chem. Acc.* 1999, 101, 396–408.
- [22] M. J. Frisch et al. *Gaussian09W*; Gaussian, Inc.: Wallingford, CT, 2009.
- [23] A. V. Marenich, C. J. Cramer and D. G. Truhlar, *J. Phys. Chem. B* 2009, 113, 6378–6396.
- [24] X. López, J. J. Carbó, C. Bo and J. M. Poblet, *Chem. Soc. Rev.* 2012, 41, 7537–7571.

- [25] J. L. Fattebert and F. Gygi, *Int. J. Quantum Chem.* 2003, 93, 139–147.
- [26] (a) M. Fishman, H. L. Zhuang, K. Mathew, W. Dirschka and R. G. Hennig, *Phys. Rev. B* 2013, 87, 245402-1–245402-7; (b) K. Mathew, R. Sundararaman, K. Letchworth-Weaver, T. A. Arias and R. G. Hennig, *J. Chem. Phys.* 2014, 140, 084106-1–084106-8.
- [27] (a) G. Kresse and J. Hafner, *J. Phys. Rev. B: Condens. Matter* 1993, 47, 558-561; (b) G. Kresse and J. Hafner, *Phys. Rev. B: Condens. Matter* 1994, 49, 14251-14269; (c) G. Kresse and J. Furthmuller, *Comput. Mater. Sci.* 1996, 6, 15–50; (d) G. Kresse and J. Furthmuller, *Phys. Rev. B: Condens. Matter* 1996, 54, 11169–11186.

Chapter 3

The Template Effects of Internal and External Cations in Polyoxopalladates



The “unconventional” type POMs based on Pd^{II}, Pt^{III}, or Au^{III} is growing rapidly owing to their structural particular and compositional novelty, as well as their potential application in catalyst. In collaboration with the group of Prof. Ulrich Kortz, in this chapter we have systematically evaluated the role of internal and external cations in constructing the polyoxopalladates. The capture of a Mⁿ⁺ ion by a peripheral Pd^{II}-oxo shell involves the competition between the mother Pd^{II} and the guest metal ion. Present study reveals that the selection of the incarcerated ion has a thermodynamic control and that the main factors governing the formation of a particular polyanion are the charge and size of the guest cation, the electrostatic-interaction between the cation and the surrounding oxo ligands and the dehydration ability of the cation.

3.1 Introduction and background

During last years, significant advances have been done in the control of different variables involved in the formation of POMs, however there is not enough systematic studies that identify unambiguously the driving forces related to the self-assembly or aggregation processes.^[1-5] The “template-directed” method is one popular and extremely important synthetic strategy for obtaining novel POMs. Nuclearity and topology of the products are proved strongly dependent on the size, shape, and charge of the templates. For example, anions such as Cl^- and SO_4^{2-} have been enclosed within the central cavities of discrete polyoxovanadates to form templated host-guest complexes.^[6] The heteroanions (e.g., $\text{As}^{\text{III}}\text{O}_3^{3-}$, $\text{Sb}^{\text{III}}\text{O}_3^{3-}$, $\text{Si}^{\text{IV}}\text{O}_4^{4-}$, $\text{Ge}^{\text{IV}}\text{O}_4^{4-}$, $\text{P}^{\text{V}}\text{O}_4^{3-}$, $\text{As}^{\text{V}}\text{O}_4^{3-}$, and $\text{I}^{\text{VII}}\text{O}_6^{5-}$) can effectively control the formation of high nuclearity polyoxotungstates.^[7]

Beyond the more classical POMs, recently, an “unconventional” POM family based on Pd^{II} , Pt^{III} , or Au^{III} is growing rapidly owing to their structural particular and compositional novelty.^[8] In 2004, Wickleder *et al.* firstly synthesized one completely d^7 metal based complex $[\text{Pt}_{12}^{\text{III}}\text{O}_8(\text{SO}_4)_{12}]^{4-}$.^[9] Towards the goal of elevating the polyoxo-noble-metalate area, Prof. Ulrich Kortz and co-workers from the Jacobs University (Bremen, Germany) paid much attention on d^8 metal, and several kinds of polynuclear palladium- and gold-based complexes have been reported.^[8, 10-11] The first discovered polyoxopalladate was known as the distorted cubic $[\text{Pd}^{\text{II}}_{13}\text{As}_8^{\text{V}}\text{O}_{34}(\text{OH})_6]^{8-}$ (**Pd₁₃**) by condensation of palladium-aqua complexes in the presence of oxyacid heterogroup AsO_4^{3-} under aqueous media in 2008.^[10] Using similar synthetic strategies, it has been found that the capping ligands AsO_4^{3-} can be replaced by other groups, such as $\text{PhAs}^{\text{V}}\text{O}_3^{2-}$ and $\text{Se}^{\text{IV}}\text{O}_3^{2-}$.^[12] On the other hand, a large range of lanthanide (Pr^{3+} , Nd^{3+} , Sm^{3+} , *etc.*) and transition metal ions (Mn^{2+} , Zn^{2+} , Fe^{3+} , *etc.*) can also be effectively encapsulated inside **Pd₁₂** to form the hetero-polyoxopalladates by substituting the central Pd^{II} in **Pd₁₃**.^[13] A general structural representation of these species is shown in Figure 3.1a, which is composed of a central metal ion surrounded by a shell of twelve Pd^{II} ions linked by eight “inner” oxo ligands. Structurally, the **MPd₁₂L₈** cluster resembles the Keggin structure $[\text{XO}_4\text{W}_{12}\text{O}_{36}]^n$ (Figure 1.4), in which twelve peripheral palladium atoms form a distorted icosahedron/cuboctahedron in **MPd₁₂L₈**, and in the Keggin ion there are also twelve octahedral MO_6 blocks located on the vertices of a distorted cuboctahedron. Pd^{II} has a square-planar coordination instead of the octahedral coordination of W^{IV} due to the individual property of the ion itself. Similarly, a **Pd₁₅** cage (Figure 3.1b) with nanostar shape is obtained in the

Chapter 3 The Template Effects of Internal and External Cations in Polyoxopalladates

presence of Na^+ , K^+ , Ag^+ , and Ba^{2+} , whereas with Sr^{2+} the lacunary open-shell Pd_{12} is formed.^[14] Some “unconventional” hetero-metal mixed polyoxopalladates $\{\text{Pd}_7\text{V}_6\}$, $\{\text{Pd}_{17}\}$, $\{\text{Cu}_2\text{Pd}_{22}\}$, $\{\text{Na}_2\text{Pd}_{22}\}$ and even macrocycle scale $\{\text{Pd}_n\}$ ($n = 60, 72, 84, 96, 108$) have been obtained nowadays.^[15, 16] It is now increasingly appreciated that the cations may induce a deep influence on the self-assembly formation of polyoxopalladates.

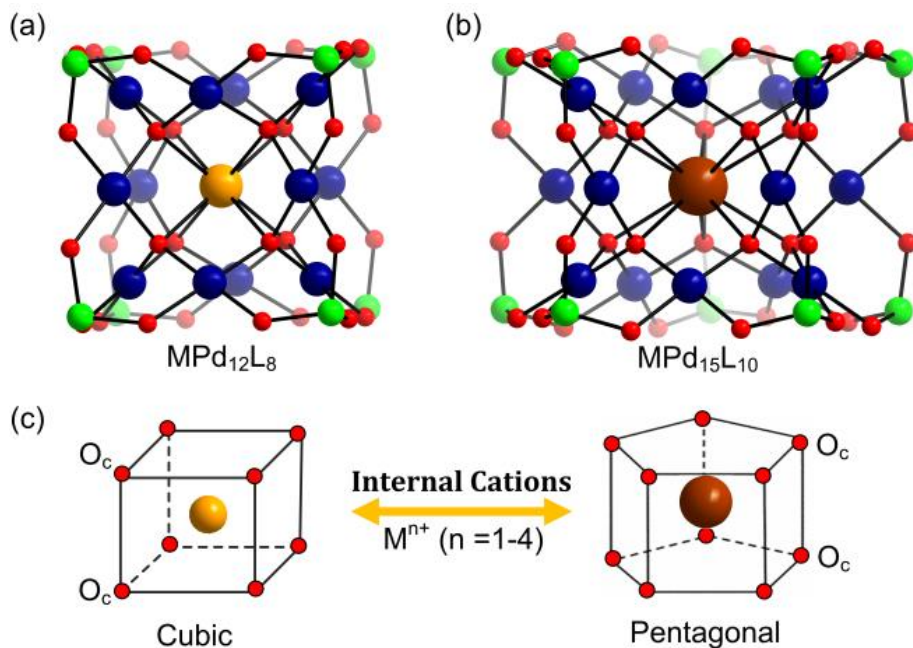


Figure 3.1. Ball and stick representation of two general polyoxopalladates, $\text{MPd}_{12}\text{L}_8$ (a) and $\text{MPd}_{15}\text{L}_{10}$ (b) ($M = \text{Metal ions}$, $L = \text{PhAs}^{\text{V}}\text{O}_3^{2-}$, $\text{PhP}^{\text{V}}\text{O}_3^{2-}$, $\text{Se}^{\text{IV}}\text{O}_3^{2-}$, $\text{P}^{\text{V}}\text{O}_4^{3-}$, or $\text{As}^{\text{V}}\text{O}_4^{3-}$), the coordinated environment of the central ions in Pd_{12} and Pd_{15} was exposed in (c). Color code: L: green, Pd: dark blue, O: red.

The cations can not only be introduced in the center of the Pd_{12} and Pd_{15} cage, very recently, Kortz’s group has synthesized one class of discrete silver (I)-palladium (II)-oxo nanoclusters such as $[\{\text{Ag}(\text{H}_2\text{O})_3\}_4\text{Pd}_{13}\text{O}_{32}(\text{AsO})_8]^{10-}$ ($\text{Ag}_4\text{Pd}_{13}$) and $[\{\text{Ag}_{4.25}(\text{H}_2\text{O})_2\}\text{AgPd}_{15}\text{O}_{40}(\text{PO})_{10}]^{14.75-}$ ($\text{Ag}_5\text{Pd}_{15}$) with several Ag^+ ions capping around the cavity. Unlike the central cations, the capped Ag^+ can directly coordinated with the Pd^{2+} with short Ag-Pd distance.^[14e]

On the other hand, the application of density functional theory (DFT) methods in the field of POMs has been getting mature in the last two decades. Our group has

performed several DFT calculations for such polyoxopalladates systems to understand their geometric and electronic properties. Initially, Antonova *et al.* studied the electronic properties for **MPd₁₂L₈** clusters with some lanthanides ions encapsulated in,^[13a] and later Jiménez Lozano *et al.* paid attention on the transitional metal (Mn^{II}, Cu^{II}, Fe^{III}) encapsulated clusters.^[13b] In both cases, it is probed that the geometric and electronic properties of the compounds can be well reproduced by including the solvent model in, and using a hybrid functional such as B3LYP. GGA functionals are less effective for late transition metal ions.

3.2 Motivation and objectives

Although many of such compounds have been reported, the controlled synthesis of the polyoxopalladates with desired size and topology remains challenging due to a poor understanding the role of the cations and the capping groups. To get more insight into the factors that governing the metal ion encapsulation, and provide an overall sense of cation selectivity in synthesizing of Pd-based nanoclusters with different size and topology, we have performed systematic theoretical analysis for a series of 35 cations (Li⁺, Na⁺, K⁺, Rb⁺, Cs⁺, Ag⁺, Be²⁺, Mg²⁺, Ca²⁺, Sr²⁺, Ba²⁺, Ra²⁺, Cu²⁺, Zn²⁺, Co²⁺, Mn²⁺, Ni²⁺, Pd²⁺, Cd²⁺, Fe³⁺, Sc³⁺, Ga³⁺, In³⁺, Tl³⁺, La³⁺, Lu³⁺, Y³⁺, Yb³⁺, Eu³⁺, Ce³⁺, Zr⁴⁺, Sn⁴⁺, Hf⁴⁺, Th⁴⁺, and U⁴⁺). The encapsulated cations were selected by considering both their charge and size, which ranged from the simplest alkali and alkaline earth metal ions to several transition metal cations, as well as trivalent and tetravalent cations. Alkali and alkaline earth metal ions are known as good template related to macrocycle-based systems.^[17] In this respect, the role of the Na⁺ used in the synthesis process will be allocated. We will reveal the main factors to govern the encapsulation of one or another cation by **Pd₁₂/Pd₁₅** from geometry and energy views, and predict some new potential candidates.

Motivated by the computational predictions, the Kortz group has studied experimentally the following cases: i) the capture of the largest trivalent cation, La³⁺; ii) the synthesis of a In³⁺ derivative in presence of Ga³⁺ in the solution and iii) the capture of the first tetravalent cation Sn^{IV}.

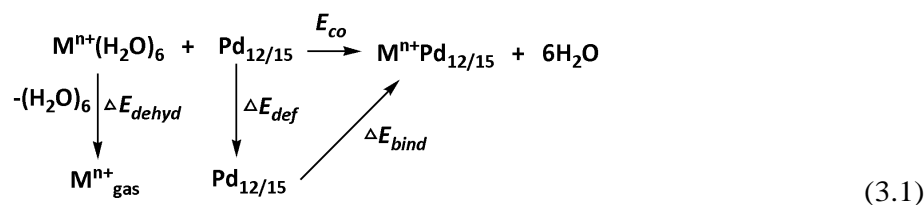
Furthermore, the special polyanions **Ag₄Pd₁₃** and **Ag₆Pd₁₅** represent very interesting examples of noble metal-capped polyoxo-noble-metalates in a fully inorganic assembly. In order to rationalize the formation mechanism of such polyanions, DFT calculations were performed to reveal the role of the external cations from Ag-Pd interactions.

3.3 Computational method

3.3.1 Computational details for internal cation encapsulation

All calculations were performed with the Gaussian 09 package.^[18] The computational scheme consists of two steps. Geometry optimization for all **Pd**₁₂ and **Pd**₁₅ based compounds were carried out at B3LYP level without any symmetry restrictions.^[19] The SDD effective core pseudopotential (ECP) basis set was used for atoms of La, Yb, Lu, Eu, Ce, Ra, Th, and U,^[20] while LANL2DZ basis set was employed for the larger metals (Rb, Cs, Sr, Ba, Ga, In, Tl, Sn) and transition metals (Co, Cu, Cd, Pd, Zn, Mn, Ni, Ag, Sc, Fe, Y, Zr, Hf) with Los Alamos relativistic core potentials (ECPs).^[21] In addition, the 6-31G** basis set was used for O, C, As, Se, H, and the encapsulated small metals (Na, K, Be, Mg, Ca).^[22] From these calculations, we obtained the energies at B3LYP level. In order to include the long range interaction and dispersion effects, single point calculations were performed for all optimized complexes with two additional functionals, M06 and ω B97XD.^[23,24] For all steps, the continuum SMD implicit solvation model was used to simulate the effect of the aqueous solution.^[25]

As shown in Figure 3.1, the cuboid-shaped **Pd**₁₂ and nanostar **Pd**₁₅ are selected as the mother framework for metal ion encapsulation, in which the ion is located in an 8- or 10-coordinated environment respectively. To evaluate their selective encapsulation for different cations, the reaction process is simulated by equation 3.1, and the complexation energy (E_{co}) was calculated by equations (3.2) and (3.3):



$$E_{co} = E(\text{M}^{n+}\text{Pd}_{12/15}) + E(6\text{H}_2\text{O}) - E(\text{Pd}_{12/15}) - E(\text{M}^{n+}(\text{H}_2\text{O})_6) \quad (3.2)$$

$$E_{co} = \Delta E_{bind} + \Delta E_{def} + \Delta E_{dehyd} \quad (3.3)$$

Where $\text{M}^{n+}(\text{H}_2\text{O})_6$ is the solvated cation model. Since the dehydration is one fundamental factor for accurate evaluation of the complexation energy, all cations were solvated by six explicit water molecules and also surrounding by the implicit model to correct the systematic errors. With this explicit and implicit solvent combination model, the dehydration energy (ΔE_{dehyd}) of the cations was well estimated when compared with the experimental hydration enthalpies (H_{hyd}),^[26] as the deviation shown in Figure 3.2 are less than 10% except for Li^+ , Rb^+ , Cs^+ , and Ra^{2+} . The whole process is assumed as the relaxed **Pd**_{12/15} cage extracts the cation from solvent and encapsulates into the cage. The complexation energies (E_{co}) of the **Pd**_{12/15} with all

Chapter 3 The Template Effects of Internal and External Cations in Polyoxopalladates

cations are computed, defined as the reaction energies involved in the encapsulation process. Three terms contribute to this process, the cage deformation of each capsule with respect to the cation-free $\text{Pd}_{12/15}$ cage (ΔE_{def}), dehydration of a cation from solvated to free ion (ΔE_{dehyd}), and the binding interaction (ΔE_{bind}) between the optimal cage and the free cation respectively.

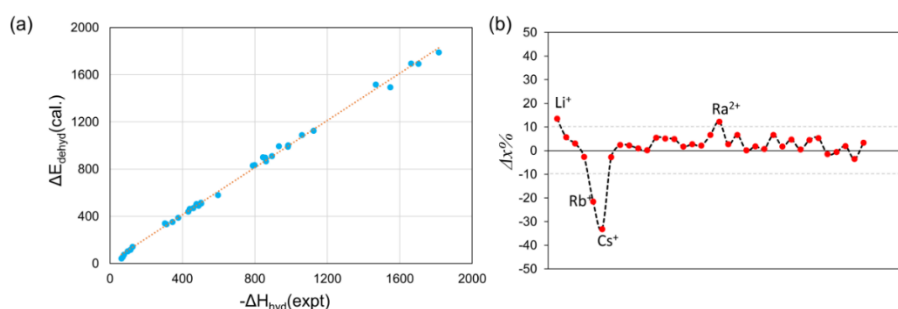


Figure 3.2. (a) Comparison of experimental hydration enthalpies and computational dehydration energies for all selected cations; (b) the deviation between experimental and theoretical values $\Delta x\% = \frac{\Delta E_{dehyd} - (-H_{hyd})}{-H_{hyd}} \%$.

$$\Delta x\% = \frac{\Delta E_{dehyd} - (-H_{hyd})}{-H_{hyd}} \%$$

3.3.2 Computational details for Ag-Pd interactions

The model systems $\text{Na}_3\text{AgMgPd}_{12}$ and $\text{Ag}_3\text{Pd}_{15}$ (Figure 3.11) were used to reveal the interactions between Ag^+ and Pd^{II} metal ions in the actual $\text{Ag}_4\text{Pd}_{13}$ and $\text{Ag}_5\text{Pd}_{15}$ compounds. Geometry optimizations were performed at B3LYP/LANL2DZ (Ag, Pd)+6-31G*(O, P, As)/PCM level. The NBO calculations were performed at the same level as optimization in Gaussian 09. To characterize the nature of the Ag-Pd, Ag-Ag, and Ag-O interactions, the topology of electron density within the quantum theory of atoms in molecules (QTAIM)^[27, 28] developed by R. F. Bader was performed using the Multiwfn software.^[29] The Multiwfn software developed by Lu was also used to calculate the critical points, potential energy density ($V(r)$), kinetic energy density ($G(r)$), and the Laplacian density between Pd^{II} ions and the adjacent Ag^+ ions.

3.4 The template effect of internal cations

3.4.1 Size matching between the cations and the bare Pd_{12/15}

Since the discovery in 2008 of the first member of the **Pd₁₂** family,^[10] [Pd^{II}₁₃As^VO₃₄(OH)₆]⁸⁻, Kortz's group has synthesized a large amount of derivatives by altering the capping As^VO₄³⁻ ligands and the central Pd^{II} cation. In order to further expand and rationalize the template role that cations play, systematic DFT calculations were performed by introducing different metal ions into **Pd₁₂** or **Pd₁₅** cages. The sole "host" cages (**Pd₁₂** and **Pd₁₅**) and the corresponding host (cage)-guest (cation) systems (capped by PhAs^VO₃²⁻) were optimized at B3LYP level. The electrostatic potential map (MEP) analysis in Figure 3.3 for free **Pd₁₂** revealed an interesting distribution of most negative partial atomic charges on the center of the O₈ cubic and on the surface of the six Pd₄O₄ faces, indicating that electrophilic groups, such as metal ions, are more likely to locate at the central position. This prediction is in line with the experimental facts where cations usually occupy such position. As shown in Table S3.1, the computed distances (O_c-O_c, M-O_c, and M-Pd) reproduce fairly well as the reported X-ray data, although they are found systematically slightly longer than in experiments.^[11,13] It is worth mentioning that for incorporating of Pd²⁺, Ni²⁺, Co²⁺, Fe³⁺, and Eu³⁺ ions, the DFT calculations suggest that the high spin state centered in [Pd^{II}₁₂O₈(As^VPhO₃)₈]⁸⁻ are more favorable than its low spin state configuration.^[13b]

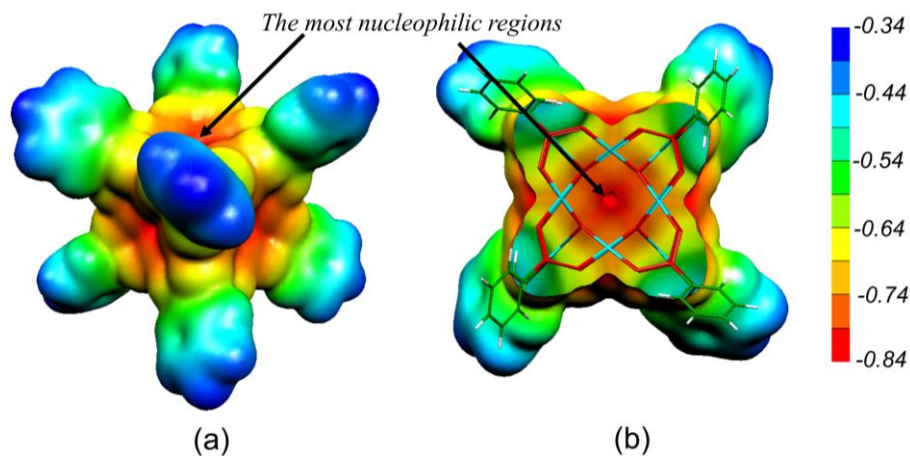


Figure 3.3. Side (a) and top (b, one half of the molecule) view of the MEP distribution for [Pd^{II}₁₂O₈(PhAs^VO₃)₈]⁸⁻, the values taken by EP at each point are coded by colors: red-yellow for nucleophilic regions and green-blue for electrophilic regions. The cavity and six Pd₄O₄ interface are the most nucleophilic regions.

Chapter 3 The Template Effects of Internal and External Cations in Polyoxopalladates

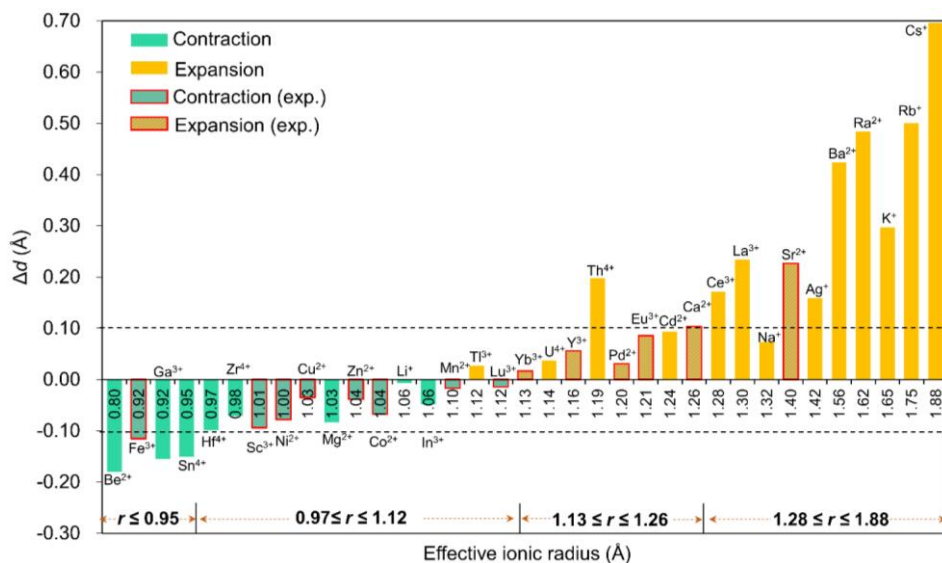


Figure 3.4. The O_c-O_c distortions ($\Delta d = d_{O-O} - 2.728$, by referring the distance in free cage) of $\{O_8\}$ cavity after encapsulation of cations, the cations from left to right are organized by the effective ionic radius. The bar with upward diagonal labelled indicates the experimental reported compounds.

To capsule the cation, the ion and the cavity should own matched size. Due to the small flexibility of the locked $\{O_8\}$ cage, all cations are optimally located in the center of the cubic. The average O_c-O_c distance generally elongates as the effective ionic radius of M^{n+} increases; this trend is absolutely in line with the change of $M-O_c$ bonds. To give insight into the effect of cation's size on the geometry of the cage, the O_c-O_c distortions after encapsulation of cations are plotted in Figure 3.4 by referring to the distance in **Pd**₁₂ cage ($d_{O_c-O_c} = 2.728$ Å) without internal cation. We find that ions with radius smaller than 1.12 Å, can induce some contraction of the $\{O_8\}$ cavity, including Co^{2+} , Ni^{2+} , Cu^{2+} , Zn^{2+} , Mn^{2+} , Sc^{3+} , Fe^{3+} , and Lu^{3+} , and also ions that have not been captured yet within the **Pd**₁₂ framework, such as Li^+ , Be^{2+} , Mg^{2+} , Ga^{3+} , In^{3+} , Sn^{4+} , Zr^{4+} , and Hf^{4+} . In particular, the Be^{2+} , Fe^{3+} , Ga^{3+} , and Sn^{4+} seem too small to be hosted efficiently, and consequently large contraction occurred to maximize $M-O_c$ interactions. When the ion size is between 1.13 and 1.26 Å, small expansions with Δd less than 0.1 Å are needed, except for Th^{4+} . However, significant distortion of $\{O_8\}$ was detected for ions larger than 1.28 Å, such as Ce^{3+} , La^{3+} , Sr^{2+} , Ag^+ , K^+ , Rb^+ , Cs^+ , Ba^{2+} , and Ra^{2+} , where for some cases elongations larger than 0.4 Å are observed. It is remarkable that for most of the experimentally observed anions, the distortion induced by metal encapsulation is no larger than 0.1 Å, and therefore the size matching between

Chapter 3 The Template Effects of Internal and External Cations in Polyoxopalladates

cations and the Pd_{12} cavity must be an important factor to be considered. Figure 3.4 also suggests that cations with size rang in 0.97~1.26 Å fit well within O_8 cavity in Pd_{12} regardless of the charge. Respect to this, small ($r \leq 0.95\text{Å}$) and large ($r \geq 1.28\text{Å}$) cations probably are not be the ideal candidates for constructing the cubic Pd_{12} cluster from a size-matching view, and the optimal cation size for designing structures is in the 0.97~1.26 Å range.

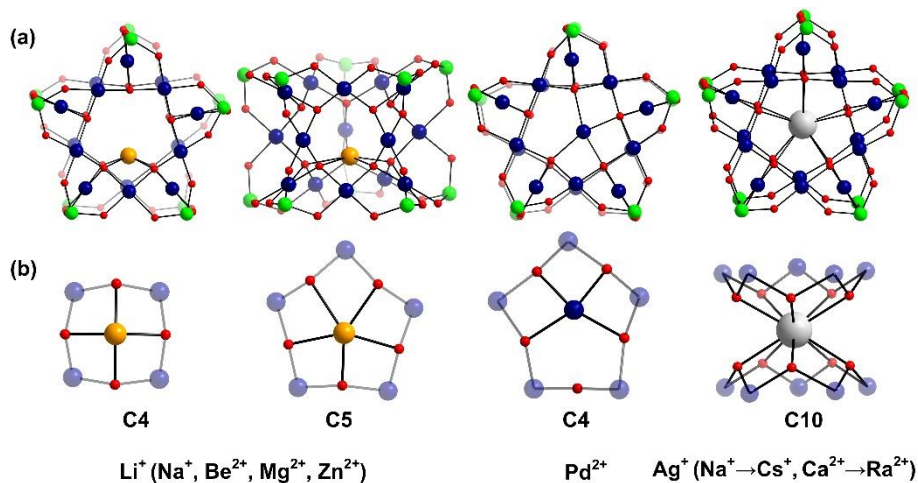


Figure 3.5. (a) Structural scheme of $[\text{Pd}^{\text{II}}_{15}\text{O}_{10}(\text{PhAs}^{\text{V}}\text{O}_3)_{10}]^{10-}$ encapsulated with different guest cations, the phenyl groups are omitted for clarity; (b) brief view of the coordination mode for the internal cations. Color code: guest metal (orange/white), As (green), Pd (dark blue), O (red).

In contrast, the large cations are more likely to accommodate more precursors around themselves and subsequently assemble into larger clusters. In order to compare with the Pd_{12} systems, some selected cations (Li^+ , Na^+ , K^+ , Rb^+ , Cs^+ , Ag^+ , Be^{2+} , Mg^{2+} , Ca^{2+} , Sr^{2+} , Ba^{2+} , Zn^{2+} , and Pd^{2+}) were incorporated in Pd_{15} . The Pd_{15} provides a five prism $\{\text{O}_{10}\}$ inner space with more flexibility. It is found that the $\{\text{O}_{10}\}$ cavity appears too large to encapsulate small ions, such as Li^+ , Be^{2+} , Mg^{2+} , and Zn^{2+} ($r < 1.2\text{Å}$), in which the cations are forced out of the C_5 axis center by coordinating with less oxygen atoms. Two non-centered coordinated modes are obtained from our DFT calculations, C_4 and C_5 as depicted in Figure 3.5. For example, the Li^+ could coordinate with five O_c from Pd_5O_5 (2.107, 2.276, 2.261, 2.457, 2.336 Å) or four O_c from Pd_4O_4 (2.002, 2.023, 2.005, 2.022 Å). Although the former configuration owns five coordinated atoms, the shorter bonds in the latter may lead to stronger interactions. As expected, the energy

differences illustrate that the C_4 mode is more stable than C_5 by $6.1 \text{ kcal}\cdot\text{mol}^{-1}$ (Table S3.2). On the other hand, encapsulation of Na^+ , K^+ , Rb^+ , Cs^+ , Ag^+ , Ca^{2+} , Sr^{2+} , Ba^{2+} , and Ra^{2+} ($r > 1.2 \text{ \AA}$) fits well the Pd_{15} . Some of them are strongly supported by the experiments, which show that NaPd_{15} , KPd_{15} , BaPd_{15} , and AgPd_{15} can be easily observed in the presence of Na^+ , K^+ , Ba^{2+} , and Ag^+ .^[14] It is worth mentioning that the Na^+ prefers to be near the Pd_5O_5 face (C_5) rather than the center, as suggested by the experiment.^[14b] Interestingly, the Pd^{2+} prefers also C_4 mode, but linking only four O from the Pd_5O_5 face, as the X-ray data shows in $\text{Pd}_2\subset \text{Pd}_{15}$.^[15d] The good reproduction of the experimental facts reveals that the size of the cation plays an important role in the control of the nuclearity of the product.

3.4.2 Complexation energy and the competition between Pd^{2+} and other metal cations

Although the size-matching has been established as an essential factor for the cluster formation, we have to be aware that the cation-cavity interaction and the dehydration ability of the cation are not included in the analysis. Thus, we next will examine why the reported cations are enable to be encapsulated by $\text{Pd}_{12/15}$ and predict some potential candidates from an energy point of view. To rationalize this point, the complexation energy (E_{co}) of Pd_{12} and Pd_{15} for each ion was computed as described in the computational section, and the results at B3LYP level (black points) are collected in Figure 3.6, as well as the energy corrections with M06 (red points) and ωB97XD (green points) functionals. The results with M06 give virtually identical values as that with B3LYP functional, whereas the addition of the dispersion correction in ωB97XD increases the values of complexation energies without changing the overall trends. Therefore, the results at B3LYP level can reasonably identify the trend analysis. Generally, the E_{co} becomes more exothermic as the formal charge increases from monovalent to tetravalent. For alkali and alkaline earth metal ions the E_{co} is significantly affected by the size of the cations. All encapsulated processes seem to thermodynamic favourable except for Cs^+ , which shows the only positive E_{co} of $18.3 \text{ kcal}\cdot\text{mol}^{-1}$. It is illustrative that the initial observed polyoxopalladate is the pure $[\text{Pd}^{\text{II}}_{13}\text{As}_8^{\text{V}}\text{O}_{34}(\text{OH})_6]^{8-}$ with one Pd^{2+} located in the center, and that the formation of the cluster occurs under the coexistence in the solution of Na^+ and Pd^{2+} . The encapsulation of Pd^{2+} by $[\text{Pd}^{\text{II}}_{12}\text{O}_8(\text{PhAs}^{\text{V}}\text{O}_3)_8]^{8-}$ is predicted to be dramatically exothermic by $-54.6 \text{ kcal}\cdot\text{mol}^{-1}$, whereas Na^+ shows relatively weak competitiveness with a complexation energy of $-42.2 \text{ kcal}\cdot\text{mol}^{-1}$. Thus, it is not difficult to understand

Chapter 3 The Template Effects of Internal and External Cations in Polyoxopalladates

why the Na^+ ions are not captured in the center of the polyoxopalladate and acts only as counter-ions.

Following this direction, all cations are divided into two parts by referring the E_{co} of Pd^{2+} (dash line in gray). Values of E_{co} located below the grey line indicate that from a thermodynamic point of view, the corresponding ions are more favorable to stabilize the Pd_{12} cluster than the mother ion Pd^{2+} , thus suggesting that are more easily to be encapsulated. For instance, the encapsulation of Fe^{3+} and Sc^{3+} cations within Pd_{12} has associated a complexation energy of -124.1 and -116.2 $\text{kcal}\cdot\text{mol}^{-1}$, respectively, both are significantly more exothermic than Pd^{2+} (-54.6 $\text{kcal}\cdot\text{mol}^{-1}$). Indeed, the closed Pd_{12} compounds with Ca^{2+} , Co^{2+} , Cu^{2+} , Ni^{2+} , Zn^{2+} , Mn^{2+} , Sc^{3+} , Fe^{3+} , Y^{3+} , Yb^{3+} , Lu^{3+} , and Eu^{3+} encapsulated inside have already been successfully synthesized by using similar synthetic procedure.^{13a,b,c} In contrast, the encapsulation of all alkali metal ions, Ag^+ , Be^{2+} , Sr^{2+} , Ba^{2+} , and Ra^{2+} ions are expected to be difficult to form thanks to the larger complexation energy with respect to Pd^{2+} , even though some of them own suitable size. This behaviour is also valid for the derivatives with other capped groups ($\text{As}^{\text{V}}\text{O}_4^{3-}$ and $\text{Se}^{\text{IV}}\text{O}_3^{2-}$), as shown in Figure S3.1. Coupled with the unfitting size, the Ag^+ , K^+ , Rb^+ , Cs^+ , and Ba^{2+} mediated complexes would be the first ions ruled out by the small Pd_{12} .

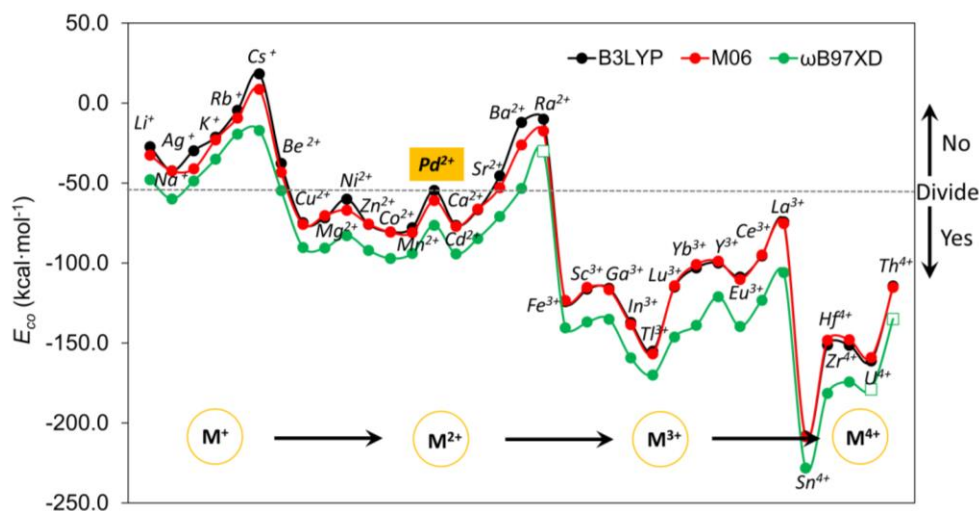


Figure 3.6. Computed complexation energies (in $\text{kcal}\cdot\text{mol}^{-1}$) of M^{n+} ($n = 1-4$) encapsulated in Pd_{12}L_8 ($L = \text{PhAs}^{\text{V}}\text{O}_3^{2-}$) as a function of cation from monovalent to tetravalent at B3LYP (black), M06 (red), and ωB97XD (green) functional level, respectively. The cations are organized by considering both the charge and the size. Note that the smaller (more negative) values indicate the higher affinity of Pd_{12} for metal ion. The E_{co} for Ra, U, and Th at ωB97XD level is not included (square) due to the unavailable vdW radius for these elements.

Chapter 3 The Template Effects of Internal and External Cations in Polyoxopalladates

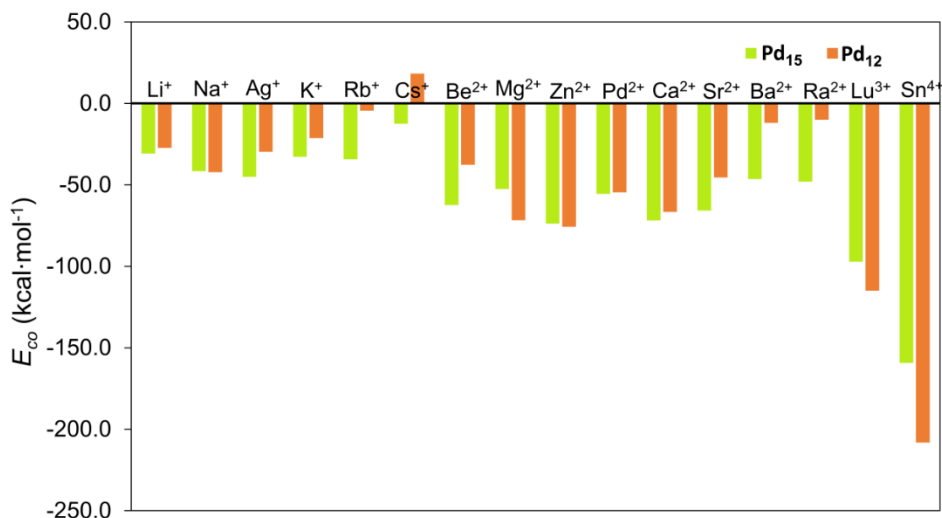


Figure 3.7. Complexation energies ($\text{kcal}\cdot\text{mol}^{-1}$) comparison for selected cations encapsulated in $[\text{Pd}_{12}\text{O}_8(\text{PhAs}^{\text{V}}\text{O}_3)_8]^{8-}$ (orange bar) and $[\text{Pd}_{15}\text{O}_{10}(\text{PhAs}^{\text{V}}\text{O}_3)_{10}]^{10-}$ (green bar) respectively.

Table 3.1. Computed complexation energy ($\text{kcal}\cdot\text{mol}^{-1}$) for La^{3+} and Sr^{2+} encapsulated in open and closed- Pd_{12} , and the experimental product yields are listed.

		B3LYP	M06	ω B97XD	ratio%
Pd²⁺	closed	-54.6	-60.8	-76.4	
Sr²⁺	open	-49.9	-61.0	-75.8	98%
	closed	-45.4	-52.9	-70.9	2%
La³⁺	open	-70.6	-74.7	-105.7	40%
	closed	-74.2	-75.2	-105.9	60%

In order to further unravel this point, the encapsulation by $[\text{Pd}_{15}\text{O}_{10}(\text{PhAs}^{\text{V}}\text{O}_3)_{10}]^{10-}$ for some selected cations was computed (Figure 3.7) to compare with Pd_{12} . As expected, the Na^+ , Ag^+ , K^+ , Rb^+ , Ba^{2+} , and Ra^{2+} ions are calculated to be both geometrically and energetically suitable for Pd_{15} instead of Pd_{12} , results that are in full agreement with the experimental facts.^[14] Most of the small cations, such as Mg^{2+} and Zn^{2+} , do not fit geometrically, nor energetically favorable in Pd_{15} . The original Pd^{2+} shows similar ability to be encapsulated by Pd_{12} and Pd_{15} , which is consistent to the observed $[\text{Pd}^{\text{II}}_{13}\text{O}_8(\text{PhAs}^{\text{V}}\text{O}_3)_8]^{6-}$ and $\text{Pd}_2\subset\text{Pd}_{15}$ clusters.^[12,15d] The middle sized Sr^{2+} was reported to form a novel *open-shell* SrPd_{12} , this inspired us to check its complexation

energy both in open and closed **Pd₁₂**, see Table 3.1.^[14d] The energy required for encapsulating into the open form was computed to be $-50.0 \text{ kcal}\cdot\text{mol}^{-1}$, whereas that in the closed **Pd₁₂** structure was a little less exothermic, $-45.4 \text{ kcal}\cdot\text{mol}^{-1}$. Therefore, the open **Pd₁₂** was preferentially formed before **Pd₁₅**. Among the unfavorable ions within **Pd₁₂**, the Sr^{2+} shows the smallest E_{co} difference with respect to Pd^{2+} , only 9.2 (4.6 in open **Pd₁₂**) $\text{kcal}\cdot\text{mol}^{-1}$, even much smaller differences at M06 and ω B97XD level. Thus, a great competition between Pd^{2+} and Sr^{2+} may be present in the reaction. Experiments show that only a 2% of closed **SrPd₁₂** is formed, and that the Sr^{2+} ion can be substituted by Pd^{2+} to form **Pd₁₃** by only increasing the pH of the solution. It is interesting to note that E_{co} for La^{3+} is very close to that calculated for Pd^{2+} , which may lead to special composition of products. In contrast to Sr^{2+} , calculations suggest that the closed form for La^{3+} of **Pd₁₂** is slightly more favorable than the open one. Accordingly, the nature and size of the cation directly influence the geometry of the products and it strongly suggests a template effect of the cation in classical polyoxopalladate synthesis.

3.4.3 Potential new candidates for the 12-palladate family

The systematic study of the complexation energy for different cations revealed that the competition from Pd^{2+} plays a critical factor in determining the type of the products. Although the energy trend should not be taken quantitatively, it appears to be qualitatively useful to design the synthesis of new compounds.

Up to now there is a predominance of transition and lanthanide elements in guest metal-incorporated polyoxopalladates (**MPd₁₂**) family. Much less attention has been paid towards *p*-block elements, whereas the encapsulation of Ga^{3+} , In^{3+} , and Tl^{3+} was found very exothermic with energies of -115.8 , -137.1 and $-155.1 \text{ kcal}\cdot\text{mol}^{-1}$, respectively. For all three cations, the encapsulation is predicted to be more favorable than for the already reported Sc^{3+} derivative, and in addition there is a clear tendency to increase the encapsulation ability from up to down within IIIA group.

On the other hand, no encapsulation of higher charged cations ($n > 3$) have been reported until now. In this regard, we analyzed the encapsulation in **Pd₁₂** for several typical tetra-valent cations, such as Sn^{4+} , Zr^{4+} , Th^{4+} , U^{4+} , and Hf^{4+} . As expected, all tetra-valent cations exhibit more energetic values due to the increasing anion-cation interactions. The small Sn^{4+} is located at the lowest position among all investigated ions.

In collaboration with the group of Prof. Kortz we have designed several experiments that should be useful to confirm the trends observed in the systematic theoretical analysis and these experiments concern to 1) elements of the *p*-block, 2) the synthesis

of a La derivative that should produce two forms for \mathbf{Pd}_{12} , 3) the capture for the first time of a tetravalent cation, and 4) the competition between more than two cations.

3.4.4 Experiments confirm theoretical observations: Synthesis and characterization of cuboid-shaped \mathbf{LaPd}_{12} -1, \mathbf{GaPd}_{12} , \mathbf{InPd}_{12} and open-shell type \mathbf{LaPd}_{12} -2

Here we have summarized very briefly the experiments performed in Jacobs University in order to corroborate the theoretical predictions described above. The La^{3+} , Ga^{3+} , and In^{3+} are selected for experimental synthesis by Prof. Kortz group. Four new members of the \mathbf{Pd}_{12} family have been successfully isolated and characterized (Figure 3.8): $[\text{La}^{\text{III}}\text{Pd}^{\text{II}}_{12}\text{O}_8(\text{PhAs}^{\text{V}}\text{O}_3)_8]^{5-}$ (**closed-LaPd₁₂-1**), $[\text{La}^{\text{III}}\text{Pd}^{\text{II}}_{12}\text{O}_6(\text{OH})_3(\text{PhAs}^{\text{V}}\text{O}_3)_6(\text{OAc})_3]^{3-}$ (**open-LaPd₁₂-2**), $[\text{Ga}^{\text{III}}\text{Pd}^{\text{II}}_{12}\text{O}_8(\text{PhAs}^{\text{V}}\text{O}_3)_8]^{5-}$ (**GaPd₁₂**), and $[\text{In}^{\text{III}}\text{Pd}^{\text{II}}_{12}\text{O}_8(\text{PhAs}^{\text{V}}\text{O}_3)_8]^{5-}$ (**InPd₁₂**), which perfectly support the above mentioned calculations (Table 3.1). Notably, La^{3+} is one of the largest trivalent cations that could be by far encapsulated inside a \mathbf{Pd}_{12} cage and its size and relatively low energy is a good test for present study. The small advantage of E_{co} in closed structure leads to a little higher yields of product respect to open for La^{3+} . In addition, we are also informed a polyoxopalladate containing a central tetravalent cation Sn^{IV} have been captured by \mathbf{Pd}_{12} capping by another ligand ($\text{As}^{\text{V}}\text{O}_4^{3-}$), however, the studies on structure and chemical properties for these anions will be reported elsewhere.

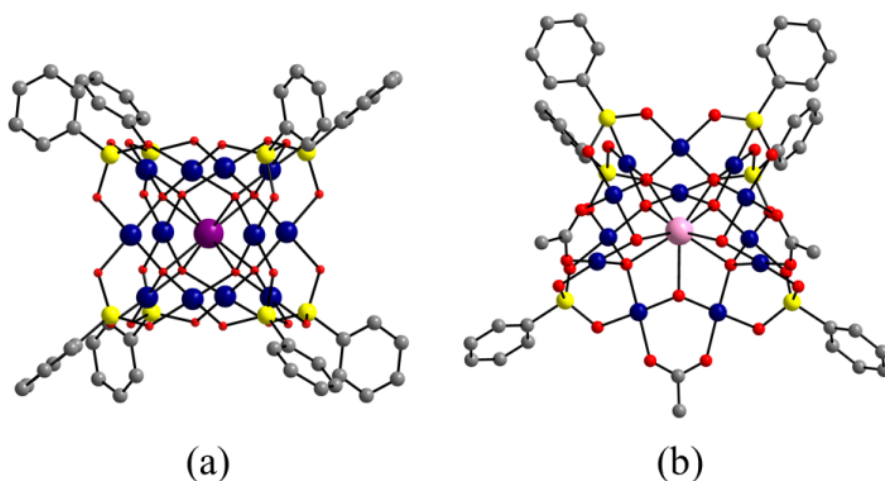


Figure 3.8. Ball-and-stick representation of (a) cuboid-shaped \mathbf{MPd}_{12} ($M = \text{La}^{3+}$, Ga^{3+} , and In^{3+}) and (b) open-shell type \mathbf{LaPd}_{12} -2. Color code: M (violet), La (pink), Pd (dark blue), As (yellow), O (red), C (gray). Hydrogen atoms are omitted for clarity.

*Chapter 3 The Template Effects of Internal and External Cations in Polyoxopalladates***3.4.5 Selective entrapment of Ga³⁺ and In³⁺ in Pd₁₂ host**

The complexation energy profile in Figure 3.6 not only helps to understand the complexation ability of a given cation, we have shown in collaboration with the group of Prof. Kortz that it can help to determine the competition in a more complex situation. In order to further illustrate this point, the selective encapsulation by the 12-palladate cage has been studied while simultaneously more than one type of guest metal ions is introduced in the solution. To be specific, under the circumstance of equimolar quantity of excess Ga³⁺ and In³⁺ ions were given at the meantime, only **Na-InPd₁₂** was formed as confirmed by ⁷¹Ga (no signal) and ¹¹⁵In NMR (singlet at 254.1 ppm, Figure 3.9a), which means that the 12-palladate cage prefers capturing In³⁺ rather than Ga³⁺, declaring the existence of a selective-entrapment feature. It is conceivable that the “rejected” Ga³⁺ ions might go through hydrolysis to generate other species in the mother solution. Later on, the free Ga³⁺ ions were detectable by ⁷¹Ga NMR while the solution was acidified to pH 1 by HNO₃ (Figure 3.9b).

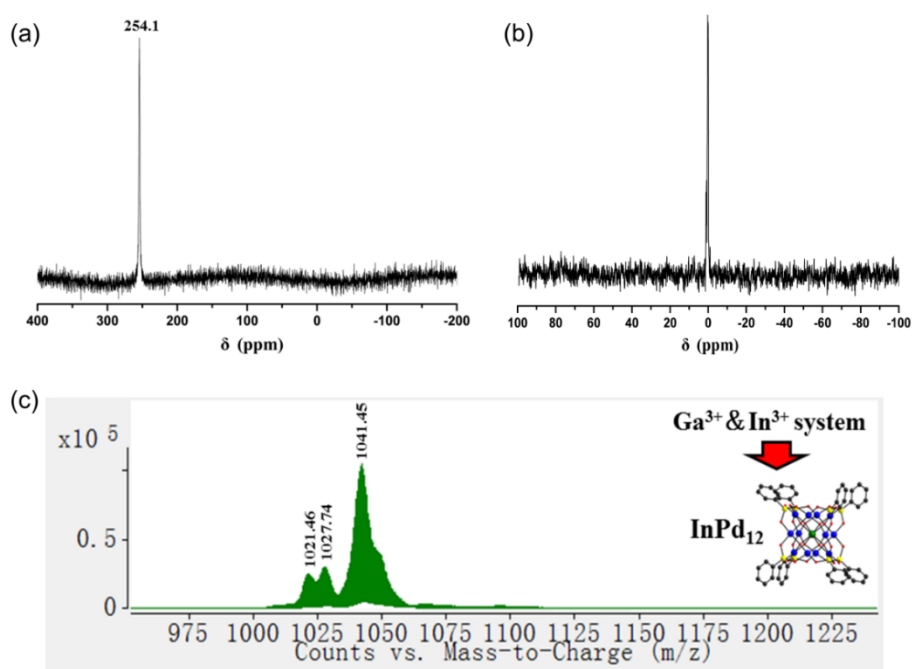


Figure 3.9. (a) ¹¹⁵In NMR spectrum of the reaction solution of Ga³⁺ & In³⁺ system recorded in H₂O at room temperature; (b) ⁷¹Ga NMR spectrum of the reaction solution of Ga³⁺ & In³⁺ system at pH 1 recorded in H₂O at room temperature; (c) Negative ion mass spectrum of crystals collected from the Ga³⁺ & In³⁺ system in aqueous solution.

Chapter 3 The Template Effects of Internal and External Cations in Polyoxopalladates

On the other hand, for the mixed system, the filtrated mother solution was allowed to evaporate until the solution level had approached to the crystals, which were then carefully collected for ESI-MS analysis. The spectrum of the product obtained from Ga^{3+} & In^{3+} system shows peaks only correspond to **InPd₁₂**-related species (Figure 3.9c). Notably, the envelopes appearing at $m/z = 1021.46$ and 1027.74 can be unequivocally ascribed to $\{\text{Na}[\text{InPd}_{12}\text{O}_8(\text{C}_6\text{H}_5\text{AsO}_3)_7(\text{AsO}_3)^+]\}^{3-}$ and $\{\text{Na}[\text{InPd}_{12}\text{O}_8(\text{C}_6\text{H}_5\text{AsO}_3)_7(\text{AsO}_3)^+](\text{H}_2\text{O})\}^{3-}$, which may dissociate from the plenary **InPd₁₂** cluster by losing one $[\text{C}_6\text{H}_5]^-$ fragment possibly during the electrospray ionization processes. Similar experiments for another two groups are furthermore checked, the Ga^{3+} & Sc^{3+} and Sc^{3+} & In^{3+} respectively. Both ^{71}Ga and ^{45}Sc NMR signals have been detected with **GaPd₁₂** and **ScPd₁₂** coexisting in solution. For Sc^{3+} & In^{3+} pair, the signal of **InPd₁₂** can be identified in a few seconds, whereas the signal of **ScPd₁₂** is obtained after overnight. Such results nicely proved again the selective-entrapment feature of the **Pd₁₂** cage in the mixed system, which fit well with the complexation energies order given in Figure 3.6. Combining the theoretical and experimental results, we obtain a selective order of $\text{In}^{3+} > \text{Ga}^{3+} \approx \text{Sc}^{3+}$. The apparent E_{co} difference between In^{3+} ($-137.1 \text{ kcal}\cdot\text{mol}^{-1}$) and $\text{Ga}^{3+}/\text{Sc}^{3+}$ ($-116.2/-115.8 \text{ kcal}\cdot\text{mol}^{-1}$) leads to a more efficient selectivity for In^{3+} , while the Sc^{3+} and Ga^{3+} are more difficult to be separated because of the similar complexation ability.

3.4.6 What properties of the metal cation govern its affinity for a given Pd₁₂?

Through the above theoretical and experimental studies, we have addressed the two main factors that control the encapsulation of metal ions: the energy associated to the complexation of a given cation by a free **Pd₁₂** cage (E_{co}) and how the guest fits inside the host cage. To gain a deeper understanding of the intrinsic factors governing the formation of **M@Pd₁₂**, we performed an energy decomposition analysis for E_{co} . From an energy point of view, we can split the process of cation complexation, as the sum of three steps: *dehydration* of the cation, *deformation* of the **Pd₁₂** cluster and the *binding* between the cation and the **Pd₁₂** cluster. Thus, E_{co} can be expressed as $\Delta E_{def} + \Delta E_{dehyd} + \Delta E_{bind}$. In Figure 3.10, the values computed for ΔE_{def} , ΔE_{dehyd} and ΔE_{bind} for a series of cations are classified according to the cation charge. From this figure, we can observe that in absolute values ΔE_{def} is much smaller than ΔE_{dehyd} and ΔE_{bind} , and that these two latter terms are very dependent of the cation charge. Thanks to the increasing charge-dipole and charge-charge interactions, the complexation energy for di- and trivalent cations is respectively two or three times more exothermic than for monovalent cations.

Chapter 3 The Template Effects of Internal and External Cations in Polyoxopalladates

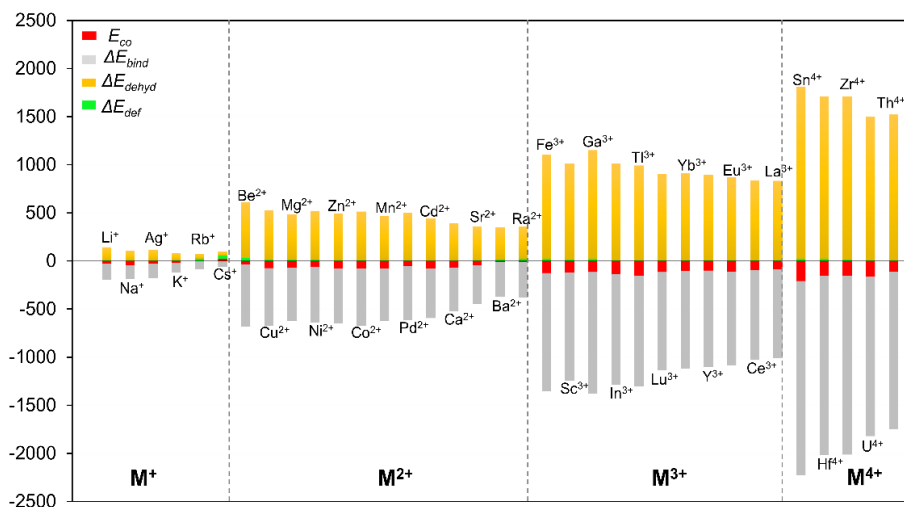


Figure 3.10. Complexation energies (in $\text{kcal}\cdot\text{mol}^{-1}$) of M^{n+} encapsulated in Pd_{12}L_8 ($L = \text{PhAs}^V\text{O}_3^{2-}$), and its decomposition terms (ΔE_{dehyd} , ΔE_{bind} , ΔE_{deform}) analysis for complexation energy.

Table 3.2. The complexation energy (in $\text{kcal}\cdot\text{mol}^{-1}$) and its decomposition analysis terms for three group of cations encapsulated in Pd_{12} .

M^{n+}	E_{co}	ΔE_{deform}	ΔE_{bind}	ΔE_{dehyd}	r	Dominant factor
Ga^{3+}	-115.8	25.7	-1267.1	1125.5	0.92	ΔE_{deform}
In^{3+}	-137.1	8.4	-1146.9	1001.5	1.06	
Lu^{3+}	-115.0	5.7	-1021.2	900.5	1.12	ΔE_{dehyd}
Yb^{3+}	-103.0	4.9	-1018.4	910.5	1.13	
Ce^{3+}	-95.5	5.8	-935.2	833.9	1.28	ΔE_{bind}
La^{3+}	-86.3	3.9	-920.6	830.4	1.30	

The free cation dehydration ability (ΔE_{dehyd}) and the electrostatic interaction (ΔE_{bind}) between the free cation and the nanocage exhibit very large values, and in all the cases ΔE_{bind} is greater than the sum $\Delta E_{\text{dehyd}} + \Delta E_{\text{def}}$, consequently, the E_{co} term is always exothermic. Can we infer from this behaviour that ΔE_{bind} is enough to describe the E_{co} trend? The answer is definitively not. In Table 3.2 we have compiled three examples that show that in absolute value ΔE_{bind} is dominant, however, this term by itself cannot predict relative values for E_{co} . Let us start with pair $\text{Ga}^{3+}/\text{In}^{3+}$, for which experiments show that In^{3+} is captured before Ga^{3+} . The largest negative value for E_{co} for In^{3+}

Chapter 3 The Template Effects of Internal and External Cations in Polyoxopalladates

originates from the largest deformation energy required in the case of Ga^{3+} , the two other terms are significantly larger, but cancel each other out. Notice that the Pd_{12} cage deforms more for Ga^{3+} because its size is too small. For the $\text{Lu}^{3+}/\text{Yb}^{3+}$ pair, we can clearly notice from the values in Table 3.2 that Lu^{3+} has a more negative complexation energy because dehydration is favoured by $\sim 10 \text{ kcal}\cdot\text{mol}^{-1}$, deformation and binding energies are rather similar for the two ions. Finally, the third ion pair $\text{Ce}^{3+}/\text{La}^{3+}$ allows to identify the relevance of the electronic structure in some cases. La^{3+} and Ce^{3+} have the same charge and similar ionic radii (differing by only 0.02 \AA), but f electrons in Ce^{3+} affect molecular orbital distribution because of the lower electron shielding of f electrons, resulting in a larger binding energy for Ce^{3+} . In summary, the E_{co} depends mainly on the following four metal properties: (1) effective ionic radius; (2) valence state; (3) dehydration ability and in minor extension on the electronic configuration (4) charge-accepting ability, and the selectivity for a given cation is a result of a delicate balance between the cation-polyoxopalladate and the cation-solvent interactions.

3.5 The role of metal–metal bonding induced by cation confinement

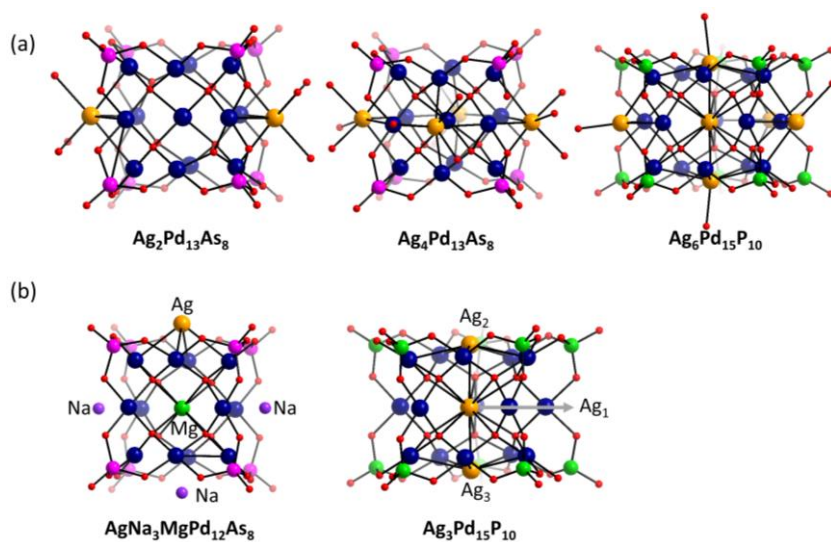


Figure 3.11. (a) Ball-and-stick representations $\text{Ag}_2\text{Pd}_{13}$, $\text{Ag}_4\text{Pd}_{13}$, and $\text{Ag}_6\text{Pd}_{15}$ from experiment; (b) The simulated models for Pd_{13} and Pd_{15} .

Recently, several special cases of Pd_{13} and Pd_{15} with silver cations capping around have been synthesized and characterized, $[\{\text{Ag}(\text{H}_2\text{O})_3\}_4\text{Pd}_{13}\text{O}_{32}(\text{AsO})_8]^{10-}$ ($\text{Ag}_4\text{Pd}_{13}$),

Chapter 3 The Template Effects of Internal and External Cations in Polyoxopalladates

$[\{\text{Ag}(\text{H}_2\text{O})_2\}_4\text{Pd}_{13}\text{O}_{32}(\text{AsO})_8]^{12-}$ (**Ag₂Pd₁₃**), and $[\{\text{Ag}_{4.25}(\text{H}_2\text{O})_2\}\text{AgPd}_{15}\text{O}_{40}(\text{PO})_{10}]^{14.75-}$ (**Ag₆Pd₁₅**) respectively, see Figure 3.11. For **Ag_nPd₁₃** compounds, two or four Ag^+ are found to be attached to the opposite side of two Pd_4 faces or cover four faces by forming an equatorial silver belt around the nanocube. The distributed position of these external Ag^+ are perfectly consistent with the MEP results shown in Figure 3.3. In these cases, the Ag^+ showing seven coordination, including three water molecules and directly contacted with four Pd atoms from the cage. At this stage, the Kortz group also isolated the **Ag₆Pd₁₅**, in which the Ag^+ not only acts as the inner cation that occupies the center of the cavity, but is also attached around the cage. The six Ag^+ ions in **Ag₆Pd₁₅** can be subdivided in three subsets, a) Ag_1 is located in the center of the Pd_{15} surrounded by ten internal oxygens, b) Ag_2 and Ag_3 located at each end of the central channel, are in contact with five Pd^{II} as well as five internal O atoms, and c) Ag_4 , Ag_5 and Ag_6 cap the polyanion externally, in a similar manner as for **Ag₄Pd₁₃**.

Obviously, the first impression for the formation of the fully inorganic Ag-Pd-oxo clusters **Ag₄Pd₁₃** and **Ag₆Pd₁₅** must be attributed to electrostatic interactions between the highly negatively charged Pd^{II} -oxo cores and Ag^{I} ions. Nevertheless, a careful analysis of their structures shows that the Ag^{I} ions are closer to Pd^{II} than to any other atom, in particular all the oxo ligands appearing at longer distances. To rationalize the formation mechanism of **Ag₄Pd₁₃** and **Ag₆Pd₁₅**, DFT calculations were carried out using the standard B3LYP functional by simulating the environment with the PCM model. Figure 3.11b shows the main models for the calculations.

The experimental XRD data indicated that the coordination number of the central Pd^{II} ion in the 12-palladate shells changes from 4 in $[\text{Pd}^{\text{II}}_{13}\text{As}^{\text{V}}_8\text{O}_{34}(\text{OH})_6]^{8-}$ to 6 and 8 in **Ag₂Pd₁₃** and **Ag₄Pd₁₃**, respectively (*vide supra*). When Pd^{II} is in a square-planar ligand field, the ground state is a singlet. The consecutive attachment of external Ag^{I} ions appears to increase the local symmetry of the central Pd^{II} ion and the ground state becomes a triplet in both **Ag₂Pd₁₃** and **Ag₄Pd₁₃**. The XRD-based main structural parameters (bond lengths and angles) of **Ag₂Pd₁₃** and **Ag₄Pd₁₃** are well reproduced by DFT in the triplet state, see Table S3.4.

Interestingly, in these two Ag-capped Pd_{13} nanocubes, the Ag-Pd distances (2.951–3.224 Å) are significantly shorter than the sum of their atomic radii (3.54 Å). To characterize the nature of such Ag-Pd interactions, we analyzed the topology of the electron density within the quantum theory of atoms in molecules (QTAIM). This theory establishes that a chemical bond exists if a line of a locally maximum electron density links two neighboring atoms and also if along that line there is a bond critical point (BCP). In addition, the value of the electron density (ρ_{bcp}) and the Laplacian of

Chapter 3 The Template Effects of Internal and External Cations in Polyoxopalladates

electron density ($\nabla^2\rho_{\text{bcp}}$) are always used to define the interactions presented in the molecules in QTAIM. For covalent interactions, the ρ_{bcp} and $\nabla^2\rho_{\text{bcp}}$ are high and negative at the BCP, while for the closed-shell interactions own a small value of ρ_{bcp} and a positive $\nabla^2\rho_{\text{bcp}}$. However, in the case of metal–metal bonds, the ρ_{bcp} and $\nabla^2\rho_{\text{bcp}}$ sometimes are not sufficient to characterize the nature of an interaction in the complex with transition metal involved in.^[30] Therefore, the total energy density (H_c) suggested by Cremer and Kraka was applied as a specific indicator in the analysis of the bonds with transition metal included in.^[31] Espinosa and Varadwaj *et al.* have proposed that the $|V(r)/G(r)|$ ratio,^[32-33] where $V(r)$ is potential energy density and $G(r)$ is kinetic energy density at the BCP, can be used as a better way to characterize a bond, with $|V(r)/G(r)| < 1$ ($\nabla^2\rho_{\text{bcp}} > 0$, $H_c > 0$) for the pure “closed-shell interactions”, those with $|V(r)/G(r)| > 2$ ($\nabla^2\rho_{\text{bcp}} < 0$, $H_c < 0$) are typical “covalent interactions”, while for $1 < |V(r)/G(r)| < 2$ ($\nabla^2\rho_{\text{bcp}} > 0$, $H_c < 0$) are of “intermediate character”.

All the intuitively expected bonds between Ag^+ and Pd^{II} ions are characterized by such BCPs. The average amount of density at the BCP is found to be $0.185 \text{ e}\cdot\text{\AA}^{-3}$, which can be considered as a small value if it is compared with a common covalent bond such as C–C, where the typical density value can reach $1.698 \text{ e}\cdot\text{\AA}^{-3}$, e.g. for an ethane molecule. However, the electron density characterized for the Ag–Pd interactions in **Ag₄Pd₁₃** with a relatively long bond length (3.027 \AA) is only slightly lower than that reported for metal–metal bonds in polynuclear complexes without bridging ligands.^[34] Furthermore, the computed density map for a plane that contains two Pd atoms and one Ag atom is represented in Figure 3.12b. In the electron density map, we determined a BCP linking Pd and Ag centers whose position is identified by a green cross. The stationary point is slightly shifted towards the silver center. Black dots representing the four BCPs found in each $\{\text{AgPd}_4\}$ unit are given in Figure 3.12a. It is worth mentioning that no BCPs have been characterized linking Ag and O atoms. The bond paths between Ag and Pd in **Ag₄Pd₁₃** are characterized by negative values of energy density (H_c), whereas all charge density of Laplacian exhibit positive values, which indicates that the Ag–Pd interaction is an “intermediate interaction” that should be termed as partially covalent and partially electrostatic (see Table S3.5). To estimate this interaction quantitatively, we have computed the energy associated with the formal complexation process $\{\text{Pd}_{13}\} + \{\text{Ag}^+(\text{H}_2\text{O})_4\} \rightarrow \{\text{Ag}^+(\text{H}_2\text{O})_3\text{Pd}_{13}\} + \text{H}_2\text{O}$, which was found to be $-61.2 \text{ kcal mol}^{-1}$. The relatively large values mainly originate from the electrostatic interaction between the AgI cation and the highly negatively charged Pd₁₃ cluster. The particular feature of this interaction is the metal–metal bond (Ag–Pd) allowing to locate the cation in the center of the Pd₄ face and hence assisting the

Chapter 3 The Template Effects of Internal and External Cations in Polyoxopalladates

formation of the overall cluster.

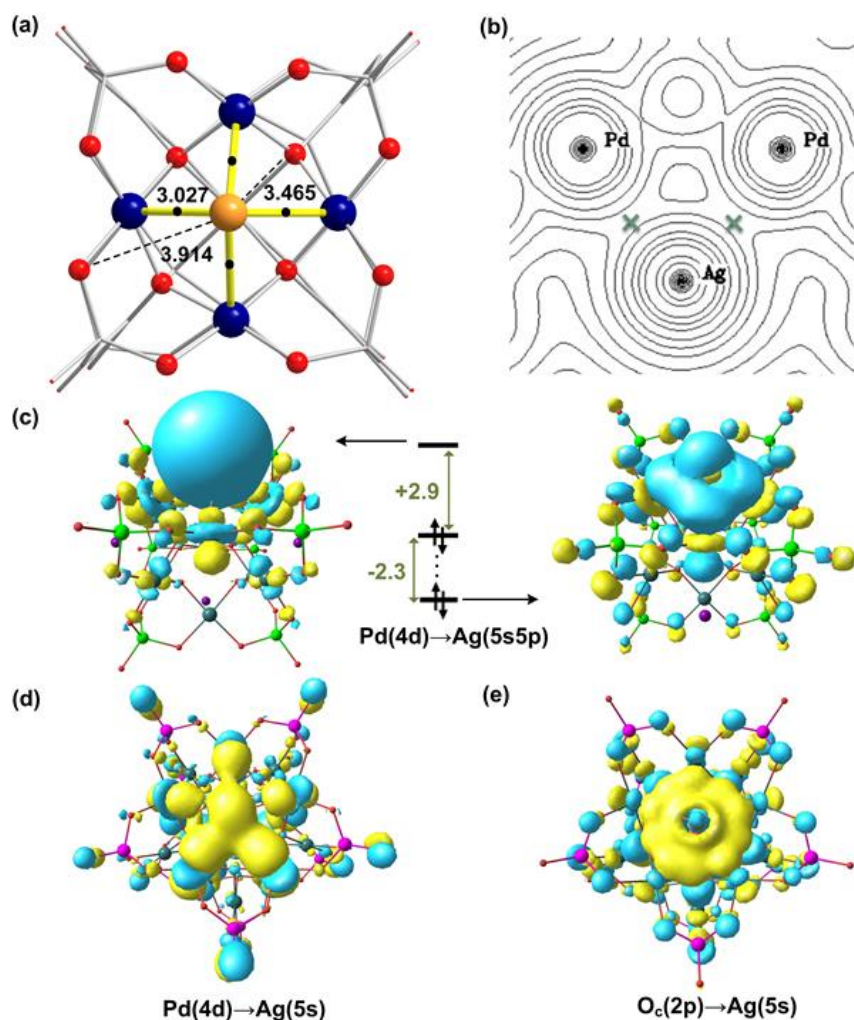


Figure 3.12. Structural and electronic elements for $\text{Ag}_4\text{Pd}_{13}$ and $\text{Ag}_5\text{Pd}_{15}$. (a) Front view of $\text{Ag}_4\text{Pd}_{13}$ (water ligands linked to silver ions not shown; Ag orange, Pd dark blue, O red). (b) Density map representation in one plane containing two Pd and one Ag centers; the positions of BCPs are represented by green crosses. (c) Relevant molecular orbitals involved in $\text{Pd}(4d) \rightarrow \text{Ag}(5s5p)$ interactions for $\text{AgNa}_3\text{MgPd}_{12}$ as model for $\text{Ag}_4\text{Pd}_{13}$. (d) Molecular orbitals showing Pd to Ag and (e) oxo to Ag electron donations in $\text{Ag}_5\text{Pd}_{15}$.

We have also analyzed the frontier molecular orbitals involved in the Ag–Pd interactions of $\text{Ag}_4\text{Pd}_{13}$. To simplify the analysis, we replaced three of the four external

Chapter 3 The Template Effects of Internal and External Cations in Polyoxopalladates

Ag⁺ ions by Na⁺. In order to avoid the open-shell electronic structure of the polyanion, we also substituted the internal Pd^{II} by Mg^{II}, which allowed us to better identify the molecular orbitals involved in a specific {AgPd₄} unit. The representation of the selected frontier orbitals is depicted in Figure 3.12c. The hypothetical *d-d* interaction between the Ag⁺ and Pd^{II} ions has been explored in detail. However, we were not able to find net overlap between *d* orbitals. According to this, natural bond orbital (NBO) analysis revealed that there is not a clear depopulation of Ag(4d), since the cations retain an electron population close to 10e (9.97e), see Table 3.3. Nevertheless, the Ag(5s) and Ag(5p) orbitals have electron populations of 0.18e and 0.15e, respectively, emphasizing a notable electron transfer from the oxo-palladate core to the silver ions. The LUMO and the occupied molecular orbital in Figure 3.12c clearly show an interaction among 5s and 5p orbitals of the silver ions with 4d orbitals of the Pd centers. One relevant point is that when Ag⁺ is replaced by Na⁺, the cation moves away from the palladate cluster due to the absence of any metal–metal interaction. Here, it is noteworthy that in the XRD structure, several Na⁺ counter cations are close to external oxo ligands, indicating that the cluster is highly negatively charged and hence prefers to have the sodium ions as close by as possible.

Table 3.3. Atomic orbital populations (*e*) for the different kinds of Ag⁺ ions in **Ag₄Pd₁₃** and **Ag₅Pd₁₅**.

	Metal	Natural configuration					Donation
		5s	4d	5p	6s	6p	
Ag₄Pd₁₃	Ag	0.18	9.97	0.15	0.00	0.01	Pd→Ag
Ag₅Pd₁₅	Ag1	0.02	9.93	0.72	0.15	0.02	O _c →Ag
	Ag2/3	0.14	9.96	0.24	0.01	0.01	Pd/O _c →Ag
	Ag4/5	0.15	9.97	0.16	0.11	0.01	Pd→Ag

The driving force for the formation of **Ag₅Pd₁₅** is rather similar to that described for **Ag₄Pd₁₃**. The **AgPd₁₅** core, which carries a charge of 19⁻, can only reduce its highly negative charge in alkaline pH by attachment of counter cations. This produces a strong confinement of five Ag⁺ ions onto the polyoxopalladate surface inducing some singular bonding situations. As already commented, the ability of the 5s and 5p orbitals of Ag⁺ to accept electron density from Pd^{II} orbitals renders cations special to construct such kind of structures. In **Ag₅Pd₁₅**, the Ag₄ and Ag₅ ions are each stabilized by four Pd

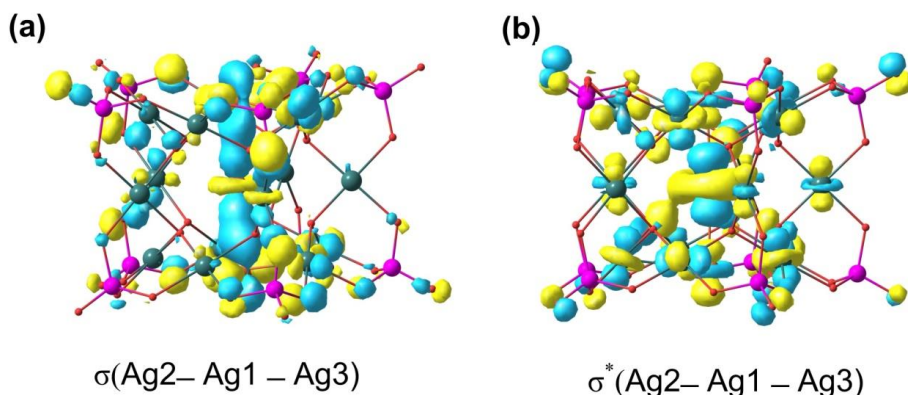
Chapter 3 The Template Effects of Internal and External Cations in Polyoxopalladates

Figure 3.13. Molecular orbitals involved in bonding and antibonding of $\text{Ag2}-\text{Ag1}-\text{Ag3}$ for $\text{Ag}_3\text{Pd}_{15}$ (Ag1 , Ag2 , Ag3), in which the additional three Ag^+ ions on Pd_4O_4 faces (similar to the case of $\text{Ag}_4\text{Pd}_{13}$) were neglected. σ and σ^* orbital representation for homometallic $\text{Ag2}-\text{Ag1}-\text{Ag3}$ interactions.

→ Ag interactions, in addition to electrostatic forces. Due to the more open core structure of AgPd_{15} , as compared to Pd_{13} , the two silver ions Ag_2 and Ag_3 located at each end of the central polyanion channel, are in contact with 5 Pd^{II} as well as 5 internal O atoms, as shown in Figure 3.11. As described above, Ag_2 and Ag_3 are almost located along the pseudo- C_5 axis and are also in contact with the internal cation Ag1 . All these contacts produce up to 12 BCPs (if the external H_2O ligand is also considered) in the electron density distribution. However, here the situation is somewhat different, because there is an important electrostatic interaction of silver cations with the internal oxo ligands. In $\text{Ag}_6\text{Pd}_{15}$, the three capping Ag^+ , including Ag_4 , Ag_5 and the not fully occupied Ag_6 , show similar topological characteristics as that in $\text{Ag}_4\text{Pd}_{13}$ with positive $\nabla^2\rho_{\text{bcp}}$ and negative H_c from QTAIM analysis. However, the Ag_2 and Ag_3 show some differences. Over half of the $\text{Ag}_{2(3)}-\text{Pd}$ and $\text{Ag}_{2(3)}-\text{O}$ interactions exhibit the pure closed-shell interactions with positive H_c and $\nabla^2\rho_{\text{bcp}}$, even some H_c are negative, the values are still smaller than in the case of $\text{Ag}_4\text{Pd}_{13}$. Furthermore, the homometallic (Ag-Ag) interactions are as well proved to be closed-shell interactions by the positive H_c and $\nabla^2\rho_{\text{bcp}}$ at the BCP. Indeed, NBO analysis (Table 3.3) shows that the 5s and 5p atomic orbitals of $\text{Ag}_{2(3)}$ receive electron density from the 4d orbitals of the five neighboring Pd^{II} ions and the 2p orbitals of the five neighboring oxo ligands. Some representative orbitals are given in Figures 3.12d and 3.12e. In fact, when we replaced Ag_2 and Ag_3 by two Na^+ , we observed that the Na^+ ions moved towards the

oxo-palladate core to reinforce the electrostatic interaction with the internal oxo ligands. Therefore, in **Ag₅Pd₁₅**, there are three external, capping Ag⁺ ion positions (Ag₄, Ag₅, Ag₆) that exhibit four Ag–Pd interactions each, in analogy to **Ag₄Pd₁₃**. The two Ag⁺ ions (Ag₂, Ag₃) that are mainly attached to the polyoxopalladate core by strong electrostatic forces produce “apparent” Ag–Ag interactions with the central Ag₁ and “mixed intermediate and closed shell” Pd–Ag and Ag–O_c interactions according to the QTAIM. However, we did not find clear evidence for a net overlap of silver orbitals, because both bonding and antibonding counterparts can be found for Ag₁–Ag₂(3) among the occupied orbitals of **Ag₃Pd₁₅**, see Figure 3.13. The presence of the BCP should be attributed to an overlap of the tail of the electron densities of the two Ag⁺ ions (Ag₂, Ag₃) in the center of the “apparent” bond, a circumstance that does not seem essential for the formation of the oxo-palladate cluster. The effect of unusual interactions in confined spaces has been reported recently in endohedral metallofullerenes.^[35] The short Ag₁–Ag₂(3), Ag₂(3)–Pd distances in **Ag₅Pd₁₅**, must, therefore, be mainly attracted by the electrostatic forces that produce the “apparent” Ag–Ag and Ag–Pd interactions.

3.5 Conclusions

In cluster chemistry, one of the challenges is to know the role that cations or small fragments play in the formation of a given species. Since the discovery in 2008 of the archetypal polyoxopalladate [Pd^{II}₁₃As^V₈O₃₄(OH)₆]⁸⁻ (**Pd₁₃**), which can be described as a {Pd₁₂O₈(AsO₄)₈} nano-cube encapsulating a central Pd^{II} ion with square-planar coordination, several structures encapsulating different cations have been reported. However, the main factors that govern the formation of a particular compound are not totally known. Here, combining computational chemistry, mass spectrometry and other analytical techniques we have been able to demonstrate when and why a polyoxopalladate self-assemble around a particular cation.

The prototype (**Pd₁₃**) is formed by condensation of Pd²⁺ ions in the presence of capping groups such as simple oxoanions do. Nevertheless, if the solution contains other cations, Mⁿ⁺@Pd₁₂ (**MPd₁₂**) species may also be formed, determined by the favourable complexation energy and the relative competition with Pd²⁺. After an exhaustive analysis of complexation and dehydration energies for a series of cations we have been able to identify the most favorable cations to be encapsulated inside a polyoxopalladate. From a thermodynamic point of view, trivalent and tetravalent cations are easily trapped inside a polyoxopalladate, while monovalent cations are much more difficult to be captured by the cluster. NMR and mass spectrometry studies

Chapter 3 The Template Effects of Internal and External Cations in Polyoxopalladates

demonstrate that In^{3+} assembles more rapidly than Ga^{3+} due to its matched size and higher complexation energy. Although La^{3+} is a rather large cation, DFT calculations suggested that it could still fit within a Pd_{12} framework. Actually, the La@Pd_{12} was synthesized and characterized by X-ray, observing for this cation two type of structures. Its posterior synthesis corroborates again that cation size and dehydration energies of the cation are the driven factors in the formation of polyoxopalladates.

Other cations such as Cd^{2+} , Tl^{3+} , Zr^{4+} , Hf^{4+} , U^{4+} , or Th^{4+} among others have been found that exhibit potential ability to be encapsulated by a Pd_{12} . Likely they will be captured in the next future.

Furthermore, theoretical calculations for $\text{Ag}_4\text{Pd}_{13}$ and $\text{Ag}_3\text{Pd}_{15}$ have revealed very useful to characterize Ag–Pd type interaction, suggesting that metal–metal bonding is best described as “intermediate interaction”, which should be termed as partially covalent and partially electrostatic. On the other hand, the Ag–Ag–Ag homometallic interactions in the channel of $\text{Ag}_5\text{Pd}_{15}$ were shown to be largely of electrostatic nature.

References and Notes

- [1] M. T. Pope, *Heteropoly and Isopoly Oxometalates*. Springer-Verlag: New York, 1983. Kluwer, 2001.
- [2] A. Müller and M. T. Pope, *Polyoxometalate Chemistry: From Topology via Self-Assembly to Applications*, Kluwer, 2001.
- [3] D. L. Long, E. Burkholder and L. Cronin, *Chem. Soc. Rev.* 2007, 36, 105–121.
- [4] (a) L. Vilà-Nadal, A. Rodríguez-Forteza, L. K. Yan, E. F. Wilson, L. Cronin and J. M. Poblet, *Angew. Chem., Int. Ed.* 2009, 48, 5452–5456; (b) L. Vilà-Nadal, E. F. Wilson, L. Cronin and J. M. Poblet, *Inorg. Chem.* 2011, 50, 7811–7819; (c) L. Vilà-Nadal, S. G. Mitchell, H. N. Miras, L. Cronin and J. M. Poblet, *Phys. Chem. Chem. Phys.* 2011, 13, 20136–20145; (d) Z. L. Lang, W. Guan, L.K. Yan, S.Z. Wen, Z.M. Su and L. Z. Hao, *Dalton Trans.* 2012, 41, 11361–11368.
- [5] R. E. Schreiber, L. Houben, S. G. Wolf, G. Leitus, Z. L. Lang, J. J. Carbó, J. M. Poblet and R. Neumann, *Nat. Chem.* 2017, 9, 369–373.
- [6] A. Müller, H. Reuter, S. Dillinger, *Angew. Chem.* 1995, 107, 2505–2539.
- [7] (a) S. S. Mal and U. Kortz, *Angew. Chem. Int. Ed.* 2005, 44, 3777–3780; (b) U. Kortz, F. Hussain and M. Reicke, *Angew. Chem. Int. Ed.* 2005, 44, 3773–3777; (c) C. Ritchie, A. Ferguson, H. Nojiri, H. N. Miras, Y.-F. Song, D. L. Long, E. Burkholder, M. Murrie, P. Kögerler, E. K. Brechin and L. Cronin, *Angew. Chem. Int. Ed.* 2008, 47, 5609–5612; (d) S. Reinoso, M. Giménez-Marqués, J. R. Galán-Mascarós, P. Vitoria and J. M. Gutiérrez-Zorrilla, *Angew. Chem.* 2010, 122, 8562–8566; (e) U. Kortz, M. Savelieff, B. Bassil and M. Dickman, *Angew. Chem. Int. Ed.* 2001, 40, 3384–3386; (f) M. Ibrahim, S. S. Mal, B. S. Bassil, A. Banerjee and U. Kortz, *Inorg. Chem.* 2011, 50, 956–962; (g) D. L. Long, Y. F. Song, E. F. Wilson, P. Kögerler, S. X. Guo, A. M. Bond, J. S. J. Hargreaves and L. Cronin, *Angew. Chem.* 2008, 120, 4456–4459; (h) J. Yan, D. L. Long and L. Cronin, *Angew. Chem.* 2010, 122, 4211–4214; (i) X. K. Fang and P. Kögerler, *Angew. Chem. Int. Ed.* 2008, 47, 8123–8126; (j) W. C. Chen, H.L. Li, X. L. Wang, K. Z. Shao, Z. M. Su, and E. B. Wang and *Chem. Eur. J.* 2013, 19, 11007–11015.
- [8] N. V. Izarova, M. T. Pope and U. Kortz, *Angew. Chem. Int. Ed.* 2012, 51, 9492–9510.
- [9] M. Pley and M. S. Wickleder, *Angew. Chem., Int. Ed.* 2004, 43, 4168–4170.

Chapter 3 The Template Effects of Internal and External Cations in Polyoxopalladates

- [10] E. V. Chubarova, M. H. Dickman, B. Keita, L. Nadjo, F. Miserque, M. Mifsud, I. W. C. E. Arends and U. Kortz, *Angew. Chem. Int. Ed.* 2008, 47, 9542–9510.
- [11] (a) N. V. Izarova, N. Vankova, T. Heine, R. Ngo Biboum, B. Keita, L. Nadjo and U. Kortz, *Angew. Chem. Int. Ed.* 2010, 49, 1886–1889; (b) Y. Xiang, N. V. Izarova, F. Schinle, O. Hampe, B. Keita and U. Kortz, *Chem. Commun.* 2012, 48, 9849–9851; (c) N. V. Izarova, A. Kondinski, N. Vankova, T. Heine, P. Jäger, F. Schinle, O. Hampe and U. Kortz, *Chem. Eur. J.* 2014, 20, 8556–8560.
- [12] N. V. Izarova, M. H. Dickman, R. Ngo Biboum, B. Keita, L. Nadjo, V. Ramachandran, N. S. Dalal and U. Kortz, *Inorg. Chem.* 2009, 48, 7504–7506.
- [13] (a) M. Barsukova, N. V. Izarova, R. Ngo Biboum, B. Keita, L. Nadjo, V. Ramachandran, N. S. Dalal, N. S. Antonova, J. J. Carbó, J. M. Poblet and U. Kortz, *Chem. Eur. J.* 2010, 16, 9076–9085; (b) M. Barsukova-Stuckart, N. V. Izarova, R. A. Barret, Z. Wang, J. van Tol, H. W. Kroto, N. S. Dalal, P. Jiménez-Lozano, J. J. Carbó, J. M. Poblet, M. S. von Gernler, T. Drewello, P. de Oliveira, B. Keita and U. Kortz, *Inorg. Chem.* 2012, 51, 13214–13228; (c) M. Barsukova-Stuckart, N. V. Izarova, R. Barrett, Z. Wang, J. van Tol, H. W. Kroto, N. S. Dalal, B. Keita, D. Heller and U. Kortz, *Chem. Eur. J.* 2012, 18, 6167–6171; (d) Z. Lin, B. Wang, J. Cao, B. Chen, C. Xu, X. Huang, Y. Fan and C. Hu, *Eur. J. Inorg. Chem.* 2013, 20, 3458–3463.
- [14] (a) Z. G. Lin, B. Wang, J. Cao, B. K. Chen, Y. Z. Gao, Y. N. Chi, C. Xu, X. Q. Huang, R. D. Han, S.-Y. Su and C. W. Hu, *Inorg. Chem.*, 2012, 51 (8), 4435–4437; (b) N. V. Izarova, R. Ngo Biboum, B. Keita, M. Mifsud, I. W. C. E. Arends, G. B. Jameson and U. Kortz, *Dalton Trans.* 2009, 43, 9385–9387; (c) M. Delferro, C. Graiff, L. Elviri and G. Predieri, *Dalton Trans.* 2010, 39, 4479–4481; (d) P. Yang, Y. X. Xiang, Z. G. Lin, B. S. Bassil, J. Cao, L. Y. Fan, Y. Fan, M. Li, P. Jiménez-Lozano, J. J. Carbó, J. M. Poblet and U. Kortz, *Angew. Chem. Int. Ed.* 2014, 53, 11974–11978; (e) P. Yang, Y. X. Xiang, Z. H. Lin, Z. L. Lang, P. Jiménez-Lozano, J. J. Carbl, J. M. Poblet, L.Y. Fan, C. W. Hu and U. Kortz, *Angew. Chem. Int. Ed.* 2016, 55, 15766–15770.
- [15] (a) N. V. Izarova, N. Vankova, A. Banerjee, G. B. Jameson, T. Heine, F. Schinle, O. Hampe and U. Kortz, *Angew. Chem. Int. Ed.* 2010, 49, 7807–7811; (b) M. Barsukova-Stuckart, N. V. Izarova, G. B. Jameson, V. Ramachandran, Z. Wang, J. van Tol, N. S. Dalal, R. Ngo Biboum, B. Keita, L. Nadjo and U. Kortz, *Angew. Chem. Int. Ed.* 2011, 50, 2639–2642; (c) N. V. Izarova, Z. Lin, P. Yang, A. Kondinski, N. Vankova, T. Heine, U. Kortz, *Dalton Trans.* 2016, 45, 2394–2398;

Chapter 3 The Template Effects of Internal and External Cations in Polyoxopalladates

- (d) F. Xu, R. A. Scullion, J. Yan, H. N. Miras, C. Busche, A. Scandurra, B. Pignataro, D. L. Long and L. Cronin. *J. Am. Chem. Soc.*, 2011, 133, 4684–4686.
- [16] (a) F. Xu, H. N. Miras, R. A. Scullion, D. L. Long, J. Thiel and L. Cronin. *Proc. Natl. Acad. Sci.* 2012, 109, 11609–11612; (b) R. Scullion, A. J. Surman, F. Xu, J. S. Mathieson, D. L. Long, F. Haso, T. Liu and L. Cronin, *Angew. Chem. Int. Ed.* 2014, 53, 10032–10037; (c) L. G. Christie, A. J. Surman, R. A. Scullion, F. Xu, D. L. Long and L. Cronin, *Angew. Chem. Int. Ed.* 2016, 55, 12741–12745.
- [17] B. R. Bowsher and A. J. Rest, *J. Chem. Soc., Dalton Trans.* 1981, 1157–1161.
- [18] M. J. Frisch et al., *Gaussian09W*, Revision A02; Gaussian, Inc.: Wallingford, CT, 2009.
- [19] (a) A. D. Becke, *J. Chem. Phys.* 1993, 98, 5648–5652; (b) C. Lee, W. Yang and R. G. Parr, *Phys. Rev. B* 1988, 37, 785–789.
- [20] (a) L. V. Szentpály, P. Fuentealba, H. Preuss, and H. Stoll, *Chem. Phys. Lett.*, 1982, 93 555–559; (b) X. Y. Cao and M. Dolg, *J. Mol. Struct. (Theochem)*, 2002, 581, 139–147; (c) M. Dolg, H. Stoll and H. Preuss, *Theor. Chem. Acc.*, 1993, 85, 441–450; (d) M. Dolg, H. Stoll, H. J. Flad and H. Preuss, *J. Chem. Phys.* 1992, 97, 1162–1173.
- [21] (a) P. J. Hay and W. R. Wadt, *J. Chem. Phys.* 1985, 82, 270–283; (b) W. R. Wadt and P. J. Hay, *J. Chem. Phys.*, 1985, 82 284–298.
- [22] (a) M. M. Francl, W. J. Pietro, W. J. Hehre, J. S. Binkley, M. S. Gordon, D. J. Defrees and J. A. Pople, *J. Chem. Phys.* 1982, 77, 3654–3665; (b) P. C. Hariharan and J. A. Pople, *Theor. Chem. Acta.* 1973, 28, 213–222; (c) G. A. Petersson and M. A. Al-Laham, *J. Chem. Phys.* 1991, 94, 6081–6090.
- [23] (a) Y. Zhao and D. G. Truhlar, *Theor. Chem. Acc.*, 2007, 120, 215–241; (b) Y. Zhao and D. G. Truhlar, *Acc. Chem. Res.* 2008, 41, 157–167.
- [24] (a) S. Grimme, *J. Comput. Chem.* 2006, 27, 1787–1799; (b) A. D. Becke, *J. Chem. Phys.* 1997, 107, 8554–8560; (c) J. D. Chai and M. Head-Gordon, *Phys. Chem. Chem. Phys.* 2008, 10, 6615–6620; (d) Q. Wu and W. T. Yang, *J. Chem. Phys.* 2002, 116, 515–524.
- [25] (a) J. Tomasi, B. Mennucci and R. Cammi, *Chem. Rev.*, 2005, 105, 2999–3094; (b) A. V. Marenich, C. J. Cramer and D. G. Truhlar, *J. Phys. Chem. B* 2009, 113, 6378–6396.
- [26] D. W. Smith, *J. Chem. Edu.* 1977, 54, 540–542.
- [27] R. F. W. Bader, *Atoms in molecules: a quantum theory* (Oxford University Press, 1990).

Chapter 3 The Template Effects of Internal and External Cations in Polyoxopalladates

- [28] C. F. Matta and R. J. Boyd, (eds) Quantum theory of atoms in molecules: recent progress in theory and application (Wiley-VCH, 2007).
- [29] T. Lu and F. Chen, *J. Comp. Chem.* 2012, 33, 580–592.
- [30] M. Benard, P. Coppens, M. L. Delucia and E. D. Stevens, *Inorg. Chem.* 1980, 19, 1924–1930.
- [31] D. Cremer and E. Kraka, *Angew. Chem. Int. Engl.* 1984, 23, 627–628.
- [32] E. Espinosa, I. Alkorta, J. Elguero and E. Molins, *J. Chem. Phys.* 2002, 117, 5529–5542.
- [33] P. R. Varadwaj and H. M. Marques, 2010, *Phys. Chem. Chem. Phys.* 2010, 12, 2126–2138.
- [34] G. Gervasio, R. Bianchi and D. Marabello, *Chem. Phys. Lett.* 2005, 407, 18–22.
- [35] A. A. Popov, S. M. Avdoshenko, A. M. Pendás and L. Dunsch, *Chem. Commun.* 2012, 48, 8031–8050.

Appendix Chapter 3

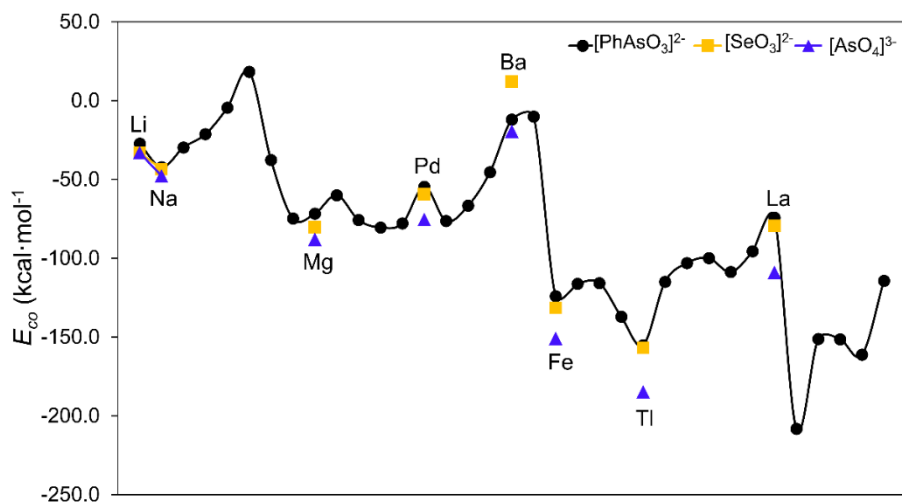


Figure S3.1. Complexation energies ($\text{kcal}\cdot\text{mol}^{-1}$) for some selected cations (Li^+ , Na^+ , Mg^{2+} , Pd^{2+} , Ba^{2+} , Fe^{3+} , Tl^{3+} , and La^{3+}) encapsulated in Pd_{12}L_8 with different capping groups. ($\text{L} = [\text{PhAs}^{\text{V}}\text{O}_3]^{2-}$ (black points), $[\text{Se}^{\text{IV}}\text{O}_3]^{2-}$ (orange square), and $[\text{As}^{\text{V}}\text{O}_4]^{3-}$ (blue triangle)).

*Chapter 3 The Template Effects of Internal and External Cations in Polyoxopalladates***Table S3.1.** Comparison of DFT-computed and X-ray distance (Å) for the MPd_{12} complexes when different cations encapsulated in, and the corresponding effective ionic radius for each cation in 8-coordinated environment was listed.

M	O _c —O _c	M—O _c	M—Pd	r
Li ⁺	2.716/2.726	2.358	3.404	1.06
Na ⁺	2.797/2.805	2.427	3.430	1.32
Ag ⁺	2.886/2.888	2.500	3.473	1.42
K ⁺	3.025	2.619	3.497	1.65
Rb ⁺	3.223/3.234	2.794	3.560	1.75
Cs ⁺	3.423/3.425	2.966	3.622	1.88
Be ²⁺	2.550/2.546	2.206	3.343	~0.80
Cu ²⁺	2.698/2.688 (2.270)	2.486/2.170 (2.631)	3.393 (3.327)	~1.03
Mg ²⁺	2.643/2.647	2.290	3.384	1.03
Ni ²⁺	2.629/2.671(2.608/2.640)	2.289 (2.277)	3.367/3.392 (3.317/3.318)	~1.00
Zn ²⁺	2.687/2.692 (2.630)	2.329 (2.269)	3.399 (3.329)	1.04
Co ²⁺	2.659/2.662 (2.574)	2.303 (2.259)	3.390 (3.320)	1.04
Mn ²⁺	2.711 (2.662)	2.347 (2.294)	3.410 (3.341)	1.10
Pd ²⁺	2.767/2.751 (2.697/2.705)	2.281/2.491 (2.244/2.437)	3.418/3.422 (3.352/3.358)	~1.20
Cd ²⁺	2.830/2.814	2.446	3.447	1.24
Ca ²⁺	2.827/2.836 (2.737/2.760)	2.453(2.384)	3.452(3.372/3.380)	1.26
Sr ²⁺	2.953/2.956	2.559	3.491	1.40
Ba ²⁺	3.149/3.154	2.729	3.543	1.56
Ra ²⁺	3.209/3.215	2.782	3.560	1.62
Fe ³⁺	2.611/2.614 (2.561)	2.262 (2.224)	3.375 (3.309)	0.92
Sc ³⁺	2.627/2.641 (2.590)	2.279 (2.257)	3.388 (3.310)	1.01
Ga ³⁺	2.576/2.569 (2.555)	2.227(2.212)	3.357(3.304)	~0.92
In ³⁺	2.679/2.681(2.667/2.685)	2.321(2.315)	3.405(3.344)	1.06
Tl ³⁺	2.753/2.757 (2.714)	2.386(2.351)	3.430((3.372/3.384)	1.12
Lu ³⁺	2.712/2.715 (2.654/2.671)	2.350 (2.304)	3.421 (3.358/3.368)	1.12
Yb ³⁺	2.738/2.751	2.363 (2.329)	3.427(3.364)	1.13

Chapter 3 The Template Effects of Internal and External Cations in Polyoxopalladates

	(2.689/2.692)			
Y ³⁺	2.780/2.788 (2.700/2.713)	2.412 (2.346)	3.442 (3.385)	1.16
Eu ³⁺	2.811/2.816 (2.744/2.753)	2.436 (2.381)	3.455 (3.381/3.389)	1.21
Ce ³⁺	2.891/2.908	2.501	3.473/3.482	1.28
La ³⁺	2.957/2.967	2.564	3.503/3.498	1.30
Sn ⁴⁺	2.574/2.581	2.231	3.373	0.95
Hf ⁴⁺	2.622/2.636	2.275	3.390/3.396	0.97
Zr ⁴⁺	2.655/2.660	2.301	3.405	0.98
U ⁴⁺	2.750/2.780	2.399	3.444	1.14
Th ⁴⁺	2.923/2.929	2.537	3.491	1.19

Table S3.2. Relative energies (kcal·mol⁻¹) for cation encapsulated in Pd₁₅ at different sites.

	Sites	ΔE		Sites	ΔE
Li ⁺	C ₄	0.0	Mg ²⁺	C ₄	0.0
	C ₅ (on Pd ₅ O ₅)	6.1		C ₅	3.9
Na ⁺	C ₄	1.2	Ca ²⁺	Center	
	C ₅ (on Pd ₅ O ₅)	0.0	Sr ²⁺	Center	
	Center	0.4	Ba ²⁺	Center	
K ⁺	Center		Ra ²⁺	Center	
Rb ⁺	Center		Zn ²⁺	C ₄	
Cs ⁺	Center			C ₅	3.2
Ag ⁺	Center		Pd ²⁺	C ₄ (on Pd ₅ O ₅)	0.0
Be ²⁺	C ₃			C ₅	8.1
				C ₆	4.9

*Chapter 3 The Template Effects of Internal and External Cations in Polyoxopalladates***Table S3.3:** *Complexation energies (in kcal·mol⁻¹) for different cations encapsulated within Pd₁₂, and its decomposition analysis terms for complexation energies.*

M^{n+}	E_{co}	ΔE_{deform}	ΔE_{bind}	ΔE_{dehyd}	r
Li ⁺	-27.2	2.7	-170.9	140.9	1.06
Na ⁺	-42.2	1.1	-146.7	103.4	1.32
Ag ⁺	-29.7	1.3	-147.6	116.6	1.42
K ⁺	-21.2	5.7	-102.0	75.0	1.65
Rb ⁺	-4.5	20.6	-80.2	55.0	1.75
Cs ⁺	18.3	35.3	-59.2	42.2	1.88
Be ²⁺	-37.7	28.8	-646.8	580.3	~0.80
Cu ²⁺	-74.8	11.1	-600.4	514.5	~1.03
Mg ²⁺	-71.7	12.3	-553.5	469.5	1.03
Ni ²⁺	-60.0	13.2	-581.7	508.5	~1.00
Zn ²⁺	-75.7	6.2	-572.2	490.2	1.10
Co ²⁺	-80.5	9.9	-594.2	503.8	1.04
Mn ²⁺	-77.9	4.4	-545.2	462.9	1.04
Pd ²⁺	-54.6	4.7	-558.3	499.0	~1.20
Cd ²⁺	-76.4	1.9	-518.0	439.7	1.24
Ca ²⁺	-66.6	1.9	-456.2	387.6	1.26
Sr ²⁺	-45.4	2.8	-400.7	352.5	1.40
Ba ²⁺	-11.9	15.3	-360.2	332.9	1.56
Ra ²⁺	-10.1	19.9	-370.0	340.0	1.62
Fe ³⁺	-124.1	19.9	-1232.3	1088.4	0.92
Sc ³⁺	-116.2	16.0	-1126.1	993.9	1.01
Ga ³⁺	-115.8	25.7	-1267.1	1125.5	~0.92
In ³⁺	-137.1	8.4	-1146.9	1001.5	1.06
Tl ³⁺	-155.1	3.1	-1147.5	989.2	1.12
Lu ³⁺	-115.0	5.7	-1021.2	900.5	1.12
Yb ³⁺	-103.0	4.9	-1018.4	910.5	1.13
Y ³⁺	-99.9	2.6	-999.7	897.1	1.16
Eu ³⁺	-108.7	3.3	-977.5	865.4	1.21

Chapter 3 The Template Effects of Internal and External Cations in Polyoxopalladates

Ce ³⁺	-95.5	5.8	-935.2	833.9	1.28
La ³⁺	-86.3	3.9	-920.6	830.4	1.30
Sn ⁴⁺	-208.2	20.9	-2018.6	1789.5	0.95
Hf ⁴⁺	-151.2	20.1	-1864.6	1693.3	0.97
Zr ⁴⁺	-151.4	14.2	-1861.0	1695.4	0.98
U ⁴⁺	-161.2	4.7	-1659.3	1493.4	1.14
Th ⁴⁺	-114.3	3.7	-1635.3	1517.3	1.19

Table S3.4. Experimental (X-ray) and calculated (DFT) geometrical parameters (Å) for **Ag₄Pd₁₃** (with coordinated water included and not) and **Ag₃Pd₁₅** (model of **Ag₅Pd₁₅**).

	X-ray Ag ₄ Pd ₁₃	Ag ₄ Pd ₁₃ with water	Ag ₄ Pd ₁₃ without water	X-ray Ag ₅ Pd ₁₅	Ag ₃ Pd ₁₅
Pd _c (Ag ₁)-O _c	2.227, 2.367, 2.426	2.300, 2.310, 2.614	2.302, 2.316, 2.632	2.550~2.792	2.677~2.844
O _c -O _c	2.651, 2.683, 2.696, 2.706	2.740, 2.751, 2.761, 2.784	2.752, 2.764, 2.769, 2.773	2.604~2.713	2.749~2.858
Ag(Ag _{2/3})-Pd	2.912~3.04 1	3.025~3. 324	2.862~2. 892	2.727~2.765	2.721~2.770
Ag(Ag _{2/3})- Pd _c (Ag ₁)	4.199, 4.205	4.380~4. 393	4.012, 4.019	2.959/2.973	2.867
Ag-O _w	2.410~2.52 5	2.514~2. 535			

*Chapter 3 The Template Effects of Internal and External Cations in Polyoxopalladates***Table S3.5.** Electron density $\rho [e \text{ \AA}^{-3}]$, its Laplacian $\nabla^2 \rho [e \text{ \AA}^{-5}]$, total energy density (H_c) and $|V(r)|/G(r)$ at the BCP of Ag–Pd, Ag–Ag, and Ag–O bonds of the **Pd₁₃** and **Pd₁₅** systems.

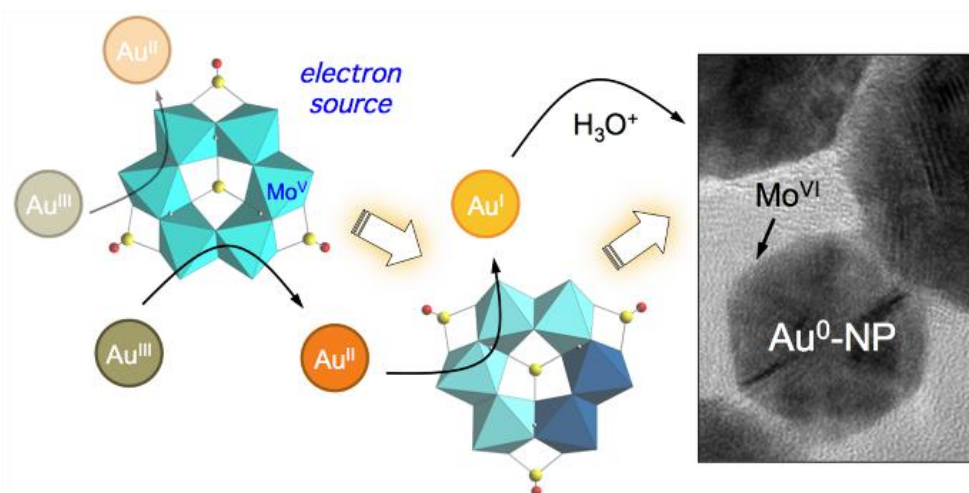
	BCP	$G(r)$	$V(r)$	H_c	$ V(r) /G(r)$	ρ_{bcp}	$\nabla^2 \rho_{\text{bcp}}$
Ag₄Pd₁₃							
Ag1–Pd	13	2.07E-02	-2.10E-02	-2.72E-04	1.013	0.172	1.972
	19	2.49E-02	-2.59E-02	-1.03E-03	1.041	0.197	2.306
	31	2.28E-02	-2.35E-02	-7.06E-04	1.031	0.187	2.136
	38	2.30E-02	-2.36E-02	-5.94E-04	1.026	0.184	2.160
Ag2–Pd	14	2.25E-02	-2.31E-02	-5.66E-04	1.025	0.182	2.118
	22	2.34E-02	-2.42E-02	-7.98E-04	1.034	0.190	2.183
	33	2.37E-02	-2.45E-02	-8.00E-04	1.034	0.191	2.206
	44	2.27E-02	-2.32E-02	-5.21E-04	1.023	0.182	2.137
Ag3–Pd	113	2.26E-02	-2.32E-02	-5.20E-04	1.023	0.182	2.137
	124	2.37E-02	-2.45E-02	-8.02E-04	1.034	0.191	2.207
	135	2.34E-02	-2.42E-02	-7.96E-04	1.034	0.190	2.182
	143	2.25E-02	-2.31E-02	-5.65E-04	1.025	0.182	2.118
Ag4–Pd	119	2.30E-02	-2.36E-02	-5.95E-04	1.026	0.184	2.160
	126	2.28E-02	-2.35E-02	-7.07E-04	1.031	0.187	2.137
	138	2.49E-02	-2.59E-02	-1.02E-03	1.041	0.197	2.304
	144	2.07E-02	-2.10E-02	-2.76E-04	1.013	0.173	1.974
Ag₃Pd₁₅							
Ag2–Pd	147	1.75E-02	-1.72E-02	3.28E-04	0.981	0.145	1.719
	148	1.86E-02	-1.84E-02	2.35E-04	0.987	0.151	1.821
	160	2.26E-02	-2.30E-02	-3.60E-04	1.016	0.176	2.150
	161	2.43E-02	-2.50E-02	-6.77E-04	1.028	0.186	2.282
	167	1.59E-02	-1.54E-02	4.78E-04	0.970	0.133	1.578
Ag2–O _c	129	2.14E-02	-2.12E-02	1.32E-04	0.994	0.151	2.074
	144	1.99E-02	-1.99E-02	-5.12E-06	1.000	0.146	1.919
	145	1.97E-02	-1.98E-02	-1.01E-04	1.005	0.146	1.895
	156	2.14E-02	-2.13E-02	9.06E-05	0.996	0.152	2.070
	158	2.07E-02	-2.07E-02	-3.15E-05	1.001	0.150	1.992
Ag3–Pd	19	2.08E-02	-2.09E-02	-1.16E-04	1.005	0.166	1.994
	20	1.61E-02	-1.57E-02	4.65E-04	0.971	0.135	1.602
	37	2.15E-02	-2.18E-02	-2.41E-04	1.011	0.171	2.056
	38	1.95E-02	-1.95E-02	4.27E-05	0.998	0.159	1.890
	46	1.71E-02	-1.69E-02	2.98E-04	0.983	0.145	1.684
Ag3–O _c	40	1.77E-02	-1.78E-02	-1.44E-04	1.001	0.136	1.691
	41	1.80E-02	-1.80E-02	6.26E-06	0.999	0.135	1.740

Chapter 3 The Template Effects of Internal and External Cations in Polyoxopalladates

	49	1.88E-02	-1.89E-02	-4.09E-05	1.002	0.140	1.813
	50	1.85E-02	-1.85E-02	-2.07E-05	1.001	0.138	1.784
	28	2.32E-02	-2.31E-02	1.09E-04	0.995	0.162	2.255
AgI-	127	1.67E-02	-1.60E-02	7.40E-04	0.956	0.126	1.688
AgI-	53	1.74E-02	-1.68E-02	6.33E-04	0.963	0.131	1.744

Chapter 4

A Non-classical Polyoxomolybdate as an Electron Source for $[\text{Au}^{\text{III}}\text{Cl}_4]^-$ Reduction



Polyoxometalate (POM)-mediated reduction and nucleation mechanisms in nanoparticle (NP) syntheses are still largely unknown. In this chapter, we carried out comprehensive theoretical analysis to gain insight in the molecular and electronic changes that occur during the reduction of $\text{HAu}^{\text{III}}\text{Cl}_4$ with the Kabanos-type polyoxomolybdate, $[\text{Na}\{(\text{Mo}_2^{\text{V}}\text{O}_4)_3(\mu_2\text{-O})_3(\mu_2\text{-SO}_3)_3(\mu_6\text{-SO}_3)_2\}]^{15-}$. Our results reveal that this particular POM is a multi-electron source and the proton-coupled electron transfer (PCET) greatly promotes the reduction process.

4.1 Introduction

Metal nanoparticles (NP) (or nanocrystals), such as Ag, Au, Pd, and Pt, possess an array of fascinating physicochemical properties (e.g. superparamagnetism, surface plasmons and radiation-to-heat transduction), that are not present in the corresponding bulk materials.^[1] The main properties of NPs are largely dependent on their size and shapes,^[2-4] thus, optimizing and understanding preparation methods and elucidating the nucleation mechanisms have become core research topics.^[5-7]

The recent application of POMs to the synthesis and stabilization of AuNPs has opened the door to environmentally friendly and energy saving methods since the redox properties of POMs allows them to be recycled and reused.^[8-10] POMs are anionic metal-oxide molecular clusters typically formed by early-row transition metals (Mo, W, V, Nb, Ta) that exhibit fascinating and applicable physical and chemical properties.^[11-18] Importantly, numerous POMs can act as effective electron-transfer catalysts due to their unique ability to reversibly accept and release electrons. Several recent reviews by Nadjo,^[19] Mitchell,^[20] and Weinstock^[21] have pointed out that POMs or POM-based materials can act both as reducing agents and stabilizers for preparation of metallic (such as Au, Ag, Pd, Pt) nanostructures. This motivated us to investigate the use of POMs with ‘*in-built*’ reduction capabilities for the preparation of AuNPs in mild reaction conditions.^[22] In spite of these advances, these processes face significant challenges due to a poor understanding of their reducing and stabilizing mechanisms coupled with the limited number of POMs that have been explored for this purpose.

4.2 Motivation and objectives

Small two-electron reduced (Mo^{IV}) thiometalates have been used to produce of AuNPs efficiently.^[23] The Mitchell group recently identified a highly-reduced POM, the Kabanos structure (Figure 4.1a), Na{(Mo₂^VO₄)₃(μ₂-O)₃(μ₂-SO₃)₃(μ₆-SO₃)₂}¹⁵⁻, that could potentially be used as a reducing agent and as an efficient multidentate capping ligand in the preparation of AuNPs (Figure 4.1).^[24, 25]

In this chapter, we will report computational evidence for the activity of the Kabanos POM in the formation of AuNPs as well as the relevant experimental data on AuNPs@POM. Through the computational research, it clarifies the role of the POM in the reduction of AuCl₄⁻ ions, and allows us to propose a route for the complete reduction of Au^{III}. We have focussed essentially in understanding the thermodynamics of the processes until the full oxidation of the anion and on the capacity of the two anions to approach each other in order to be ready for electron transfer from the

reduced polyoxometalate to gold species. It is worth mentioning that the reaction does not require electrochemical reduction of gold (all of the electrons are supplied by the Kabanos POM itself), which greatly simplifies the computational analysis of the thermodynamic aspects of the reaction.

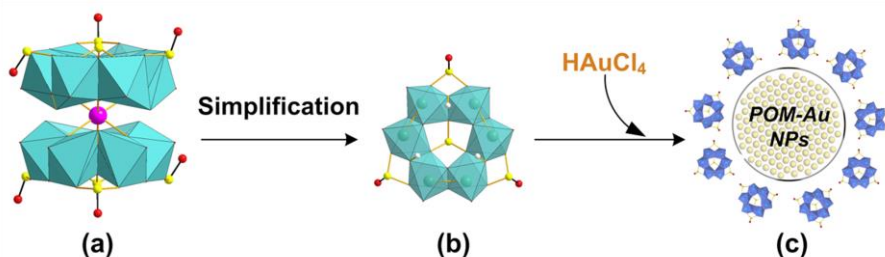


Figure 4.1. Relevant species acting in the HAuCl_4 reduction: (a) dimeric form $[\text{Na}\{(\text{Mo}_2^{\text{V}}\text{O}_4)_3(\mu_2\text{-O})_3(\mu_2\text{-SO}_3)_3(\mu_6\text{-SO}_3)\}_2]^{15-}$, (b) simplified protonated monomeric form $[(\text{Mo}_2^{\text{V}}\text{O}_4)_3(\mu_2\text{-OH})_3(\mu_2\text{-SO}_3)_3(\mu_6\text{-SO}_3)]^{5-}$ used for modelling and (c) schematic view of the final AuNP with the resulting POM stabilising the AuNP core (AuNPs@POM). Color code: green octahedra – reduced MoO_6 , yellow –S, magenta –Na, red –O, blue octahedra – oxidised MoO_6 .

4.3 Computational details

All geometric and electronic properties were obtained from DFT calculations as implemented in the Gaussian 09 software package.^[26] In a first step, we optimized the geometries of all the compounds with the B3LYP functional^[27,28] and double- ζ type basis sets: LANL2DZ for Mo and Au, and 6-31G (d, p) for nonmetal atoms (O, S, Cl, and H).^[29-32] On top of these structures we re-optimized the geometries using large triple- ζ type basis sets: 6-311++G (d, p) for O, S, Cl and H, and def2-TZVPP for Au and Mo,^[33,34] together with dispersion effects with the B3LYP-D3(BJ) approach.^[35] These accurate structures furnished total electronic energies (E_{elec}) and molecular orbitals. From the double-type basis set calculations, we performed molecular frequency calculations to get estimates for the thermal correction to the Gibbs free energy (ΔG_{corr}). This parameter, combined with E_{elec} from the large basis set calculations, gives the thermal free energy in solution (G_{sol}). In all the calculations, the solvation effects were introduced to mimic an aqueous solution by using the ‘self-consistent reaction field’ based on the Polarizable Continuum Model (PCM).^[36]

4.4 Results and discussions

4.4.1 Selection of the POM model

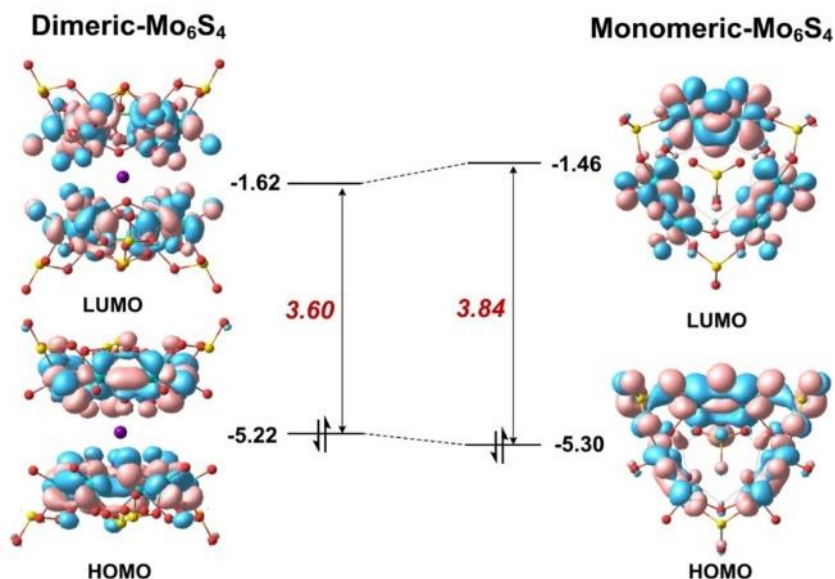


Figure 4.2. Energy (in eV) and composition of the highest occupied (HOMO) and lowest unoccupied (LUMO) molecular orbitals for {dimeric- $\text{H}_3\text{S}_4\text{Mo}_6$ } and { $\text{H}_3\text{S}_4\text{Mo}_6$ }. The HOMO-LUMO (H-L) gaps are 3.60 and 3.84 eV for the dimer and monomer structures, that is, the latter is only 0.24 eV (ca. 6%) larger. The three highest occupied orbitals (six for the dimer) have significant contributions from the $\text{Mo}^{\text{V}}_2\text{O}_4$ core and have Mo-Mo bonding character, where each couple of electrons occupying them are provided by two Mo^{V} .

For a detailed understanding of the role of POM in the reduction of AuCl_4^- ions, DFT calculations were performed for the process until complete reduction of Au^{III} . In the first step of our computational study, we focused on the selection of the POM model. The Kabanos structure (Figure 4.1a) $[\text{Na}\{(\text{Mo}_2^{\text{V}}\text{O}_4)_3(\mu_2\text{-O})_3(\mu_2\text{-SO}_3)_3(\mu_6\text{-SO}_3)_2\}]^{15-}$, features a dimeric structure (abbreviated as {dimeric- $\text{H}_3\text{S}_4\text{Mo}_6$ } because the Kabanos anion would be protonated under the experimental reaction conditions used in this research) that was simplified to the monomeric form, { $\text{H}_3\text{S}_4\text{Mo}_6$ } without interstitial Na^+ , shown in Figure 4.1b, which carries a total charge of -5 in the three-fold protonated form. This simplification is aimed at minimising the computational resources necessary to correctly describe the effect of the POM on the mechanism of formation of AuNPs. After geometry optimization of both forms, the unprotonated {dimeric- S_4Mo_6 } structure features a distance of 9.082 Å (to be compared with 7.905

Å obtained from X-ray data) between the two S atoms placed at the centre of each monomer, whereas the average Mo-O_{μ2} distance (1.976 Å) is 0.17 Å shorter than the experimental one (2.146 Å). Only the inclusion of six protons on μ₂-O generates optimized structures in excellent agreement with the X-ray data (7.965 vs. 7.905 Å). It is worth mentioning that previous studies on isostructural compounds —based on C, P and As— suggest that the three bridging μ₂-O atoms are typically protonated.^[37-40] Therefore, we conclude that it is more reasonable to consider the current complex to be six-fold protonated in acidic solution. As expected, when only monomeric **{H₃S₄Mo₆}** was optimized, the geometrical parameters reproduced the X-ray data with accuracy.

The energies and compositions of the frontier molecular orbitals are examined to evaluate the appropriateness of the **{H₃S₄Mo₆}** model for exploring the role of the Kabanos structure in the formation of metallic gold. It is important to note that negligible differences were observed when comparing the frontier orbitals —the highest occupied and the lowest unoccupied ones (HOMOs and LUMOs, respectively, Figure 4.2). The calculated orbital energies obtained for the monomeric form show that the energy gap between HOMO and HOMO-2 (HOMO-5 for the dimer) is only 0.12 eV (respectively 0.28 eV). This phenomenon clearly demonstrates that it is possible to sequentially remove six electrons from the monomer (twelve from the dimer) during the redox cycle. In addition, a *sine qua non* condition for the reaction $\text{POM}^{n-} + \text{Au}^{m+} \rightarrow \text{POM}^{(n-1)-} + \text{Au}^{(m-1)+}$ to occur is that the POM features an adequate oxidation potential so that electron transfer towards the gold salt is a favourable process. We calculated the oxidation energy for **{H₃S₄Mo₆}** and **{dimeric-H₃S₄Mo₆}** to be 0.22 and 0.24 eV (vs. NHE), respectively. Further calculations (triple- ζ level basis set) on the monomer show that orbital energies are overall down shifted less than 0.3 eV and that the HOMO–LUMO energy gap remains almost unchanged.. In summary, the above analysis shows that the monomer model behaves similarly to **{dimeric-H₃S₄Mo₆}** and, hence, it can be used to explore the reduction mechanism of gold. The following theoretical discussion is therefore based entirely on the role of the monomeric **{H₃S₄Mo₆}** species.

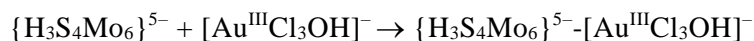
4.4.2 Possible mechanisms of **{H₃S₄Mo₆}**-mediated Au^{III} to Au^I reduction

Since the [AuCl₄]⁻ species is not stable in aqueous solution and always undergoes spontaneous hydrolysis, the existence of intermediates of the type [AuCl_xOH_{4-x}]⁻ is largely pH dependent. The experiments reported herein adjusted the pH close to 5, thus in our calculations we have only considered the most representative [Au^{III}Cl₃OH]⁻ species as the reactant in that conditions.^[41,42] In the pathway to the AuNPs, the

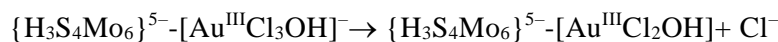
Chapter 4 A Non-classical Polyoxomolybdate as an Electron Source for [Au^{III}Cl₄]⁻ Reduction

fundamental questions we wished to solve were: How do the [Au^{III}Cl₃OH]⁻ ions and the POM interact? And by which mechanism are the electrons transferred from {H₃S₄Mo₆} to Au^{III}? Despite a considerable number of theoretical reports on the growth of AuNPs, the role of POMs has never been addressed until now.

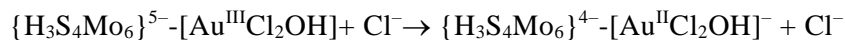
The following discussion goes through the initial reaction stages, when the first gold unit approaches the fully reduced POM⁵⁻ and gains two electrons, from Au^{III} to Au^I. Considering explicitly the molecular charges for a better understanding of the electron transfer processes, the associated general mechanism for such initial steps can be proposed as:



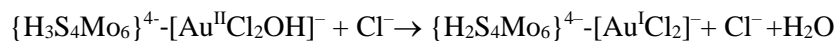
(Precursor complex);



(Cl substitution);



(1st electron transfer);



(2nd electron transfer);

It must be mentioned that further oxidation of {H₂S₄Mo₆}⁴⁻ can occur if more [Au^{III}Cl₃OH]⁻ molecules react with it given that four Mo(d¹) electrons are still present in {H₂S₄Mo₆}⁴⁻. The associated thermodynamical data is discussed later on.

Because both the gold complex (like the *substrate*) and {H₃S₄Mo₆}⁵⁻ are anionic species, the interaction between them should be weak. Most probably, hydrogen-bonding patterns in aqueous solution prevail. The corresponding binding mode between POM and [Au^{III}Cl₃OH]⁻ is depicted in Figure 4.3. The optimized structures show two strong hydrogen bonds formed between the -OH ligand of [AuCl₃OH]⁻ and H (and O) from {H₃S₄Mo₆}⁵⁻, and Au approaching the O between two Mo^V. Also weak Cl...H bonds are formed that must be helpful for the interaction. Figure 4.4 shows the computed free energy profile (*G*, relative to the reactants) following the reduction process. Unlike classical reducing agents, such as citrate,^{[43],[44]} the highly reduced {H₃S₄Mo₆}⁵⁻ POM structure offers multiple reduction sites (in the present case six Mo^V centres). Hence, once the substrate is attached to the POM surface (*precursor* complex, **A**), the electron transfer may lead to different configurations, a fact that is herein assumed. We found that formation of **A** —[Au^{III}Cl₃OH]⁻ adsorption on the bottom of

the POM mainly by hydrogen bonding— is slightly exothermic even if the separate parts are both anions, with a reaction free energy of $-6.5 \text{ kcal}\cdot\text{mol}^{-1}$. Because release of Cl^- from the substrate is easier than that of OH^- before electron transfer, the first reaction step is subject to Cl^- elimination from $[\text{Au}^{\text{III}}\text{Cl}_3\text{OH}]^-$ associated with attachment to the POM, giving species **B**. This step was also found to be thermodynamically favourable with an associated energy of $-1.3 \text{ kcal}\cdot\text{mol}^{-1}$ referred to **A**. On the other hand, releasing the OH^- group costs about $60 \text{ kcal}\cdot\text{mol}^{-1}$, making this hypothetical process unlikely.

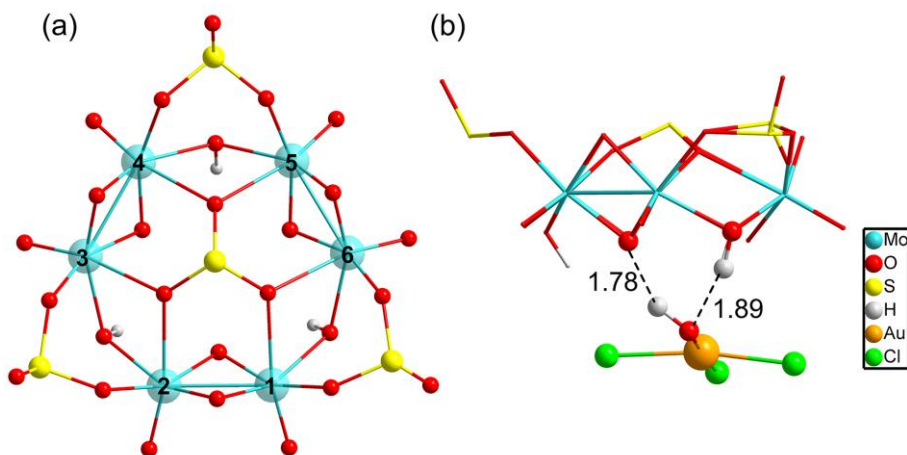


Figure 4.3. (a) Top view of $[(\text{Mo}_2^{\text{V}}\text{O}_4)_3(\mu_2\text{-OH})_3(\mu_2\text{-SO}_3)_3(\mu_6\text{-SO}_3)]^{5-}$, Mo(d^1) centres of the POM are numbered 1–6. (b) The most plausible binding mode for $[\text{Au}^{\text{III}}\text{Cl}_3\text{OH}]^-$ attaching on the POM surface, via strong $\text{O}\cdots\text{H}$ and weak $\text{Cl}\cdots\text{H}$ interaction.

Reduction of Au^{III} should occur through intramolecular $\text{Mo}^{\text{V}} \rightarrow \text{Au}^{\text{III}}$ electron transfer. Obviously, there are six electron-providing centres, as shown in Figure 4.3a, the attaching $\text{Mo}^{\text{V}}_{(1)}\text{-Mo}^{\text{V}}_{(2)}$ group being the logical site when the distance effect is considered. The first electron transfer from the POM to Au^{III} leads to species **C-1**, with $G = -12.3 \text{ kcal}\cdot\text{mol}^{-1}$. **C-1** exhibit a diradical nature, with spin densities of 0.96e on one Mo_2 group and 0.90e on the $[\text{Au}^{\text{II}}\text{Cl}_2\text{OH}]^-$ moiety, namely with unpaired electrons respectively on one $\text{Mo}^{\text{IV}}\text{-Mo}^{\text{V}}$ group and on Au^{II} . Following **C-1**, a more exergonic process is obtained for the reduction of Au^{II} to Au^{I} . The proton-coupled electron transfer (PCET) is a reaction mechanism that is thought to be common in redox reactions.^[45-47] In our case, we observe that when 2e-oxidation occurs in the

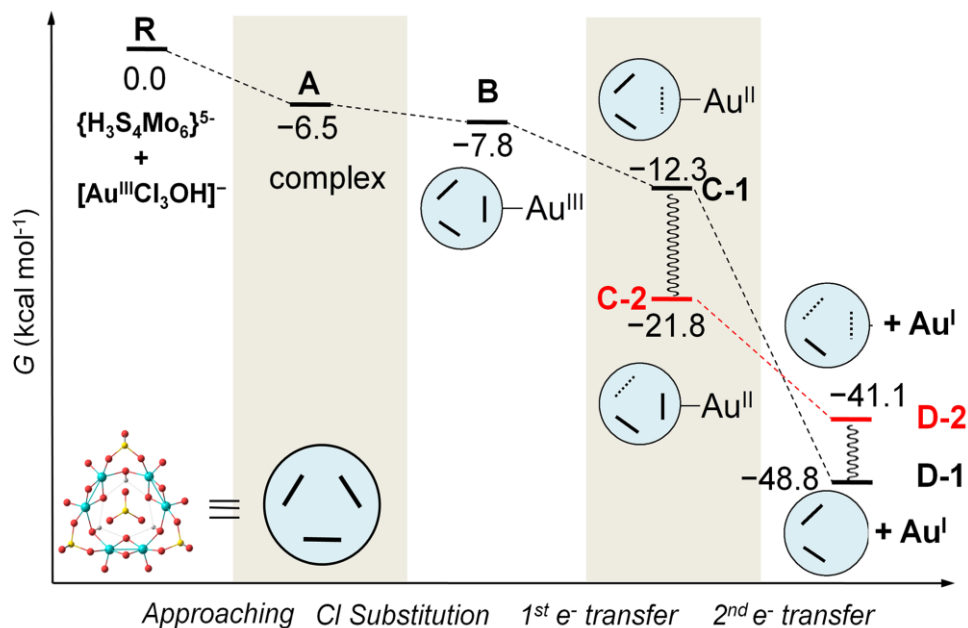
Chapter 4 A Non-classical Polyoxomolybdate as an Electron Source for $[Au^{III}Cl_4]^-$ Reduction

Figure 4.4. Computed free energy profile (in kcal mol^{-1} , values relative to reactants) associated to the gold reduction process. We use the schematic notation defined for the POM monomer, $\{H_3S_4Mo_6\}^{5-}$, with thick lines denoting Mo-Mo bonds and dotted lines denoting one-electron Mo-Mo bonds. Species **C-2** is assumed to rearrange from **C-1**. Species **D-1** has lost two electrons from the same Mo-Mo bond, whereas **D-2** has two one-electron Mo-Mo bonds. Geometrical details of the computed intermediates are shown in Figure 4.5.

POM, an intramolecular hydrogen bond cleavage takes place and this hydrogen is transferred to the $-\text{OH}$ of the gold complex with associated H_2O release and formation of the linear $[\text{Au}^{\text{I}}\text{Cl}_2]^-$ species. The proton transfer forming H_2O significantly promotes the Au^{II} to Au^{I} reduction. On the basis of **C-1**, the continuous reduction by the Mo from the $\text{Mo}_1\text{-Mo}_2$ group will lead to the $2e^-$ -reduced product **D-1**, with $\Delta G \approx -48 \text{ kcal}\cdot\text{mol}^{-1}$ from reactants at the present level of calculation. On the other hand, we also considered one more isomeric structure of **D-1**, giving $[\text{Au}^{\text{I}}\text{Cl}(\text{H}_2\text{O})]$ instead of $[\text{Au}^{\text{I}}\text{Cl}_2]^-$, which is $3.6 \text{ kcal}\cdot\text{mol}^{-1}$ less stable than **D-1**. In other words, $[\text{Au}^{\text{I}}\text{Cl}(\text{H}_2\text{O})]$ can convert to $[\text{Au}^{\text{I}}\text{Cl}_2]^-$ by exchanging H_2O with Cl^- in solution. Furthermore, calculations show that the $\text{Au}^{\text{II}} \rightarrow \text{Au}^{\text{I}}$ step is thermodynamically more advantageous than $\text{Au}^{\text{III}} \rightarrow \text{Au}^{\text{II}}$, suggesting that Au^{II} could be a short-lived intermediate. This fact can also be ascribed to the favourable evolution from d^9 to d^{10} in this step.

C-1 may undergo electron rearrangement in the POM moiety due to the available electrons from the other Mo-Mo groups. If one electron is transferred from $\text{Mo}_3\text{-Mo}_4$ to

Chapter 4 A Non-classical Polyoxomolybdate as an Electron Source for [Au^{III}Cl₄]⁻ Reduction

the Mo₁-Mo₂ group to form **C-2**, the energy changes by $-9.5 \text{ kcal}\cdot\text{mol}^{-1}$, which we attribute to the stronger binding between the [Au^{II}Cl₂OH]⁻ group and the almost intact Mo₂O₂ group in **C-1** (see Figure 4.4). In the last step of the energy profile, a 2e-unpaired configuration, **D-2**, was computed based on the possibility that the electrons are transferred from Mo₁-Mo₂ and Mo₃-Mo₄ groups, one each, at variance with **D-1**, in which the two electrons have migrated to the gold atom from the same Mo-Mo group. We found that **D-1** is more stable than **D-2** by about $7 \text{ kcal}\cdot\text{mol}^{-1}$ (-48.8 vs. $-41.1 \text{ kcal}\cdot\text{mol}^{-1}$), indicating that two electrons coming from the same Mo-Mo group and breaking this Mo-Mo bond, is preferred over two electrons coming from different Mo-Mo groups. Alternatively to the direct **B** → **C-1** → **D-1** pathway, in which electrons flow between the closest sites of the POM to Au, the results also suggest that the electronic rearrangement **C-1** → **C-2** is thermodynamically favoured and it could supply the second electron to Au^{II} to form **D-2**. From the present data we cannot say with total confidence which pathway (1 or 2) is the most effective.

To analyse the structural evolution in the POM⁵⁻-Au^{III}Cl₂OH → POM³⁻-Au^ICl₂ process, Figure 4.5 focuses on the binding region of intermediates **B** → **C-1** → **D-1**. Addition of the first electron to Au^{III}Cl₂OH does not cause significant variations in Au-Cl and Au-OH bond lengths, with variations being less than 0.2 Å. However, a two-electron transfer from the POM to Au^{III}Cl₂OH can pull one chlorine ligand or water group (H release from the POM to the -OH group to form H₂O) out of the Au^I center. From intermediate **B** to **D-1**, the Au-O_b distance increases to 2.919 Å, evidencing a very weak interaction between the POM and [Au^ICl₂]⁻. The short distance between O (-OH in the Au complex) and H (in the POM) in **B** and **C**, around 1.4–1.5 Å, indicates strong hydrogen interaction. From **B** to **C**, the electron transfer induces the hydrogen bonding to become much stronger. After the second POM → Au electron transfer, the proton is completely re-located to release a H₂O molecule. Concerning the geometry of **B**, the Mo-Mo bond is stretched to 2.652 Å, notably longer than the initial 2.560 Å in the free closed-shell POM. However, allowing for an open-shell configuration, we obtain **C-1** with metal-metal bond breaking and spontaneous electron transfer. We found that further electron loss from the same Mo₂ group elongates dramatically this Mo-Mo distance to 3.503 Å in species **D-1**. In the latter system, oxidation of the two Mo^V from the same group leads to hydrogen bond cleavage and transfer to the OH of the gold complex, which possibly produces a SO₂ unit detachment. One of the S-O bonds is clearly stretched to 2.118 Å, implying that SO₂ units have a natural tendency to leave as the POM loses electrons.

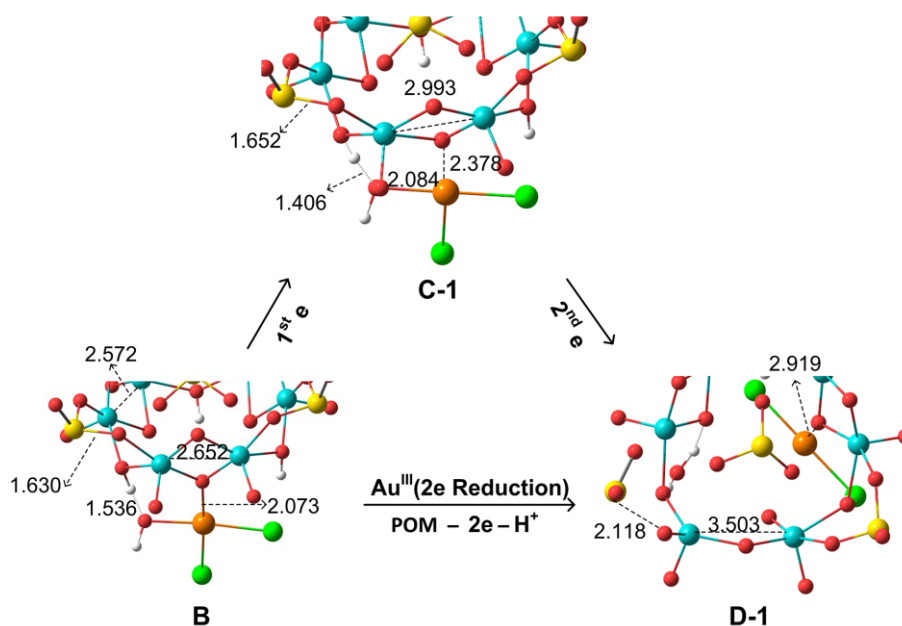
Chapter 4 A Non-classical Polyoxomolybdate as an Electron Source for [Au^{III}Cl₄]⁻ Reduction

Figure 4.5. Main structural changes (distances in Å) for the intermediate structures **B** → **C-1** → **D-1**. Hydrogen bonds and Au–O interactions are fundamental in the formation of the intermediates.

A relevant point for the following discussion is the identification of the strong driving force for gold reduction. Besides the energies of the intermediate species, their molecular orbitals contain very useful information concerning the reaction mechanism, especially for redox processes. To go into the details of the reaction, we analysed the most important orbitals of intermediates **B**, **C-1** and **D-1**, shown in Figure 4.6.

When the orbital energies of **B** are compared with those of the free {**H₃S₄Mo₆**} moiety, one notices that the addition of Au^{III}Cl₂OH increases the energy of the HOMO by 0.02 eV only, and that of HOMOs in **B** are more localized on each Mo–Mo group than in {**H₃S₄Mo₆**} (Figure S4.1), which acts as the electron source during the reduction process. At variance with the possible electron donations from Mo–Mo groups with participation in HOMO and HOMO-1, the HOMO-2 also shows contributions from Au^{III}Cl₂OH and some bonding interaction between the Au and O. It is also remarkable that the LUMO of **B** resembles much that of the Au^{III}Cl₂OH and the connected Mo₁–Mo₂ unit, showing antibonding character between the Au and O atoms, which would promote Au–O bond cleavage by electron occupation upon reduction. Considering the overlap between HOMO-2 and LUMO, the electron transfer is reliable via these two orbitals separated by 2.0 eV. We cannot neglect the contribution from the

Chapter 4 A Non-classical Polyoxomolybdate as an Electron Source for [Au^{III}Cl₄]⁻ Reduction

HOMO to electron donation even if the electron density on Mo₁-Mo₂ is very small. **B** → **C-1** involves a one-electron transfer from HOMO-2 into the Au^{III} moiety. In **C-1**, 0.44 e can be attributed to Au (mainly $d_{x^2-y^2}$ character) and 0.36 e are shared by two Cl and H₂O ligands. The spin density representation of **C-1** (Figure 4.6) clarifies this electron distribution. The unrestricted formalism applied to the electronic open shell gives HOMO–LUMO gaps for α and β orbitals of 2.26 and 2.01 eV, respectively. α -LUMO has no contribution from the [Au^{II}Cl₂OH]⁻ group and leads to 2.26 eV, making the α -HOMO → α -LUMO electron transfer unlikely. However, the composition and energy of β -LUMO resembles much that in **B**, suggesting that the second electron will go into this orbital to form **D-1** via α -HOMO → β -LUMO electron transfer, with a smaller energy gap of 1.90 eV. Despite this energy gap is very similar to the one in **B**, the second electron transfer is thermodynamically much more favourable in comparison to the first one.

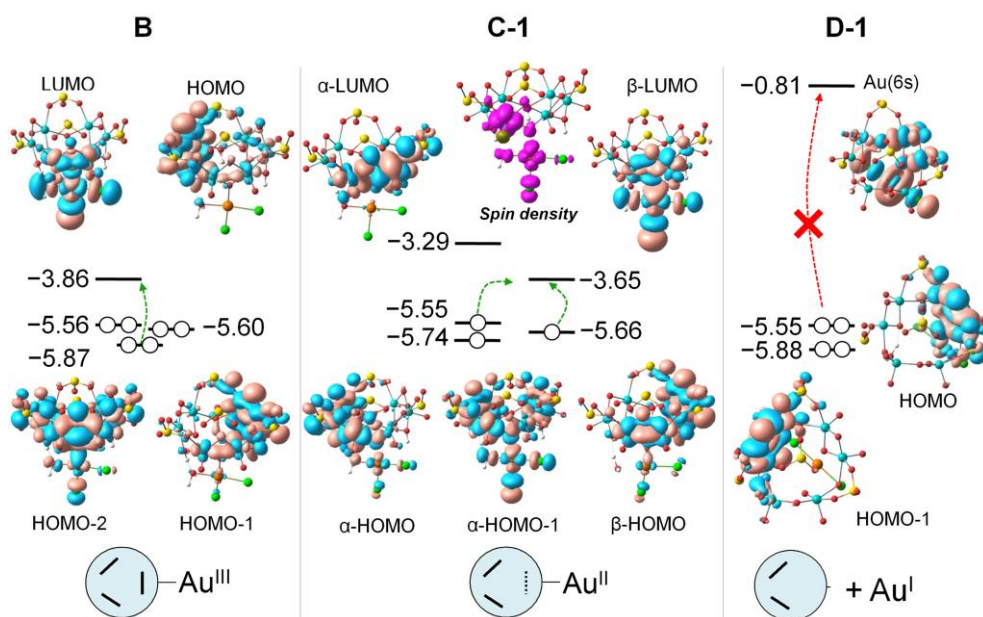


Figure 4.6. Computed orbital energies (values in eV) involved in the main electron transitions (dashed green arrows) during the reduction process of Au^{III} to Au^I. The spin density representation for species **C-1** (magenta) corresponds to the triplet state.

The formation of **D-1** can take place either by direct electron transfer to β -LUMO, as mentioned. However, a different thermodynamically stable conformation was found in step C (species **C-2**, Figure 4.4). This can be produced

after internal electron reorganization from Mo₃-Mo₄ (α -HOMO or β -HOMO) to Mo₁-Mo₂ due to the low energy of the β -LUMO, with concomitant geometric rearrangement. The **C-1** \rightarrow **C-2** process has $\Delta G = -9.5 \text{ kcal}\cdot\text{mol}^{-1}$. Indeed, the α -HOMO is the result of the first reduction, and the next occupied orbital (α -HOMO-1) lies 0.19 eV below, indicating the strong preference of the [Au^{II}Cl₂OH]⁻ unit to accept the electrons to form a stable doubly occupied orbital, that is, the HOMO-1 in **D-1**. Therefore, a two-electron transfer can take place from the POM to the Au unit, causing complete cleavage of the Au-O bond to minimize the electron-electron repulsions between the two anions (AuCl₂⁻ and POM⁴⁻).

4.4.3 Au^I to Au⁰ step

As mentioned above, the [AuCl₄]⁻ can be easily reduced to form the AuCl₂⁻ species. To achieve the first seed in the formation of AuNPs, namely one Au⁰ atom, Au^I should be further reduced. It features a stable d^{10} electronic configuration; hence, the additional electron must be accommodated in the 6s orbital. As shown in Figure 4.6, the unoccupied orbital labelled 'Au (6s)' is the lowest Au^I orbital but it is not the lowest empty orbital available. The gap between the POM-localised HOMO and the lowest Au-like empty orbital is very large (4.7 eV). At variance with the first two reduction steps (Au^{III} \rightarrow Au^{II} \rightarrow Au^I), the Au^I + e \rightarrow Au⁰ process is expected to be very difficult. So, the question of how Au^I intermediates can be reduced to Au⁰ arises. The calculated results proved that two or three [Au^ICl₂]⁻ units can, from thermodynamic considerations, form dimeric or trimeric species when dispersion corrections are applied to the calculations. We found an exothermic nucleation energy of -4.7 and -3.9 kcal·mol⁻¹ to form gold dimer and trimer species, respectively. If dispersion corrections are not considered, repulsive coulombic interactions are dominating giving an endothermic process of 2.8 kcal·mol⁻¹. Therefore, inclusion of dispersion corrections is required in order to correctly describe the incipient processes.

Moreover, the computed reduction energies (REs, or electron affinities in solution) for the [Au^{III}Cl₄]⁻/[Au^ICl₂]⁻ and [Au^ICl₂]⁻/Au⁰ processes are -5.21 and -2.60 eV, respectively. The RE = -5.21 eV is in good agreement with the experimental value (-5.17 eV). However, the computational estimate for [Au^ICl₂]⁻/Au⁰ is far from the experimental -5.39 eV. We found this discrepancy to be caused mainly by the cohesion energy missing of solid gold when only the single Au atom is calculated. As presented in one recently published work, the disproportionation reaction $3[\text{Au}^{\text{I}}\text{Cl}_2]^- \rightarrow \text{AuCl}_4^- + 2\text{Au}_{(\text{s})} + 2\text{Cl}^-$ was one possible route for the

reduction of Au^I.^[48] It is true that the formation of AuNPs will be promoted by this way with the increasing of the Au^I and Au⁰ species. However, for the first or initial reduction of Au^I, the effect of the oxidant and the environment should be taken into account. We argue that the endergonic reaction energy (estimated to be ~70 kcal·mol⁻¹) was obtained when only the POM and [Au^ICl₂]⁻ species are considered to react. This finding led us to consider and include additional effects that may affect the thermochemistry, such as the presence of other species in solution. Notably, in our reaction conditions Na⁺, NH₄⁺ and H₃O⁺ coexist with the POM and Auⁿ⁺ species. Thus, either one NH₄⁺, Na⁺ or H₃O⁺ molecule was explicitly added to the [Au^ICl₂]⁻ model calculations. The originally computed Au^I electron affinity in solution (-2.60 eV with only [AuCl₂]⁻ in the model) remain unchanged when NH₄⁺ (-2.88 eV) or Na⁺ (-2.63 eV) are considered. However, including one H₃O⁺ molecule in the calculations has a large effect in the electron affinity (-3.40 eV).

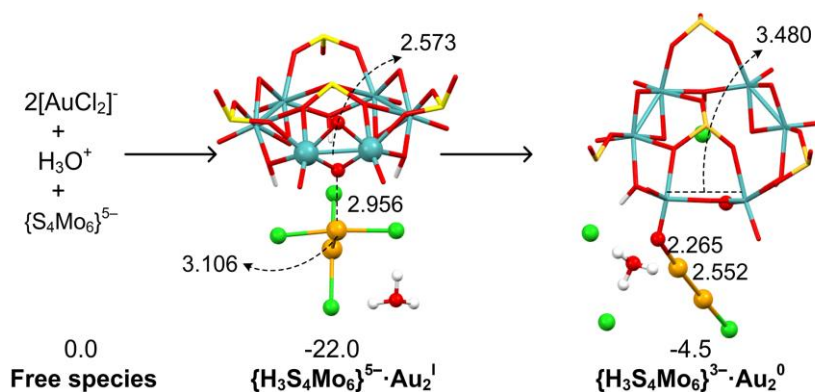


Figure 4.7. Structural (in Å) and energetic (in kcal mol⁻¹) variations during the reduction of the [Au^ICl₂]⁻ dimer by the initial {H₃S₄Mo₆} in the presence of one H₃O⁺.

To analyse the energy demands associated with this reduction process we choose the initial {S₄Mo₆}⁵⁻ species to interact with the [AuCl₂]⁻ dimer surrounded by one H₃O⁺ (Figure 4.7), which makes the reaction exergonic, ΔG = -4.5 kcal·mol⁻¹. Additionally, the formation of a Au–Au bond promotes the reduction of Au^I to Au⁰.^[49] Instead, including Na⁺ in the reaction still makes the process unfavourable, with 30.1 kcal·mol⁻¹. We have to remark that even the concentration of H₃O⁺ is quite small in solution; we believe that H₃O⁺ promotes the Au^I species to approach each other, helps the charge balance on the new gold cluster and stabilizes the released Cl⁻ in the initial steps. As soon as the first Au⁰ species is formed, it is

expected that the gold reduction process will be less energy demanding as the gold nanoparticle increases in size. We remark here that Au/Au^I (solid) has a positive redox potential of 1.68 V vs. NHE from Lange's Handbook of Chemistry, whereas the value for atomic Au/Au^I is negative (-1.5 V vs. NHE), explaining that only the first steps must be aided by H₃O⁺.^[50,51]

Because the Au^{III} species is pH-dependent, the [AuCl₃OH]⁻ itself has been considered instead of [AuCl₄]⁻, since the experimental pH is 5. Following the crucial role of protons, we also explored if the protonated Au^I dimer can be reduced by a two-electron-oxidised Kabanos anion. In fact, the computed reaction free energy for this step is roughly the same as that of the initial reduced structure. From this viewpoint, it is evident that the two-electron-oxidised Kabanos can be further oxidised, and we deduce that the reduction of Au^I to Au⁰ can occur by the co-action of POM and H₃O⁺ at the first stage.

4.4.4 Persistence of POM activity until full oxidation

To explore further the POM-related redox processes, one can successively introduce the second and third [Au^{III}Cl₃OH]⁻ units for reaction with the partially oxidised {H₂S₄Mo^{VI}₂Mo^V₄}⁴⁻ compound. Our goal is to analyse on-going electron transfer from it to other gold units until complete oxidation to {S₄Mo^{VI}₆}²⁻, as shown in Chart 4.1.

It has been stated above that the 2e-reduction product **D-1** (with two electrons coming from one Mo-Mo group) are more stable than the open shell product. Indeed, it is a reasonable assumption that some [Au^{III}Cl₃OH]⁻ groups may attach to the POM at the beginning of the reaction. We chose **D-1** as the starting point for the successive processes to simplify the electronic state, and the reduction of the second [Au^{III}Cl₃OH]⁻ was studied considering the routes with oxidation of Mo^V from the same group only. These calculations indicate that addition and reduction of the second Au^{III} to Au^I by the partially oxidised {H₂S₄Mo^{VI}₂Mo^V₄}⁴⁻ is exergonic, with $\Delta G = -69.6$ kcal·mol⁻¹. In addition, the final state in Chart 4.1 (formation of the third Au^I unit) is obtained after a very favourable step, with $\Delta G = -70.1$ kcal·mol⁻¹ if the four-electron-oxidised POM, {HS₄Mo^{VI}₄Mo^V₂}³⁻, is considered as reducing agent for this step. It is worth mentioning that successive POM-Au electron transfers are increasingly exergonic compared with the fully reduced POM, which may be attributed to the concomitant favourable SO₂ release observed as {S₄Mo₆} loses electrons. Calculations show that it is highly reasonable that the reduced molybdo-sulphate POM can provide six electrons in the presence of Au^{III}. This fact supports the experimental XPS data (Figure S4.2) taken for

Chapter 4 A Non-classical Polyoxomolybdate as an Electron Source for [Au^{III}Cl₄]⁻ Reduction

AuNPs@POM, which reveals the presence of only Mo^{VI} in the surface of the AuNP, corresponding to total oxidation of the POM.

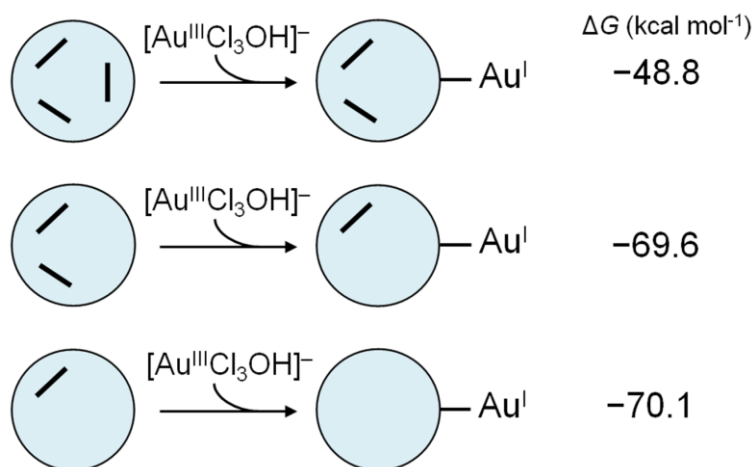


Chart 4.1. Computed free energies (in kcal·mol⁻¹) associated to the second and third [AuCl₃OH]⁻ reduction based on the 2e-oxidised {H₂S₄Mo^{VI}₂Mo^V₄}⁴⁻.

As deduced from the structural change analysis associated to the first 2e-reduction of [AuCl₃OH]⁻, one SO₂ unit is very likely to be released from the POM. Interestingly, three SO₂ units are completely detached after reaction with two more [AuCl₃OH]⁻ complexes to convert all six Mo^V to Mo^{VI}. The present calculations strongly suggest that the fully oxidised oxomolybdate that might be attached to AuNPs may be viewed as a re-organisation of the initial structure with partial loss of SO₂, namely the [SMo^{VI}₆O₂₁]²⁻ structure. We propose that it is ring-shaped with a central SO₃ unit weakly bound to the external framework, reminiscent of the previously reported [SeMo₆O₂₁]²⁻ (Figure S4.3).^[52] The total energy associated with the loss of three SO₂ units has been estimated to be -26 kcal·mol⁻¹ (referenced to the fully oxidised POM intermediate), confirming that SO₂ release takes place spontaneously as electrons are removed from the POM. On the other hand, the hypothetical process of removing one SO₂ unit from the fully reduced {H₃S₄Mo₆} is computed to be 55.5 kcal·mol⁻¹. Such a largely endothermic process evidences that SO₂ loss occurs as electrons are removed from the POM unit. The proposed oxidised structure is presumably stable owing to the large HOMO-LUMO gap of 4.68 eV. These results are experimentally supported. From the ICP data obtained for AuNPs@POM (Au 97.69%, Mo 2.08% and S 0.19%),^[53] we determined a molar ratio Mo/S = 3.65, a value much larger than the one

deduced from the initial reduced form of the POM (Mo/S = 1.5), and between 6/1 and 6/2 (loss of three and two SO₂ units, respectively). Thus, the experimental and theoretical parts allow concluding that at least two SO₂ have been detached from the POM.

4.5 Conclusions

This work discloses a mechanistic route for the complete reduction of a Au^{III} salt to Au⁰ using an *'in built'* electron source, the Kabanos POM ([Na{Mo₂^VO₄})₃(μ₂-O)₃(μ₂-SO₃)₃(μ₆-SO₃)₂]¹⁵⁻), which provides several electrons and proves to be thermodynamically favourable for the reduction. The reduction process is greatly driven by the coupled electron and proton transfer process. Both theoretical and experimental data presented show that all Mo^V centres of the Kabanos POM were completely oxidised to Mo^{VI} with a concomitant loss of SO₂ units from the original Kabanos form, as ICP data and DFT calculations suggest. Considering the Au^I to Au⁰ step a key process, calculations indicate that the Au^I complex is not tightly attached to the POM surface and, in combination with a high HOMO(POM)-6s (Au^I) energy gap, we suggest that the POM is not directly responsible for Au^I → Au⁰ step. Instead, a Au^I dimer is formed before the first Au⁰ atom is generated, the presence of H₃O⁺ in solution boosting this step without further oxidation of the POM. This is commensurate with the most favorable experimental conditions encountered when the pH is varied from neutral to acidic.

References and Notes

- [1] V. V. Mody, R. Siwale, A. Singh and H. R. Mody, *J. Pharm. Bioallied Sci.* 2010, 2, 282–289.
- [2] M. Grzelczak, J. P. Perez-Juste, P. Mulvaney and L. M. Liz-Marz-an, *Chem. Soc. Rev.* 2008, 37, 1783–1791.
- [3] S. J. Soenen, P. Rivera-Gil, J.-M. Montenegro, W. J. Parak, S. C. De Smedt and K. Braeckmans, *Nano Today* 2011, 6, 446–465.
- [4] B. Pelaz, V. Grazú, A. Ibarra, C. Magen, P. del Pino and J. M. de la Fuente, *Langmuir* 2012, 28, 8965–8970.
- [5] A. Roldán, S. González, J. M. Ricart and F. Illas, *ChemPhysChem* 2009, 10, 348–351.
- [6] T. Yao, Z. H. Sun, Y. Y. Li, Z. Y. Pan, H. Wei, Y. Xie, M. Nomura, Y. Niwa, W. S. Yan, Z. Y. Wu, Y. Jiang, Q. H. Liu and S. Q. Wei, *J. Am. Chem. Soc.* 2010, 132, 7696–7701.
- [7] D. Toroz and S. Corni, *Nano Lett.* 2011, 11, 1313–1318.
- [8] B. Keita, I. M. Mbomekalle, L. Nadjó and C. Haut, *Electrochem. Commun.* 2004,6, 978–983.
- [9] A. Dolbecq, J.-D. Compain, P. Mialane, J. Marrot, F. S. Secheresse, B. Keita, L. R. B. Holzle, F. Miserque and L. Nadjó, *Chem.Eur. J.* 2009, 15, 733–741.
- [10] S. G. Mitchell and J. M. de la Fuente, *Eur. J. Inorg. Chem.* 2013, 32, 5517–5522.
- [11] M. T. Pope, *Heteropoly and Isopoly Oxometalates*. Springer-Verlag: New York, 1983.
- [12] A. Müller and M. T. Pope, *Polyoxometalate Chemistry: From Topology via Self-Assembly to Applications*, Kluwer, 2001.
- [13] D. L. Long, E. Burkholder and L. Cronin, *Chem. Soc. Rev.* 2007, 36, 105–121.
- [14] C. Busche, L. Vilà-Nadal, J. Yan, H. N. Miras, D. L. Long, V. P. Georgiev, A. Asenov, R. H. Pedersen, N. Gadegaard, M. M. Mirza, D. J. Paul, J. M. Poblet and L. Cronin, *Nature* 2014, 515, 545–549.
- [15] H. Lv, Y. V. Geletii, C. Zhao, J. W. Vickers, G. Zhu, Z. Luo, J. Song, T. Lian, D. G. Musaev and C. L. Hill, *Chem. Soc. Rev.* 2012, 41, 7572–7589.
- [16] S.-X. Guo, Y. Liu, C.-Y. Lee, A. M. Bond, J. Zhang, Y. V. Geletii and C. L. Hill, *Energy Environ. Sci.* 2013, 6, 2654–2663.
- [17] J. J. Baldoví, S. Cardona-Serra, J. M. Clemente-Juan, E. Coronado, A. Gaita-Ariño and H. Prima-García, *Chem. Commun.* 2013, 49, 8922–8924.

Chapter 4 A Non-classical Polyoxomolybdate as an Electron Source for [Au^{III}Cl₄]⁻ Reduction

- [18] Y. Nishimoto, D. Yokogawa, H. Yoshikawa, K. Awaga and S. Irlé, *J. Am. Chem. Soc.* 2014, 136, 9042–9052.
- [19] B. Keita, T. B. Liu and L. Nadjo, *J. Mater. Chem.* 2009, 19, 19–33.
- [20] S. G. Mitchell and J. M. de la Fuente, *J. Mater. Chem.* 2012, 22, 18091–18100.
- [21] Y. F. Wang and I. A. Weinstock, *Chem. Soc. Rev.* 2012, 41, 7479–7496.
- [22] G. J. Zhang, B. Keita, R. N. Biboum, F. Miserque, P. Berthet, A. Dolbecq, P. Mialane, L. Catala and L. Nadjo, *J. Mater. Chem.* 2009, 19, 8639–8644.
- [23] B. Keita, R. N. Biboum, I. M. Mbomekallé, S. Floquet, C. Simonnet-Jégat, E. Cadot, F. Miserque, P. Berthet and L. Nadjo, *J. Mater. Chem.* 2008, 18, 3196–199.
- [24] M. J. Manos, J. D. Woollins, A. M. Z. Slawin and T. A. Kabanos, *Angew. Chem., Int. Ed.* 2002, 15, 2801–2808.
- [25] I. M. Gabas, G. Stepien, M. Moros, S. G. Mitchell and J. M. de la Fuente, under review.
- [26] M. J. Frisch et al., *Gaussian09W*, Revision A02; Gaussian, Inc.: Wallingford, CT, 2009.
- [27] A. D. Becke, *J. Chem. Phys.* 1993, 98, 5648–5652.
- [28] C. Lee, W. Yang and R. G. Parr, *Phys. Rev. B* 1988, 37, 785–789.
- [29] P. J. Hay and W. R. Wadt, *J. Chem. Phys.* 1985, 82, 270–283.
- [30] M. M. Francl, W. J. Pietro, W. J. Hehre, J. S. Binkley, M. S. Gordon, D. J. Defrees and J. A. Pople, *J. Chem. Phys.* 1982, 77, 3654–3665.
- [31] P. C. Hariharan and J. A. Pople, *Theor. Chem. Acta.*, 1973, 28, 213–222.
- [32] G. A. Petersson and M. A. Al-Laham, *J. Chem. Phys.* 1991, 94, 6081–6090.
- [33] D. Feller, *J. Comp. Chem.*, 1996, 17, 1571–1586.
- [34] K. L. Schuchardt, B. T. Didier, T. Elsethagen, L. Sun, V. Gurumoorthi, J. Chase, J. Li and T. L. Windus, *J. Chem. Inf. Model.*, 2007, 47, 1045–1052.
- [35] S. Grimme, S. Ehrlich and L. Goerigk, *J. Comp. Chem.*, 2011, 32, 1456–1465.
- [36] J. Tomasi, B. Mennucci, and R. Cammi, *Chem. Rev.* 2005, 105, 2999–3094.
- [37] M. J. Manos, A. D. Keramidis, J. D. Woollins, A. M. Z. Slawin and T. A. Kabanos, *J. Chem. Soc., Dalton Trans.* 2001, 3419–3420.
- [38] E. Cadot, A. Dolbecq, B. Salignac and F. Sécheresse, *Chem. Eur. J.* 1999, 5, 2396–2403.
- [39] A. Leclaire, A. Guesdon, F. Berrah, M. M. Borel and B. Raveau, *J. Solid State Chem.* 1999, 145, 291–301.
- [40] A. Leclaire, C. Biot, H. Rebbah, M. M. Borel and B. Raveau, *J. Mater. Chem.* 1998, 8, 439–444.

Chapter 4 A Non-classical Polyoxomolybdate as an Electron Source for [Au^{III}Cl₄]⁻ Reduction

- [41] D. V. Goia and E. Matijevic, *Colloids Surf. A* 1999, 146, 139–152.
- [42] S. Wang, K. Qian, X. Z. Bi and W. X. Huang, *J. Phys. Chem. C* 2009, 113, 6505–6510.
- [43] J. Turkevich, P. C. Stevenson and J. Hillier, *Discuss. Faraday Soc.* 1951, 11, 55–75.
- [44] J. Turkevich, P. C. Stevenson and J. Hillier, *J. Phys. Chem.* 1953, 57, 670–673.
- [45] M. H. V. Huynh and T. J. Meyer, *Chem. Rev.* 2007, 107, 5004–5064.
- [46] See special issue devoted to reviews on proton-coupled electron transfer, *Chem. Rev.* 2010, 110, 6937–6938.
- [47] A. Sartorel, P. Miró, E. Salvadori, S. Romain, M. Carraro, G. Scorrano, M. D. Valentin, A. Llobet, C. Bo and M. Bonchio, *J. Am. Chem. Soc.* 2009, 131, 16051–16053.
- [48] K. Theilacker, H. B. Schlegel, M. Kaupp and P. Schwerdtfeger. *Inorg. Chem.* 2015, 54, 9869–9875.
- [49] H. Schmidbaur and A. Schier, *Chem. Soc. Rev.* 2012, 41, 370–412.
- [50] S. Mosseri, A. Henglein and E. Janata. *J. Phys. Chem.* 1989, 93, 6791–6795.
- [51] E. Gachard, H. Remita, J. Khatouri, B. Keita, L. Nadjo and J. Belloni. *New J. Chem.*, 1998, 1257–1265.
- [52] D. Yang, S. Li, P. Ma and J. Niu, *Inorg. Chem.* 2013, 52, 14034–14039.
- [53] Z. L. Lang, I. M. Gabas, X. López, A. Clotet, J. M. de la Fuente, S. G. Mitchell and J. M. Poblet, *New J. Chem.*, 2016, 40, 1029–1038.

Appendix Chapter 4

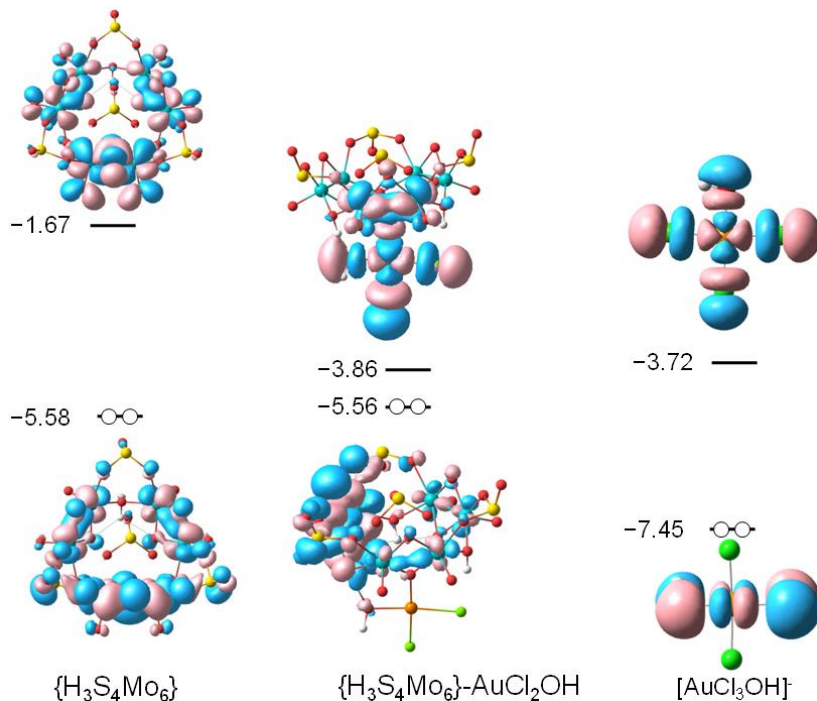


Figure S4.1 Schematic view of the frontier molecular orbitals of the $\{H_3S_4Mo_6\}-AuCl_3$ adduct (A-I), compared with the independent $\{H_3S_4Mo_6\}$ and $[AuCl_3OH]^-$ units at B3LYP-D3(BJ)/6-311++G(d,p),def2-TZVPP level. The HOMO of the adduct resembles in energy and shape to that of $\{H_3S_4Mo_6\}$, whereas the LUMO is $[AuCl_3OH]^-$ -like. Even though, there is some mixing of the orbitals leading to stabilization of the HOMO and destabilization of the LUMO.

Chapter 4 A Non-classical Polyoxomolybdate as an Electron Source for $[Au^{III}Cl_4]^-$ Reduction

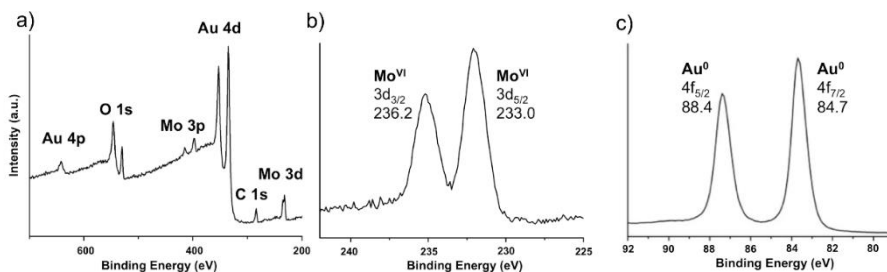


Figure S4.2 XPS spectra of AuNPs@POM showing a) general spectrum in the 200-700 eV range; b) the characteristic doublet for Mo^{VI} in the 230-235 eV region; c) the spin-orbit doublet of Au⁰ at 88.4 and 84.7 eV (splitting of 3.7 eV) for 4f_{5/2} and 4f_{7/2}, respectively. Note that there was no evidence of any Mo^V.

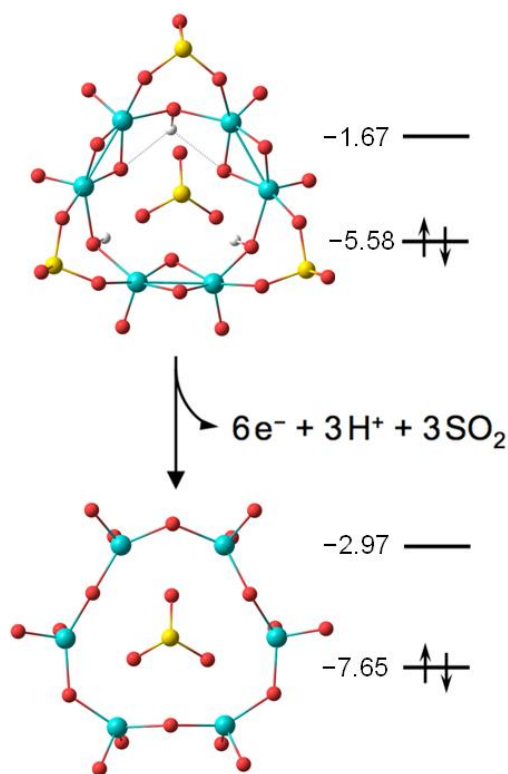
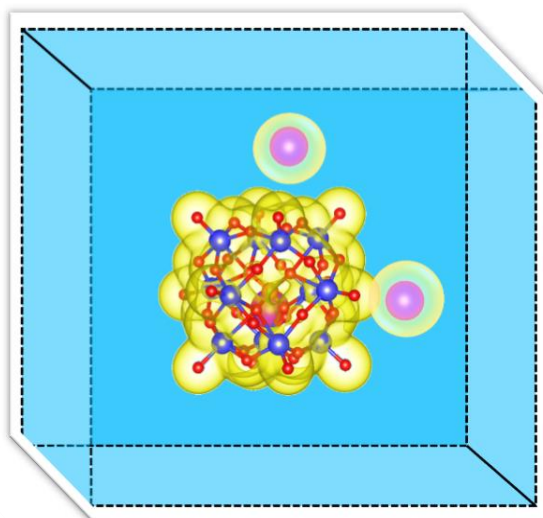


Figure S4.3 Evolution from the initial POM structure, $[(Mo_2^V O_4)_3(\mu_2-OH)_3(\mu_2-SO_3)_3(\mu_6-SO_3)]^{5-}$, to the proposed final one, $[SMo^{VI}_6O_{21}]^{2-}$, with the associated loss of electrons, protons and SO_2 . Indicated are the corresponding HOMO and LUMO energies, in eV.

Chapter 5

Effect of Solvent and Cation on the Lindqvist/Keggin-surface Composites



It is known that POMs exist in solution as negatively charged species stabilized by solvent and counterions. To reproduce the experimental facts, it is usually required the inclusion of the environment effects in the modelling. In this chapter, we compared the solvation for some classical isolated polyoxometalates based on the implicit solvent models in VASP (VASP sol) and Gaussian (PCM) respectively. Then we present the adsorption of POMs on the metallic surfaces both in vacuum and implicit solvent environment, in order to check the solvent effects on POM-surface composites. In addition, the cation effects are also discussed.

5.1 Introduction and background

Incorporation of solvent in computational chemistry has gained high popularity during the last decade thanks to the continuous development of software and hardware. Although solvent effects can be very important in many physical, biological and chemical processes, they were not considered in the initial stages of computational chemistry. The reason was not because theoretical chemists or physicists were not aware of its relevance; it was technical limitations that prevented its use as a general tool. To include the solvent effects is important in many cases, but it is crucial in the modelling of charged species in general, and in anions, in particular, where its existence is only possible in presence of the external field created by the solvent and counterions. The solvent effects can be taken into account through an explicit way by using molecular dynamics simulations, in which solute-solvent and solvent-solvent interactions are involved. Because the huge number of solvent molecules the computational cost may increase rapidly, and in periodic systems the complexity of the problem restricts its universal use. On the other hand, the solvation effects can be further simplified by employing an implicit continuum model. For molecular systems, two of the most common used methods for describing the solvent are the well-known *COSMO*^[1] and *PCM*^[2] models as described in chapter 2. However, the use of this methodology in periodic boundary systems is very recent, and so far only some few works have been published.^[3]

As mentioned POMs are anions and many of their properties are consubstantial with its activity in solution, as for example their redox-active.^[4] Therefore, the solvent effects will be a very important factor to be considered in order to correctly describe their reactivity and electronic properties, particularly for high q/m systems.^[5] Beyond the classical studies for POMs at molecular level, nowadays, one of the main hot-topics regarding polyoxometalates is to adsorb them on planar surfaces or on metal nanoparticles (NPs) to obtain more functional composite materials.^[6] Over the past two decades, the organized arrays of individual POMs onto metallic or graphite surfaces have been extensively exploited by Anson *et al.*, Keita *et al.*, Gewirth *et al.*, Weinstock *et al.*, and others.^[7-9] The experiment structural characterization of POMs on the surfaces or NPs has been great improved by using cyclic voltammetry (CV), scanning tunneling microscopy (STM), atomic force microscopy (AFM), and X-ray specular reflectivity. However, none of these techniques is available in colloidal solution until the utilization of cryogenic-transmission electron microscopy (Cryo-TEM) by the Weinstock group, which can directly image the intact solution-state

structure of POM-protected NPs in water. Using this technique, they have pointed out that the stability of POM SAMs on metal NPs,^[10-13] was largely dependent on the nature of the counter-cations, understood to be structurally integrated into the POM-NP composites.

From a computational point of view, the investigations for POM-surface composites are much challenging. In order to describe the electronic structures and the interactions between the POMs and surfaces more accurately, in this chapter, we intend to introduce the continuum implicit solvent model (VASP sol) for our systems, to reveal the impacts of solvent on the geometric and electronic structures of isolate slab, POMs, and the combined systems. The small and low charged $[\text{Mo}_6\text{O}_{19}]^{2-}$ adsorbed on the gold surface was chosen to illustrate how does the continuum model work on the POM-surface composites. We benchmark our strategy with the full Keggin anion $[\text{SiW}_{12}\text{O}_{40}]^{4-}$ on the silver surface which has been investigated using density functional theory (DFT) calculations and molecular dynamic (MD) simulations by Aparicio Anglès *et al.*^[14] This allows us to determine the main factors that have to be considered in modelling ions on surfaces in a computational saving manner.

5.2 Computational details

All first principle calculations were performed using the VASP 5.3 code, with the Perdew–Wang 91 functional (PW91) GGA exchange-correction functional.^[15] The valence electrons for each element are described by plane waves with a kinetic energy cut-off at 500 eV, while the core electrons are represented by using the projector augmented wave (PAW) pseudopotentials.^[16,17] All optimizations were performed until self-consistence, with thresholds of $1 \cdot 10^{-5}$ eV and $3 \cdot 10^{-2}$ eV·Å⁻¹ for the electronic and the ionic convergence respectively. The reciprocal space for the slab and adsorbed systems was described using two different Monkhorst Pack Schemes^[18]: $3 \times 3 \times 1$ for structure optimization, and $5 \times 5 \times 1$ for calculating of density of states (DOS). All isolated molecules were calculated in a cubic box with a 25 Å side with Γ -point. Bader’s AIM (Atoms in Molecules) atomic charges^[19] were determined using the Henkelmann algorithm.^[20] Solvent effects were included by means of the implicit solvation model (named VASP sol) implemented by Hennig and co-workers.^[21] In addition, we have also carried out geometry optimizations for the isolated molecules both in gas and solvation (PCM model) phases at PW91/6-31G(d) + LANL2DZ level by using the Gaussian 09 code.^[22]

5.3 Results and discussions

5.3.1 Solvent effects on the isolated POMs and bare slabs

To describe reactivity or electrochemical behaviour of POMs, both molecular orbital (MO) ordering and energies must be corrected by introducing solvent effects. We firstly focus on the solvent effects on the solvation energy of the isolated POMs, which are important factors in determining the adsorption of POMs on the surfaces. Because the methodologies with periodic boundary conditions have intrinsic problems with charged systems, it is much easier to work on models where the total charge is neutral. Thus, the equal number of K atoms was introduced to compensate the charge of isolated POM anions. The whole system was calculated in both gas and implicit solvation phases. The solvation energies were estimated for the classical isolated $\text{K}_3\text{PW}_{12}\text{O}_{40}$, $\text{K}_3\text{PMo}_{12}\text{O}_{40}$, and $\text{K}_4\text{SiW}_{12}\text{O}_{40}$, as well as the pure Au(111) and Ag(111) slabs. In order to evaluate whether the solvation model provided by Hennig *et al.* is adequate for describing the geometric and electronic structure for isolate POMs, we have also included the results using the PCM model, which has been widely used in the computational study of POMs. The solvation energies (E_{sol}) are computed as the difference between the total energies for the system obtained from results with ($E_{tot-sol}$) and without ($E_{tot-vac}$) implicit solvent model respectively:

$$E_{sol} = E_{tot-sol} - E_{tot-vac} \quad (5.1)$$

As seen from Table 5.1, the POM is significantly stabilized by the solvent with solvation energies greater than 3 eV regardless of the solvent model. The values for the neutral POMs obtained from VASP *sol* is within 26–34% of the Gaussian09 PCM model, which agree closely with the errors obtained for the isolated water and methanol.^[23] However, significant differences are detected when the POMs are considered as anionic species, which are poorly solvated with VASP *sol*. Even no experimental data is available for these systems; the closing results between PCM and VASP *sol* model for neutral polyoxometalates suggest that it is possible to include the solvent effects by the method developed by Hennig *et al.* On the other hand, the solvent effects for the clean Au(111) and Ag(111) slabs are almost negligible with solvation energies lower than 0.1 eV.

Chapter 5 Effect of Solvent and Cation on the Lindqvist/Keggin-surface composites

Table 5.1. The solvation energies (eV) for isolated polyoxometalates and the clean slabs.

	^a $E_{\text{VASP sol}}$	^b E_{PCM}	^c $\Delta x\%$
$\text{K}_3\text{PW}_{12}\text{O}_{40}$	-4.68	-3.58	30.7
$\text{K}_3\text{PMo}_{12}\text{O}_{40}$	-4.33	-3.43	26.2
$\text{K}_4\text{SiW}_{12}\text{O}_{40}$	-5.39	-4.03	33.8
$[\text{PW}_{12}\text{O}_{40}]^{3-}$	-2.31	-10.35	77.7
$[\text{PMo}_{12}\text{O}_{40}]^{3-}$	-2.31	-10.41	77.8
$[\text{SiW}_{12}\text{O}_{40}]^{4-}$	-4.31	-18.45	77.6
Au(111)	0.08		
Ag(111)	0.02		

a and *b* stand for the calculated solvation energies with VASP sol and Gaussian 09 package using the PCM model respectively; *c* represents the deviation between PCM and VASP sol of energies: $\Delta x\% = \frac{E_{\text{vasp-sol}} - E_{\text{PCM}}}{E_{\text{PCM}}} \%$.

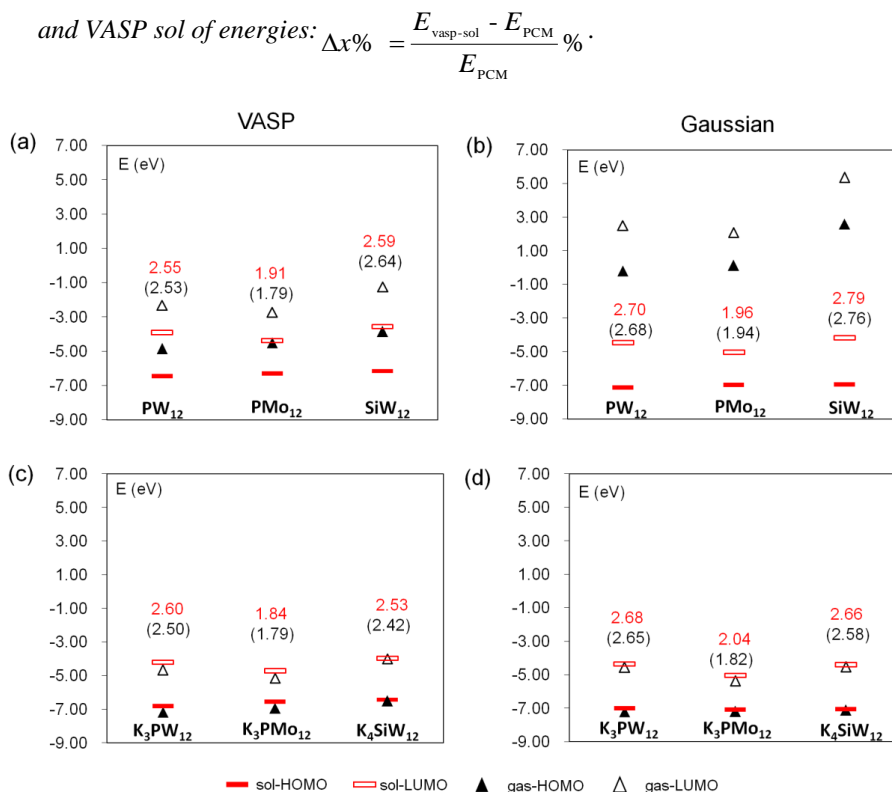


Figure 5.1. Schematic representation of frontier orbital energies and HOMO-LUMO gaps in gas (values in parenthesis) and solution for anions $[\text{PW}_{12}\text{O}_{40}]^{3-}$, $[\text{PMo}_{12}\text{O}_{40}]^{3-}$, and $[\text{SiW}_{12}\text{O}_{40}]^{4-}$ and its neutralized K_n -POM partners obtained from VASP (a, c) and Gaussian (b, d).

The electronic properties for anionic and neutral POMs were presented in Figure 5.1 by computing with Gaussian and VASP. In order to compare the results between Gaussian and VASP, the orbital energies obtained from VASP were not referred to the Fermi energy. Results are unequivocal, the HOMO-LUMO gap keeps consistent in both codes whether the solvent models were included or not. Both PCM and VASP *sol* could apparently stabilize the MOs with respect to gas phase when counterions are excluded. Although relatively higher MO energies were obtained in the latter, the small differences still suggest that the VASP *sol* was also able to estimate the electronic structure of molecular POMs. On the other hand, the results for neutral systems between VASP and Gaussian agree much better than the anions. The implicit solvent around the KPOMs does not reflect significant differences for the absolute values of orbital energies and orbital gaps regardless of the solvation models. The main stabilizations for MOs are generated from the strong cation-anion interactions, which are partially reduced by the solvation. Considering the good consistence of solvation energies and MOs properties shown by PCM and VASP *sol* approaches, we have assumed that the solvation effects can be introduced to POMs in periodic boundary condition via the implicit model (VASP *sol*). However, due to the limitation of VASP for charged system, we have preferentially used in the calculations the neutral system, that is, POM + counterions embedded by the set of point charges that model the solvent.

5.3.2 Solvent and cation effects for a combined system—the low charged $[\text{Mo}_6\text{O}_{19}]^{2-}$ on Au(111)

In a second step, we have applied the implicit solvent model to a periodic model: the adsorption of Lindqvist polyoxometalate $[\text{Mo}_6\text{O}_{19}]^{2-}$ on the Au(111) surface. The small polyoxoanion $[\text{Mo}_6\text{O}_{19}]^{2-}$ was chosen to test how the continuum solvent model works on the POM-surface type systems.

Firstly, we optimized 16 configurations shown in Figure 5.2 to determine the favourable adsorption sites of $[\text{Mo}_6\text{O}_{19}]^{2-}$ on Au(111). The gold surface in a high coverage situation was modelled by using the $\begin{pmatrix} 4 & 0 \\ 2 & 4 \end{pmatrix}$ Au(111) slab model, consisting of three gold layers with 16 gold atoms per layer. The dimensions of the unit cell were 11.81 and 10.22 Å in *a* and *b* directions respectively. In this step, the cations were not included, and the models were relaxed by keeping the bottom two Au layers fixed at their bulk position. As shown in Table 5.2 and Figure 5.3, those energy favourable adsorptions consistent with sites that have more oxygens over the top Au atom. The F₃₀, H₉₀, and B₉₀ sites are the most stable adsorption sites, which are almost degenerate in

Chapter 5 Effect of Solvent and Cation on the Lindqvist/Keggin-surface composites

energy, differing by less than 1.0 kcal·mol⁻¹. It is worth mentioning that the B₉₀ is finally rearranged to H₉₀ site. The top Au can not only contact via three O_t atoms, but also interact with three O_b atoms, with distances in range of 2.22-2.48 Å.

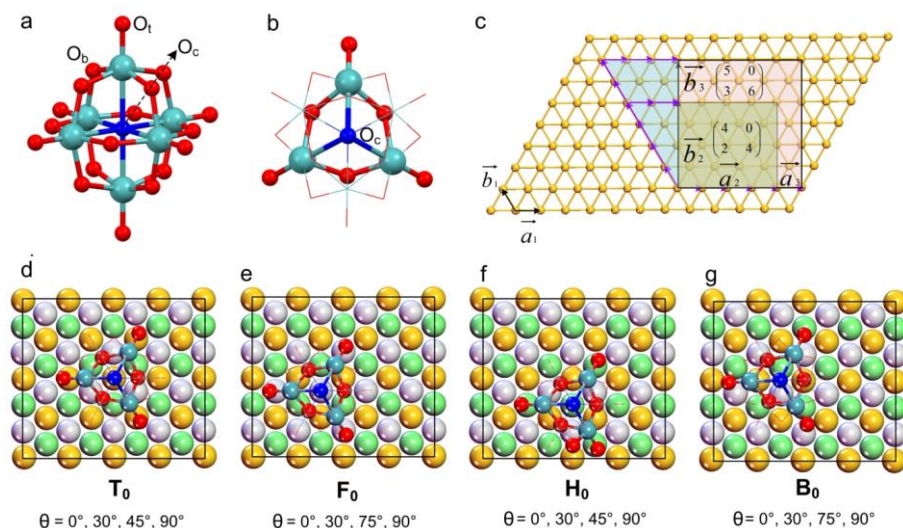


Figure 5.2. (a) Side view and oxygen labels of Lindqvist $[Mo_6O_{19}]^{2-}$ with ball and stick representation; (b) Top view of $[Mo_6O_{19}]^{2-}$ from C_3 axis; (c) Proposed unit cells for Au(111) in high and low coverage situations; (d) (e) (f) (g) Representation of the possible adsorption sites (T: Top, F: Fcc, H: Hcp, B: Bridge and θ : rotation angles) of Mo_6O_{19} on Au (111) via its proper C_3 symmetry axis (Orange: 1st Au layer, green: 2nd Au layer, grey: 3rd Au layer).

Table 5.2. Relative energies (kca mol⁻¹) for Mo_6O_{19} adsorbed on high covered Au(111) in vacuum.

Site	Rotation	ΔE	Site	Rotation	ΔE
O _c -T	0°	8.3	O _c -H	0°	10.4
	30°	4.8		30°	19.4
	45°	8.9		45°	10.0
	90°	15.5		90°	0.2
O _c -F	0°	9.8	O _c -B	0°	12.3
	30°	0.0		30°	1.4
	75°	7.4		75°	1.4
	90°	18.7		90°	0.8

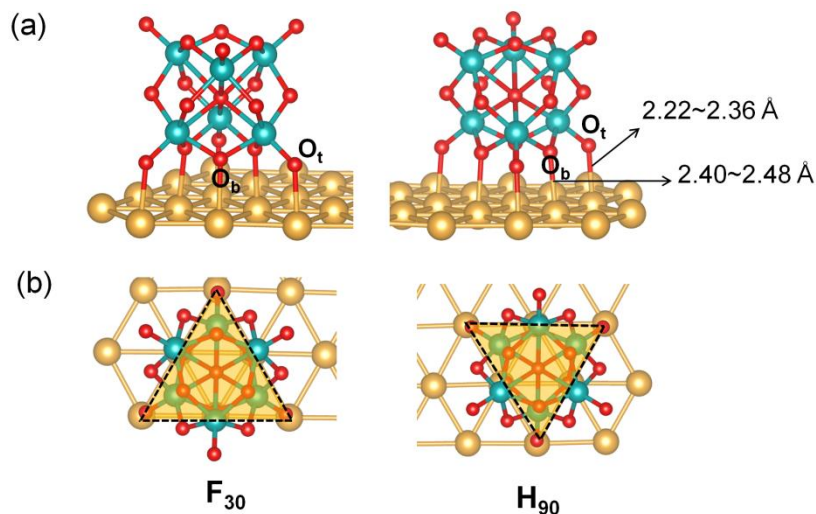


Figure 5.3. Ball and stick representation of two most stable adsorption sites for Mo_6O_{19} on $Au(111)$ from side (a) and top (b) views.

5.3.2.1 The effects of the counterions

Indeed, the model that does not include the counterions overestimates the oxidant strength of the POM, and very likely, it will tend to capture the electrons from the surface to fill its empty oxygen orbitals. Consequently, the interaction between the POM and the surface would be overestimated. In order to unravel the interaction between the POM and the surface, and also to evaluate how does the presence of counterions corrects the POM oxidant strength, we have incorporated two explicit K atoms close to the $[Mo_6O_{19}]^{2-}$ on the F_{30} site to compensate the charge of POM. This model provides a suitable non-biased reference and avoids a charged supercell. One aspect that must be considered is where the counterions to be located. Three different cation distributions were calculated, and the relative energies are presented in Figure 5.4. Close connections between K and POMs with K-O (POM) distances between 2.7 and 2.9 Å were obtained. The position of the cations brings great influence for the stability of the system. Model A corresponds to the most stable distribution with two K^+ linked to the O_3 faces (three bridging oxygens), as well as stabilized by the surface. Respect to the geometry in cation free model, the Au- O_t distances are enlarged from 2.22-2.36 to 2.75-2.88 Å, as listed in Table 5.3 and Figure 5.4. This can be easily understood as the counterions correct the overestimated POM oxidant strength and therefore the interaction between POM and surface becomes weaker.

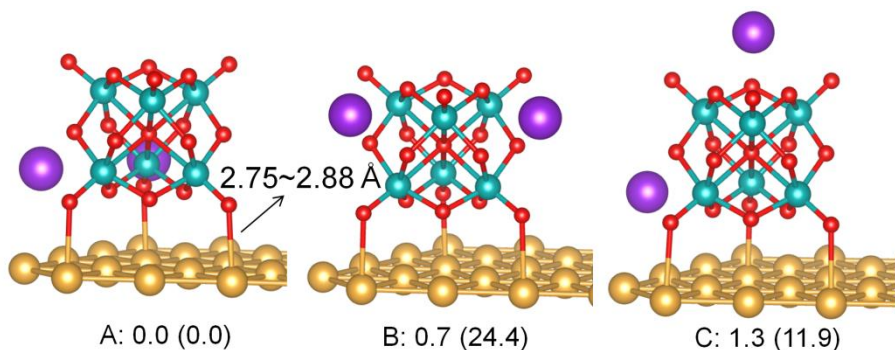


Figure 5.4. 3D representation and relative energies (in kcal·mol⁻¹) for three models with different cation distributions. Values out/in parenthesis are the relative energies computed in solution (vacuum).

Table 5.3. The Au–O_t, Au–O_b distances (in Å), adsorption energies (kcal mol⁻¹), and bader AIM charges of K₂Mo₆O₁₉ adsorbed on Au(111) in Fcc₃₀ orientation for high and low coverage. (Θ_{high}/low = high/low coverage, sol = solvent (water)).

Type	$d(\text{Au-O}_t)$	$d(\text{Au-O}_b)$	E_{ads}	Bader		
				Au	Mo ₆ O ₁₉	K
Mo ₆ O ₁₉ -Θ _{high}	2.292–2.336	2.401–2.440	-50.9	1.42	-1.42	
Mo ₆ O ₁₉ -Θ _{high} -sol	2.297–2.362	2.431–2.495	-10.6	1.69	-1.69	
K ₂ Mo ₆ O ₁₉ -Θ _{high}	2.747–2.879	2.926–2.981	-20.4	0.09	-1.89	1.80
K ₂ Mo ₆ O ₁₉ -Θ _{high} -sol	2.785–2.954	3.008–3.080	-1.4	0.07	-2.05	1.98
K ₂ Mo ₆ O ₁₉ -Θ _{low}	2.710–2.713	2.879–2.885	-15.3	0.05	-1.85	1.80
K ₂ Mo ₆ O ₁₉ -Θ _{low} -sol	2.706–2.715	2.828–2.870	-2.2	0.02	-2.01	1.99

To quantitatively determine how strong the Mo₆ is adsorbed on gold, the adsorption energy was defined as:

$$E_{ads} = E_{tot} - E_{surf} - E_{KPOM} \quad (5.2)$$

Where these terms represent the energy for the whole system (E_{tot}), for the relaxed clean surface (E_{surf}), and the POM surrounded by the counterions. It should be noted that for the cation exclusion system, the adsorption energy was estimated by the ionic binding energy (IBE) that is defined in equation 5.3, in which the $E_{POM(n-)}$ is the total

energy of the anion, and $-n\cdot\phi$ is an approximation to the energy of the cationic surface. n is the formal charge of the POM, and ϕ is the slab workfunction.

$$E_{\text{IBE}} = E_{\text{tot}} - E_{\text{surf}} - E_{\text{POM}(n-)} - n\cdot\phi \quad (5.3)$$

As expected, very strong interactions are obtained in the cation free model with binding energy reaching up to $-50.9 \text{ kcal}\cdot\text{mol}^{-1}$, while the adsorption for the $\text{K}_2\text{Mo}_6\text{O}_{19}$ is only $-20.4 \text{ kcal}\cdot\text{mol}^{-1}$. The large exothermic values indicate the $\text{K}_2\text{Mo}_6\text{O}_{19}$ is very likely to covalently adsorb on the gold surface; however, this may not be the real behaviour of POMs on gold surfaces as experiments suggest.^[24]

5.3.2.2 The effects of the solvent

To understand the role of the solvent for the adsorbed system, the model based on F_{30} that we initially was optimized in vacuum, then was reoptimized under the implicit solvent environment, with the VASP *sol* method. Unlike classical dynamics simulations, the DFT calculations with an implicit solvent environment only slightly increase the computation time with respect to the vacuum. Small elongations of Au-O_{vb} distances are observed in solution. The solvation reduces the strong K-O and K-Au interactions; leads to the K⁺ distribution becomes less sensitive to their position, with relative energy differences that are now less than $1.5 \text{ kcal}\cdot\text{mol}^{-1}$. On the other hand, the adsorption energies are significantly weakened. The $\text{K}_2\text{Mo}_6\text{O}_{19}$ is adsorbed on Au(111) with only $-1.4 \text{ kcal}\cdot\text{mol}^{-1}$. The adsorption energy for $[\text{Mo}_6\text{O}_{19}]^{2-}$ without including the cations decreases up to $-10.6 \text{ kcal}\cdot\text{mol}^{-1}$. In addition, the adsorption of $\text{K}_2\text{Mo}_6\text{O}_{19}$ on the gold surface is not influenced by the coverage of the surface, which presents similar E_{ads} in high and low coverage situations as shown in Table 5.3.

5.3.2.3 Electronic structure in gas phase and solution

We analysed the Density of States (DOS) and Projected Density of States (PDOS) (PDOS) for $\text{Mo}_6\text{O}_{19}\text{-Au}(111)$ and $\text{K}_2\text{Mo}_6\text{O}_{19}\text{-Au}(111)$ in vacuum and solution, see Figure 5.5. The effect of counterions for the electronic structure is enormous, both the O(sp) and Mo(d) bands are lowered by up to $\sim 0.5 \text{ eV}$ with respect to E_{F} , namely, the presence of counterions results in a significant stabilization of the orbitals of polyoxometalate. However, the relative position of Mo(d) and O(sp) bands obtained in vacuum and implicit solvation show very small differences, which are slightly decreased by 0.1 eV in solution. Because the Mo(d) bands in all cases are located above the E_{F} , it expected that the anion will not be reduced when adsorbed on the gold surface. The Bader charge analysis in Table 5.3 also support no charge transfer occurs between the gold and $\text{K}_2\text{Mo}_6\text{O}_{19}$ both in vacuum and solution. Lastly, it should be

noted that in the cation free model, the supercell is treated neutral (no compensating background charge). That is, the POM framework (Mo_6O_{19}) is neutral in a VASP calculation, which means that the oxo band is not completed and consequently there is a charge transfer from gold orbitals to the oxo orbitals in order to have a stabilized POM. In this line, the computed charge for the POM in vacuum was computed to be $1.42e$ and it raises up to $1.69e$ when the solvent was introduced in the calculations. Despite the relative close value to -2 it does not mean that the system is well described in a cation free model because the gold is formally oxidized.

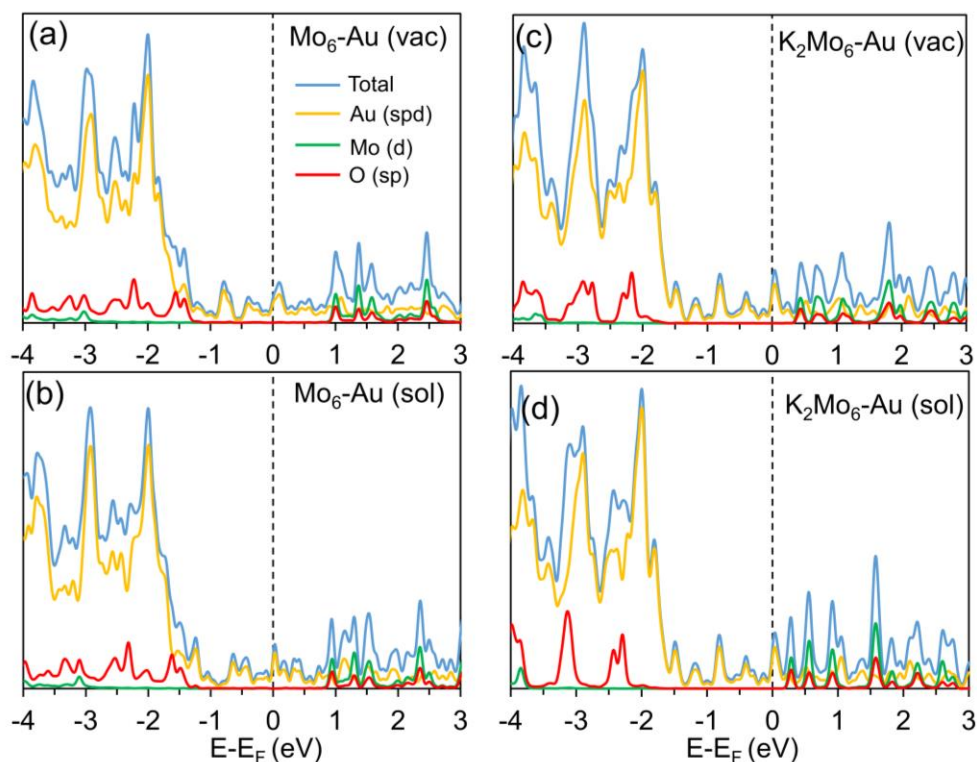


Figure 5.5. Density of States and Projected Density of States for Mo_6O_{19} (a, b) and $\text{K}_2\text{Mo}_6\text{O}_{19}$ (c, d) on Au (111) in vacuum and solution respectively. (DOS: light blue, Au (spd) PDOS: orange, Mo (d) PDOS: green, O (sp) PDOS: red.)

5.3.3 Extending the modeling to moderate charged α -[SiW₁₂O₄₀]⁴⁻ on the silver/gold surfaces

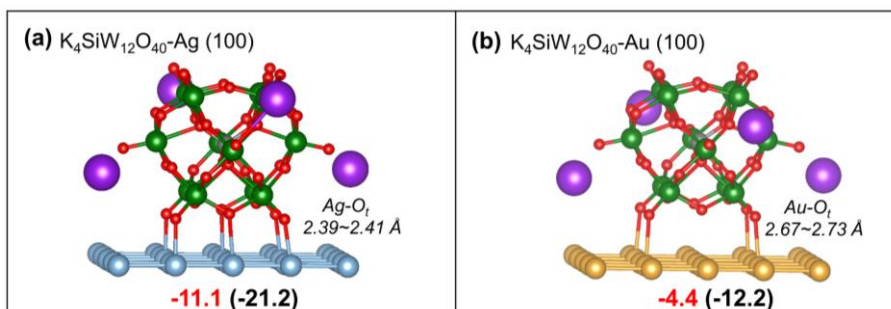


Figure 5.6. Computed adsorption energies ($\text{kcal}\cdot\text{mol}^{-1}$) for $K_4SiW_{12}O_{40}$ on **a)** Au(100) and **b)** Ag(100). Values out/in parenthesis are corresponded to the results in solution (vacuum).

Previous studies on the electrochemical response of α -[SiW₁₂O₄₀]⁴⁻ adsorbed on Ag and Au electrodes have suggested that α -[SiW₁₂O₄₀]⁴⁻ would be reduced after its adsorption on the silver surface, but not on a gold surface.^[24] Our group has reproduced the reduction of [SiW₁₂O₄₀]⁴⁻ on the Ag surface from theory when the environmental effects from both cations and solvent are taken into account by combining DFT calculations with MD simulations.^[14] However, this approach is quite computationally demanding and not very efficient for calculating the adsorption energy. In this part, we re-analyzed α -K₄SiW₁₂O₄₀ adsorbed on Ag(100) with a simpler way. That is, considering the solvent effects by the implicit solvent model in VASP. The adsorption on Au(100) was also calculated for comparison. Both gold and silver surfaces were simulated with a 5×5 slab model, consisting of four gold layers with 25 gold or silver atoms per layer. The adsorption mode for K₄SiW₁₂ both on Ag(100) and Au(100) is focused only on the S₄ orientation as discussed previously.^[14] As expected, the Au(100) surface has poor affinity for [SiW₁₂O₄₀]⁴⁻ in solution, with an adsorption energy of only -4.4 $\text{kcal}\cdot\text{mol}^{-1}$. Both PDOSs and Bader charges indicate that [SiW₁₂O₄₀]⁴⁻ is not reduced on the Au(100) surface, which is consistent to the experimental result. For the silver surfaces, however, the affinity for [SiW₁₂O₄₀]⁴⁻ is much stronger, with an adsorption energy of -11.1 $\text{kcal}\cdot\text{mol}^{-1}$ (Figure 5.6). Compared to the adsorption energy in vacuum, it is largely decreased with the solvent mediated. The analysis of the DOSs function shown in Figure 5.7 and the atomic charges, which are listed in Table 5.4, clearly indicate that [SiW₁₂O₄₀]⁴⁻ is spontaneously reduced when it is adsorbed on a silver surface. This behavior is totally consistent with the experimental data reported by Gewirth and also with our previous results, which combined classical MD

simulations and DFT calculations. In other words, the continuum solvent model gives rise to the same results we obtained when we included explicit water molecules through MD simulations, but in an easiest way.

Table 5.4. Bader charges for the $K_4SiW_{12}O_{40}$ adsorbed on $Au(100)$ and $Ag(100)$. $M(1)$ is the metal layer which closest to the POM ($M = Au$ or Ag).

Species	Phase	Anion	ΣK^+	ΣM	M(1)	M(2)	M(3)	M(4)
$K_4SiW_{12}O_{40}$	vac.	-3.66	3.66					
	sol.	-3.95	3.95					
$K_4SiW_{12}-Au$	vac.	-3.61	3.61	-0.01	-0.89	0.92	0.90	-0.94
	sol.	-3.94	3.95	-0.01	-0.76	0.96	0.88	-1.09
$K_4SiW_{12}-Ag$	vac.	-4.26	3.59	0.68	0.16	0.47	0.62	-0.56
	sol.	-4.89	3.93	0.95	0.49	0.49	0.62	-0.65

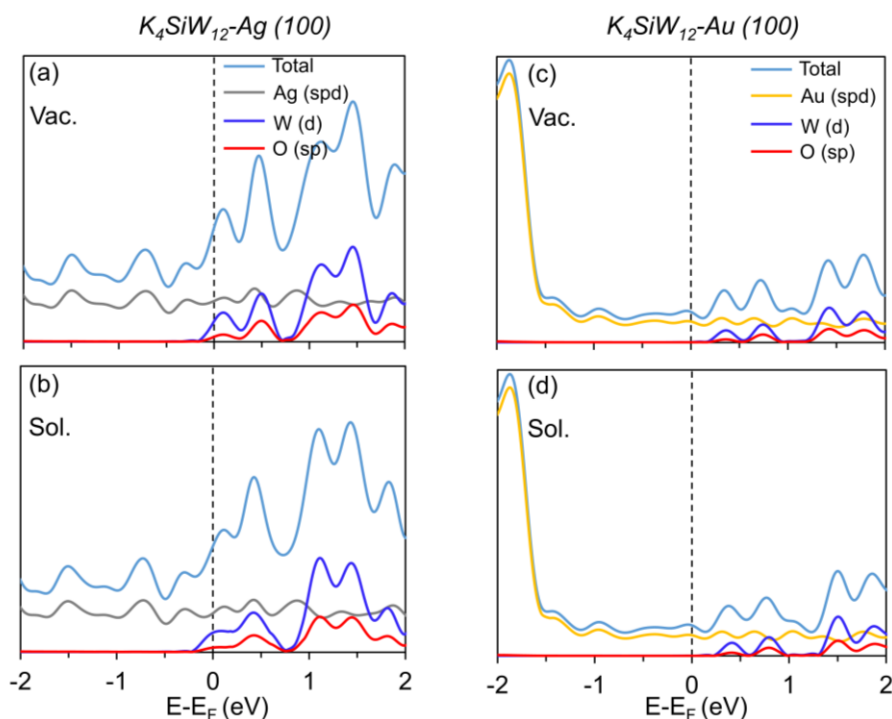


Figure 5.7. Density of States and projected Density of States for K_4SiW_{12} adsorbed on $Ag(100)$ (a, b) and $Au(100)$ (c, d) in vacuum and solution respectively. (DOS: light blue, $Ag(sp d)$ PDOS: gray, $Au(sp d)$ PDOS: orange, $Mo(d)$ PDOS: green, $O(sp)$ PDOS: red.)

5.4 Conclusions

In this chapter, the effects of counterions and solvent effects have been discussed. We applied a continuum solvation model implemented by Hennig et al. (VASP *sol*) for the isolated POMs and POM-surface combined systems. Firstly, the calculated solvation energies and electronic structure with VASP *sol* for a set of isolated POMs are found consistent with the results obtained from PCM model in Gaussian 09. It should be noted that this consistence is more suitable for cation neutralized POMs. $\text{K}_2\text{Mo}_6\text{O}_{19}$ adsorbed on Au(111) was selected as the model to test the computational efficiency of solvent model for POM-adsorbed systems. This model showed that the solvent mainly avoids the overestimation of the POM-surface and cation-anion interactions, while the counterions play important role in correctly describe the electronic structure of the system. Very weak interactions were obtained between $\text{K}_2\text{Mo}_6\text{O}_{19}$ and the gold surface under solvation. Incorporation of explicit counterions around the POM, induces great stabilization for the bands of the POM. Additionally, we computed the moderately charged anion $[\text{SiW}_{12}\text{O}_{40}]^{4-}$ on Ag/Au(100), the results being perfectly consistent with experimental evidences and previous calculations using a less expensive procedure.

In summary, the incorporating of explicit counterions and implicit solvent in the calculation provide an efficient strategy for modelling of POM-surface system. This approach involved compensating the charge of the POM by including explicit counterions in the calculations in order to ensure the electroneutrality of the system, and correctly locate the electronic property of the system. The role of the implicit solvent was to stabilize all the ionic species involved in the solid-liquid interface, thus preventing an over-interaction between them. These considerations allowed the correct modelling of the adsorbate and ensured an accurate description of the adsorption itself.

References and Notes

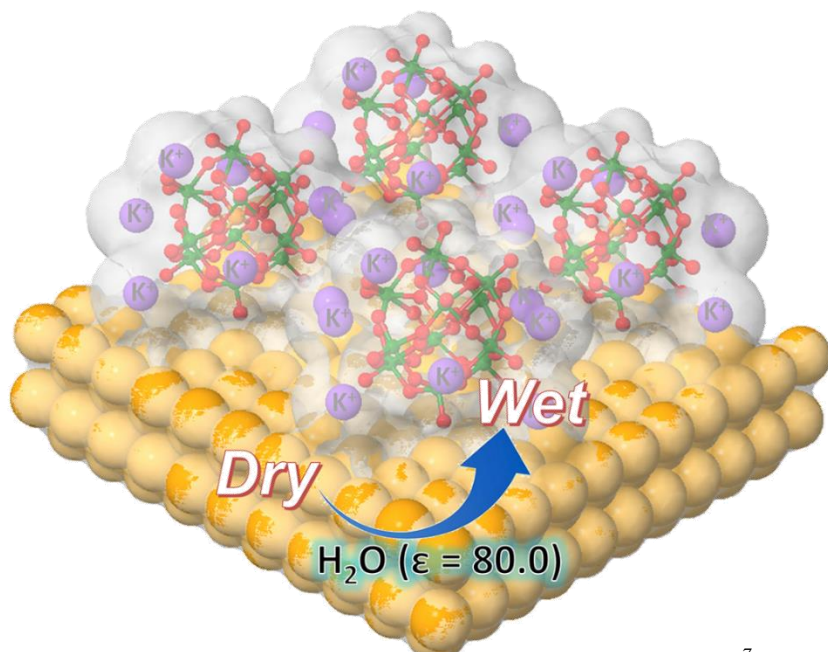
- [1] (a) A. Klamt and G. J. Schüürmann, *Chem. Soc. Perkin Trans. 2*, 1993, 799–805; (b) J. Andzelm, C. Kölmel and A. Klamt, *J. Chem. Phys.* 1995, 103, 9312–9320; (c) A. Klamt, *J. Chem. Phys.* 1995, 99, 2224–2235.
- [2] J. Tomasi, B. Mennucci, and R. Cammi, *Chem. Rev.* 2005, 105, 2999–3094.
- [3] (a) P. Zhang, J. S. Lian and Q. Jiang, *Phys. Chem. Chem. Phys.* 2012, 14, 11715–11723; (b) Z. Zuo, W. Huang and P. Han, *Appl. Surf. Sci.* 2012, 258, 3364–3367; (c) M. Cossi, *Chem. Phys. Lett.* 2004, 384, 179–184; (d) B. Delley, *Mol. Simul.* 2006, 32, 117–123.
- [4] C. L. Hill, *Chem. Rev.* 1998, 98, 1–2.
- [5] X. López, J. J. Carbó, C. Bo and J. M. Poblet, *Chem. Soc. Rev.*, 2012, 41, 7537–7571.
- [6] Y. F. Wang and I. A. Weinstock, *Chem. Soc. Rev.* 2012, 41, 7479–7496.
- [7] C. Rong and F. C. Anson, *Anal. Chem.*, 1994, 66, 3124–3130.
- [8] M. Ge, B. Zhong, W. G. Klemperer and A. A. Gewirth, *J. Am. Chem. Soc.*, 1996, 118, 5812–5813.
- [9] (a) L. Lee, J. X. Wang, R. R. Adzic, I. K. Robinson and A. A. Gewirth, *J. Am. Chem. Soc.*, 2001, 123, 8838–8843; (b) L. Lee and A. A. Gewirth, *J. Electroanal. Chem.*, 2002, 522, 11–20; (c) C. M. Teague, X. Li, M. E. Biggin, L. Lee, J. Kim and A. A. Gewirth, *J. Phys. Chem. B*, 2004, 108, 1974–1985.
- [10] A. Neyman, L. Meshi, L. Zeiri and I. A. Weinstock, *J. Am. Chem. Soc.*, 2008, 130, 16480–16481.
- [11] Y. F. Wang, A. Neyman, E. Arkhangelsky, V. Gitis, L. Meshi and I. A. Weinstock, *J. Am. Chem. Soc.*, 2009, 131, 17412–17422.
- [12] Y. F. Wang, O. Zeiri, S. Sharet and I. A. Weinstock, *Inorg. Chem.*, 2012, 51, 7436–7438.
- [13] S. Sharet, E. Sandars, Y. F. Wang, O. Zeiri, A. Neyman, L. Meshi and I. A. Weinstock, *Dalton Trans.*, 2012, 41, 9849–9851.
- [14] X. Aparicio-Angles, P. Miro, A. Clotet, C. Bo and J. M. Poblet, *Chem. Sci.*, 2012, 3, 2020–2027.
- [15] J. P. Perdew, J. A. Chevary, S. H. Vosko, K. A. Jackson, M. R. Pederson, D. J. Singh and C. Fiolhais, *Phys. Rev. B: Condens. Matter*, 1992, 46, 6671–6687.
- [16] (a) G. Kresse and J. Hafner, *J. Phys. Rev. B: Condens. Matter*, 1993, 47, 558–561; (b) G. Kresse and J. Hafner, *Phys. Rev. B: Condens. Matter*, 1994, 49, 14251–

Chapter 5 Effect of Solvent and Cation on the Lindqvist/Keggin-surface composites

- 14269; (c) G. Kresse and J. Furthmuller, *Comput. Mater. Sci.*, 1996, 6, 15–50; (d) G. Kresse and J. Furthmuller, *Phys. Rev. B: Condens. Matter*, 1996, 54, 11169–11186.
- [17] (a) P. E. Blöchl, *Phys. Rev. B: Condens. Matter*, 1994, 50, 17953–17979; (b) J. Hafner, *J. Comput. Chem.*, 2008, 29, 2044–2078.
- [18] H. J. Monkhorst and J. D. Pack, *Phys. Rev. B: Solid State*, 1976, 13, 5188–5192.
- [19] Bader, R. F. W. *Atom in Molecules. A Quantum Theory*, Oxford University Press, Oxford, 1990.
- [20] G. Henkelman, A. Arnaldsson and H. Jonsson, *Comput. Mater. Sci.*, 2006, 36, 354–360.
- [21] (a) M. Fishman, H. L. Zhuang, K. Mathew, W. Dirschka and R. G. Hennig, *Phys. Rev. B* 2013, 87, 245402-1–245402-7; (b) K. Mathew, R. Sundararaman, K. Letchworth-Weaver, T. A. Arias and R. G. Hennig, *J. Chem. Phys.* 2014, 140, 084106-1–084106-8.
- [22] (a) Gaussian09W, Revision A02; Gaussian, Inc.: Wallingford, CT, 2009. (b) J. Tomasi, B. Mennucci and R. Cammi, *Chem. Rev.*, 2005, 105, 2999–3094.
- [23] M. Garcia-Ratés and N. Lópe, *J. Chem. Theory Comput.* 2016, 12, 1331–1341.
- [24] L. Lee and A. A. Gewirth, *J. Electroanal. Chem.*, 2002, 522, 11–20.

Chapter 6

Counter-intuitive Adsorption of $[\text{PW}_{11}\text{O}_{39}]^{7-}$ on Au(100)



In this chapter, the highly charged polyoxometalates ($[\text{PW}_{11}\text{O}_{39}]^{7-}$) adsorbed on the gold surface were modeled by using periodic DFT, and revealing that the PW_{11} cluster does not preferentially adsorb onto the gold surface via its more nucleophilic mono-defect face, but rather, through less negatively charged terminal oxygen ligands, with an orientation similar to that found for the non-defective Keggin anion $[\text{SiW}_{12}\text{O}_{40}]^{4-}$, inducing by the strong anion-cation interactions. This counter-intuitive result is important in ongoing efforts to understanding and utilizing the properties of polyoxometalate monolayers on gold and other reactive metal surfaces.

6.1 Introduction and background

The role of polyoxometalates in composite materials is not only limited to improving catalytic activities,^[1,2] but also act as stabilizing agents, leading to the formation of organized self-assembled monolayers (SAM).^[3-5] Weinstock *et al.* pointed out that the stability of POM SAMs on metal NPs, observed by Cryo-TEM images,^[6-9] was largely dependent on the nature of the counter-cations, understood to be structurally integrated into the POM-NP composite. Whether the adsorption takes place on a flat surface or on a metal nanoparticle, the interaction between moieties is central to understand the final properties of the material.

A good example of that is the stabilization of gold and silver nanoparticles by means of the defective lacunary anion $[XW_{11}O_{39}]^{n-}$ ($X=P^V, Si^{IV}, Al^{III}$).^[6-9] As depicted in Figure 6.1, the $[XW_{11}O_{39}]^{n-}$ mono-defective (lacunary) POM is formed by removing one single WO^{4+} unit from the complete Keggin structure, thereby resulting in a remarkable increase of the charge. The extra charge is not uniformly distributed and it is slightly concentrated at the defective region or lacuna. Hence, the lacuna is more reactive, and allows the lacunary POM either to act as intermediate species in the transformation of molecular metal oxides,^[10] or its functionalization with more active moieties.^[11]

Using cryo-TEM images, it has provided valuable information about the thickness of the POM interface and the separation between AlW_{11} .^[9] Given the more nucleophilic character of the lacuna, it would be expected that the AlW_{11} was adsorbed *via* this side. Unfortunately, the cryo-TEM images could not confirm or disprove this hypothesis, despite their strong potential in elucidating structural information. Rather, solution-state binding studies suggested that total POM charge, rather than specific binding of the nucleophilic lacunae site, was most important in determining the stabilities of POM monolayers on gold nanoparticles.^[6-9] More detailed understanding of this counter-intuitive result would provide valuable information about the nature of interactions between POMs and surfaces.

The pre-studies of our group have shown that the reduction of $[SiW_{12}O_{40}]^{4-}$ on the Ag surface can be reproduced by combining DFT calculations with MD simulations.^[12] This property can also be reproduced by using an easier and less computational cost way, in which was modelled with the counterions and implicit solvent model taken into account. The initial calculations were performed only for the low charged systems.

Chapter 6 Counter-intuitive Adsorption of $[PW_{11}O_{39}]^{7-}$ on $Au(100)$

Hence, in the current chapter we will utilize this computational strategy for the modelling of highly ionic species on surfaces. Using the PW_{11} as test system, we are intend to discuss about the possible adsorption orientations, electronic properties, and the nature of the interaction between the PW_{11} and the $Au(100)$ surface in both vacuum and solution, thus allows us to determine the main factors that have to be considered in modelling ions on surfaces.

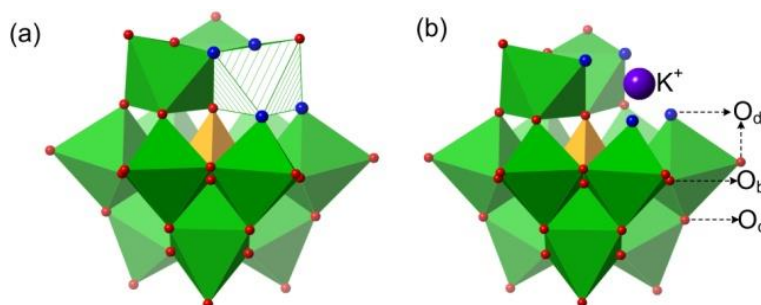


Figure 6.1. Polyhedral-ball representations of (a) a generic Keggin anion $[\alpha-PW_{12}O_{40}]^{3-}$, and (b) its mono-defect (or lacunary) derivatives $[\alpha-PW_{11}O_{39}]^{7-}$ (PW_{11}) with one K^+ filled in the lacuna. Color code: tungsten (green), oxygen (red, and the four oxygen at the lacuna site were labeled as blue), phosphorus (orange), potassium (violet).

6.2 Computational details and models

6.2.1 Computational details

DFT calculations: All first principle calculations were performed using the Vienna *ab-initio* simulation package (VASP5.3), which is based on periodic DFT, using plane waves as a basis set.^[13] Based on our previous work, we set the kinetic energy cut-off at 500 eV, and used the Perdew–Wang 91 functional (PW91) to describe the exchange correlation potential.^[14] Per species, the valence electrons considered were the following: $5d^{10}6s^1$ for Au, $4d^{10}5s^1$ for Ag, $3p^64s^1$ for K, $2s^22p^4$ for O, $3s^23p^3$ for P, and $5d^46s^2$ for W. The interaction between these valence electrons and the corresponding pseudopotential was described using the projector augmented wave (PAW) scheme with scalar relativistic effects.^[15] All the models are relaxed by keeping the bottom three Au layers fixed at their bulk truncated position. All optimizations were performed until self-consistence, with thresholds of $1 \cdot 10^{-5}$ eV and $3 \cdot 10^{-2}$ eV·Å⁻¹ for the electronic and the ionic convergence respectively. The reciprocal space was described using two

Chapter 6 Counter-intuitive Adsorption of $[PW_{11}O_{39}]^{7-}$ on Au(100)

different Monkhorst Pack Schemes^[16]: $3 \times 3 \times 1$ for structure optimizations, and $5 \times 5 \times 1$ for calculating the density of states (DOS). Bader's AIM (Atoms in Molecules) atomic charges^[17] were determined using the Henkelmann algorithm.^[18] Solvent effects were included by means of the implicit solvation model (named VASP sol) implemented by Hennig and co-workers.^[19] In addition, frequency calculations were performed to ensure the stability of each model.

MD simulation: The molecular dynamic simulations were performed for the isolated K_7POM and the adsorbed $K_7POM-Au(100)$ (S_4-K orientation) systems using the DL_POLY classical code in saturated solution.^[20] Starting configurations of both cases were generated by the PACKMOL code,^[21] in which we included the POM, either free or adsorbed on gold from VASP optimization, the water TIP3P model,^[22] and the counterions. For the unadsorbed system, a 7.5 M concentration of K_7POM in water (7087 H_2O molecules) was considered in a 60.48 Å cubic box. On the other hand, 256 water molecules were filled in the adsorbed system to keep a density of $1 \text{ g}\cdot\text{cm}^{-3}$. Long-range Coulombic interactions were evaluated using the Ewald Summation in the reciprocal space describing by a $7 \times 7 \times 21$ scheme and a convergence factor α of 0.323 Å, whereas the short-range interactions were described using the Lennard-Jones potential, previously used for a similar system.^[12b, 23] In addition, the cut-off for electrostatic and Lennard-Jones potential was set to 7.38 Å. For the isolated POM simulation we used the Nosé-Hoover NPT ensemble whereas for the adsorbed system we used the Nosé-Hoover NVT ensemble instead. It should be noted that the gold surface, PW_{11} , and the K^+ were kept frozen during the simulations for the adsorbed model, to reduce the computational cost. The simulations last 3ns and 2ns respectively for the isolated and adsorbed model.

6.2.2 Models

With regard to the average distance between the centers of the neighboring POM anions being $1.57 \pm 0.04 \text{ nm}$ in the experiment,⁷ the gold surface was modeled in a high coverage situation by using the $5 \times 5 \text{ Au}(100)$ slab model, consisting of four gold layers with 25 gold atoms per layer. The calculated lattice parameter for the gold bulk was 4.17 Å, which is in a reasonable agreement with the experimental bulk parameter of 4.07 Å.^[24, 25] Accordingly, the dimensions of the unit cell were 14.76 Å for a and b directions, corresponding to the $P \cdots P$ distance of the neighboring POM anions. The c direction was set at 35.17 Å, considering a vacuum space of more than 15 Å, which was proven to be sufficient to avoid the interactions between the replicated cells. All isolated molecules were calculated in a cubic box of side 25 Å.

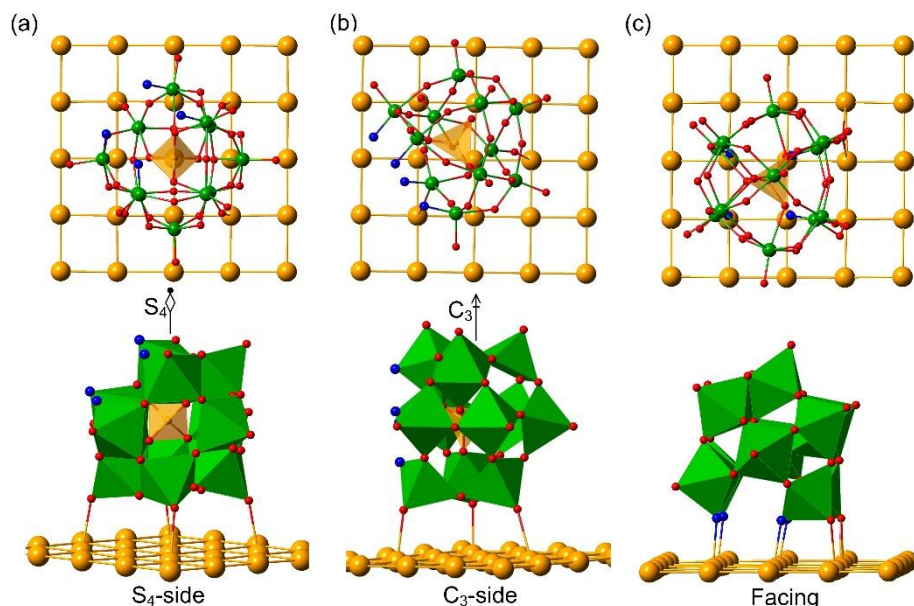
Chapter 6 Counter-intuitive Adsorption of $[PW_{11}O_{39}]^{7-}$ on $Au(100)$ 

Figure 6.2. Ball-stick (top) and polyhedral (bottom) representations of the optimized geometries for PW_{11} deposited on the $Au(100)$ surface via a) the S_4 improper rotation axis, b) C_3 proper rotation axis, and c) with the lacuna facing the surface.

We have considered three different adsorption orientations for PW_{11} : S_4 , C_3 , and lacuna with maximum number of $Au-O_d$ connections and the optimized orientations are depicted in Figure 6.2. Notice that although we use S_4 and C_3 rotational axes for labeling the two adsorption modes, they are formally present in the $[\alpha-PW_{12}O_{40}]^{4-}$ but not in the PW_{11} . In addition, we did not take into account different adsorption sites nor rotations of the POM on the surface because we proved that the main properties of the system are not strongly influenced by these two factors.^[12]

The charge of the POM was compensated using potassium atoms displayed around the POM, and the solvent was modeled using an implicit model with dielectric constant of water as $\epsilon = 80$.^[19] By locating the equal number of K atoms around the POM, the neutral POM is very likely to accept the valence electron of K, thus resulting the K^+ and POM^{7-} . In our study, the vacuum and the implicit solvent situations are symbolized as two extreme situations. The vacuum represents an ideal situation in which the surface, the POM, and the counterions are completely dehydrated, whereas the solvent model represents a situation in which all the species are in contact with the solvent. We designate these extreme situations as “dry” and “wet” surfaces.

6.3 Results and discussions

6.3.1 Cation distribution around the $[PW_{11}O_{39}]^{7-}$ anion

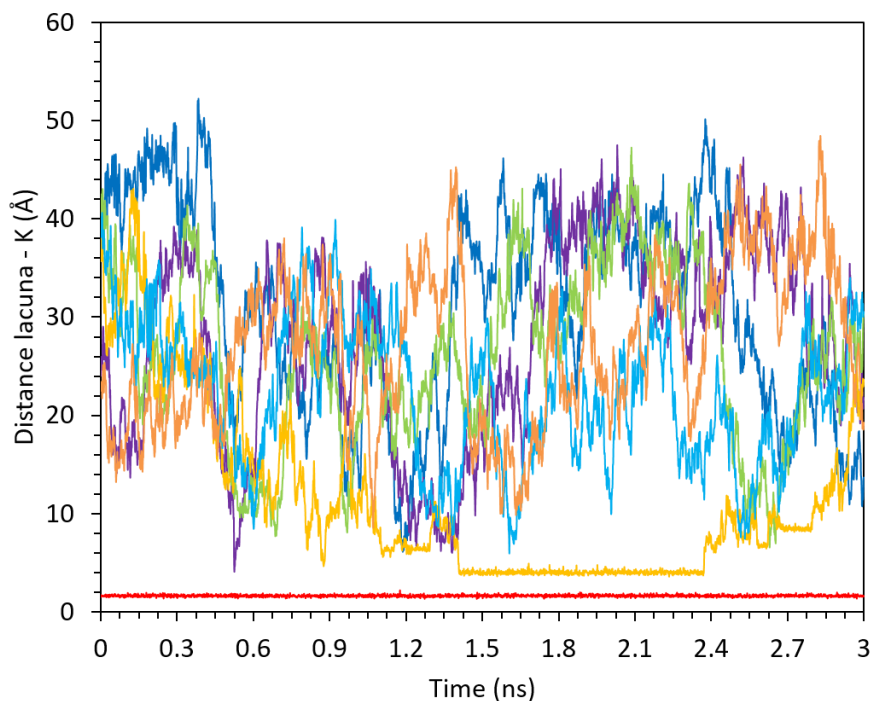


Figure 6.3. Distances between the different counterions and the lacuna during 3ns of production run.

Due to the large amount of cations in the system, the first step is to determine the potential cation distribution around the PW_{11} anion. To that end, we performed molecular dynamic simulations with the POM using the DL_POLY code in a saturated solution. From the MD simulations (Figure 6.3), we observed that in solution the lacuna was always filled with one counterion (red line), which is in fact permanently coordinated to the terminal oxygens of the lacuna, suggesting that it is highly possible that it will remain in that position after adsorption. In addition, after 1.4 ns and for almost 1 ns, a second counterion remains close, but not in, to the lacuna (orange line), at a distance of 4.0 Å approximately. The location of this second cation is in the O_4 quartet next to the lacuna. Unfortunately, the rest of counterions were found between 12.0 and 45.0 Å away from the PW_{11} , which was not close enough to fit the whole

Chapter 6 Counter-intuitive Adsorption of $[PW_{11}O_{39}]^{7-}$ on $Au(100)$

system in the surface unit cell. From these calculations, we can deduce that cations are, on average, at large distances from the POM.

In order to fit the POM and the counterions on the surface unit cell, we screened different potassium distributions around the adsorbate at very short distances using DFT, so ensure that they will be close enough. We optimized seven cation distributions (labeled from **A** to **G**), which differ in the position of the counterions. These positions are: the quartet O_4 , the O_b triads, the O_c triads, and the lacuna, a full description of the cation distributions can be found in Figure S6.1. Optimization was performed in the vacuum and using implicit solvent, and the system's relative energies are collected in Table 6.1.

Table 6.1. Relative energies (in $\text{kcal}\cdot\text{mol}^{-1}$) for the different cation distributions around the POM in vacuum and with implicit solvent.

K distribution	ΔE (vacuum) ^{a)}	ΔE (solution) ^{b)}
A	0.0	0.0
B	23.5	6.2
C	55.8	12.0
D	31.6	5.1
E	68.9	12.0
F	27.0	5.3
G	27.7	9.7

a) System consists of $POM+7K$; b) In solution the solvent is simulated by a continuum model.

In the vacuum, the total energy of the K_7PW_{11} system is highly influenced by the cation distribution, as evidenced by the large range of energies, which is $\sim 69 \text{ kcal}\cdot\text{mol}^{-1}$. The most stable structure, **A**, has one cation at the lacuna, four near the O_4 -site and two near O_{4-1} site. In fact, molecular dynamic simulations already suggested that these two sites would be occupied by cations. The rest of structures were found between 23 and $69 \text{ kcal}\cdot\text{mol}^{-1}$ higher in energy.

However, in solution the range of relative energies is only $12.0 \text{ kcal}\cdot\text{mol}^{-1}$, implying that the energy of the system is less sensitive to the cation distribution. These findings are reasonable, because in solution POM and counterions are surrounded by their

Chapter 6 Counter-intuitive Adsorption of $[PW_{11}O_{39}]^{7-}$ on $Au(100)$

respective solvation spheres, shielding their ionic interaction.^[26-28] Regardless, structure **A** is still the most stable distribution.

We also observe that for those structures lower in energy (**A**, **D**, and **F**), one cation is placed at the lacuna, in agreement with the observations obtained from the molecular dynamic simulations. However, in solution the difference in energy between the structures with a cation and those without a cation on the lacuna is significantly smaller.

6.3.2 Adsorption of $K_7PW_{11}O_{39}$ on the $Au(100)$ surface

Assuming the three adsorption modes represented in Figure 6.2, we have explored the following systems, labeled from 1) to 6) as: 1) S_4-K , 2) S_4 , 3) C_3-K , 4) C_3 , 5) Facing- K , and 6) Facing respectively, where “(mode)- K ” indicates that one K^+ is directly linked to the four terminal oxygens of the lacuna. Additionally, the other K^+ are arbitrarily distributed around the POM. Detailed information of the models is shown in Figure S6.2.

In vacuum, $Au-O_d$ (av) distances were found in a range between 2.52 and 2.61 Å, and slightly larger values, between 2.59 and 2.72 Å, for the solvated surface, as shown in Table 6.2. These distance ranges agreed with the experiments regarding the adsorption of $[AlW_{11}O_{39}]^{9-}$ on gold NPs, in which that range was set to be between 2.5 and 3.0 Å.^[7, 9] The only exception was for the Facing- K (system 5 in Table 6.2), which showed an average distance of 3.67 Å, more than 1 Å longer than the other structures. In this case, however, this enlargement is a consequence of the K^+ placed at the lacuna.

The $K-O$ distances enlarged when the solvent was included in the calculations, from 2.69-2.77 Å to 2.92-2.97 Å. This increase is a consequence of the stabilization that the solvent exerts onto the PW_{11} anion and the counterions. Finally, the $W-O_d$ distances, referring to those O_d that are closest to the surface, showed almost no change with respect to the non-adsorbed PW_{11} (1.75 Å), evidencing the poor affinity that POMs and gold surfaces have, in contrast to silver surfaces.^[12]

As we observed for the non-adsorbed PW_{11} , the more stable systems in vacuum are those that have the lacuna filled with one K^+ , all found in a range of 3.2 kcal·mol⁻¹, regardless of their adsorption orientation (Table 6.3 and Figure 6.4). On the other hand, those structures that do not have a K^+ at the lacuna are found between 6.0 and 30.2 kcal·mol⁻¹ with respect to the most stable system. Interestingly the most unstable system is the *Facing* with no K^+ . This is also counterintuitive, as anionic protecting ligands might be assumed to directly interact with the gold surface via their most negatively charged regions, as shown by the molecular electrostatic potential

Chapter 6 Counter-intuitive Adsorption of $[PW_{11}O_{39}]^{7-}$ on $Au(100)$

representation of the free anion in Figure S6.3. According to these results, however, the key factor in stabilizing the system in vacuum is the presence of the counterion in the lacuna and not the adsorption orientation. Notably, this is supported by experimental data by Weinstock, who showed that POM charge, rather than structure (*i.e.*, the presence or absence of a lacunary site) controls the thermodynamics of POM-monolayer assembly on Au NPs.^[6-9] Along the same lines, Finke has shown that the complete Nb substituted Wells-Dawson anion, $[P_2W_{15}Nb_3O_{62}]^9$, is more effective for the formation and stabilization of Ir(0) NPs, than the lacunary anion $\{H[\alpha_2-P_2W_{17}O_{61}]\}^9$ with the equal charge.^[29] In other words, the presence of lacunary site in the POM framework appears to produce no special effect on the stabilization of Ir(0) NPs.

Table 6.2 Selected distances (in Å) for different POM adsorption orientations (1 to 6) on “dry” (Vac.) and “wet” (Sol.) surface. ^{a)}

Sites	Phase	Au–O _d	Au–O _d (av)	K–O (av)	W–O _d (av)
(1) S ₄ –K	Vac.	2.58-2.67	2.61	2.69	1.74
	Sol.	2.68-2.81	2.72	2.92	1.75
(2) S ₄	Vac.	2.53-2.69	2.60	2.77	1.75
	Sol.	2.56-2.71	2.62	2.97	1.75
(3) C ₃ –K	Vac.	2.37-2.75	2.59	2.74	1.75
	Sol.	2.50-2.70	2.60	2.92	1.75
(4) C ₃	Vac.	2.29-2.75	2.59	2.74	1.77
	Sol.	2.32-2.91	2.67	2.97	1.75
(5) Facing– K	Vac.	3.36-3.94	3.67	2.75	1.79
	Sol.	3.66-3.96	3.80	2.92	1.77
(6) Facing	Vac.	2.42-2.69	2.52	2.74	1.76
	Sol.	2.44-2.88	2.59	2.93	1.76

- a) Au–O_d (O_{d(av)}) is the distance (average) between those O_d and the contact Au atoms. The K–O_(av) is the average distance between K⁺ and the nearby oxygen (less than 3.5 Å). As well, W–O_{d(av)} refers to those O_d in contact with the surface.

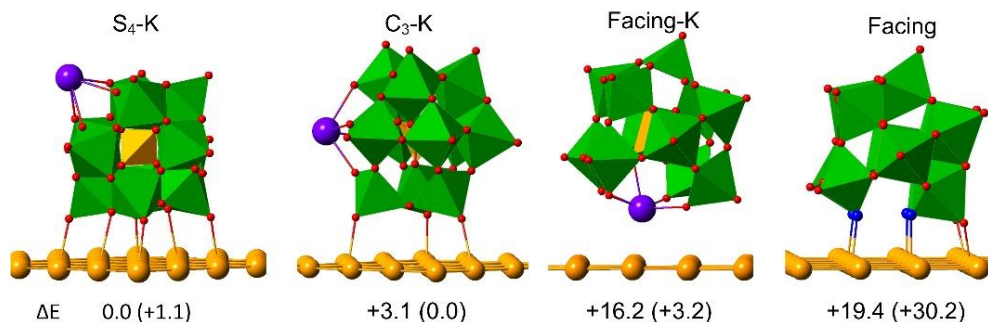
Chapter 6 Counter-intuitive Adsorption of $[PW_{11}O_{39}]^{7-}$ on $Au(100)$ 

Figure 6.4. 3D representations and relative energies (in $\text{kcal}\cdot\text{mol}^{-1}$) for some selected structures. Values in parenthesis are relative energies computed in vacuum, see text.

In solution, results are somewhat different because now the difference in energy between having the lacuna filled or not is very small, although the former is still more stable than the latter. When the implicit solvent is included, the S_4 orientation with the K^+ fully exposed to the solvent (Figure 6.4) becomes the most stabilized form. The C_3 form is slightly higher in energy because the cation is in less contact with the solvent, especially if we are dealing with a high coverage situation, and finally, the facing-K form is quite high in energy ($+16.2 \text{ kcal}\cdot\text{mol}^{-1}$) because the cation in no way can interact with the solvent. This means that on gold surface the lacunary anions will try to have the cations in contact with the solvent and as a general behavior the linkage with the surface will be similar to that of the complete anions.

Table 6.3. Relative energies (ΔE) between different adsorbed systems and adsorption energies (E_{ads} and E'_{ads}) for the PW_{11} adsorbed on $Au(100)$.

Adsorption Type	Vacuum			Solution		
	ΔE	E_{ads}	E'_{ads}	ΔE	E_{ads}	E'_{ads}
(1) S_4 -K	1.2	0.5	-16.8	0.0	-2.5	-5.1
(2) S_4	11.3	10.4	-19.4	4.6	2.3	-4.6
(3) C_3 -K	0.0	-0.7	-13.4	3.1	0.6	-2.2
(4) C_3	6.0	5.3	-18.0	6.7	4.2	-2.8
(5) Facing-K	3.2	2.5	-21.9	16.1	13.8	8.8
(6) Facing	30.2	29.3	-28.1	19.4	16.8	6.2

a) All values are in $\text{kcal}\cdot\text{mol}^{-1}$.

Chapter 6 Counter-intuitive Adsorption of $[PW_{11}O_{39}]^{7-}$ on $Au(100)$ **6.3.3 Affinity of Au(100) for PW_{11}**

The relative energies discussed above allow us to determine rather well the different adsorption modes on gold surfaces. However, it is more difficult to have a *quantitative* measure of the interaction between the POM and the surface. To analyze how strong the POM is attached to the gold surface, we have used two adsorption energies: E_{ads} and E'_{ads} . The former is the traditional adsorption energy, which is defined by eq. 6.1,

$$E_{ads} = E_{tot} - E_{surf} - E_{KPOM} \quad (6.1)$$

where E_{tot} is the energy of the whole system, E_{surf} is the energy of the clean surface, and E_{KPOM} is the energy of the POM surrounded by the counterions in its optimal distribution (model A in Table 6.1). On the other hand, E'_{ads} (eq. 6.2) differs from E_{ads} in the term E_{KPOM} .

$$E'_{ads} = E_{tot} - E_{surf} - E'_{KPOM} \quad (6.2)$$

To determine E'_{ads} , the term E'_{KPOM} is computed considering the cation distribution of the POM when it is adsorbed. Hence, E'_{ads} can be understood as the minimum energy that is required to detach the POM from the gold surface.

Therefore, in vacuum, the surface represents a situation in which no water is present and the stabilization of the POM over-relies on both surface and cations. On the other hand, under the continuum solvent environment, the surface represents a fully hydrated situation that not only involves a potential over stabilization of the POM due to the inclusion of the implicit solvent, but also because it assumes that all the cations will be surrounding the adsorbate. In conclusion, these energies should not be taken as a quantitative reference but as a qualitative value.

Hence, E'_{ads} reflects a very exothermic adsorption in vacuum, between -17.0 and -30.0 kcal·mol⁻¹, although these values increase if we consider E_{ads} instead. This is because the cation's position has a strong influence in the energy of the whole system. Therefore, if we take as a reference a cation distribution that it is not the most stable, it will result in a lower adsorption energy, as shown in Table 6.3. In addition, the very exothermic values are an evidence of the over stabilizing role that the surface and the cations have on the “dry” surface.

Under “wet” condition, the situation is completely different. The E'_{ads} are now closer to 0 kcal·mol⁻¹, with the lowest energy being of only -5.1 kcal·mol⁻¹ for the S₄-K. Indeed, this structure is the only one that shows exothermic E_{ads} (-2.5 kcal·mol⁻¹) whereas the rest of the adsorption modes owned very small but positive values. Thus, when the solvent is included, the polyoxometalate and the gold surface show a very

Chapter 6 Counter-intuitive Adsorption of $[PW_{11}O_{39}]^{7-}$ on Au(100)

weak interaction, which is consistent with the experimental evidence that polyoxoanions like the $[SiW_{12}O_{40}]^{4-}$ spontaneously desorbs from the Au(111) surface after rinsing,^[30] and are comparable to other oxo-systems adsorbed on gold as well, like the $AsMo_{11}VO_{40}^{4-}$, which has an estimated free energy of adsorption of -4.8 kcal·mol⁻¹,^[31] or the organomercaptan with an adsorption energy of approximately -12 kcal·mol⁻¹ from water onto gold.^[32, 33]

We have also evaluated the *vdW* effects for the adsorption energies of S₄-K model in solution by using default VASP *vdW* parameters (methods DFT-D3, DFT-D2 and, vdW-DF have been tried). However, these calculations revealed that when *vdW* corrections were included, in combination with the implicit solvent model, the POM's adsorption energies (E_{ads}) were larger than 47 kcal·mol⁻¹ for S₄-K model, which represents 10 times more. In our calculations, and without including the *vdW* correction, the adsorption energies (E_{ads}) that we obtained fall within the expected range of 5 kcal·mol⁻¹ from one analogous work of Dong et al.,^[31] which is an indication that to our particular system *vdW* may not be necessary. The very negative adsorption energies obtained in our test may be caused by the unreasonable default parameters for W⁶⁺ and O²⁻. Sauer *et al.* in the analysis of the interaction between CH₄ and MgO(100) proved that it is necessary to find specific *vdW* parameters for Mg²⁺ and O²⁻ ions, since the default *vdW* values provided by VASP are based on the neutral atoms and not the ionic species. To determine the specific *vdW* values it is necessary to calculate accurate ionization potentials and to estimate the cation/anion polarizability according to its environment.^[34]

6.3.4 The origin of the counter-intuitive adsorption

To improve our understanding of the reasons that explain the orientation of the POM on metal surface, we have analysed the variation in the charge density upon adsorption for S₄-K and Facing systems in solution, by subtracting the electronic charge of a K₇PW₁₁O₃₉/Au(100) system from its components K₇PW₁₁O₃₉ and Au(100). As expected, adsorption of the POM induces a positive image charge in the gold region in contact with the adsorbed anion, fact that is manifested by an electron density reduction in Figure 6.5. In the representation of charge density differences we have used very low isovalues in order to visualize better the small electron density reorganization induced by the adsorption of POMs on gold surfaces. Similar effects are observed in the gold atoms near counterions, but that regions show charge accumulations because of the positive charge of the cations. However, no electron accumulations are observed in the bonding Au-O region, discarding any covalent

Chapter 6 Counter-intuitive Adsorption of $[PW_{11}O_{39}]^{7-}$ on $Au(100)$

interaction between gold surface and POM for any of the orientations of the anion, the main interaction being of electrostatic nature. A smaller electron deficit exists in S₄-K, leading to an electrostatic attraction weaker than that in Facing.

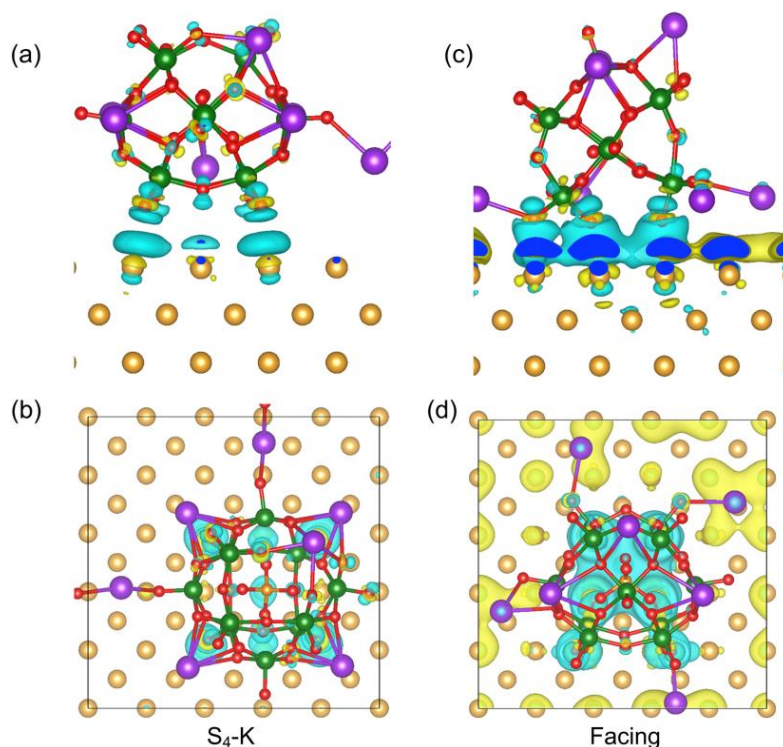


Figure 6.5. Three-dimensional charge density difference for S₄-K (a, b), and Facing (c, d) systems with views from side and top, respectively, $\rho_{diff}(r) = \rho_{K7POM/Au(100)}(r) - \rho_{K7POM}(r) - \rho_{Au(100)}(r)$. The yellow region represents charge accumulations (electron density increase), and the cyan regions indicates charge depletion (electron density decrease). The isovalue is set to 0.001 e/Bohr³ in Vesta code.^[35] And the maximum to minimum charge difference in S₄-K is -0.013~0.005 e/Bohr³ and -0.025~0.011 e/Bohr³ for Facing.

However, it is important to remark that anion-cation interactions are very relevant in the adsorption process, which has previously been revealed.^[8] Furthermore, with respect to the stabilization generated when a K⁺ occupies the defect site in S₄-K, additional interactions between K⁺ ions neighbouring units are very important, in particular four K⁺ strongly interact at the same time with two anions as shown in Figure S6.4. In this context, we have verified that the relative stability of S₄-K and Facing adsorptions decreases from 19.4 up to 5.3 kcal·mol⁻¹ when the calculations are performed in solution with two POMs separated enough to avoid the interactions of

Chapter 6 Counter-intuitive Adsorption of $[PW_{11}O_{39}]^{7-}$ on $Au(100)$

POM \cdots K \cdots POM type. In the low coverage situation, the P \cdots P distance between two neighboring POMs is about 23.6 Å, whereas for the high coverage representation that value is only 14.8 Å. Therefore, the strong cation–anion interactions, especially the donation from the defect site, bring more stability than the electrostatic interactions do, leading to the S4–K orientation being more favorable than the Facing orientation.

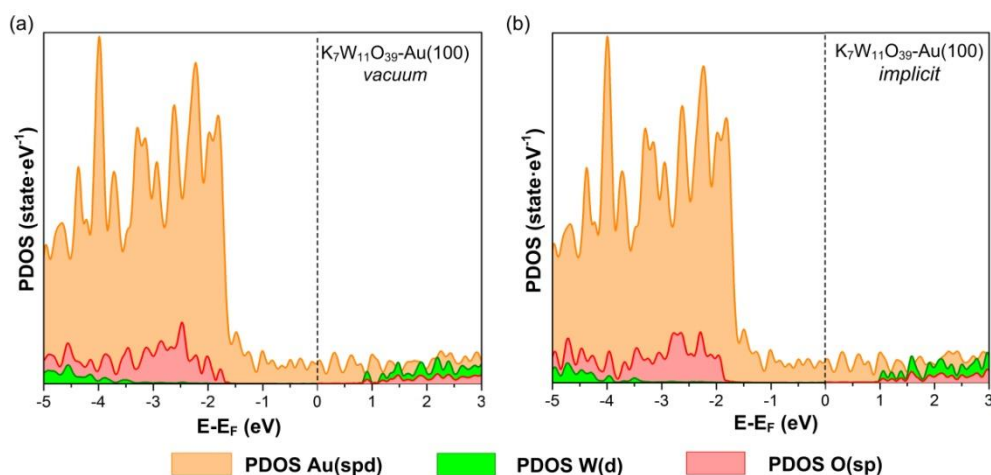


Figure 6.6. Projected density of states for system S₄-K in a) vacuum, and b) solvent. Similar results are obtained for C₃-K and Facing models in Figure S6.5.

6.3.5 Electronic structure

The electronic structure of the adsorbed POM in S₄-K is depicted in Figure 6.6 by means of the projected density of states (PDOS). In this representation, we have referred the energy range to the energy of the Fermi level (E_F). Consequently, all bands found below 0 represent occupied orbitals whereas bands with positive energy mean virtual orbitals.

The results obtained in vacuum and with implicit solvent are mainly the same. Electronic conduction undergoes through the gold surface in both cases, since this is the only contribution observed at the E_F (0 eV). Therefore, the POM does not play any role in the electronic conduction when it is adsorbed on gold. The only slightly difference between both situations is that the POM's conduction band, *i.e.* the front of the W(d) band, is found at 0.8 eV in the vacuum and at 1.0 eV in solution. This difference can be attributed to the stronger interaction between K and POM that exists in the vacuum that leads to an insignificant over-stabilization of these bands. Anyway, since the W(d) bands are not below the E_F , no charge transfer between surface and

Chapter 6 Counter-intuitive Adsorption of $[PW_{11}O_{39}]^{7-}$ on $Au(100)$

POM can occur. These results are in line with the calculated Bader charges listed in Table 6.4. The charge of the POM is -6.2 and $-6.5 e$ for the vacuum and solvent respectively. This charge is supplied by the counterions, as their total charge is 6.2 and $6.6 e$ respectively. Another common feature is the high polarization of the surface, as all layers are charged. Although this would indicate that more layers should be considered in our system, the surface polarization does not alter the main properties of the adsorbed POM. It should be noted that this polarization was also found for the free gold slab.

Table 6.4. Bader charges for the $K_7PW_{11}O_{39}$ adsorbed on $Au(100)$ and $Ag(100)$. $M(1)$ is the metal layer which closest to the PW_{11} ($M = Au$ or Ag).

Species	Phase	Anion	ΣK^+	ΣM	M(1)	M(2)	M(3)	M(4)
$K_7PW_{11}O_{39}$	vac.	-6.27	6.27					
	sol.	-6.53	6.53					
$K_7PW_{11}-Au$	vac.	-6.20	6.24	-0.04	-1.01	1.04	0.96	-1.04
	sol.	-6.47	6.64	-0.17	-0.81	0.94	0.86	-1.17
$K_7PW_{11}-Ag$	vac.	-6.52	6.23	0.29	-0.22	0.44	0.62	-0.56
	sol.	-6.53	6.63	-0.04	-0.31	0.45	0.61	-0.79

6.3.6 The effect of explicit water for the electronic properties

In order to consider the effects of explicit water on the electronic structure, we performed the optimization for S_4-K site by including the first solvation sphere, which was selected from a snapshot of a 2ns molecular dynamics simulation. In addition to the gold surface and the polyoxoanion, totally 46 water molecules and 7 K^+ are involved in the unit. As seen in Figure 6.7b, the electronic structure of gold is almost not affected by the presence of explicit waters, and the position of $W(d)$ and $O(sp)$ bands show only $0.27 eV$ stabilization with respect to that in implicit solvent. Furthermore, the band gap between $W(d)$ and $O(sp)$ is well reproduced by introducing the implicit solvent (2.61 versus $2.65 eV$ in explicit water). It is worth mentioning that the calculations using explicit waters are much more computationally demanding, and that in this context to locate the overall energy minimum is very complicate because of the large number of local minima. Thus, the implicit solvent approach provides a much easier way to include the solvent effects in this type of studies.

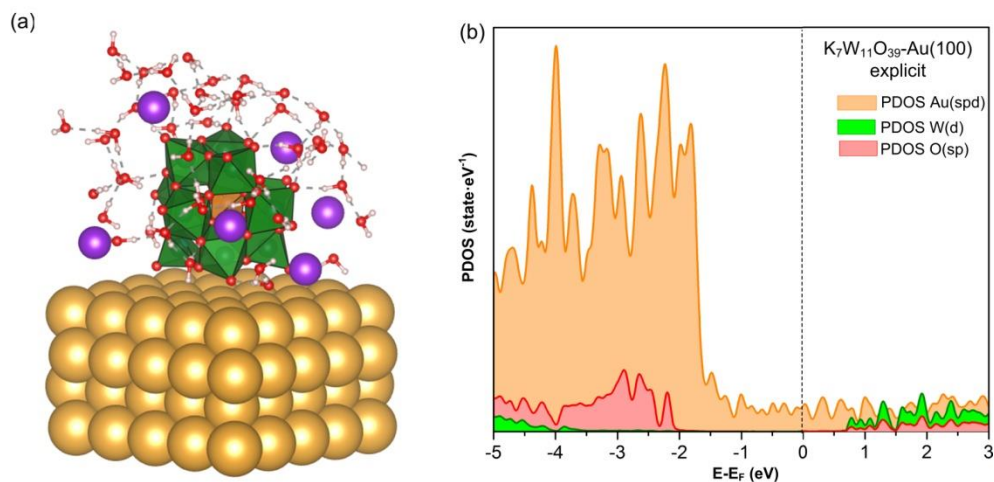
Chapter 6 Counter-intuitive Adsorption of $[PW_{11}O_{39}]^{7-}$ on Au(100)

Figure 6.7. (a) Polyhedral and balls and stick representation of the selected model for electronic structure calculations, with 46 explicit water surrounding the POM; (b) Projected density of states for system S_4 -K in explicit environment.

6.3.7 The modeling of $[PW_{11}O_{39}]^{7-}$ on silver

Finally, we have also analyzed the effect of the surface nature by performing the adsorption of $[PW_{11}O_{39}]^{7-}$ on Ag(100) surface in both vacuum and solution. Notice that for the silver surface we have used the gold surface unit cell, adjusting the cell parameter to $a = 14.67\text{\AA}$, accordingly to our previously calculated bulk parameter for silver.^[24, 25] The adsorption mode for PW_{11} on Ag(100) is focused only on the S_4 orientation as discussed above.

Firstly, E'_{ads} shows the same trend we previously observed regarding to the magnitude of the adsorption energy when we consider the surface in vacuum and solution (Table 6.4). It is worth noting once again, that this difference arises from the over-stabilization role of the surface in the absence of the solvent. For the PW_{11} and considering in vacuum, E'_{ads} is $5.6\text{ kcal}\cdot\text{mol}^{-1}$ more stable for silver than for gold (-22.4 vs. $-16.8\text{ kcal}\cdot\text{mol}^{-1}$). With the solvent mediated, the adsorption energy is practically the same, $-5.1\text{ kcal}\cdot\text{mol}^{-1}$ for Au(100) and $-5.8\text{ kcal}\cdot\text{mol}^{-1}$ for Ag(100). However, this is much weaker than the adsorption of $[\text{SiW}_{12}\text{O}_{40}]^{4-}$ on Ag(100) ($-11.1\text{ kcal}\cdot\text{mol}^{-1}$) as discussed in chapter 5. The density of states (Figure 6.8) and Bader charge analysis (Table 6.4) for this system suggest that there is no charge transfer between surface and POM regardless of the metal, which could explain why the adsorption energies are very similar for $[PW_{11}O_{39}]^{7-}$ on Ag(100) and Au(100), and also smaller than that $[\text{SiW}_{12}\text{O}_{40}]^{4-}$ on Ag(100).

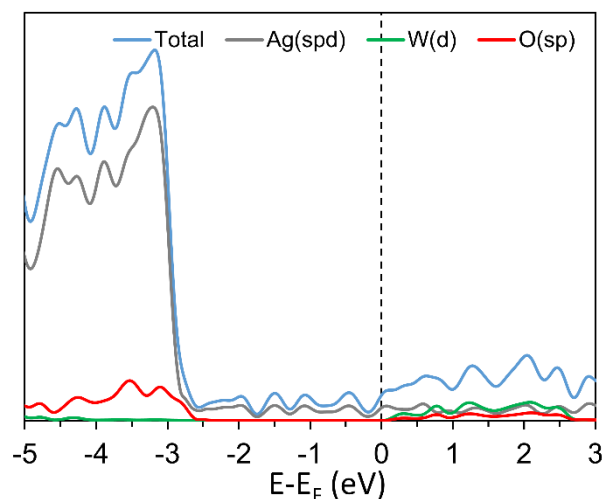
Chapter 6 Counter-intuitive Adsorption of $[PW_{11}O_{39}]^{7-}$ on $Au(100)$ 

Figure 6.8. Density of States and projected Density of States for K_7PW_{11} adsorbed on $Ag(100)$ in solution.

6.4 Conclusions

In chapter 5, we have presented a general strategy based on periodic density functional theory and an implicit solvent model to study the adsorption of low charged species on surfaces. To that end, we investigated the adsorption orientation of highly charged $[PW_{11}O_{39}]^{7-}$ anion on $Au(100)/Ag(100)$ by using such strategy.

In this particular case, the adsorption of $[PW_{11}O_{39}]^{7-}$ on $Au(100)$, our calculations have revealed that unexpectedly, the POM does not adsorb through the lacuna, which is its more nucleophilic region, but it adsorbs on the surface in a similar fashion with respect to the atomic connectivity as the non-defective $[SiW_{12}O_{40}]^{4-}$ anion on silver surfaces, supporting the critical role of cation-anion interactions in stabilizing the PW_{11} -monolayer. $Au(100)$ and $Ag(100)$ show similar affinity for the adsorption of $[PW_{11}O_{39}]^{7-}$, no electron transfer was detected between PW_{11} and surfaces, and no spontaneous reduction occurred on the POM.

Additionally, although the lacuna position is always filled with a counterion, the positions of the rest of the counterions around the POM do not influence the properties of the system. Notably, these findings are in agreement with the available experimental data. Therefore, by using a highly charged system to test our model, we have demonstrated the efficiency and the robustness of our approach, which will be very helpful for the modelling of similar systems, as well as for the study of catalysis and electrocatalysis involving ionic species.

References and Notes

- [1] (a) K. P. Hsu-Yao Browne, N. Honesty and Y. J. Tong, *Phys. Chem. Chem. Phys.* 2011, 13, 7433–7438. (b) S. Li, X. Yu, G. Zhang, Y. Ma, J. Yao, B. Keita, N. Louis and H. Zhao, *J. Mater. Chem.* 2011, 21, 2282–2287; (c) A. Corma, S. Iborra, F. X. Llabrés i Xamena, R. Montón, J. J. Calvino and C. Prestipino, *J. Phys. Chem. C* 2010, 114, 8828–8836.
- [2] M. F. Zhang, J. C. Hao, A. Neyman, Y. F. Wang and I. A. Weinstock, *Inorg. Chem.* 2017, 56, 2400–2408.
- [3] Y. F. Wang and I. A. Weinstock, *Chem. Soc. Rev.* 2012, 41, 7479–7496.
- [4] B. Keita, T. B. Liu and L. Nadjo, *J. Mater. Chem.* 2009, 19, 19–33.
- [5] S. G. Mitchell and J. M. de la Fuente, *J. Mater. Chem.* 2012, 22, 18091–18100.
- [6] A. Neyman, L. Meshi, L. Zeiri and I. A. Weinstock, *J. Am. Chem. Soc.* 2008, 130, 16480–16481.
- [7] Y. F. Wang, A. Neyman, E. Arkhangelsky, V. Gitis, L. Meshi and I. A. Weinstock, *J. Am. Chem. Soc.* 2009, 131, 17412–17422.
- [8] Y. F. Wang, O. Zeiri, S. Sharef and I. A. Weinstock, *Inorg. Chem.* 2012, 51, 7436–7438.
- [9] S. Sharef, E. Sandars, Y. F. Wang, O. Zeiri, A. Neyman, L. Meshi and I. A. Weinstock, *Dalton. Trans.* 2012, 41, 9849–9851.
- [10] J. M. Cameron, L. Vila-Nadal, R. S. Winter, F. Iijima, J. C. Murillo, A. Rodríguez-Forteza, H. Oshio, J. M. Poblet and L. Cronin, *J. Am. Chem. Soc.* 2016, 138, 8765–8773.
- [11] A. Proust, B. Matt, R. Villanneau, G. Guillemot, P. Gouzerh and G. Izzet, *Chem. Soc. Rev.* 2012, 41, 7605–7622.
- [12] (a) X. Aparicio-Angles, A. Clotet, C. Bo and J. M. Poblet, *Phys. Chem. Chem. Phys.* 2011, 13, 15143–15147; (b) X. Aparicio-Angles, P. Miro, A. Clotet, C. Bo and J. M. Poblet, *Chem. Sci.* 2012, 3, 2020–2027.
- [13] (a) G. Kresse and J. Hafner, *J. Phys. Rev. B: Condens. Matter* 1993, 47, 558–561; (b) G. Kresse and J. Hafner, *Phys. Rev. B: Condens. Matter* 1994, 49, 14251–14269; (c) G. Kresse and J. Furthmuller, *Comput. Mater. Sci.* 1996, 6, 15–50; (d) G. Kresse and J. Furthmuller, *Phys. Rev. B: Condens. Matter* 1996, 54, 11169–11186.
- [14] J. P. Perdew, J. A. Chevary, S. H. Vosko, K. A. Jackson, M. R. Pederson, D. J. Singh and C. Fiolhais, *Phys. Rev. B: Condens Matter*, 1992, 46, 6671–6687.

Chapter 6 Counter-intuitive Adsorption of $[PW_{11}O_{39}]^{7-}$ on $Au(100)$

- [15] (a) P. E. Blöchl, *Phys. Rev. B: Condens. Matter* 1994, 50, 17953–17979; (b) J. Hafner, *J. Comput. Chem.* 2008, 29, 2044–2078.
- [16] H. J. Monkhorst and J. D. Pack, *Phys. Rev. B: Solid State* 1976, 13, 5188–5192.
- [17] R. F. W. Bader, *W. Atom in Molecules. A Quantum Theory*, Oxford University Press, Oxford, 1990.
- [18] G. Henkelman, A. Arnaldsson and H. Jonsson, *Comput. Mater. Sci.* 2006, 36, 354–360.
- [19] (a) M. Fishman, H. L. Zhuang, K. Mathew, W. Dirschka and R. G. Hennig, *Phys. Rev. B* 2013, 87, 245402-1–245402-7; (b) K. Mathew, R. Sundararaman, K. Letchworth-Weaver, T. A. Arias and R. G. Hennig, *J. Chem. Phys.* 2014, 140, 084106-1–084106-8.
- [20] W. Smith and T. R. Forester, *J. Mol. Graphics Modell.* 1996, 14, 136–141.
- [21] L. Martinez, R. Andrade, E. G. Birgin and J. M. Martinez, *J. Comput. Chem.*, 2009, 30, 2157–2164.
- [22] W. Jorgensen, *J. Chem. Phys.*, 1983, 79, 926–935.
- [23] (a) X. Lopez, C. Nieto-Draghi, C. Bo, J. B. Avalos and J. M. Poblet, *J. Phys. Chem. A* 2005, 109, 1216–1222; (b) F. Leroy, P. Miro, J. M. Poblet, C. Bo, J. B. Avalos, *J. Phys. Chem. B* 2008, 112, 8591–8599; (c) H. Heinz, R. A. Vaia, B. L. Farmer, R. R. Naik, *J. Phys. Chem. C* 2008, 112, 17281–17290.
- [24] S. Elliot, *Physics of Amorphous Materials*, 2nd revised edition ed., 1990.
- [25] J. R. Hook, H. E. Hall, *Solid State Physics*, 2nd Edition ed., Wiley, 1995.
- [26] P. Miró, J. M. Poblet, J. B. Ávalos and C. Bo, *Can. J. Chem.* 2009, 1296–1301.
- [27] R. E. Schreiber, L. Houben, S. G. Wolf, G. Leitus, Z. L. Lang, J. J. Carbó, J. M. Poblet and R. Neumann, *Nat. Chem.* 2017, 9, 369–373.
- [28] A. Solé-Daura, V. Goovaerts, K. Stroobants, G. Absillis, P. Jiménez-Lozano, J. M. Poblet, J. D. Hirst, T. N. Parac-Vogt and J. J. Carbó, *Chem. Eur. J.* 2016, 22, 15280–15289.
- [29] C. R. Graham, L. S. Ott and R. G. Finke, *Langmuir* 2009, 25, 1327–1336.
- [30] L. Lee and A. A. Gewirth, *J. Electroanal. Chem.* 2002, 522, 11–20.
- [31] Z. Y. Tang, S. Q. Liu, E. K. Wang and S. J. Dong, *Langmuir*, 2000, 16, 4946–4952.
- [32] J. S. Kirk and P. W. Bohn, *J. Am. Chem. Soc.* 2004, 126, 5920–5926.
- [33] H. M. Schessler, D. S. Karpovich and G. J. Blanchard, *J. Am. Chem. Soc.* 1996, 118, 9645–9651.
- [34] J. Sauer, T. Sergio, *Phys. Chem. Chem. Phys.* 2010, 12, 14330–14340.

Chapter 6 Counter-intuitive Adsorption of $[PW_{11}O_{39}]^{7-}$ on Au(100)

[35] K. Momma and F. Izumi. J. Appl. Cryst. 2008, 41, 653–658.

Chapter 6 Counter-intuitive Adsorption of $[PW_{11}O_{39}]^{7-}$ on $Au(100)$

Appendix Chapter 6

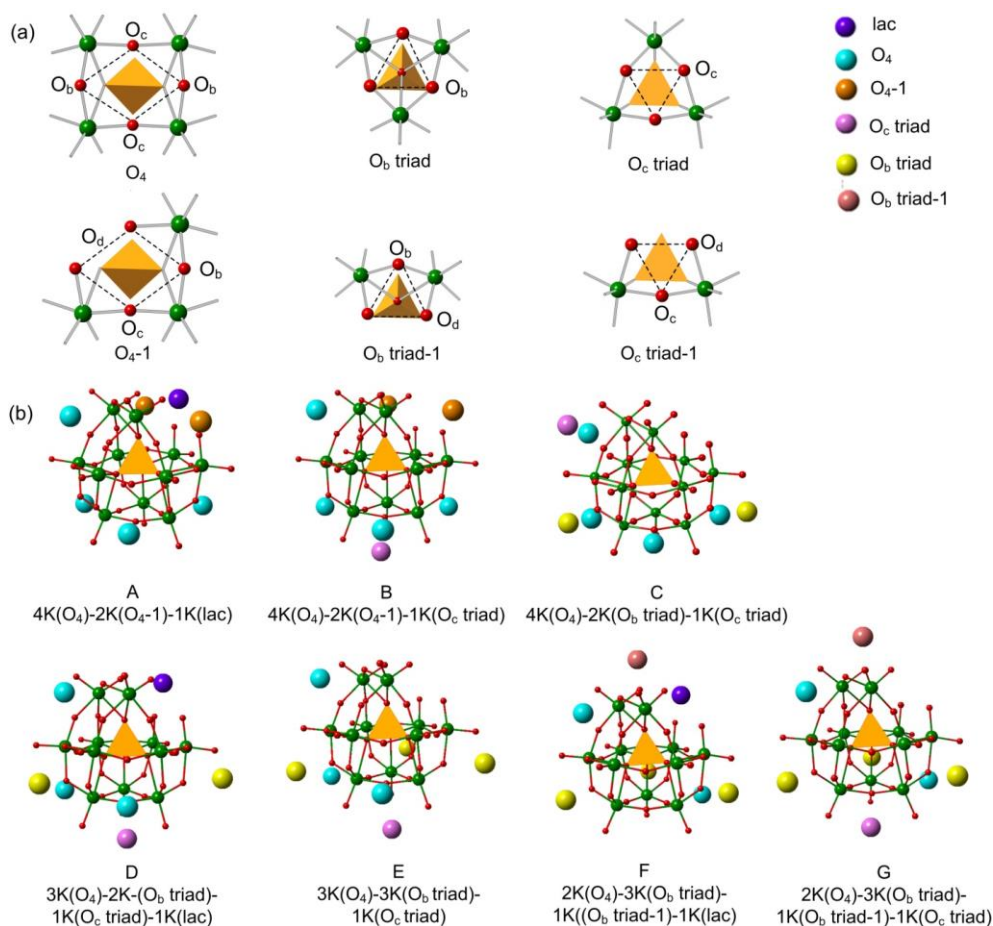


Figure S6.1. Ball-and-stick plus polyhedral representation for the seven cation distributions around the $[PW_{11}O_{39}]^{7-}$ that were considered in this work, labeled from A to G for simplification. Color legend: red for O, green for W, yellow polyhedral for P, and for K atoms at different position are labeled as different colors as seen from the Figure.

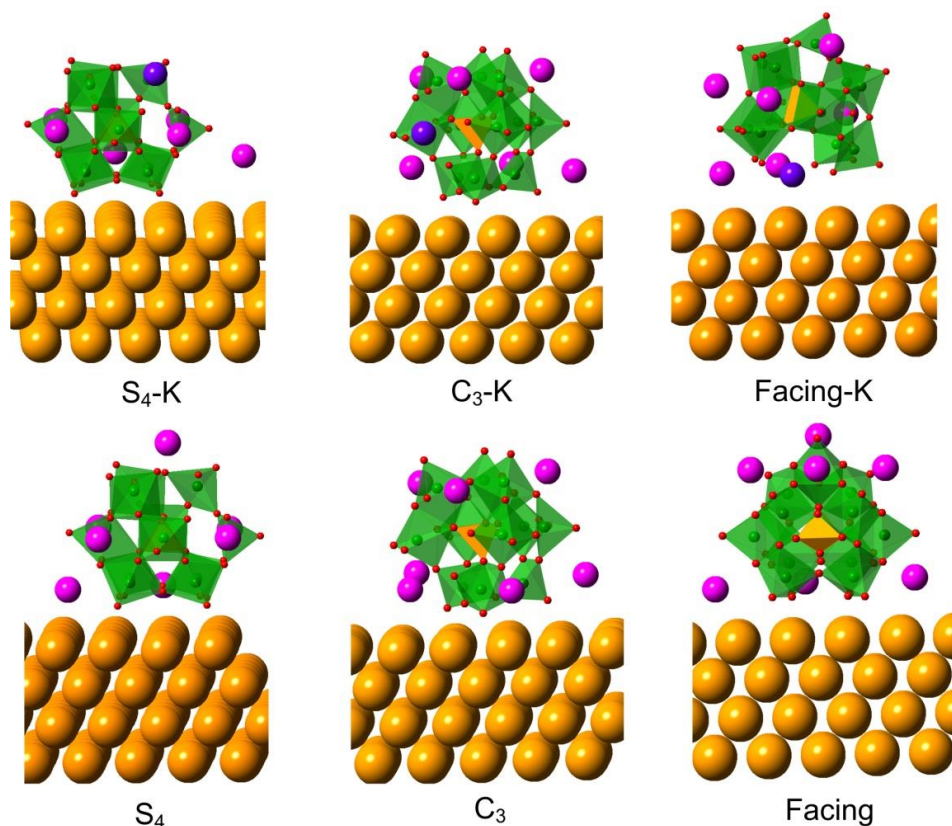
Chapter 6 Counter-intuitive Adsorption of $[PW_{11}O_{39}]^{7-}$ on $Au(100)$ 

Figure S6.2. Ball and polyhedral representation for the adsorbed models, labeled as S_4 -K, S_4 , C_3 -K, C_3 , Facing-K, and Facing respectively. $-K$ represents that one K is directly linked to the four terminal oxygens of the lacuna, which is labeled as color of violet, while those K atoms in other positions are pink.

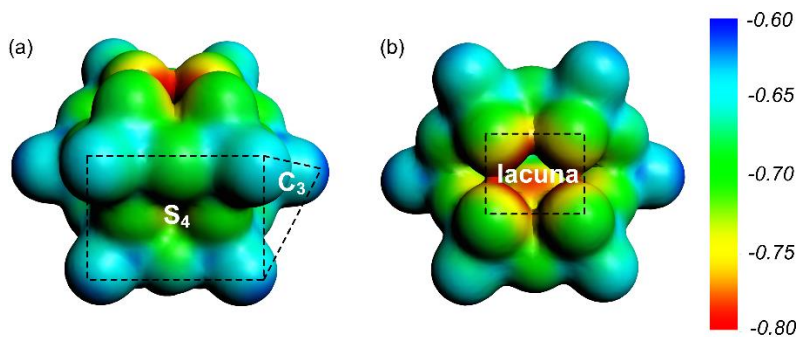


Figure S6.3. Side (a) and top (b) view of the MEP distribution for $PW_{11}O_{39}^{7-}$. The lacuna region shows the most nucleophilic (negative) part (red region).

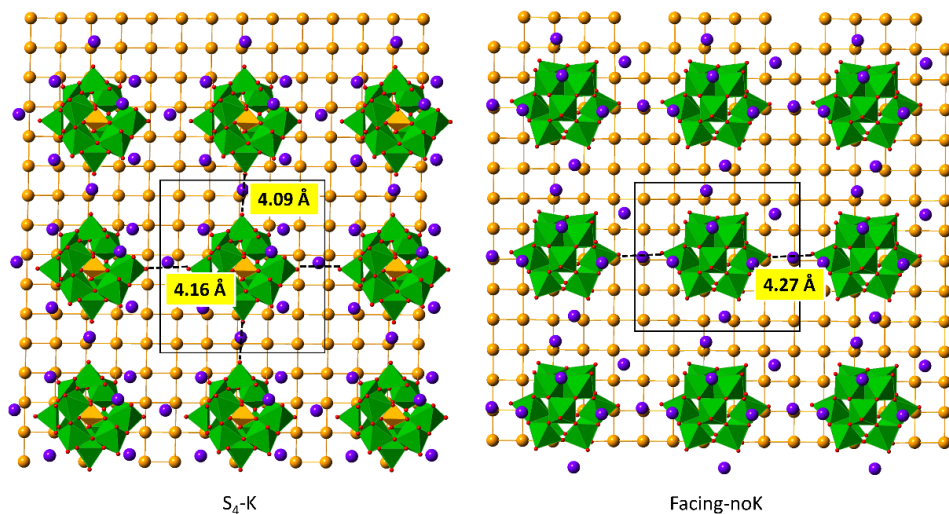
Chapter 6 Counter-intuitive Adsorption of $[PW_{11}O_{39}]^{7-}$ on $Au(100)$ 

Figure S6.4. The supercell representation for S_4 -K and Facing systems, the short O_a - O_a distances are labeled.

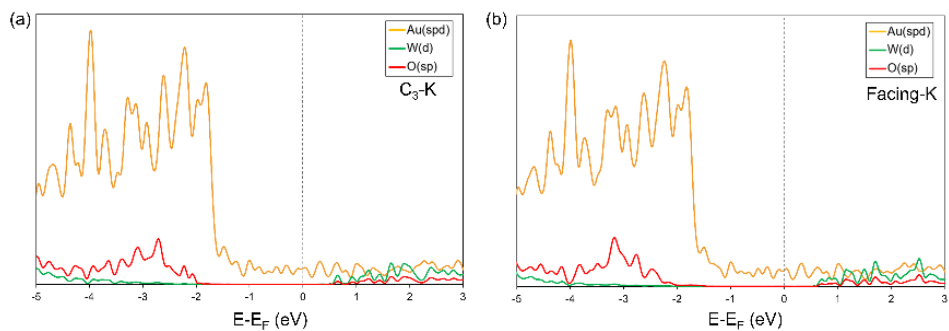
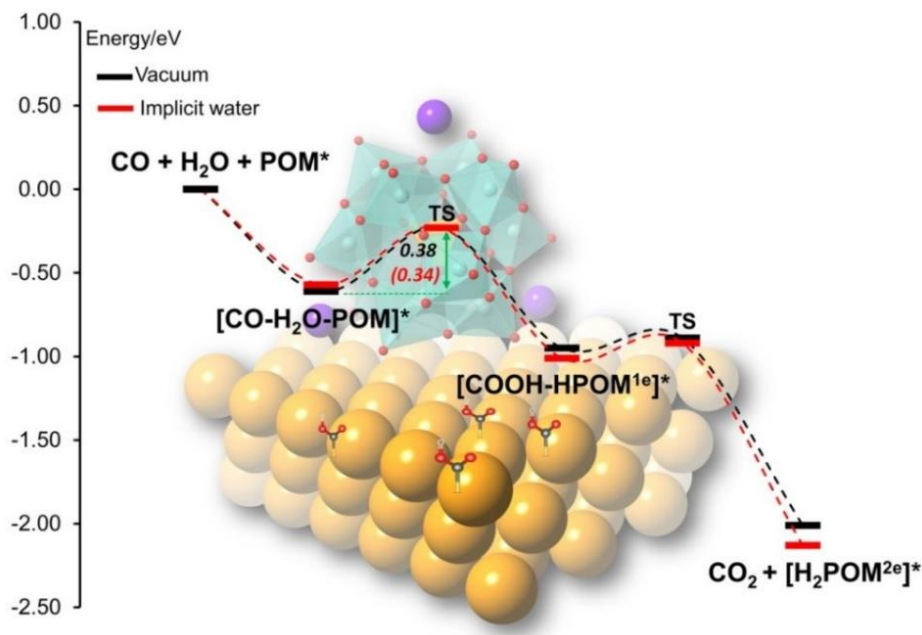


Figure S6.5: Projected density of states for PW_{11} adsorbed on $Au(100)$ with C_3 -K and Facing orientation.

Chapter 7

WGSR Cocatalyzed by the POM-gold Composites: The Magic Role of the POMs

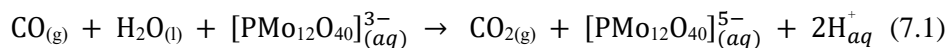


Water-gas shift reaction (WGSR, $\text{CO} + \text{H}_2\text{O} \rightarrow \text{CO}_2 + \text{H}_2$) has been extensively investigated because of its relevance in industry. Ab initio density functional theory calculations combined with the periodic continuum solvation model were applied to provide a mechanistic network of WGSR co-catalyzed by Au(111) and a polyoxometalate in aqueous solution. The contributions of Mo(d) and O(sp) bands near the Fermi level of $\text{PMo}_{12}\text{-Au}(111)$ were found to be responsible for the activity of POM modified gold catalyst, serving as both electron and proton acceptors. We show that the interfacial water can easily dissociate at room temperature in the presence of CO and a PMo_{12} adsorbed on the surface, via proton transfer to the O of the POM and electron transfer from the surface to the POM. A detailed mechanism study from electronic and energy views are presented in this chapter.

7.1 Introduction

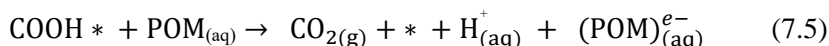
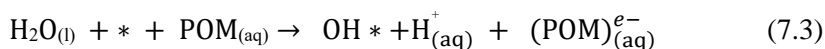
The so-called “*water-gas shift*” reaction (WGSR), $\text{CO} + \text{H}_2\text{O} \leftrightarrow \text{CO}_2 + \text{H}_2$ ($\Delta H = -41.1$ kJ/mol), is one of the most important industrial reactions, which can not only effectively reduce the concentration of carbon monoxide, but also manufacture hydrocarbons, methanol, and high purity hydrogen.^[1,2] Since the high demand for clean energy and fuels, the development of water gas shift catalysts has gained attention in the scientific community. Numerous experimental and computational efforts have been carried out to find the best catalysts and elucidate the related mechanisms.^[3-11] On one hand, a moderate amount of liquid water on the surface of late-transition metals can directly promote low-temperature WGSR, as shown experimentally using gold-nanotube membrane catalysts.^[12] On the other hand, catalysts with precious metal (Pt, Au, Pd, *etc.*) nanoparticles on oxide supports (Ceria, Titania, *etc.*) are the current pioneers owing to their unexpectedly high stability and catalytic activity.^[13,14] For example, TiO_2 -Au and CeO_2 -Au based materials are proved to efficient catalysts for the WGSR at low temperature; both oxides and metals have significant influences on the activity.^[15-17] These species are critical samples that help to understand the role of the metal-oxide interface and guide the further explorations by taking advantage of the unique properties of each component and the interaction between them.

Polyoxometalates (POMs) constitute a group of soluble and charged metal oxides with diverse structural and electronic properties, holding a special position between monomeric oxometalate units and in finite metal oxide frameworks.^[18-20] Similar to classical metal oxides, POMs can also spontaneously adsorb on the metallic planar surfaces or nanoparticles (NPs).^[21] The role of POMs in these composite materials is not only limited to stabilize the materials, but provide more functions such as improving catalytic activities and enhancing proton electron conductivity.^[22-24] In a related work, Dumesic and co-workers have discovered the room temperature CO oxidation with liquid water assisted by aqueous $\text{H}_3\text{PMo}_{12}\text{O}_{40}$ over noble metallic (Au, Pd, Pt, Ir, Ag) nanoparticles or nanotubes, as the process described in equation (7.1).^[25-28]



Importantly, the reduced PMo_{12} can then serve as a fuel for electrical energy generation through re-oxidation in a fuel cell carbon anode. The utilization of the POM’s reversible reduction–oxidation provides one useful method for energy generation.

Some elemental reactions for this process have been proposed by experiment, as shown in equations (7.2)-(7.5). Asterisk “*” represents the surface site of metal.



The proposed mechanism assumes a heterolytic dissociation of water to form protons that are solvated by liquid water molecules, and electron subsequently transferred from the gold surface to POM. It is proposed water plays an important role in the reaction. The involvement of adsorbed hydroxyl and carbonyl radical intermediates was postulated in this proposal. In order to understand the mechanism more in detail, in this chapter we provide some perspectives from a theoretical point of view. Concerning the role of water, there are many dark points because of many contradictory proposals have been suggested. In this work, solvation effects were studied with a periodic continuum solvation model.^[29,30]

Actually, computational modeling of the interaction between the POMs and surfaces or NPs is one urgent but rather complicate task due to the charge carried by POMs. After some of our early efforts, we know that the incorporation of counterions in the calculations is strictly necessary to obtain reasonable electronic properties for such systems.^[31] In addition, the introduction of an implicit solvent model in the system weakens the over stabilization from the counterions and surfaces, which provided an easy way to consider the solvent effects. With these factors involved herein, we computationally investigate the WGSR activated by gold surface with POMs supported on. The first part of the discussion will focus on the interactions between the POMs and gold surfaces to help us to know the relationships between the structure and reactivity, and then a systematic analysis of reaction mechanism on the POM-Au(111) interface is presented. The role of POM and water will be revealed through the study.

7.2 Computational details and models

7.2.1 DFT parameters

The geometry optimizations and energy calculations for all species were performed by means of periodic DFT with VASP 5.3 code.^[32] The generalized gradient

approximation (GGA) with the Perdew–Wang 91 functional (PW91) was applied to describe the exchange and correlation term,^[33] while the core-valence electron interactions were represented by using the project-augmented wave (PAW) method.^[34] The valence electrons for each atom were expanded in plane wave basis sets with cut-off energy at 500 eV, and the details are expressed as the following: $5d^{10}6s^1$ for Au, $3p^64s^1$ for K, $2s^22p^4$ for O, $3s^23p^3$ for P, $4d^45s^2$ for Mo, $5d^46s^2$ for W, $1s$ for H, and $2s^22p^2$ for C. All intermediate states (I) were optimized until the self-consistence reaches to $1 \cdot 10^{-5}$ eV and $0.03 \text{ eV} \cdot \text{Å}^{-1}$ for the electronic and the ionic convergence respectively. The transition states (TS) related to the water dissociation and CO oxidation processes were searched by combining of the climbing-image nudged-elastic-band (CI-NEB)^[35] and improved-dimer^[36] (IDM) approaches. The TS were further confirmed by the existence of one imaginary frequency along the reaction coordinate. The preliminary CI-NEB steps were converged to energies $< 1 \cdot 10^{-4}$ eV and forces $< 0.1 \text{ eV} \cdot \text{Å}^{-1}$ for electronic energies and geometries respectively, while the convergence criteria for dimer steps were $< 1 \cdot 10^{-6}$ and $< 0.05 \text{ eV} \cdot \text{Å}^{-1}$. The reciprocal space in slab models was described by using a $3 \times 3 \times 1$ k -point grid mesh,^[37] and Γ point was used for isolated molecules, such as H_2O , CO , and $\text{K}_3\text{PMo}_{12}\text{O}_{40}$. The energy corrections for solvent effects were achieved under the implicit solvation model (named *VASPsol*) that was developed by Hennig and co-workers.^[38, 39]

7.2.2 Models

Since {111} facet is always the most stable and one prevalent configuration in metal NPs, the mechanistic study on {111} would be very useful for understanding the mechanism on NPs.^[40] Regarding to the large size of gold NPs used in the experiment (10.5nm), the Au(111) surface was selected as the NP model, which was considered by a $\begin{pmatrix} 5 & 0 \\ 3 & 6 \end{pmatrix}$ (matrix notation) periodic slab consisting of 3 atomic layers with 30 gold atoms per layer. Accordingly, the dimensions of the unit cell were 14.76 and 15.34 Å in a and b directions. A vacuum space of more than 10 Å was added in c direction to avoid the interactions between the replicated cells. As depicted in Figure 7.1, we have only considered the preferable S_4 orientation of $\text{K}_3\text{PMo}_{12}$ (PMo_{12}) and K_3PW_{12} (PW_{12}) on Au(111) for the mechanism study, because the main properties of the system are not strongly influenced by the different adsorption sites or rotation angles. This adsorption represents four bottom O_d atoms adsorbed on four top Au sites and the P center faced the bridge site. The charge of the POM was compensated using three potassium atoms. The bottom two layers of Au were kept fixed at their bulk-truncated position, while all other atoms were fully relaxed during the optimization. For comparison, the reaction

was also performed on a bare Au(111) surface, modelled by a $\begin{pmatrix} 4 & 0 \\ 2 & 4 \end{pmatrix}$ cell with four Au layers.

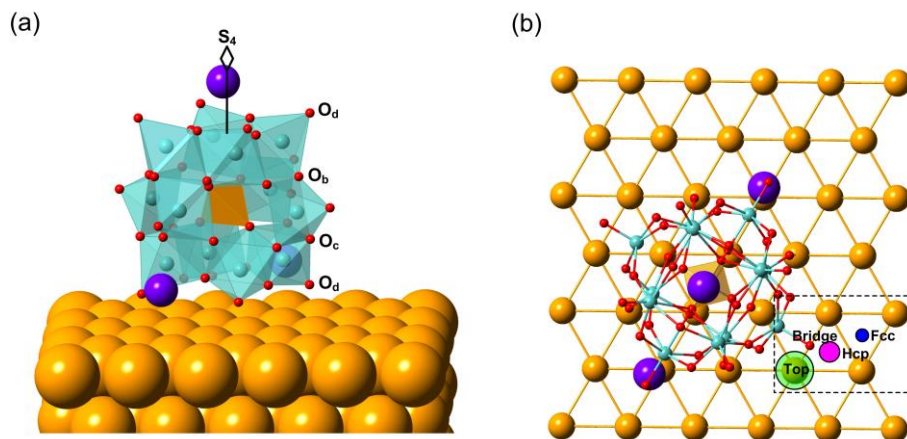


Figure 7.1. (a) Polyhedral and ball representation for the $\alpha\text{-K}_3\text{PMo}_{12}\text{O}_{40}$ deposited on Au(111) via S_4 rotation axis from side view; (b) Top view of the model and the label for four different active sites on Au(111).

7.3 Results and discussions

7.3.1 Formation of POM-metal interface

Because neither the bulk Au nor polyoxometalates show activity for WGRS, the origin for the unique catalytic activity of the current gold catalyst with POM supported on must be related to the synergy between the two components. To fully understand the catalytic mechanism, it is important to determine the electronic properties of the material. We first computed the adsorption of PMo_{12} and PW_{12} on Au(111). Only the S_4 orientation with four O_d atoms directly contact to the top site of gold was considered in the current case. Other sites and adsorption modes were discussed elsewhere by Aparicio-Anglès.^[31a] Similar to the behavior of PW_{11} and SiW_{12} on the gold surface, the interaction between $\text{K}_3\text{PMo}_{12}$ and gold is not very strong. Our results suggest that PMo_{12} can spontaneously adsorb on Au(111), with an adsorption energy (E_{ads}) of -0.60 eV in vacuum, and decreased to only -0.18 eV when the solvent was taken into account by using the implicit model. The adsorption for PW_{12} on Au(111) is slightly less favourable than PMo_{12} , with

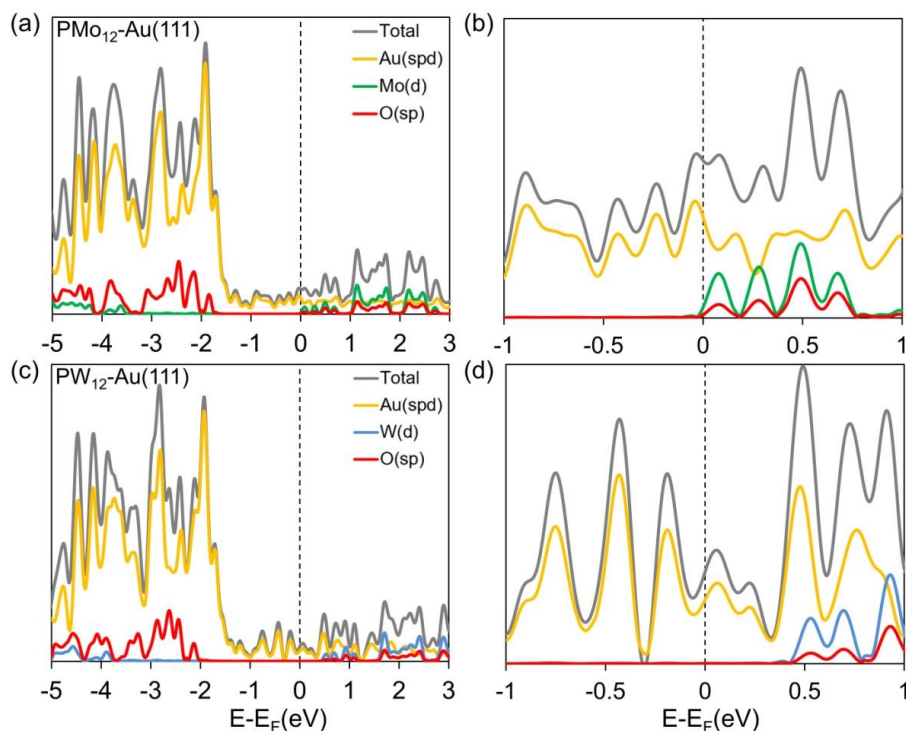


Figure 7.2. (a, c) Density of States (DOS) and Projected Density of States (PDOS) for systems PMO_{12} -Au(111) and PW_{12} -Au(111) respectively; (b, d) 500% extension of (a, c).

energies of -0.50 and -0.04 eV in vacuum and solution respectively. In the presence of water, the gold surface show weak affinity for the adsorption of polyoxometalates.

In order to discuss the electronic properties of PMO_{12} and PW_{12} supported on Au(111), we depicted in Figure 7.2 the density of states (DOS) projected on all involved atoms. For the PMO_{12} -Au(111) case, the front of the Mo(d) band is found very close to the Fermi level but has not yet been crossed, therefore it suggests that the PMO_{12} cannot be spontaneously reduced by gold when adsorbed on Au(111). Additionally, AIM Bader charge analysis also demonstrates that no remarkable charge transfer occurred between the gold surface and PMO_{12} (Table 7.2). However, the origin of catalytic active for a composite catalyst is always related to its electronic features near the Fermi level. Due to the nearness of the Mo(d) band to the Fermi level, it is expected that the Mo(d) bands could potentially accept electrons from the gold surface if extra electrons are donated by the surfaces or other species. Analogously, the adsorbed PW_{12} also keeps its redox property and the W(d) band locates 0.5 eV higher than Mo(d), indicating that

to accept incoming electrons is more difficult than for Mo(d). Such electronic differences may be very relevant in the catalytic activity.

7.3.2 Stability of adsorbed intermediates

Table 7.1. The adsorption energies (eV) for K_3PMo_{12} , K_3PW_{12} on Au(111), H_2O , CO, and CO_2 adsorbed on clean and PMo_{12} -Au(111).

Species	Preferred site	^a E_{ads} (Gas.)	E_{ads} (Sol.)	^b ΔE
PMo_{12} -Au		-0.60	-0.18	0.42
PW_{12} -Au		-0.50	-0.04	0.46
H_2O -Au	top	-0.14	-0.13	0.01
CO-Au	fcc	-0.33	-0.37	-0.04
CO_2 -Au	top	-0.04	-0.05	-0.01
H_2O -(PMo_{12} -Au)	top/bridge	-0.26/-0.24	-0.07/-0.13	0.19/0.11
CO-(PMo_{12} -Au)	top/fcc	-0.31/-0.29	-0.51/-0.51	-0.20/-0.22
CO_2 -(PMo_{12} -Au)	top	-0.06	-0.33	-0.27

^aAll adsorption energies are calculated through $E_{ads} = E_{tot} - E_{surf(POM/surf)} - E_X$, Where E_{tot} is the total energy of the system and the $E_{surf(POM/surf)}$ is the energy of the relaxed bare or POM supported surface. ^b ΔE is the adsorption energy difference between gas and solution.

To analyze how strong the key reaction intermediates are attached on the surface, the E_{ads} for H_2O , CO, and CO_2 are presented in Table 7.1. The results show that *water* adsorbs weakly on both clean Au(111) and PMo_{12} -Au(111), with E_{ads} as low as -0.14 and -0.26 eV, respectively. When surrounded with solvent, the interaction between solvated water and Au(111) become more weakly due to the increased contribution of water-water interactions. The behavior of CO on clean Au(111) and PMo_{12} -Au(111) show similar results in vacuum with $E_{ads} \sim -0.3$ eV. However, the CO adsorption in solution increases up to -0.51 eV on PMo_{12} -Au(111), and its configuration is almost isoenergetic on the top and fcc sites. CO_2 adsorbed on dry Au(111) and PMo_{12} -Au(111) surfaces are both very weak, whereas its adsorption on solvated PMo_{12} -Au(111) has raised to -0.33 eV. The inclusion of solvent shows stabilization for the adsorption of CO and CO_2 molecules, and unfavorable adsorption for the others. Significant changes were obtained for the adsorption of POM as discussed above. It should be mentioned

that the adsorption for OH and COOH species are not listed, given that there are still significant limitations to obtaining accurate energies for radical species.

7.3.3 WGSR mechanism on clean Au(111)

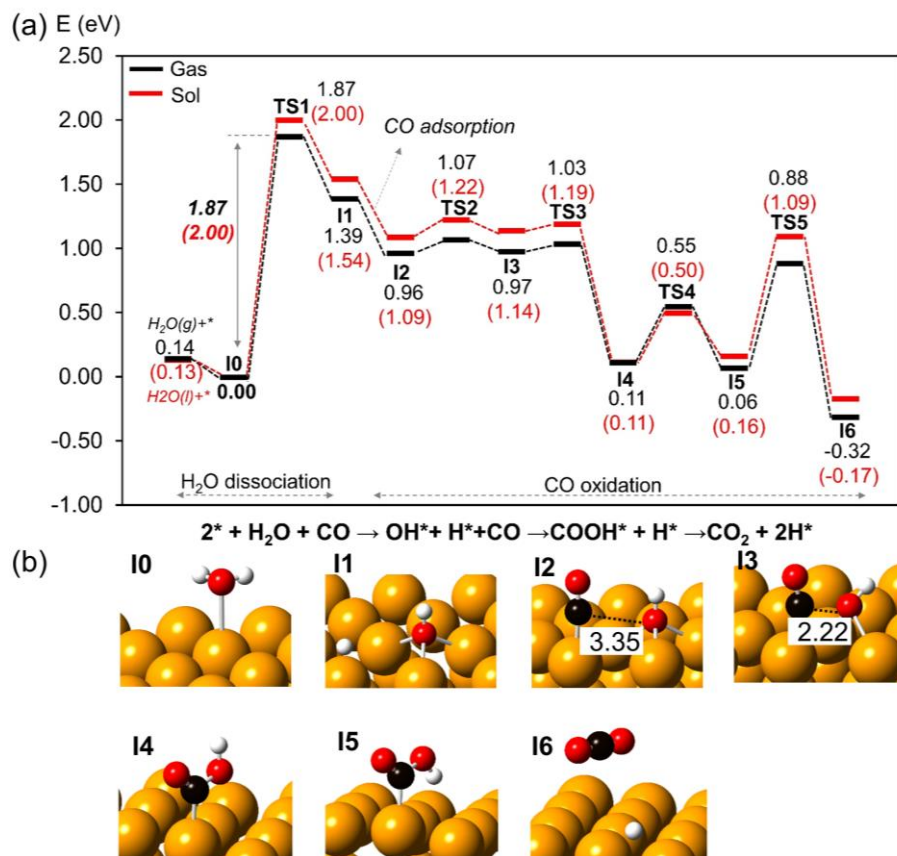


Figure 7.3. (a) Calculated energy (eV) profile for WGSR on bare Au(111) with (red) and without (black) solvent considered. All energies are referred to the water adsorbed state **I0** (defined as energy zero); (b) the main intermediates involved in the mechanism.

Computationally, the WGSR mechanism on the clean Au surfaces or NPs has been widely analyzed, and mostly it is proposed that the reaction follows the redox and carboxyl pathways in which adsorbed CO interacts with O and OH to form CO₂ and carboxyl, respectively. In both routes, the rate-determining step is the initial water dissociation, which determines the poor activity of bare gold surfaces. To compare with the WGSR on the POM-Au(111) system, we firstly performed the reaction on clean Au(111). Importantly, in this work we have also computed the reaction in a

continuum solvent model to reveal the contribution of solvent to the energy balance. The energy profiles and the main intermediates are represented in Figure 7.3. Consistent with the reported data, H₂O weakly adsorbs on the top site of Au(111) with small exothermic of -0.14 eV, and a considerable barrier of 1.87 eV (**TS1**) is required to reach the dissociated state H* + OH* (**I0** → **I1**).^[41] The reaction proceeds when adsorbed OH and CO are in contact and react to form *cis*-COOH*. OH* diffuses easily from fcc to bridge site by overcoming a very low barrier of 0.11 eV (**TS2**), then combine with CO to form *cis*-COOH* with low barrier (0.06 eV) and high exothermic (0.86 eV) process (**I3** → **I4**). Because the H atom in *cis*-COOH sits on the opposite direction of the surface, a transformation step occurs before decomposition to product. *cis*-COOH* evolves to its *trans*-state surpassing a barrier of 0.44 eV. Except for the water dissociation step, the H releasing from *trans*-COOH* to the surface also required a relatively high barrier of 0.82 eV (**TS5**). Apparently, the high barrier to break the hydroxyl bond in water is the key limitation for the catalytic activity of gold for WGSR, once OH* formed, subsequent steps occurred readily on the gold substrate. On the other hand, introduction of the solvent environment in the calculations did not provide any improvement for the activity of Au(111); even make it worse with barrier of 2.00 eV for the rate-determining step. This trend is in line with the recent calculations for water dissociation on the Ru (0001) surface in an implicit solvent model.^[42] Therefore, it is clear that the solvent (water) is not the origin of the catalytic activity of the Au(111).

7.3.4 Activation of H₂O by PMo₁₂-Au(111)

Based on the understandings for the electronic structure of PMo₁₂-Au(111), we now discuss its interaction with interfacial water. For water adsorption, both top and bridge sites (**m-I0**) where can form one H-bond with the neighbouring O_c of PMo₁₂ were considered (Figure S7.1). Unlike the classical metal oxide surface, water molecule is impossible to directly coordinate with the Mo^{VI} due to the absence of oxygen vacancies. The calculated results show the water is slightly more stable on the bridge than on the top by 0.02 eV. H₂O spontaneously adsorbs on the POM modified surface with an adsorption energy of -0.26 eV (**m-I0**), which is 0.12 eV more favorable than that on clean Au(111). To start the WGSR, the initial step should be the dissociation of water to form adsorbed OH or O. As shown in Figure 7.4, the dissociated state with one H transferred to PMo₁₂ (**m-I1a**) is calculated to be 0.75 eV more stable than H located on the surface (**m-I1b**), which supposes the water dissociation is very likely to occur through transferring its H to the adjacent oxygen of the POM, and the dissociated OH

binds on the Au bridge site and link with the POM via H-bond. By comparing the electronic structure and Bader charge differences between **m-I1a** and **m-I1b** (Figure 7.4 and Table 7.2), we observed that the electronic structure of the polyoxomolybdate in **m-I1b** almost keeps unaltered without reduction. Hence, Bader charge analysis shows that the net charges on PMo_{12} changed only in $0.1|e|$ from **m-I0** to **m-I1b**. The net charge on the adsorbed H is $0.12|e|$ and $-0.01|e|$ at the **m-TS1b** and **m-I1b** respectively, while it is $0.64|e|$ at the initial state, thus suggesting a homolytic dissociation of water in the **m-I0** \rightarrow **m-TS1b** \rightarrow **m-I1b** route. Simultaneously, the charges on gold surface increased from $0.29|e|$ to $0.67|e|$, which entails an electron depletion on the gold surface to stabilize the dissociated OH.

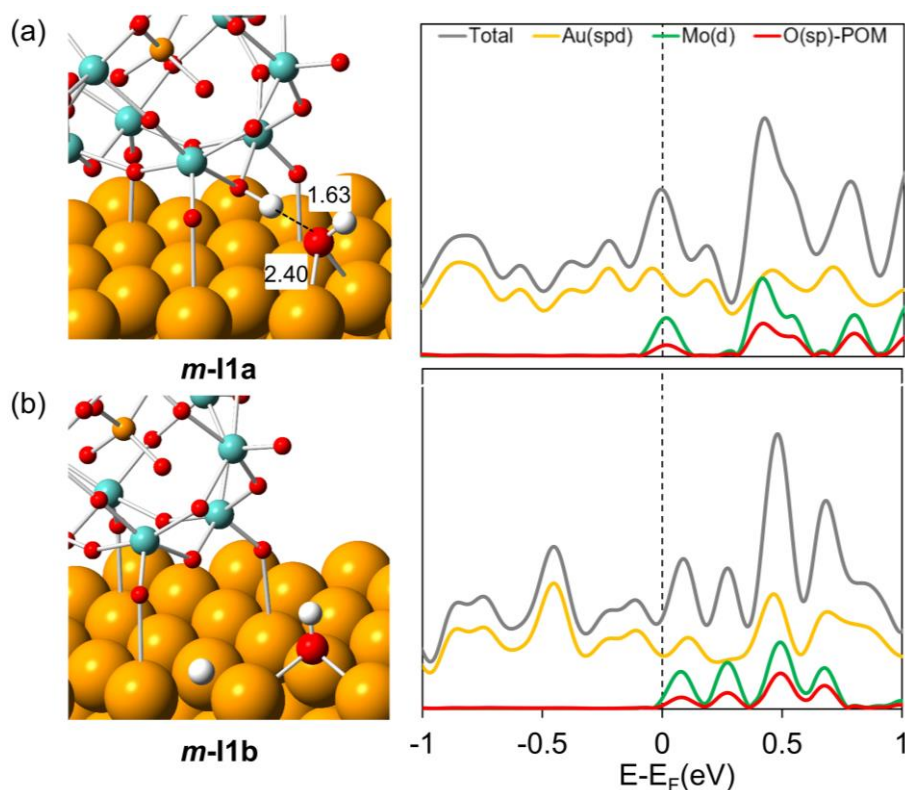


Figure 7.4. Left: Optimized structures for **m-I1a** (a) and **m-I1b** (b); Right: DOS and PDOS representations for **m-I1a** and **m-I1b**.

However, the charge of PMo_{12} in **m-I1a** is noticeably increased by $0.35e$ with respect to that in **m-I0**, meanwhile the Mo(d) band is found that has already crossed the E_F . This means that the PMo_{12} has been reduced along the dissociation (**m-I0** \rightarrow **m-TS1a**

Chapter 7 WGS_R Co-catalyzed by the POM-gold Composites: The Magic Role of the POMs

→ ***m*-I1a**). The net charge for the transferred H in ***m*-TS1a** is $0.66|e|$, this character supposes a heterolytic O-H cleavage via proton transfer to the POM and results in the OH⁻ anion remaining on the surface. Because Mo(d) bands are near the Fermi level, the electron from adsorbed OH⁻ will be transferred to the POM leading to a less charged OH adsorbate on the bridge site of Au. In addition, the presence of O_{2p} bands above but nearby the Fermi level from PMo₁₂ also promote the proton transfer.

Table 7.2. Calculated Bader AIM charge for the main intermediates and transition states mediated by PMo₁₂-Au(111).

	$\sum\text{PMo}_{12}$	$\sum\text{K}$	$\sum\text{Au}$	H _{w1}	H _{w2}	O _w	C	O _{CO}
PMo₁₂-Au	-2.86	2.69	0.17					
<i>m</i>-I0	-3.01	2.69	0.29	0.67	0.62	-1.27		
<i>m</i>-TS1a	-3.29	2.69	0.46	0.64	0.62	-1.11		
<i>m</i>-TS1b	-2.84	2.69	0.42	0.12	0.61	-1.01		
<i>m</i>-I1a	-3.35	2.70	0.48	0.66	0.60	-1.09		
<i>m</i>-I1b	-2.91	2.68	0.67	-0.01	0.62	-1.06		
<i>m</i>-I2	-3.46	2.69	0.54	0.68	0.62	-1.11	1.02	-0.98
<i>m</i>-TS3	-3.46	2.69	0.55	0.62	0.64	-1.11	1.05	-0.98
<i>m</i>-I5	-3.47	2.70	0.26	0.62	0.60	-1.08	1.44	-1.07
<i>m</i>-I8	-3.49	2.71	0.25	0.67	0.64	-1.17	1.47	-1.08
<i>m</i>-TS7	-3.54	2.71	0.20	0.65	0.63	-1.16	1.57	-1.06
<i>m</i>-I9	-3.97	2.70	0.07	0.62	0.60	-1.07	2.09	-1.04
<i>m</i>-I10	-3.07	2.70	0.23	0.66	0.63	-1.22	1.10	-1.03
<i>m</i>-TS8	-3.22	2.71	0.24	0.65	0.63	-1.07	1.13	-1.06

From an energy point of view (Figure 7.5a), the water dissociation is dramatically promoted by the presence of PMo₁₂ on the surface. Herein, the energy zero is referred to the adsorbed water on PMo₁₂-Au(111). Dissociation ***m*-I0** → ***m*-I1a** is a somewhat endothermic process with reaction energy of 0.53 eV, which is much lower than the route with H and OH located both on the surface (1.28eV, ***m*-I0**→***m*-I1b**). The activation of H₂O needs to overcome a barrier of 0.55 eV, whereas 1.87 eV was required for the homolytic path. However, the heterolytic route is considered reversible,

as the reverse barrier is only 0.02 eV to give back H₂O if the reaction stopped at the current step.

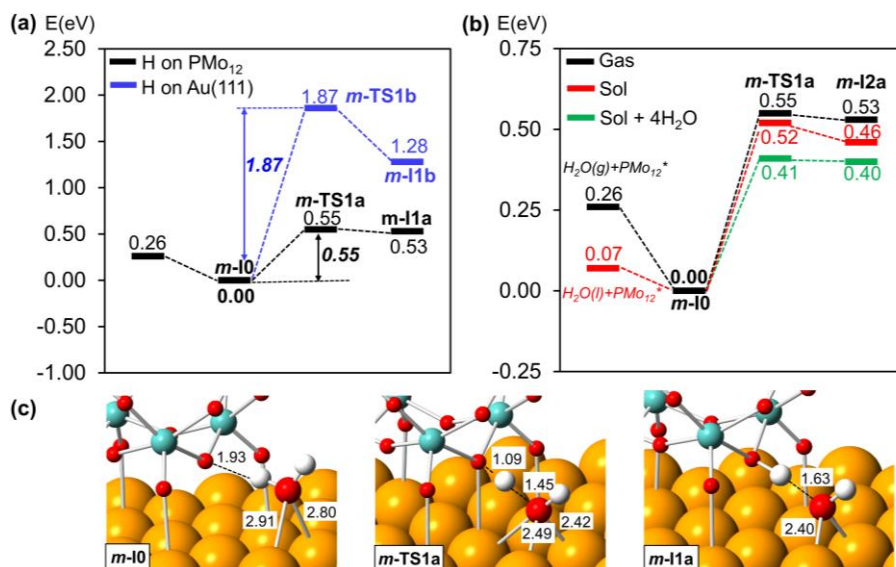


Figure 7.5. (a) Energy comparison of two different pathways for water dissociation on PMo₁₂-Au (111) performed in gas phase; (b) Energy profile for the water dissociation with (red and green) and without (black) solvent considered in the calculation; (c) The optimized intermediates and transition states in the main steps.

7.3.5 Solvation effects on H₂O activation

Both experiments and DFT calculations have proposed that the presence of liquid water in the reactor plays critical role for the WGSR.^[43-45] To provide insight into the solvation effects for the water dissociation, energy corrections were performed for each species by including the implicit solvent model. Figure 7.5b shows that the energy profile with solvent (red curve) is generally lower than without solvent (black curve). In the aqueous surroundings, the adsorption for the liquid H₂O becomes very weak with only -0.07 eV. However, the solvent reduces slightly the barrier (0.52 vs. 0.55 eV) and reaction energies (0.46 vs. 0.53 eV) involved in this step, which shows a little favorable than that in gas phase without changing the trend.

On the other hand, we have also considered a combined solvent model by locating four water molecules close to the PMo₁₂-Au interface (Figure S7.2), to further check the role of water. The transition state involves a dissociation of neighboring water,

which mediates the fast proton transfer to the POM along the H-bond chain in the water cluster. Due to the explicit H-bonds in the water network, the dissociation was found 0.11 eV more favourable than when only the implicit solvent is considered, with barrier of only 0.41 eV (green curve). No notable stabilization was obtained for OH in the presence of solvent; the reverse reaction is still very easy to occur. In other words, the dissociation of water would be almost impossible when only Au, K₃POMo₁₂, and water are included in the system. Beyond the POMs, the water molecule may also act as proton acceptor to form H₃O⁺ and OH⁻ intermediates. However, the calculations show the H₃O⁺ is quite unstable on gold, which in turn results in spontaneously recombine of H₃O⁺ and OH⁻ to water, this result is also obtained by Site *et.al.*^[46] According to our calculations, we obtained that the adsorption of POMo₁₂ on the gold surface favored the kinetics of the water dissociation notably by decreasing the reaction energy and dissociation barrier. Importantly, the reverse reaction to adsorbed water is always thermodynamically more favorable independent of the presence of solvent or not and also of the solvent model.

7.3.6 CO oxidation steps

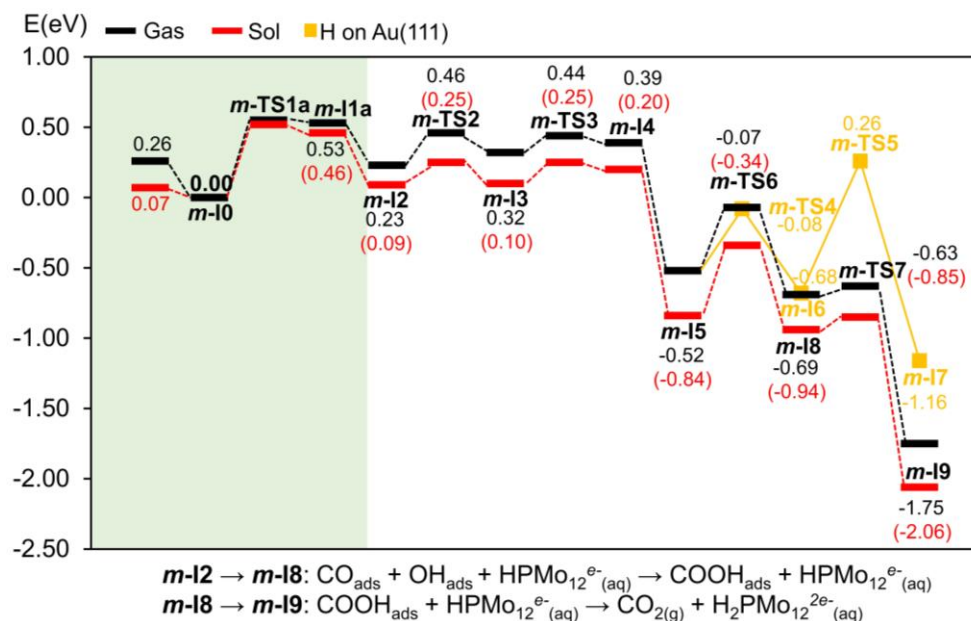


Figure 7.6. Energy profile (eV) for CO oxidation steps “ $CO_{ads} + OH_{ads} + HPMo_{12}^{e-}(aq) \rightarrow COOH_{ads} + HPMo_{12}^{e-}(aq) \rightarrow CO_{2(g)} + H_2PMo_{12}^{2e-}(aq)$ ” with (red) and without (black) solvent considered in the calculation.

In the presence of CO, the oxidation of CO may take place as soon as the hydroxyl is formed (**m-I1a**). The elementary reaction steps with involved energies and geometries are displayed in Figure 7.6 and Figure 7.7 respectively. Two possible positions for CO adsorption were considered in the presence of OH*. When the CO occupies a top site (**m-I2**), the exothermic adsorption of CO (-0.30 eV) may supply the reaction to the next step. The two diffusion processes of OH* from the bridge to the contiguous fcc (**m-I2** → **m-I3**) and then to another bridge site (**m-I3** → **m-I4**) require overcoming low barrier of 0.23 eV and 0.12eV respectively. Once the OH* and CO* are ready, *cis*-COOH is spontaneously formed with a reaction energy of -0.91 eV (**m-I4** → **m-I5**). The final stages should be the decomposition of the carboxyl occurring by the cleavage of the OCO-H bond. Two possible paths for COOH* decomposition are computed. Following the typical channel on bare Au(111), *cis*-COOH* (**m-I5**) will undergo an isomeric transformation to *trans*-COOH* (**m-I6**) before splitting with a barrier of 0.44 eV (**m-TS4**), leading to a more favourable position for H releasing. The COOH* dissociates to CO₂ and H (**m-I7**) by desorbing the CO₂ and transferring the H to the gold surface. This process is exothermic with an energy of -0.48 eV (orange square), although it requires a high barrier of 0.94 eV (**m-TS5**). A second pathway involves the dissociation of *cis*-COOH giving directly to the one electron reduced PMo₁₂, but previously it is necessary to diffuse the COOH* nearby the PMo₁₂. The diffusion of *cis*-COOH* from one top (**m-I5**) to the adjacent top (**m-I8**) needs a barrier of 0.45 eV, and two hydrogen bonds can be formed between HPMo₁₂^{e-} and COOH*, see **m-I8** in Figure 7.7. Although the PMo₁₂ has been one electron reduced in the initial water dissociation step, the CO₂ formation (**m-I9**) is still largely promoted by transferring a proton to the O of HPMo₁₂^{e-}, with low barrier and high exothermic energy by 0.06 eV and -1.06 eV (black line) respectively. The proton transfer and weak interaction of CO₂ with the surface will lead to a fast electron transfer from the surface to the POM, resulting in more reduced H₂PMo₁₂^{2e-} species.

This is evidenced by the Bader charge change of PMo₁₂, where an electron transfer of 0.5e from the surface (with COOH adsorbed) to PMo₁₂ is obtained (**m-I8** → **m-I9**). It is worth remarking that the net electron accumulation on PMo₁₂ is less than two electrons after water dissociation and CO oxidation steps. The decreasing of net charge on the gold from initial (**m-I0**: 0.29|e|) to the final state (**m-I9**: 0.07|e|), suggesting a small amount of electrons are remaining on the surface. In summary, the water dissociation step is the rate determining step for the whole WGSR when the reaction is co-catalyzed by the hybrid PMo₁₂-Au(111) system, the energy barrier being only 0.53 eV.

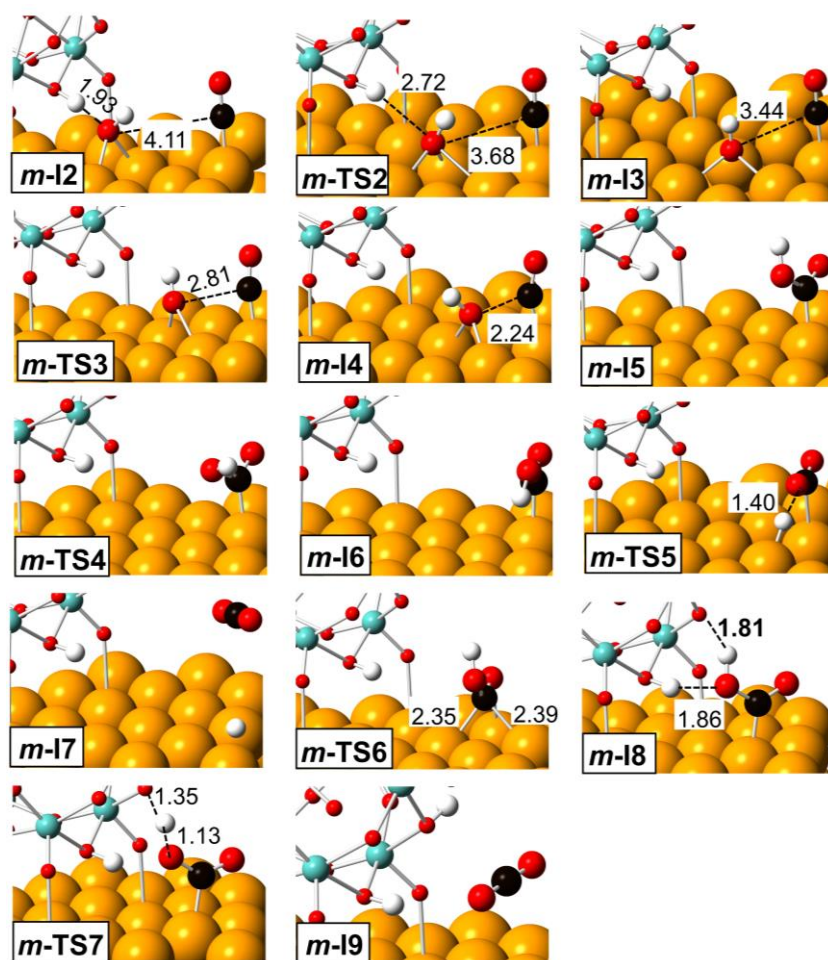


Figure 7.7. The main intermediates and transition states involved in the CO oxidation steps on $PMo_{12}\text{-Au}(111)$.

Alternatively, CO could also adsorb nearby the adsorbed OH and $HPMo_{12}^{e-}$ by locating on the short bridge of Au. Interestingly, as the CO and OH approach, the desorbed OH effortlessly re-abstracted the H (transferred in the first step) from POM to give H_2O due to the small reverse barrier for water dissociation as discussed in section 7.3.4. Consequently, it returns to the initial state with H_2O and CO co-adsorbed on two adjacent top Au sites (**m-I10**). It is therefore expected that this equilibrium may provide a new channel for water dissociation. The co-adsorption energy is calculated to be -0.61 eV, which is a little lower than the sum of the independent adsorption energy of H_2O and CO (-0.57 eV). Instead of forming the intermediate with OH adsorbed on the surface, the interplay of H_2O and CO can lead to the adsorbed *cis*-COOH (**m-I8**)

species directly. H₂O can easily transfer its H atom to the nearest neighboring O_c by overcoming a barrier as low as 0.39 eV (see *m-TS8* in Figure 7.8, 0.34 eV in solution), and electron is transferred via the surface to the PMO₁₂, simultaneously. It is worth noting that this process is an exothermic process with energy of -0.27 eV (*m-I10* → *m-I8*), and the reverse barrier in this route is 0.73 eV (0.78 eV in solution). With such relatively high barrier, the reverse reaction of H₂O dissociation may not be facile. The remaining steps followed by decomposition COOH* to yield CO₂ are the same as the discussed above. CO oxidation steps are also promoted by the solvent, with decreased barrier and more favourable reaction energies. Comparing to the dissociation of water to OH* state, such a route with CO and H₂O interact to form COOH* directly can avoid the low barrier of reverse process, and also reduce the reactive barrier, which suggest a CO-assisted water dissociation mechanism in the current case.

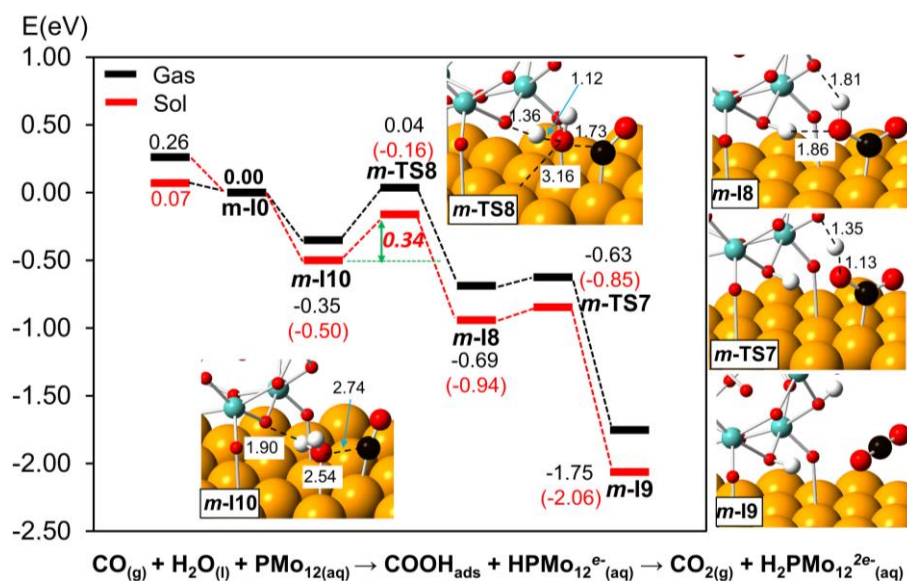
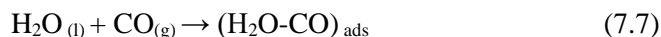


Figure 7.8. Energy profile for WGS_R in the presence of H₂O and CO co-adsorbed on the surface with (red) and without (black) solvent considered in the calculation, and the main intermediates and transition states are displayed.

7.3.7 Complete reaction network

Based on the computational results, a simple mechanism was proposed. The reaction pathways with the minimum-energy barriers involve the following steps:





Among these steps, the PMo_{12} and CO assisted water dissociation to form COOH^* (7.8) is the *key* step, the barrier being as low as 0.34 eV in solution. This very low energy allows understanding why the WGSR can proceed easily at room temperature on gold in the presence of aqueous PMo_{12} . The proposed mechanism is comparable to the electrochemical CO oxidation on gold published by Weaver *et al.* ^[47] In acidic solution, they suggested the following mechanism:



In which the rate-determining step also corresponds to the first electron transfer step. Because POMs can generally display multiple and reversible electron reductions without significant deformation of the POM framework. In the current case, the first and second electron related process are computed based on the same PMo_{12} , which are found both exothermic from a thermodynamic point of view. The role of PMo_{12} herein is twofold: first to retain the H^+ before going to the solvent, and second to act as electron reservoir. These properties are directly related to its electronic feature near the Fermi level of PMo_{12} -Au(111). The process can be assumed as a proton assisted electron transfer as occurs in many catalytic reactions in the presence of POMs.

7.3.8 The activity of PW_{12} -Au(111)

Having obtained the detailed WGSR mechanism for PMo_{12} -Au(111), we are in a position to extend our investigation to other POMs, with the aim of obtaining a comprehensive understanding of the relevance of the POM in heterogeneous catalyst. By analysing the electronic structures, the PW_{12} adsorbed on Au(111) is expected to be relatively difficult for the WGSR respect to PMo_{12} due to the higher energy of W(d) bands. To confirm this issue, the energy profile associated to the PW_{12} -Au(111) system is summarized in Figure 7.9. As expected, the water dissociation barrier increases up to 0.59 eV (0.45 eV in solution) and the process becomes endothermic by 0.26 eV (**w-I10** \rightarrow **w-I8**). In addition, the decomposition of COOH^* is also higher in energy than in the PMo_{12} case, needing to overcome a barrier of 0.29 eV (**w-I8** \rightarrow **w-TS7**) and the reaction to form the CO_2 being exothermic by only -0.29 eV (**w-I8** \rightarrow **w-I9**). Present calculations clearly confirm that the reaction is sensitive to the nature of the POM.

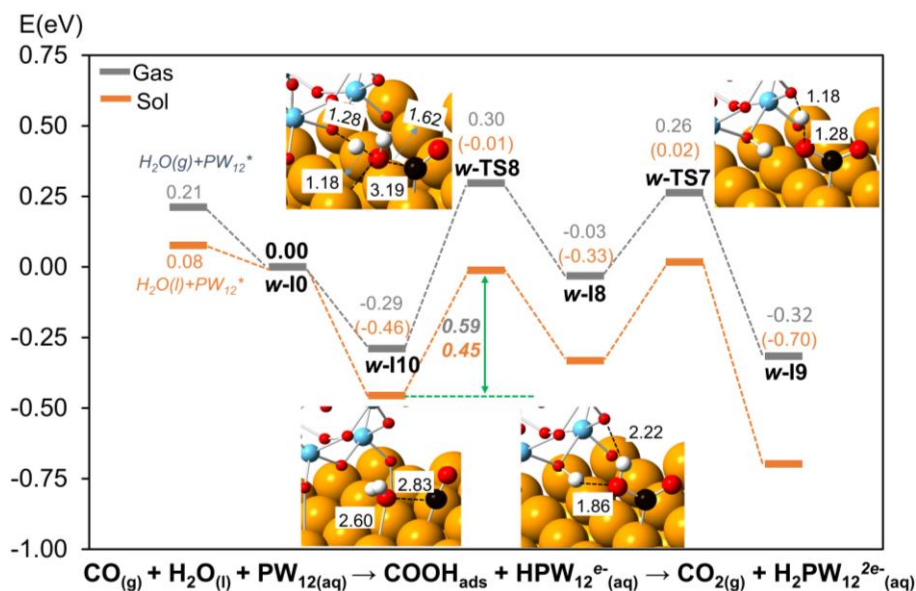


Figure 7.9. Energy profile for WGS_R in the presence of H₂O and CO co-adsorbed on the PW₁₂-Au(111) surface with (orange) and without (gray) solvent considered in the calculation, and the main intermediates and transition states are displayed.

Table 7.3. Calculated Bader AIM charge for the main intermediates and transition states in the reaction steps when mediated by PW₁₂-Au(111).

	ΣPW_{12}	ΣK	ΣAu	$\text{H}_{\text{w}1}$	$\text{H}_{\text{w}2}$	O_{w}	C	O_{CO}
w-I10	-2.84	2.72	0.12	0.62	0.63	-1.19	1.10	-1.04
w-TS8	-2.85	2.72	-0.18	0.64	0.67	-1.09	1.19	-1.10
w-I8	-3.04	2.72	-0.18	0.67	0.62	-1.12	1.42	-1.10
w-TS7	-3.23	2.72	-0.21	0.69	0.63	-1.14	1.59	-1.05
w-I9	-3.45	2.72	-0.44	0.58	0.63	-1.05	2.09	-1.06

In addition, the trend of Bader charge (Table 7.3) changes for PW₁₂-Au(111) and PMo₁₂-Au(111) are consistent with the energy profiles. The PW₁₂ anion accepts only 0.6e from the initial to the final state (**w-I10** → **w-I9**), whereas the electrons transferred to PMo₁₂ (**m-I10** → **m-I9**) are 0.9e. The relatively higher barrier in PW₁₂-Au(111) should be ascribed to two aspects, one is the decreased basicity of O in PW₁₂ related to the H accepting process, and another is the lower reduction ability of the polyoxotungstate with respect to polyoxomolybdate. Nevertheless, it is worth

mentioning that the deposition of both type of POMs on the surface improve the catalytic activity of the bare gold surface.

7.4 Conclusions

In this chapter, a systematic mechanism study for the low temperature WGSR on Au(111) with polyoxometalates supported on a gold surface was performed using an integrated approach based on first principles calculations and a periodic continuum solvation model. This work outlines the activity of a POMs-Au(111) catalyst for WGSR in aqueous solution. The main conclusions obtained from our calculations are as follows: (1) based on the electronic structures and atomic Bader charge analysis, we noticed that both PMo_{12} and PW_{12} are not reduced when adsorbed on the gold surface. The presence of conduction bands dominated by Mo(d) and O(sp) atomic orbitals, especially near the Fermi level, it allows the POM to accept electrons and protons. (2) In the presence of PMo_{12} , the interfacial water dissociation and COOH decomposition steps turn out to be much more feasible by accommodating protons and electrons on the POMs. The most favourable reaction channel is proposed to be co-adsorption of H_2O and CO on the PMo_{12} -Au(111) surface, and leads to the direct formation of COOH^* by avoiding the reversed water dissociation, highest barrier being less than 10 kcal mol⁻¹ (0.34 eV in solution). (3) The solvent effects were identified to accelerate the reaction by reducing the energy barrier and also increasing the exothermicity of the reaction in POM-Au(111). (4) The same reaction on PW_{12} -Au(111) catalyst is calculated to be more difficult, that is, with higher barriers, which is fairly consistent with their redox properties. Overall, these results provide a mechanistic understanding of WGSR catalyzed by the PMo_{12} -Au(111) system, revealing the crucial “magic” role played by the POM.

Preliminary studies on PMo_{12} supported Pd, Pt, Ag systems show less activities, behaviour that clearly differs from the activity order on the clean surfaces. A systematic analysis on these systems is under way in our group.

References and Notes

- [1] D. S. Newsome, *Catal. Rev.* 1980, 275-318.
- [2] W. Vielstich, A. Lamm and H. A. Gasteiger. *Handbook of fuel cell: fundamentals, technology, applications* (Reprinted ed.). New York: Wiley.
- [3] J. A. Rodriguez, S. Ma, P. Liu, J. Hrbek, J. Evans and M. Pérez, *Science*, 2007, 1757–1760.
- [4] F. Boccuzzi, A. Chiorino, M. Manzoli, D. Andreeva and T. Tabakova, *J. Catal.* 1999, 176–185.
- [5] D. Andreeva, V. Idakiev, T. Tabakova, L. Ilieva, P. Falaras, A. Bourlinos and A. Travlos, *Catalysis Today* 2002, 51-57.
- [6] R. Burch, *Phys. Chem. Chem. Phys.* 2006, 8, 5483-5500.
- [7] P. Liu and J. A. Rodriguez, *J. Chem. Phys.* 2007, 126, 164705-164712.
- [8] Z. P. Liu, S. J. Jenkins and D. A. King, *Phys. Rev. Lett.* 2005, 94, 196102–196104.
- [9] M. Haruta, N. Yamada, T. Kobayashi and S. Iijima, *J. Catal.*, 1989, 115, 301-309.
- [10] W. L. Deng, A. I. Frenkel, R. Si and M. Flytzani-Stephanopoulos, *J. Phys. Chem. C* 2008, 112, 12834–12840.
- [11] G. Jacobs, S. Ricote, P. M. Patterson, U. M. Graham, A. Dozier, S. Khalid, E. Rhodus and B. H. Davis, *Appl. Catal. A* 2005, 292, 229–243.
- [12] M. A. Sanchez-Castillo, C. Couto, W. B. Kim and J. A. Dumesic, *Angew. Chem. Int. Ed.* 2004, 43, 1140–1142.
- [13] C. Ratnasamy and Jon P. Wagner, *Catal. Rev.* 2009, 325–440.
- [14] Q. Fu, H. Saltsburg and M. Flytzani-Stephanopoulos, *Science*, 2003, 301, 935-938.
- [15] R. Burch, *Phys. Chem. Chem. Phys.* 2006, 8, 5483–5500.
- [16] X. Wang, J. A. Rodriguez, J. C. Hanson, M. Perez and J. Evans, *J. Chem. Phys.* 2005, 123, 221101–221105.
- [17] J. A. Rodriguez, P. Liu, J. Hrbek, J. Evans and M. Perez, *Angew. Chem. Int. Ed.* 2007, 46, 1329–1332.
- [18] M. T. Pope, *Heteropoly and Isopoly Oxometalates*. Springer-Verlag: New York, 1983.
- [19] A. Müller, M. T. Pope, *Polyoxometalate Chemistry: From Topology via Self-Assembly to Applications*, Kluwer, 2001.
- [20] D. L. Long, E. Burkholder and L. Cronin, *Chem. Soc. Rev.* 2007, 36, 105–121.
- [21] Y. F. Wang and I. A. Weinstock, *Chem. Soc. Rev.* 2012, 41, 7479–7496.

- [22] B. Keita, T. B. Liu and L. Nadjo, *J. Mater. Chem.* 2009, 19, 19–33.
- [23] S. G. Mitchell and J. M. de la Fuente, *J. Mater. Chem.* 2012, 22, 18091–18100.
- [24] R. J. Liu, G. G. Zhang, H. B. Cao, S. J. Zhang, Y. B. Xie, A. Haider, U. Kortz, B. H. Chen, N.S. Dalal, Y. S. Zhao, L. J. Zhi, C. X. Wu, L.K. Yan, Z. M. Su and B. Keita, *Energy Environ. Sci.* 2016, 9, 1012–1023.
- [25] W. B. Kim, T. Voithl, G. J. Rodriguez-Rivera and J. A. Dumesic, *Science*, 2004, 305, 1280–1284.
- [26] W. B. Kim, T. Voithl, G. J. Rodriguez-Rivera, S. T. Evans and J. A. Dumesic, *Angew. Chem. Int. Ed.* 2005, 44, 778–782.
- [27] W. B. Kim, G. J. Rodriguez-Rivera, S. T. Evans, T. Voithl, J. J. Einspahr, P. M. Voyles and J. A. Dumesic, *J. Catal.* 2005, 235, 327–332.
- [28] G. J. Rodriguez-Rivera, W. B. Kim and S. T. Evans, *J. Am. Chem. Soc.* 2005, 127, 10790–10791.
- [29] G. M. Mullen and C. B. Mullins, *Science*, 2014, 345, 1564–1565.
- [30] J. Saavedra, H. A. Doan, C. J. Pursell, L. C. Grabow and B. D. Chandler, *Science*, 2014, 345, 1599–1602.
- [31] (a) X. Aparicio-Angles, P. Miro, A. Clotet, C. Bo and J. M. Poblet, *Chem. Sci.* 2012, 3, 2020–2027; (b) Z. L. Lang, X. Aparicio-Anglès, I. Weinstock, A. Clotet and Josep M. Poblet, *Inorg. Chem.* 2017, 56, 3961–3969.
- [32] (a) G. Kresse and J. Hafner, *J. Phys. Rev. B: Condens. Matter* 1993, 47, 558–561; (b) G. Kresse and J. Hafner, *Phys. Rev. B: Condens. Matter.* 1994, 49, 14251–14269; (c) G. Kresse and J. Furthmuller, *Comput. Mater. Sci.* 1996, 6, 15–50; (d) G. Kresse and J. Furthmuller, *Phys. Rev. B: Condens. Matter*, 1996, 54, 11169–11186.
- [33] J. P. Perdew, J. A. Chevary, S. H. Vosko, K. A. Jackson, M. R. Pederson, D. J. Singh and C. Fiolhais, *Phys. Rev. B: Condens. Matter.* 1992, 46, 6671–6687.
- [34] P. E. Blöchl, *Phys. Rev. B: Condens. Matter*, 1994, 50, 17953–17979.
- [35] G. Henkelman, B. P. Uberuaga and H. J. Jonsson, *Chem. Phys.* 2000, 113, 9901–9904.
- [36] G. Henkelman and H. J. Jonsson, *Chem. Phys.*, 1999, 111, 7010–7022.
- [37] H. J. Monkhorst and J. D. Pack, *Phys. Rev. B: Solid State* 1976, 13, 5188–5192.
- [38] K. Mathew, R. Sundararaman, K. Letchworth-Weaver, T. A. Arias, R. G. Hennig, *J. Chem. Phys.* 2014, 140, 084106-1–084106-8.

- [39] M. Fishman, H. L. Zhuang, K. Mathew, W. Dirschka, R. G. Hennig, *Phys. Rev. B* 2013, 87, 245402-1–245402-7.
- [40] R. A. Ojifinni, N. S. Froemming, J. Gong, M. Pan, T. S. Kim, J. M. White, G. Henkelman, C. B. Mullins, *J. Am. Chem. Soc.* 2008, 130, 6801–6812.
- [41] A. A. Phatak, W. N. Delgass, F. H. Ribeiro, W. F. J. Schneider, *J. Phys. Chem. C* 2009, 113, 7269–7276.
- [42] M. Garcia-Ratés and N. López, *J. Chem. Theory. Comput.* 2016, 12, 1331-1334.
- [43] M. A. Sanchez-Castillo, C. Couto, W. B. Kim, J. A. Dumesic, *Angew. Chem. Int. Ed.* 2004, 43, 1140–1142.
- [44] S. K. Desai and M. Neurock, *Phys. Rev. B* 2003, 68, 075420–075427.
- [45] S. Desai and M. Neurock, *Electrochim. Acta* 2003, 48, 3759–3773.
- [46] R. Scipioni, D. Donadio, L. M. Ghiringhelli, and L. Delle Site, *J. Chem. Theory Comput.* 2011, 7, 2681–2684.
- [47] G. J. Edens, A. Hamelin and M. J. Weaver, *J. Phys. Chem. B* 1996, 100, 2322–2329.

Appendix Chapter 7

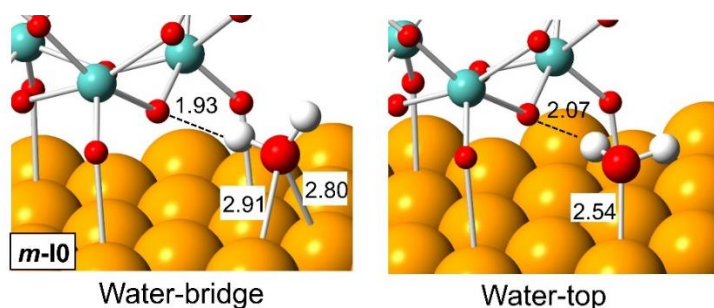


Figure S7.1. The adsorption modes of water on $K_3PMo_{12}-Au(111)$.

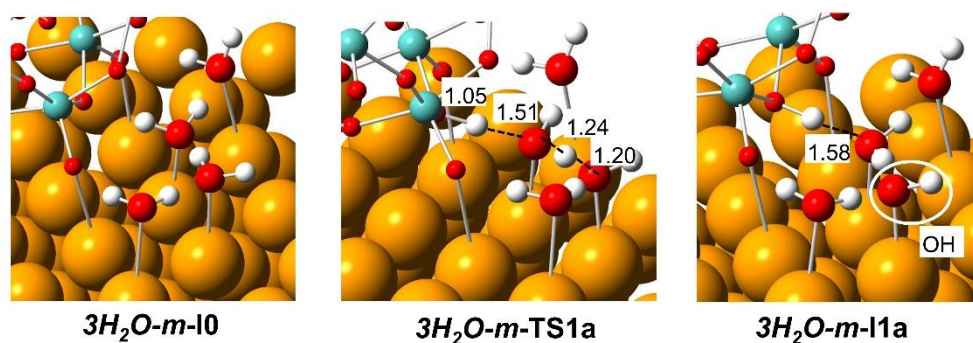
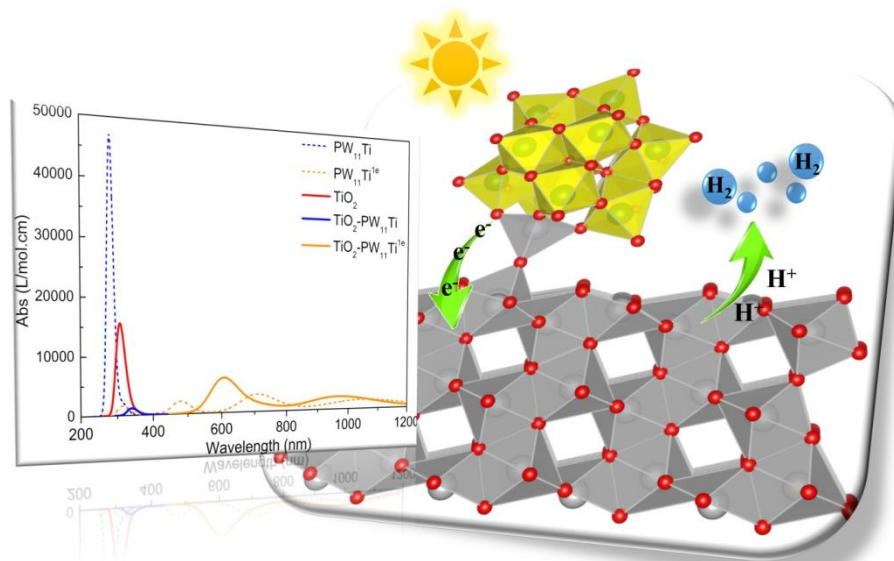


Figure S7.2. The optimized structures for water dissociation in the presence of three explicit water molecules on $PMo_{12}-Au(111)$.

Chapter 8

DFT and TD-DFT Calculations for Polyoxometalate-TiO₂ Interface



Polyoxometalates loading on TiO₂ particles are always utilized as a cocatalyst in the photocatalytic area. In this chapter, we are extending our strategy to model the interaction between PW₁₁Ti and TiO₂ surface, to give an insight into how the polyoxometalate affect the electronic properties of TiO₂ and its photocatalytic activity.

UNIVERSITAT ROVIRA I VIRGILI

DFT STUDIES ON POLYOXOPALLADATES AND POLYOXOMETALATES-SURFACE COMPOSITES: FROM STRUCTURE TO CATALYSIS

Zhongling Lang

8.1 Introduction and experimental background

Titanium dioxide (TiO₂) has received a lot of attention in energy conversion and environmental fields owing to its good stability, low cost, and less pollution as a photocatalyst.^[1] In spite of these advances, the application of TiO₂ still faces significant challenges due to the poor response to ultraviolet light (5% in solar light). To improve optical absorption of TiO₂-based materials, approaches such as dye-sensitization, doping or deposition of metal (or nonmetal) elements, *etc.* have been widely exploited.^[2]

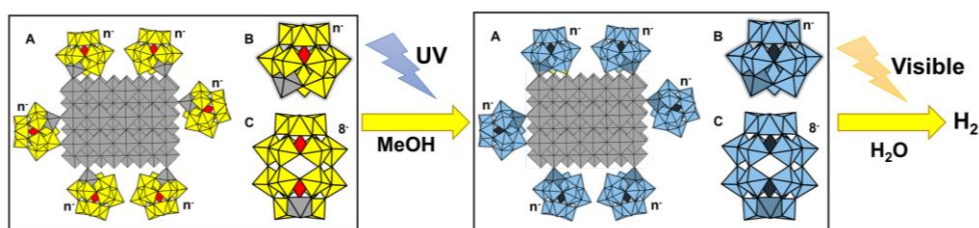


Figure 8.1. Direct coordination of Ti^{IV}-substituted POM clusters to anatase-TiO₂ cores and the photo-catalytic processes for hydrogen evolution reaction. Color code: Ti: light gray, W^{VI}: yellow, W^{IV}: blue.

Polyoxometalates (POMs) is one well-defined class of molecular metal-oxides of the early transition metals (Mo, W, V, Nb, and Ta) with a wide-ranging of properties and applications.^[3] These molecules have attracted large attentions as charge- or electron-storages due to the ability to accept multiple electrons reversibly. Composite materials by incorporating of POMs have been thoroughly investigated for solar energy conversion,^[4] molecular electronics,^[5] batteries,^[6] and catalysis.^[7] For example, the modified materials by adsorption polyoxometalates on carbon, Au, and Hg electrodes, showing much more active towards the hydrogen evolution reaction.^[8] The formation of POM monolayers on planar surface or nanoparticles has been well reviewed by several groups.^[9] Recently, Weinstock and co-workers have reported that polyoxometalates can serve as covalently coordinated redox-active ligands for anatase-TiO₂ nanocrystals as shown in Figure 8.1, evidenced by the combination of solid and solution-state analytical methods.^[10] By expansion, they found high activity of this material for hydrogen evolution reaction upon two light excitation steps. The POM-TiO₂ cores were firstly excited by UV light in MeOH/water solution to reduce POM. A further visible light driven electron transfer mechanism from the reduced POM to TiO₂

core was proposed to create high reduced TiO₂ nanocrystals (NCs). Once reduced, the TiO₂ NCs rapidly reduce protons in water to H₂. In cooperation with Weinstock group, we have attempted to understand the photocatalytic activity of this material by combining of DFT and time-dependent DFT method.

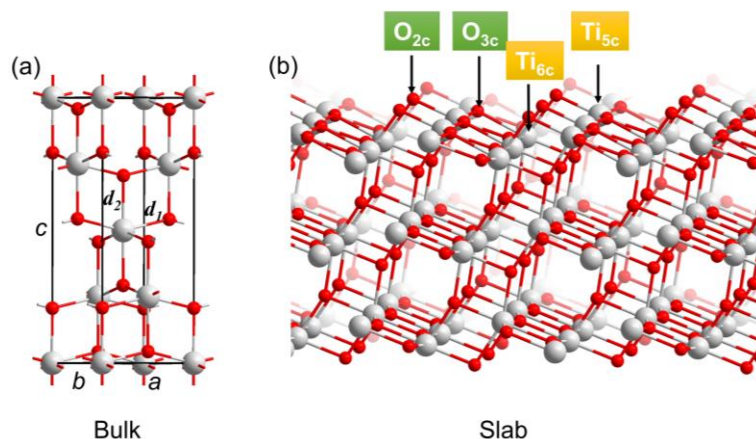


Figure 8.2. (a) Anatase TiO₂ unit cell; (b) Side view of anatase TiO₂(101) surface and the active sites on the surface. Color code: Ti: light gray, O: red.

8.2 Computational details

8.2.1 Models

On one hand, the reaction of amorphous TiO₂ with the lacunary α -PW₁₁O₃₉⁷⁻ at 170° can give the freely solvated $[\alpha\text{-PW}_{11}\text{TiO}_{40}]^{5-}$, and it is assumed that the POM remains coordinated to the anatase surface through the (101) planes. A periodically repeated slab of TiO₂(101) with cell dimensions 20.80 × 15.27 Å² was used to simulate the TiO₂ core, composed of six atomic layers with the bottom four layers fixed at its bulk configuration. A vacuum region higher than 15 Å was set to avoid interaction between the repeated cells. Considering the unsaturated sites on TiO₂(101) (Figure 8.2b), Ti_{5c} and O_{2c}, the Ti=O ligand in $[\alpha\text{-PW}_{11}\text{TiO}_{40}]^{5-}$ was readily coordinated with surface Ti_{5c} to form the PW₁₁TiO-Ti_{5c} linkage, as the model shown in Figure 8.3c. On the other hand, the POM-ligated Ti^{IV} atoms might coordinate to the anatase surface directly. Namely, the $[\alpha\text{-PW}_{11}\text{O}_{39}\text{Ti}^{\text{IV}}]^{3-}$ interacts with the surface via the active O_{2c} or O_{3c}. Totally, five possible coordination modes (Figure 8.3) were constructed to ascertain the adsorption mode of POM capping ligands on TiO₂(101). The details correspond to

model **a**: α -Na₃PW₁₁O₃₉Ti^{IV}-O_{2c}-2Ti, **b**: α -Na₃PW₁₁O₃₉Ti^{IV}-O_{3c}-3Ti, **c**: α -Na₅PW₁₁O₃₉Ti^{IV}-O-Ti_{5c}, **d**: α -Na₅PW₁₀TiO₃₉WO-Ti_{5c}, and **e**: α -Na₅PW₁₁TiO₄₀ bounded to TiO₂ via both WO-Ti_{5c} and TiO-Ti_{5c} linkages.

To simulate the absorption spectrum of TiO₂ nanoparticles modified by polyoxometalates, we considered a (TiO₂)₃₈ cluster, obtained by appropriately “cutting” an anatase slab exposing the majority (101) surface. This model has been widely used and shown to accurately reproduce the electronic and structural properties of anatase TiO₂.

8.2.2 Methodology

The geometry optimization and electronic structure calculations are performed using the projector augmented wave (PAW) method implemented in the Vienna *ab initio* simulation package.^[11,12] The electron exchange and correlation potential are treated with the Perdew-Wang 91 functional (PW91) and the kinetic energy cut-off was set to 500 eV.^[13] The DFT+U^[14] approach is used to describe the TiO₂, by setting U = 6.0 eV and J = 0.5 eV to treat the 3d electrons of Ti atoms (VASP).^[15] Bulk lattice parameters of anatase TiO₂ were obtained by allowing the ion position, cell shape, and volume to vary throughout minimization, with a Monkhorst-Pack k-point mesh of 7 × 7 × 4.^[16] The reciprocal space for POM-TiO₂ combined systems was described using two different Monkhorst Pack Schemes due to the large number of atoms: 1 × 1 × 1 for structure optimizations, and 5×5×1 for plotting the density of states (DOS). Solvent effects were included by means of the implicit solvation model (named VASP sol) implemented by Hennig and co-workers.^[17] All optimizations were performed until self-consistence with thresholds of 1·10⁻⁵ eV and 3·10⁻² eV·Å⁻¹ for the electronic and the ionic convergence respectively. The charge of the POM was compensated by using the equivalent sodium atoms displayed around the POM.

The geometry optimization of the clean and combined PW₁₁Ti- and PW₁₁Ti^{1e}-(TiO₂)₃₈ clusters were previously optimized in VASP with the same parameters as above for the slab calculations. The optimized geometries are then utilized to the single point time dependent density functional theory (TD-DFT) studies for the lowest 80 transitions, by using B3LYP functional together with 3-21G* and LANL2DZ/6-31G* basis sets for TiO₂ and POM respectively in Gaussian 09.^[18-19] The water effect was considered with the CPCM model.^[20] Finally, with the aid of Multiwfn 3.2 software, the UV-vis spectrum for the designed model was generated as a sum of Gaussian curves with a 0.3 eV half-height width, as well as the transition analysis.^[21]

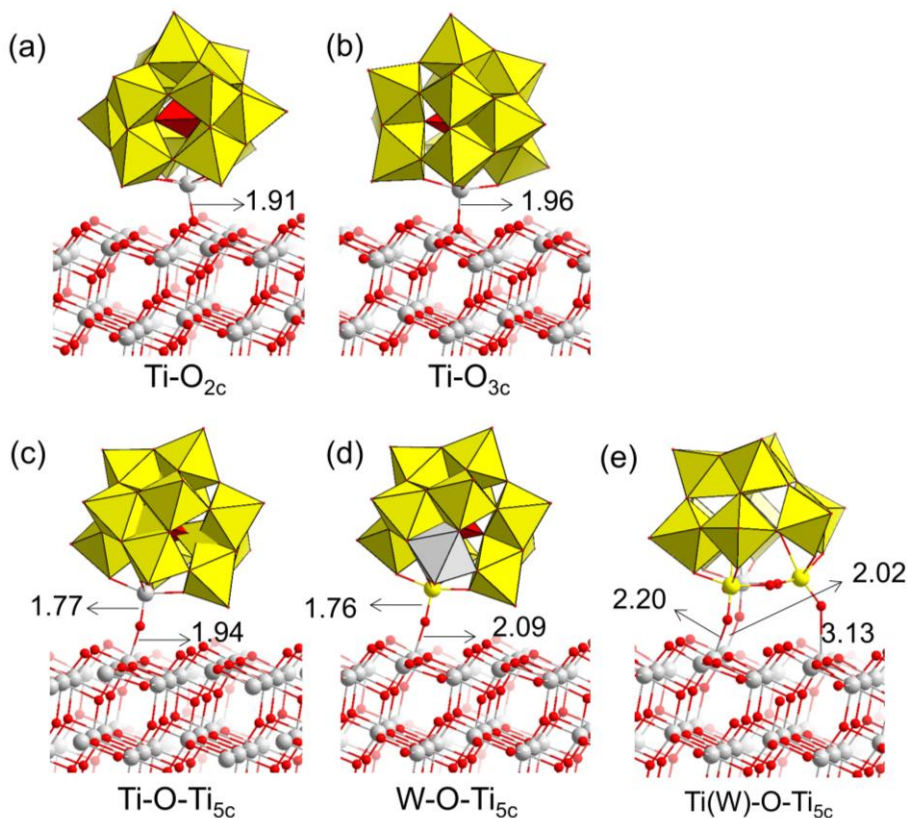


Figure 8.3. Polyhedral and Ball-stick representation of five possible coordination modes. **a**, $Na_3PW_{11}TiO_{39}$ bounded to TiO_2 via $Ti-O_{2c}$; **b**, $Na_3PW_{11}TiO_{39}$ bounded to TiO_2 via $Ti-O_{3c}$; **c**, $Na_5PW_{11}TiO_{40}$ bounded to TiO_2 via $TiO-Ti_{5c}$; **d**, $Na_5PW_{11}TiO_{40}$ bounded to TiO_2 via $WO-Ti_{5c}$; **e**, $Na_5PW_{11}TiO_{40}$ bounded to TiO_2 via both $WO-Ti_{5c}$ and $TiO-Ti_{5c}$ linkages. Color code: Ti: light gray, O: red, W: yellow.

8.3 Results discussions

8.3.1 Bulk anatase TiO₂ and clean TiO₂(101)

Table 8.1 compiles the calculated and experimental lattice parameters for the bulk anatase TiO₂, showing good coincidence between experimental observed and computed values. It is well known that pure DFT functionals, such as PBE and also PW91 used in our case, always underestimated the band gap of TiO₂ due to the self-interaction errors. Thus the GGA+U approach was considered in our calculation to treat the 3d electrons of Ti atoms. The band gaps of the bulk and TiO₂(101) slab were computed to 2.75 eV, which have been largely improved with respect to GGA, differing from the experimental value in only 0.45 eV ($E_{exp} = 3.2$ eV). The DOS for the

(101) surface are illustrated in Figure 8.5a, which exhibits typical semiconductor character with valence band (VB) and conduction band (CB) states dominated mainly by the O_{2p} and Ti_{3d} states, respectively. Conversely, small densities from O_{2p} (Ti_{3d}) also contributes for the CB (VB). The overlap of Ti_{3d} and O_{2p} orbitals in the valence and conduction bands suggest the presence of covalent interaction between Ti and O atoms.

Table 8.1. Comparison of calculated and experimental lattice parameters (Å) and bond lengths (Å) of bulk anatase TiO₂.

Å	Exp.	Cal. (gas)	Cal. (sol)
Lattice parameters			
<i>a</i>	3.782	3.818	3.814
<i>c</i>	9.502	9.678	9.574
Bond length			
<i>d</i> ₁	1.932	1.954	1.948
<i>d</i> ₂	1.979	2.000	1.994

8.3.2 Affinity of TiO₂(101) for PW₁₁Ti (PW₁₁Ti^{Ie})

The anatase (101) surface exhibits some unsaturated ions, five-fold coordinated Ti_{5c}, two-fold coordinated O_{2c}, and the saturated Ti_{6c} and O_{3c} ions, as labeled in Figure 8.2b. These sites are important in directing the adsorption of the polyoxometalates. Two forms of polyoxometalates were taken into account, [PW₁₁TiO₃₉]³⁻ and [PW₁₁TiO₄₀]⁵⁻, which are distinguished by whether one terminal -O ligand is coordinated on Ti atom or not. Thus the O defect [PW₁₁TiO₃₉]³⁻ is more likely to approach the nucleophilic region (O_{2c} or O_{3c}), whereas the latter prefers the electrophilic region (Ti_{5c}). Finally, five binding modes were constructed in Figure 8.3. Instead of the preferred S₄ orientation on the Au or Ag surfaces, the polyoxometalate was more likely to tilt adsorbed on TiO₂(101) via Ti-O_{2c} and TiO-Ti_{5c} linkages, with distances located in 1.91 to 2.02 Å. To have a *quantitative* measure of the interaction between the POM and the surface, the adsorption energies (*E*_{ads}) were defined by eq. 8.1:

$$E_{\text{ads}} = E_{\text{total}} - E_{\text{surf}} - E_{\text{NaPOM}} \quad (8.1)$$

Where *E*_{tot} is the energy of the whole system, *E*_{surf} is the energy of the relaxed bare surface, and *E*_{NaPOM} is the energy of the POM surrounded by the counterions. In Table

8.2, the adsorption energies calculated in vacuum and solution are presented. As discussed in previous chapters, the adsorption energies in vacuum are overestimated due to the over stabilization from the counterions and, in general, to use adsorption energies in solution is more appropriate to better understand the real interactions between POMs and surfaces.

Table 8.2. Adsorption energies (E_{ads}) for the $PW_{11}Ti$ and $PW_{11}Ti^{1e}$ adsorbed on $TiO_2(101)$ in vacuum and solution.

Sites	$E_{ads}(vac)$	$E_{ads}(sol)$
a	-42.6	-13.3
b	-26.5	4.5
c	-41.5	-11.4
d	-15.9	-2.9
e	-55.0	-10.0
c^{1e}	-57.4	-12.0
e^{1e}	-58.6	-12.9

a) All values are in $kcal\cdot mol^{-1}$;

b) **c^{1e}** and **e^{1e}** indicate the one electron reduced *c* and *e*.

As expected, the adsorption of $Na_3PW_{11}TiO_{39}$ on O_{3c} site (**b**) is unstable with an endothermic energy of $4.5 kcal\cdot mol^{-1}$, which is much energetic unfavorable than O_{2c} (**a**). Due to the more basic nature of $-TiO$ group than $-WO$, the connection between POM and $TiO_2(101)$ through $-OTi$ (**c**) site is obviously stronger than that $-OW$ (**d**), consistent with the longer $Ti_{5c}-O$ distance obtained in the latter. The model (**e**) with both $TiO-Ti$ and $WO-Ti$ linking in the model also strongly adsorbed on the surface. It can be seen that **a**, **c**, and **e** models in Figure 8.3 meet the most favorable adsorptions, with E_{ads} all more than $10 kcal\cdot mol^{-1}$, indicating one side that these two forms ($Na_3PW_{11}TiO_{39}$ and $Na_3PW_{11}TiO_{40}$) of the POMs would both possible be present on the surface. On the other hand, the small differences between **c** and **e** also suggest the $Na_3PW_{11}TiO_{40}$ can adsorb on the TiO_2 via more than one connection. Indeed, the strong exothermic values also support the covalent adsorption of polyoxometalate on the TiO_2 surface, which agrees fairly well with the experimental proposal by Weinstock *et al.* Furthermore, we have also considered the adsorptions of **c** and **e** with the POM in its reduced form. We

found that they are still tightly adsorbed on the surface with a little stronger with respect to its oxide form.

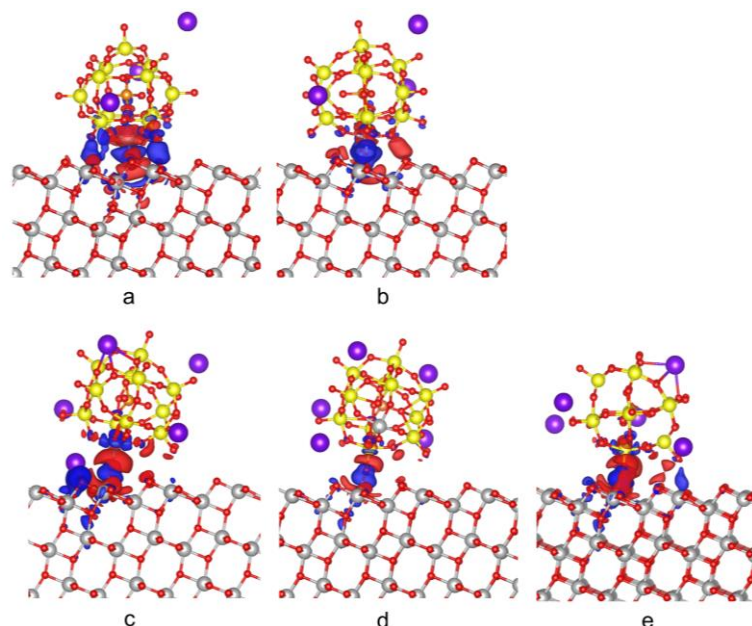


Figure 8.4. 3D charge density difference map for models **a-e** from side view, $\rho_{diff}(r) = \rho_{NaPOM/TiO_2(101)}(r) - \rho_{NaPOM}(r) - \rho_{TiO_2(101)}(r)$. Blue regions represent charge accumulations (electron density increase), whereas red regions represent charge depletions (electron density decrease). The charge differences are plotted with isovalue of $0.001 e/Bohr^3$ in Vesta code.

Partitioning the charge density in real space can be used to define the interactions and charge transfer between the two subsystems. In Figure 8.4, the variation in the charge density was plotted for **a-e** systems in solution, by subtracting the electronic charge of a NaPOM/TiO₂(101) system from its components NaPOM and TiO₂(101). In all cases, the charge redistribution mostly takes place at the NaPOM/TiO₂ interface region and relaxes a bit into the TiO₂ slab, whereas almost no charge transfer on the POM far away from the interface was detected. With different binding manners, one can notice that there is only little density change between the interface of POM and TiO₂ in **b** and **d** situations, while a significant density change occurs in **a**, **c**, and **e**, which support the stronger chemical bonding as obtained for adsorption energies.

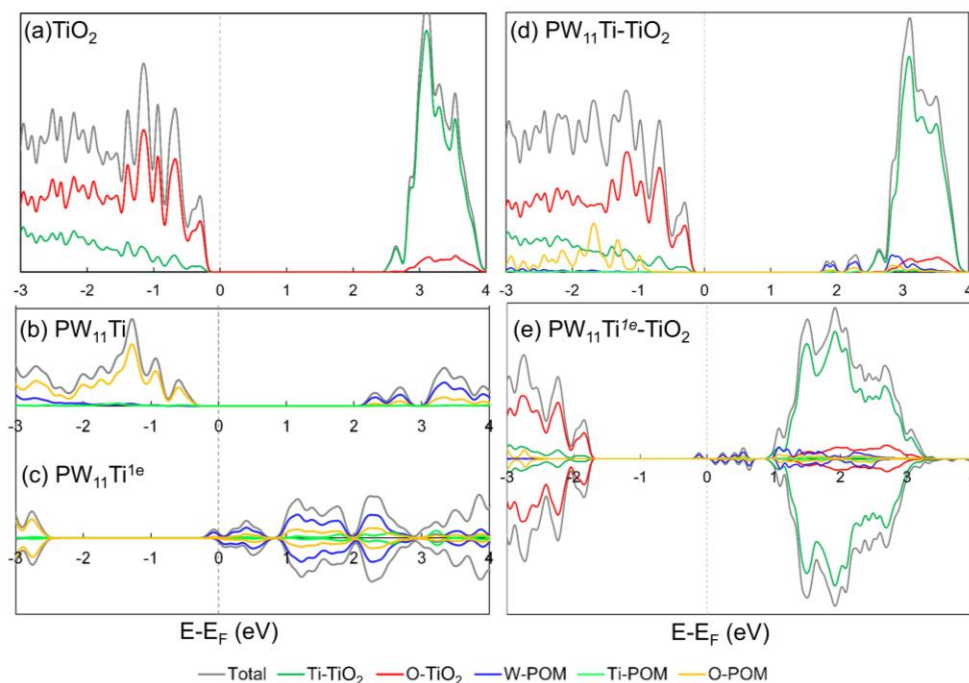


Figure 8.5. DOS and PDOS for the clean TiO₂(101) surface (a), the isolated polyoxometalates (b) (c); PW₁₁Ti-TiO₂(101) (d); and PW₁₁Ti^{1e}-TiO₂(101) (e) systems in solution.

8.3.3 Change in electronic structure of TiO₂ by POM adsorption

The covalent linkage between PW₁₁Ti and TiO₂ modifies some properties of the anatase. Figure 8.5 shows the DOS and PDOS for the clean and combined systems. Compared to the clean TiO₂(101), the fully oxidized Keggin PW₁₁Ti owns similar band gap of 2.5 eV by overall left shifting of the W(d) and O(sp) bands respect to that VB and CB in TiO₂. The modification of TiO₂ by this PW₁₁Ti results almost no shift for the VB. However, the insert of small density of W(d) band at the bottom of the TiO₂ conduction band, has the consequence of overall band gap decreasing for the composite, which was found 0.8 eV lower than the band gap of clean TiO₂ (2.75 eV). The narrowing of the band gap may induce some visible light absorption respect to the pure TiO₂ or isolated polyoxometalate materials. Comparing the DOS given in Figure 8.5d and 8.5e, with the reduced polyoxometalate (POM^{1e}) on the TiO₂, we observe that the W(d) bands appear below the Fermi energy and above the VB edge of the TiO₂ surface, namely, a new valence state was formed on the reduced polyoxometalate. There also show some empty (d) states just below the anatase conduction band. The

gap between the valence W(d) state and the high density of TiO₂ acceptor states is only 1.2 eV, expecting that electron transfer from POM^{1e} to TiO₂ could be easily occurred if further excitation are applied.

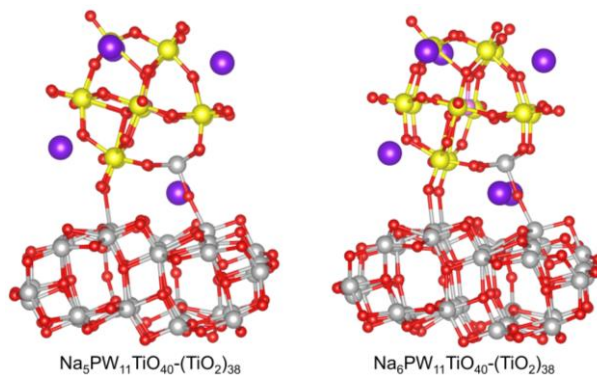


Figure 8.6. The optimized structure of $\text{Na}_5\text{PW}_{11}\text{TiO}_{40}$ (PW_{11}Ti) and $\text{Na}_6\text{PW}_{11}\text{TiO}_{40}$ ($\text{PW}_{11}\text{Ti}^{1e}$) adsorbed on the $(\text{TiO}_2)_{38}$ cluster.

8.3.4 UV-vis spectrum simulation

To simulate the absorption spectrum of TiO₂ nanoparticles modified with PW_{11}Ti and reduced $\text{PW}_{11}\text{Ti}^{1e}$, time-dependent DFT (TDDFT) calculations were performed based on a cluster model. Following the work by Angelis et al., we considered a neutral stoichiometric $(\text{TiO}_2)_{38}$ cluster by exposing the anatase {101} surface, which has shown to accurately reproduce the electronic and structural properties of anatase TiO₂.^[22] The clusters were firstly relaxed in VASP by using the similar parameters as for the slab model. The optimized geometries for the full oxide and one electron-reduced configurations are represented in Figure 8.6. Next, the geometries obtained from VASP were used for single point TDDFT calculations.

Figure 8.7 shows the simulated UV-visible absorption spectra of pure and combined systems at B3LYP level. For the bare $(\text{Ti}_2\text{O}_2)_{38}$ cluster, a H-L (HOMO-LUMO) gap of 4.24 eV is obtained, with a TDDFT lowest transition at 3.50 eV. This computed lowest excitation energy for TiO₂ cluster is in good agreement with the reported band gap value for TiO₂ nanoparticles of a few nanometres size, as well as with the experimental band gap (3.2 eV). It is worth noting that we have also performed the calculation for $(\text{Ti}_2\text{O}_2)_{38}$ with CAM-B3LYP, the lowest excitation energy for this pure TiO₂ is computed to 0.66 eV higher than the experimental value. Therefore, the calculations for combined systems are performed at B3LYP level.

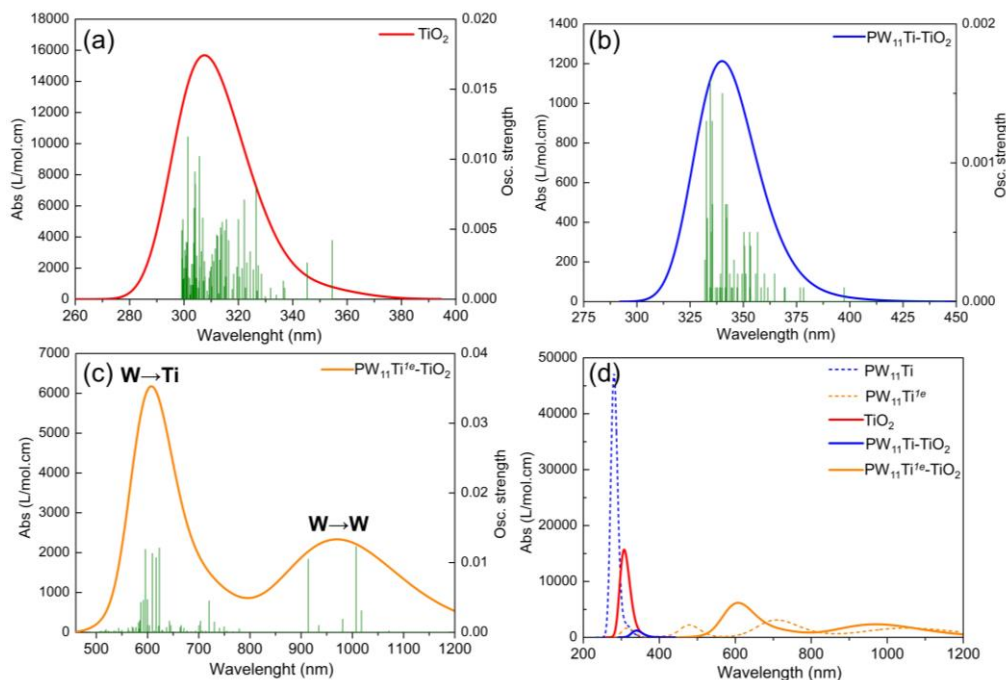
Chapter 8 DFT and TD-DFT Calculations for Polyoxometalate-TiO₂ Interface

Figure 8.7. Comparison of simulated UV-visible spectrum computed at B3LYP level for pure (TiO₂)₃₈ cluster (a), PW₁₁Ti-(TiO₂)₃₈ (b), PW₁₁Ti^{7e}-(TiO₂)₃₈ (c), and also a comparison for all species (d).

The isolated PW₁₁Ti anion displays a H-L gap of 4.35 eV with the most important transitions (highest oscillator strengths) appearing at 4.42 eV. The combined PW₁₁Ti-TiO₂ system has an absorption band that extends between ~ 3.1–3.7 eV (331–397 nm) with the peak centred at around 3.65 eV. Compared with the pure TiO₂ adsorption range (299–354 nm), the absorption band edge of the PW₁₁Ti-TiO₂ is slightly red-shifted. Here the two excited states (S59 and S75) that contributed in the transition with highest oscillator strengths are listed in Table 8.3. As for the molecular orbitals involved, the transition responsible for the band at 340 nm is essentially (ca. 32%) a HOMO-3 → LUMO+5 transition with partial oxygen ligand to Ti charge transfer character on TiO₂ (Figure 8.8). In addition, we have also checked some lower intensity peaks, many of them showing transition character from TiO₂ to POM. For the lowest excited state at 3.12 eV (S6), corresponding to the lowest transition at 397 nm, which is found a main contribution (77%) can be assigned to the HOMO-5 → LUMO transition. The occupied orbitals involved in this transition are almost localized on the TiO₂ part, whereas the unoccupied states are localized on the POM. Therefore, one would also expect a potential transfer from the titania to the POM by visible light irradiation. This

result provides evidence for potential photo-activity of the POM-TiO₂ based material. However, the experimental results provide by Weinstock *et al.* showing the POMs are more likely to behave as a local UV “filter”, due to the cover of POMs on the TiO₂ cores decreased the absorbance of TiO₂. The photoexcited POMs outside the TiO₂ core are easily accepted the electron from methanol in solution and lead to reduced POMs.

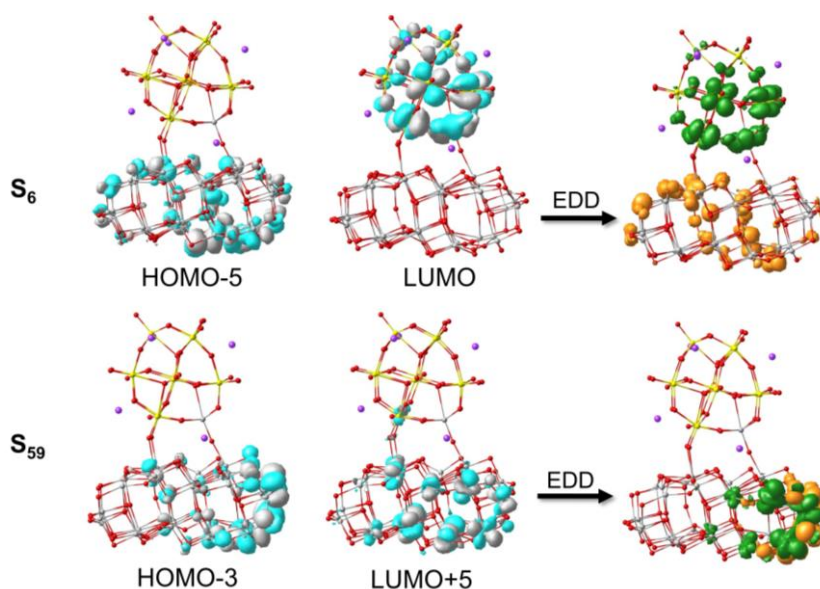


Figure 8.8. Molecular orbitals (isovalue = 0.02) and electron density difference (EDD, sovalue = 0.001) representations involved in the S_6 and S_{59} transitions for the $PW_{11}Ti-(TiO_2)_{38}$. Electron density difference (EDD) shows that the HOMO-5 to LUMO transition involves electron transfer from titania to the POM. In the EDD representation green and yellow identify regions where the electron density increase and decrease, respectively.

For the pristine $PW_{11}Ti^{le}$ and $PW_{11}Ti^{le}-TiO_2$, two broad bands in the visible region are observed. The spectrum of $PW_{11}Ti^{le}-TiO_2$ is obviously red-shifted compared to TiO_2 , and the bottom of the spectrum has reached to 485 nm and extended to visible region, which effectively compensates the weak absorption of titania in the visible region. The calculated bands contain several excitations and the most important transitions are listed in Table 8.3. The simulated spectrum shows two peaks around 600 nm and 1000 nm in visible region (Figure 8.7c). All these transitions take place from the HOMO of the complex, which is mostly localized on the d-type orbitals of W atoms in the POM. The HOMO of the combined system retains the nature of the

Chapter 8 DFT and TD-DFT Calculations for Polyoxometalate-TiO₂ Interface

Table 8.3. Excitation energy (ΔE , eV), wavelength (λ , nm), oscillator strength (f) and orbitals of POM. This character suggests a MMCT mechanism type, where electrons are transferred from the W(d) orbital of POM to the Ti(3d) of TiO₂ under visible composition of some representative transitions (S_n) in terms of MOs for $PW_{11}Ti - (TiO_2)_{38}$ and α -MOs for $PW_{11}Ti^{Ie} - (TiO_2)_{38}$.

S_n	λ_{max} (nm)	ΔE (eV)	f	Main contribution
$PW_{11}Ti - (TiO_2)_{38}$				
S0 → S6	397	3.12	0.0001	H-5 → L (77%)
S0 → S59	340	3.65	0.0015	H-3 → L+5 (32%), H-3 → L+6 (12%) H-3 → L+7 (9%), H-2 → L+6 (9%)
S0 → S75	334	3.71	0.0016	H-8 → L+5 (8%), H-6 → L+5 (3%) H-4 → L+5 (3%), H-3 → L+6 (3%)
$PW_{11}Ti^{Ie} - (TiO_2)_{38}$				
S0 → S46	595	2.08	0.01	H → L+38 (13%), H → L+37(9%) H → L+63 (11%), H → L+65 (9%)
S0 → S42	609	2.04	0.01	H → L+34 (10%), H → L+36 (8%) H → L+62 (19%), H → L+65 (6%)
S0 → S40	616	2.01	0.01	H → L+30 (12%), H → L+31 (13%) H → L+60 (20%), H → L+64 (11%)
S0 → S38	622	1.99	0.01	H → L+28 (14%), H → L+30 (11%) H → L+31 (12%), H → L+34 (16%)
S0 → S10	913	1.36	0.01	H → L+15 (85%), H → L+18 (5%)
S0 → S7	1006	1.23	0.01	H → L+8 (69%), H → L+7 (7%) H → L+9 (7%)

isolated anion. However, the composition of the unoccupied states involved in the transition at about 600 nm is quite different from those at 1000 nm. For example, the adsorption at 622 nm (S0 → S38, 1.99 eV) mainly arises from the α -HOMO to α -LUMO+28 (30, 31, and 34) excitations, those unoccupied states show major donations from Ti(3d), and relatively smaller contributions from the W(4d) and O(2p) orbitals of POM. This character suggests a MMCT mechanism type, where electrons are

transferred from the W(d) orbital of POM to the Ti(3d) of TiO₂ under visible light irradiation, resulting in the reduction of TiO₂. It is worth mentioning that there are POM excited states that are strongly coupled to the TiO₂, which may give rise to large rates of electron injection. The electron density difference map (EDDM) representation for state 38 shown in Figure 8.9 also supports the electron transfer from W orbitals to TiO₂ upon visible excitation. All these results clearly support the experimental proposed mechanism for the hydrogen evolution. On the other hand, the most important (α -LUMO+15 and α -LUMO+8) unoccupied orbitals for the adsorption at 913 (1.36 eV) and 1006 nm (1.23eV) are orbitals with significant W(d) contributions of POM, resulting that the excitation occurs mainly inside the POM. Hence, the DFT simulations help to understand how the reduced polyoxometalate improve the adsorption of TiO₂ in visible region, and confirm the electron transfer mechanism between the reduced polyoxometalates and TiO₂.

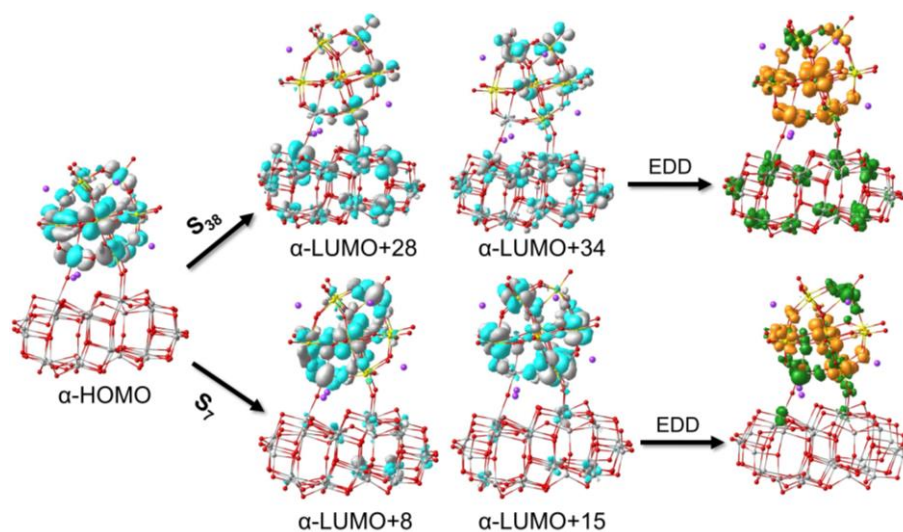


Figure 8.9. Molecular orbitals and electron density difference representations involved in the S_{38} and S_7 transitions for $PW_{11}Ti^{Ie}-(TiO_2)_{38}$.

8.4 Conclusions

In this chapter, based on DFT and TDDFT calculations we have provided a detailed characterization of the electronic structure and absorption spectrum for the fully oxidized and reduced polyoxometalate modified TiO₂ systems. Our results show that there is a covalent adsorption of the POM on the TiO₂(101) surface with $E_{ads} > 10$

Chapter 8 DFT and TD-DFT Calculations for Polyoxometalate-TiO₂ Interface

kcal·mol⁻¹ in water. This interaction can take place via more than one POM-TiO₂ surface contact. By modification, a considerable decrease of band gap has been obtained for reduced PW₁₁Ti^{1e} adsorbed on TiO₂(101) and UV-*vis* spectrum simulations further reveal that reduced POM can efficiently improve the weak absorption of TiO₂ in visible region, thus improve its photocatalytic activity for hydrogen evolution reaction. Through the theoretical understanding, we are expected to provide more valuable insights into the POM-TiO₂ system, and offer a molecular engineering guide to design novel highly efficient photocatalysts.

References and Notes

- [1] A. L. Linsebiger, G. Q. Lu and J. T. Yates, *Chem. Rev.* 1995, 95, 735–758.
- [2] (a) J. Willkomm, K. L. Orchard, A. Reynal, E. Pastor, J. R. Durrant and E. Reisner, *Chem. Soc. Rev.* 2015, 45, 9–23; (b) L. G. Devi and R. Kavitha, *RSC Adv.* 2014, 4, 28265–28299; (c) A. Bumajdad and M. Madkour, *Phys. Chem. Chem. Phys.* 2014, 16, 7146–7158; (d) W. Ong, L. Tan, S. Chai, S. Yong and A. R. Mohamed, *Nanoscale* 2014, 6, 1946–2008.
- [3] M. T. Pope, *Heteropoly and Isopoly Oxometalates*. Springer-Verlag: New York, 1983.
- [4] (a) B. Matt, J. Fize, J. Moussa, H. Amouri, A. Pereira, V. Artero, G. Izzet and A. Proust, *Energy Environ. Sci.* 2013, 6, 1504–1508. (b) X. Z. Luo, F. Y. Li, B. B. Xu, Z. X. Sun, L. Xu, *J. Mater. Chem.* 2012, 22, 15050–15055.
- [5] (a) T. He, J. L. He, M. Lu, B. Chen, H. Pang, W. F. Reus, W. M. Nolte, D. P. Nackashi, P. D. Franzon and J. M. Tour, *J. Am. Chem. Soc.* 2006, 128, 14537–14541. (b) A. M. Douvas, E. Makarona, N. Glezos, P. Argitis, J. A. Mielczarski and E. Mielczarski, *ACS Nano* 2008, 2, 733–742; (c) M. Lu, W. A. Nolte, T. He, D. A. Corley and J. M. Tour, *Chem. Mater.* 2009, 21, 442–446.
- [6] H. Wang, S. Hamanaka, Y. Nishimoto, S. Irle, T. Yokoyama, H. Yoshikawa and K. Awaga, *J. Am. Chem. Soc.* 2012, 134, 4918–4924. (b) Y. Nishimoto, D. Yokogawa, H. Yoshikawa, K. Awaga and S. Irle, *J. Am. Chem. Soc.* 2014, 136, 9042–9052.
- [7] T. Hsu-Yao, K. P. Browne, N. Honesty and Y. J. Tong, *Phys. Chem. Chem. Phys.* 2011, 13, 7433–7438. (b) S. Li, X. Yu, G. Zhang, Y. Ma, J. Yao, B. Keita, N. Louis and H. Zhao, *J. Mater. Chem.* 2011, 21, 2282–2287.
- [8] (a) B. Keita and L. Nadjo, *J. Electroanal. Chem.*, 1985, 191, 441–448; (b) B. Keita and L. Nadjo, *J. Electroanal. Chem.* 1987, 227, 265–270; (c) B. Keita, L. Nadjo and J. P. Haeussler, *J. Electroanal. Chem.* 1987, 230, 85–97; (d) B. Keita and L. Nadjo, *J. Electroanal. Chem.*, 1988, 247, 157–172; (e) B. Keita and L. Nadjo, *J. Electroanal. Chem.* 1988, 243, 87–103; (f) B. Keita, L. Nadjo and J. M. Saveant, *J. Electroanal. Chem.* 1988, 243, 105–116.
- [9] (a) B. Keita, T. B. Liu and L. Nadjo, *J. Mater. Chem.* 2009, 19, 19–33; (b) S. G. Mitchell and J. M. de la Fuente, *J. Mater. Chem.* 2012, 22, 18091–18100; (c) Y. F. Wang and I. A. Weinstock, *Chem. Soc. Rev.* 2012, 41, 7479–7496.
- [10] R. Manoj, G. G. Or, M. Saganovich, O. Zeiri, Y. F. Wang, M. R. Chierotti, R. Gobetto and I. A. Weinstock, *Angew. Chem. Int. Ed.* 2015, 54, 12416–12421.

- [11] (a) G. Kresse and J. Hafner, *J. Phys. Rev. B: Condens. Matter.* 1993, 47, 558–561; (b) G. Kresse and J. Hafner, *Phys. Rev. B: Condens. Matter.* 1994, 49, 14251–14269; (c) G. Kresse and J. Furthmüller, *Comput. Mater. Sci.* 1996, 6, 15–50; (d) G. Kresse and J. Furthmüller, *Phys. Rev. B: Condens. Matter.* 1996, 54, 11169–11186.
- [12] (a) P. E. Blöchl, *Phys. Rev. B: Condens. Matter* 1994, 50, 17953–17979; (b) J. Hafner, *J. Comput. Chem.* 2008, 29, 2044–2078.
- [13] J. P. Perdew, J. A. Chevary, S. H. Vosko, K. A. Jackson, M. R. Pederson, D. J. Singh and C. Fiolhais, *Phys. Rev. B: Condens. Matter* 1992, 46, 6671–6687.
- [14] S. L. Dudarev, G. A. Botton, S. Y. Savrasov, C. J. Humphreys and A. P. Sutton, *Phys. Rev. B* 1998, 57, 1505–1509.
- [15] A. Du, Y. H. Ng, N. J. Bell, Z. Zhu, R. Amal, S. C. Smith, *J. Phys. Chem. Lett.* 2011, 2, 894–899.
- [16] H. J. Monkhorst and J. D. Pack, *Phys. Rev. B: Solid State* 1976, 13, 5188–5192.
- [17] (a) M. Fishman, H. L. Zhuang, K. Mathew, W. Dirschka and R. G. Hennig, *Phys. Rev. B* 2013, 87, 245402-1–245402-7; (b) K. Mathew, R. Sundararaman, K. Letchworth-Weaver, T. A. Arias and R. G. Hennig, *J. Chem. Phys.* 2014, 140, 084106-1–084106-8.
- [18] (a) A. D. Becke, *J. Chem. Phys.* 1993, 98, 5648–5652; (b) C. Lee, W. Yang and R. G. Parr, *Phys. Rev. B* 1988, 37, 785–789.
- [19] M. J. Frisch et al., *Gaussian09W*, Revision C01; Gaussian, Inc.: Wallingford, CT, 2009.
- [20] J. Tomasi, B. Mennucci and R. Cammi, *Chem. Rev.* 2005, 105, 2999–3094.
- [21] T. Lu and F. J. Chen, *Comp. Chem.* 2012, 33, 580–592.
- [22] F. D. Angelis, A. Tilocca and A. Selloni, *J. Am. Chem. Soc.* 2004, 126, 15024–15025.

Chapter 9

Concluding Remarks



Chapter 9 Concluding Remarks

In addition to the conclusions presented in each chapter, the following general conclusions can be drawn from this thesis:

- The capture of a M^{n+} ion by a peripheral Pd^{II} -oxo shell involves the competition between the mother Pd^{II} and the guest metal ions, the main factors governing the formation of a particular MPd_{12} are the electrostatic-interaction between the cation and the surrounding oxo ligands and the dehydration ability of the cation in solution, in which the charge and size of the guest cation are critical.
- The nature of the interaction for Pd-Ag and Ag-Ag-Ag in novel Ag_4Pd_{13} and Ag_5Pd_{15} compounds have been characterized with QTAIM method. Whereas Pd-Ag link shows “intermediate interaction” that be termed as partially covalent and partially electrostatic, the Ag-Ag-Ag homometallic interactions have a largely electrostatic nature.
- A mechanistic study for the complete reduction of a Au^{III} salt to Au^0 using an ‘*in built*’ electron source, the Kabanos POM ($[Na\{(Mo_2^VO_4)_3(\mu_2-O)_3(\mu_2-SO_3)_3(\mu_6-SO_3)_2\}]^{15-}$), has shown that the process is highly favourable from a thermodynamic point of view.
- We have established a robust strategy for the modelling of charged species adsorbed on surfaces. The incorporation of counterions in the computational models is crucial for accurately reproducing the electronic properties. The inclusion of solvent reduces the over stabilization of the anion-cation or anion-surface interactions, describing much better the adsorbed system.
- The lacunary PW_{11} cluster does not preferentially adsorb on the gold surface via its more nucleophilic mono defect face but, rather, through less negatively charged terminal oxygen ligands, induced by the strong anion-cation interactions from the same and neighbouring units.
- The water gas shift reaction is proposed to have a mechanism that mainly involves the carboxyl ($COOH^*$) intermediate directly produced from CO and H_2O at the PMo_{12} supported Au interface, with a barrier as low as $7.8 \text{ kcal mol}^{-1}$ in solution for the determining step. The high catalytic activity is contributed

Chapter 9 Concluding Remarks

by the nature of Mo(d) and O(sp) bands nearby the Fermi energy of $\text{PMo}_{12}\text{-Au}(111)$. The role of POMs is to serve as both electron and proton acceptors.

- The interaction of the TiO_2 surface with both the fully oxidized PW_{11}Ti and its reduced partner exhibits a covalent nature. The presence of the reduced anion efficiently improves the weak absorption of TiO_2 in the visible region. Simulated UV-Vis spectrum suggests that reduced PW_{11}Ti can transfer electrons to TiO_2 under visible light irradiation.

Acknowledgements

Acknowledgements

Undertaking this PhD study in UVR has been a really life-changing and poignant experience for me and it would not be possible to finish without the support and guidance that I received from many people.

First of all, I would like to give the special mention and great thanks to my supervisors, Prof. Poblet and Dr. Anna. Thanks for offering me a great opportunity to pursue my PhD within the quantum chemistry group. Thanks for your excellent supervision, all the helps and supports during my PhD period. Thanks for reading and correcting through my thesis carefully. Over the past three years, I have learned a lot from both of you, which goes beyond the world of science. Your patience and enthusiasm make me feel quite relax in every discussion. Even it is impossible to list all in detail, I hope you to know that I really enjoy the research under your supervision. With all my heart, "muchas gracias"!

I would like to thank all the collaborators from the quantum group, Xavi L., Jordi, Xavi Aparicio, and Gerard Novell, thanks for the suggestions of our collaboration work and corrections for the manuscripts. And also other "bosses" in the group, Toni, Coen, Mar, and Rosa, thanks for the tips and good times we spent. Thanks Jose, Elisenda, and Moisés for technical helps.

I would also like to thank some international collaboration groups, the Prof. Kortz, Dr. Mitchell, and Prof. Weinstock groups, our works together are absolutely smooth and fruitful.

Many thanks to all the student members of the Quantum Chemistry Group (Those graduated: Pablo Jiménez, Pablo A., Marc, Núria, Gian, Pedro, Sergi, Gerard, Josep Casellas, Mariano, Ximo. And at Present: Laura, Albert, Roser, Diego, Magda, Almudena, Jianfang, Antonio, *et al.*) As a non-Spanish speaking member, you all always did your best to help me to understand well everything, and invited me to participate in different parties. Because of you, my staying in Spain became much easier and wonderful. This will be an unforgettable experience in my life. I know a simple thank you is far from enough to express my deepest gratitude, but even so, I would still say to all of you: thanks very much.

I gratefully acknowledge the funding received towards my PhD study from the Universitat Rovira i Virgili.

I would like to thank all my Chinese friends in Spain.

Acknowledgements

At last, I would like to thank my families, especially my parents and husband, your support make me less stressful and more confident of what I am doing.

值此博士论文完成之际，我要由衷的感谢我辛勤的父母和家人，是你们的鼓舞与支持让我能不断地找到前进的动力。感谢我的丈夫李超对我学业的支持，生活上的关心与照顾，使我能安心学习和研究。感谢在异国他乡认识的中国朋友们，谢谢你们对我生活学业的帮助。人说，心存感恩，处处可感恩，一路走来，很幸运，在此向曾经所有关心、支持、帮助过我的老师、同学及朋友表示深深的谢意。

Tarragona, May 31, 2017

UNIVERSITAT ROVIRA I VIRGILI

DFT STUDIES ON POLYOXOPALLADATES AND POLYOXOMETALATES-SURFACE COMPOSITES: FROM STRUCTURE TO CATALYSIS

Zhongling Lang



UNIVERSITAT
ROVIRA i VIRGILI